5-2-2022

Fundamental Properties of Active Galaxies: Distances and Black Hole Masses of Nearby Seyferts

Justin H. Robinson
Georgia State University

Fundamental Properties of Active Galaxies: Distances and Black Hole Masses of Nearby Seyferts

by

JUSTIN H. ROBINSON

Under the Direction of Misty C. Bentz, PhD

ABSTRACT

The past 20 years of observations have revealed correlations between supermassive black holes (SMBHs) and large scale galaxy properties. These correlations are generally interpreted to be the signature of coevolution between galaxies and black holes, therefore accurate measurements of the properties on which these correlations are constructed is crucial for understanding galaxy-black hole evolution over cosmic time. We first present HI 21 cm spectroscopy for 31 AGN host galaxies with direct black hole mass ($M_{\rm BH}$) measurements from reverberation mapping (RM), 12 of which are the first published detections at 21 cm. We measure emission-line fluxes, widths, and recessional velocities from which we derive HI mass, gas mass ($M_{\rm GAS}$), and redshift. Combining $M_{\rm GAS}$ with stellar mass ($M_\star$) allows the baryonic mass ($M_{\rm BARY}$) to be estimated. We then combine the emission line measurements with *Hubble Space Telescope* and ground-based optical and near-infrared images to measure Tully-Fisher distances to 24 of the 31 galaxies, 14 of which are the first reported distances independent of redshift. We estimate dynamical mass ($M_{\rm DYN}$) within the HI radius, and a comparison to $M_{\rm BARY}$ constrains the dark matter mass ($M_{\rm DM}$). We find significant correlations

between $M_{\rm BH}$ and $M_{\rm BARY}$, $M_{\rm DYN}$, and $M_{\rm DM}$, suggesting black hole-galaxy connections on scales larger than commonly considered. Finally, we present preliminary results of dynamical modeling of the broad line regions (BLRs) of five AGNs, four of which are the first reported. Direct modeling of the continuum light curve and broad emission lines yields constraints on BLR geometry and kinematics in addition to constraints on $M_{\rm BH}$ that do not depend on the scale factor $\langle f \rangle$ required by traditional RM methods. This work presents measurements of fundamental properties of RM AGNs and their host galaxies that may serve as important tools for future analyses devoted to furthering our understanding of black hole-galaxy coevolution.

INDEX WORDS: Observational astronomy, Seyfert galaxies, Active galactic nuclei, Supermassive black holes, Spectroscopy, Distance, Redshift, Broad line region, Dynamical modeling

Fundamental Properties of Active Galaxies: Distances and Black Hole Masses of Nearby Seyferts

by

JUSTIN H. ROBINSON

A Dissertation Submitted in Partial Fulfillment of the Requirements of

Doctor of Philosophy

in the College of Arts and Sciences

Georgia State University

2022

Fundamental Properties of Active Galaxies: Distances and Black Hole Masses of Nearby Seyferts

by

JUSTIN H. ROBINSON

Committee Chair:	Misty C. Bentz
Committee:	D. Michael Crenshaw
	Megan C. Johnson
	Hélène M. Courtois
	Sebastien Lépine

Electronic Version Approved:

Office of Graduate Studies

College of Arts and Sciences

Georgia State University

May 2022

DEDICATION

I dedicate this dissertation to my friends, my family, and my loving girlfriend. It is an astronomical understatement to say I would not have been able to complete the work presented here without their immense support, and I am forever grateful.

In loving memory of Vivian Biondi.

ACKNOWLEDGEMENTS

I am indebted to my high school mathematics and physics instructor Andrew Jolliff, who not only persuaded me to pursue physics, but ignited my passion for black holes and astronomy. I am grateful for my undergraduate advisors Drs. Ronald Olowin and Brian Hill for preparing me for graduate studies and providing me with fundamental research skills and opportunities, including training at and conducting research with the Arecibo Observatory. I am thankful to Drs. Rebecca Koopmann, Martha Haynes, and Aparna Venkatesan for their incredible mentorship with the Arecibo Pisces-Perseus Supercluster Survey undergraduate research program, providing me with skills and knowledge that proved instrumental in my graduate studies. I thank Drs. Edward Boyda and Jessica Kintner for their patience and advisement in physics curricula, research, and my graduate career. I am enormously thankful to my girlfriend Allison Cash, who has filled the last year of my life with love, care, and unwavering support, rendering the thought of completing this work without her unimaginable.

I would like to thank my committee members, Drs. D. Michael Crenshaw, Megan Johnson, Hélène Courtois, and Sebastien Lépine for their suggestions that improved this thesis. I am thankful to my collaborators including Drs. Megan Johnson, Hélène Courtois, D. Michael Crenshaw, Peter Williams, Gisella De Rosa, and Michael Fausnaugh for their guidance and advice on the works included in this dissertation. I would also like to thank Dr. Justin Cantrell for assistance in cluster computations, Dr. Bokyoung Kim for programming assistance, Rachael Merritt for helpful conversations, suggestions on public talks and colloquia, and an unending amount of support, and Dr. Mitchell Revalski for helpful conversations, programming advice, tutelage on *Hubble Space Telescope* data reduction and analysis, suggestions on research presentations, and overall

mentorship throughout my graduate career. Finally, I would like to express the greatest gratitude to my advisor Dr. Misty Bentz, whose seemingly infinite amount of patience, expertise, and guidance have allowed me to achieve more than I ever thought possible, and I am and will be forever grateful.

We thank the referees for helpful suggestions that improved the clarity of the two published works presented here. M.C.B. gratefully acknowledges support from the NSF through CAREER grant AST-1253702 and grant AST-2009230. H.M.C. acknowledges support by the CNES and Institut Universitaire de France. We thank Joy Skipper for helpful comments on observing scripts and data reduction. We thank Mitchell Revalski for advisement of drizzling techniques for archival *HST* data. We thank Wesley Peters for helpful observing strategies with the APO ARC telescope. We also thank Joanne Hughes for obtaining sky flat observations for the ARCTIC instrument.

This research has made use of the NASA/IPAC Extragalactic Database (NED), which is operated by the Jet Propulsion Laboratory, California Institute of Technology, under contract with the National Aeronautics and Space Administration.

This work is based on observations obtained at the MDM Observatory, operated by Dartmouth College, Columbia University, Ohio State University, Ohio University, and the University of Michigan.

This work is based on observations obtained with the Apache Point Observatory 3.5 m telescope, which is owned and operated by the Astrophysical Research Consortium, and with Apache Point Observatory's 0.5 m Astrophysical Research Consortium Small Aperture Telescope.

This research has been supported by RECONS (`www.recons.org`) members Michele Silverstein, Todd Henry, and Wei-Chun Jao, who provided data as part of the long-term astrometry/photometry program at the CTIO/SMARTS 0.9 m, which is operated as part of the SMARTS Consortium.

Funding for SDSS-III has been provided by the Alfred P. Sloan Foundation, the Participating Institutions, the National Science Foundation, and the U.S. Department of Energy Office of Science. The SDSS-III web site is http://www.sdss3.org/.

Table of Contents

List of Tables

List of Figures

Chapter 1

Introduction

1.1 *A Galactic Handbook*

Our home galaxy, The Milky Way, and all other galaxies that inhabit the universe hurtle through space as vast collections of gas, dust, billions of stars, and colossal cocoons of dark matter. Efforts to categorize the expanding collection of observations of galaxies include the Hubble diagram for galaxy classification (Hubble, 1926), which is displayed in Figure 1.1 and is generally divided into two main categories. Galaxies that contain little to no gas, harbor mainly older, redder stars, and appear spherical to oblate in shape are classified as ellipticals (E). Hubble denoted the shape of ellipticals with a numerical scheme dictated by their ellipticity, where a near-circular appearance is classified as 'E0' and a highly elliptical appearance as 'E7.' Galaxies that populate the opposite side of the diagram feature large disks of gas and dust arranged in magnificent spiral patterns, and are thus designated as spirals (S). The disks of these galaxies encompass a central, spherical bulge composed of older stars. The transition between bulge-dominated and disk-dominated spirals is denoted as the sequential classifications 'Sa,' 'Sb,' and 'Sc.' Lenticulars display morphological features of both main categories, namely an oblate appearance in addition to a dusty disk. Irregulars (or Peculiars) are named such that their morphological features cannot be simply categorized as elliptical or spiral.

Spirals can exhibit more unique structures, creating two distinct branches of classification. Those with disks and bulges occupy the top branch, whereas the bottom branch classifies spirals boasting an additional linear bar structure, denoted as 'B.' The central bulge sitting amongst the

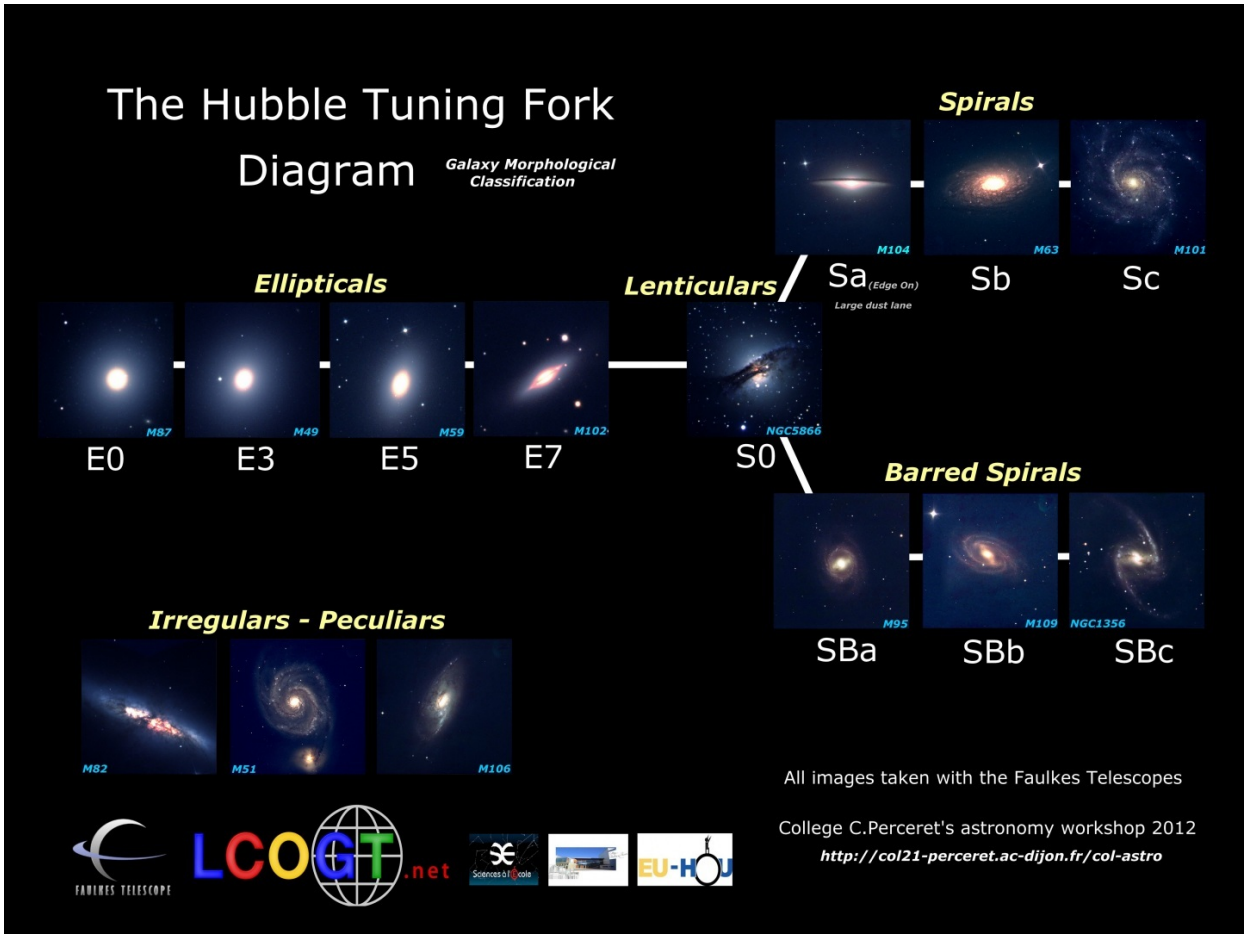

Figure 1.1: Edwin Hubble's diagram for galaxy morphological classification. Images taken with the Faulkes Telecopes operated by Las Cumbres Observatory. Image credit: College C. Perceret.

Figure 1.2: Color-composited image of spiral galaxy NGC 4051. The bulge structure is found in the center, traced out by billions of older, yellow stars. The young, bright, blue stars light up the surrounding gas and dust, all of which compose the spiral arms of the galactic disk. Image credit: ESA/Hubble NASA, D. Crenshaw and O. Fox.

bar and galactic disk of the SBbc-type galaxy NGC 4051 is shown in Figure 1.2. The sequence of elliptical classifications joined to the branches of spirals garnered the term 'tuning fork' for Hubble's diagram. Hubble originally believed the tuning fork to be an evolutionary sequence, where galaxies would evolve sequentially from left to right, thus ellipticals are referred to as 'early-type' galaxies and spirals 'late-type.' However, mergers and interactions between spirals were originally theorized to produce ellipticals (Toomre & Toomre, 1972), as opposed to ellipticals evolving to spirals. This notion has been supported by both observations, where higher prevalences of spirals have been seen in distant galaxy clusters compared to nearby clusters (e.g., Dressler et al. 1997; Postman et al. 2005; Smith et al. 2005; Fasano et al. 2006; Desai et al. 2007), and large hydrodynamical

simulations, where high density environments induce interactions between spirals which then evolve into ellipticals over cosmic time (e.g., Martel et al. 1998; Genel et al. 2014).

Detailed investigations of the centers of galaxies began to reveal truly strange behavior lurking in the central bulges. It slowly became clear that whatever the source may be necessitated an incredible amount of mass ($\sim 10^6 - 10^9$ solar masses, or $M_\odot$) localized to a very small area ($\lesssim$1 light year). The nature of such an object is understood today as a supermassive black hole (SMBH).

1.2 *A Brief History of Supermassive Black Holes*

The first inkling of a black hole-like object came from a letter by a clergyman detailing a thought experiment for measuring the mass of a star (Michell, 1784). He pondered that if light was truly comprised of particles (photons) with mass as per Newton's theory (Newton, 1704), then their speed would be reduced by the gravitational pull of a massive star. One would be able to measure the star's mass through the reduced speed of photons, however if the force of gravity was large enough (i.e., if the star was massive enough), the speed of light would be insufficient to escape the star, and thus it would be invisible to any observer. Today, we know photons are massless and the speed of light is constant regardless of reference frame (Einstein, 1905), however this seed of an invisible massive star would grow into the concept of a black hole.

Black holes would reemerge over 100 years later, predicted with the first exact solution to Einstein's field equations by Schwarzschild (1916). Observational evidence followed with the investigation of the unresolved radio source 3C 273 (Schmidt, 1963). The object was originally believed to be a star, however its spectrum revealed emission lines so dramatically redshifted that they were not immediately identified. The Hubble-Lemaître Law (Hubble, 1929) predicted the distance to the object to be $\sim$1-2 billion light years, thus revealing its immensely powerful energy output for such a bright apparent magnitude at such a large distance. Schmidt (1963) offered an explanation that the object, referred to as a quasar, could be the nuclear region of another galaxy, which would dictate the size of the nucleus to be $<$ 1 kiloparsec (1 pc $\approx$ 3.26 light-years).

A possible explanation of the behavior of 3C 273 and other QSOs observed at the time came from Salpeter (1964) and Zeldovich & Novikov (1964), who postulated the inner mechanism may be driven by accretion of interstellar gas onto compact objects, requiring masses of $\gtrsim 10^6\, M_\odot$ to reproduce the observed luminosities of these extremely distant objects. Lynden-Bell (1969) later proposed a model for the central engines of quasars as an accretion disk around a SMBH. As gas in the disk could not experience infall towards the black hole without relinquishing angular momentum, there would thus be ample time for the gas to radiate its energy while falling through the immense gravitational potential of the black hole. The gas would also have time to thermalize enough to generate the necessary observed emission across the EM spectrum, specifically X-ray emission.

Lynden-Bell (1969) also compared the enormous energy output of distant quasars to the comparatively low output of galaxy nuclei in the nearby universe, and the dichotomy between the two suggested that the nearby galactic cores were the older, less active siblings of quasars. The work of Lynden-Bell & Rees (1971) later argued that if nearby galaxies were truly older quasars, and hence harbored an inactive version of the same central mechanism, then these galaxies may also serve as hosts to dormant SMBHs. Definitive evidence of this hypothesis came from proof of the existence of a dormant SMBH at the center of the Milky Way from the highly detailed monitoring of the motions of stars in the inner central parsecs of the Milky Way's bulge (Ghez et al., 2000; Genzel et al., 2000; Ghez et al., 2008). Simultaneously, the revolution of observational astronomy ushered in by the *Hubble Space Telescope* (*HST*) revealed SMBHs (both active and inactive) to lie at the heart of nearly every major galaxy in the observable universe (Magorrian et al. 1998; Kormendy 2004; see Tables 2 and 3 from the review of Kormendy & Ho 2013).

1.2.1 *Active Galactic Nuclei*

Today, the mechanism for producing the immense energies and luminosities of quasars is understood to be a SMBH undergoing a period of accretion, creating an active galactic nucleus (AGN). The gas that fuels the accretion of the black hole can be driven by gravitational interactions between galaxies (Kauffmann & Haehnelt, 2000; Hopkins et al., 2006; Alonso et al., 2007; Hopkins et al., 2008;

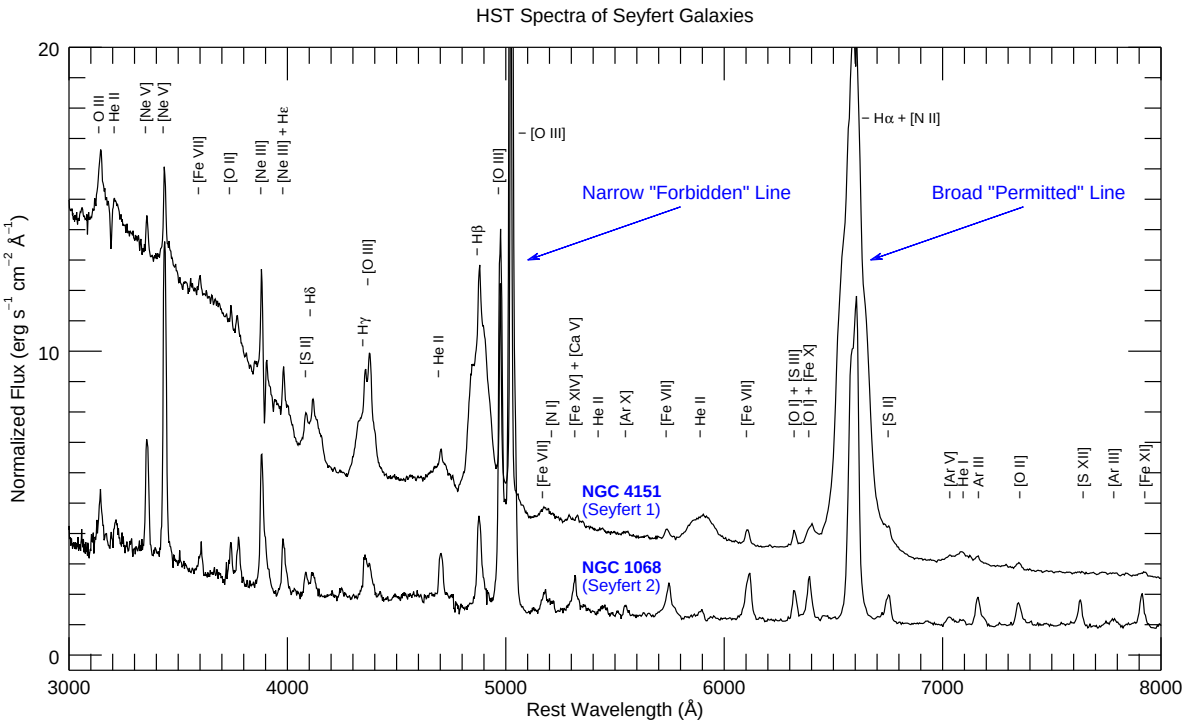

Figure 1.3: Example AGN spectra of archetypal Seyfert galaxies NGC 4151 (Type I) and NGC 1068 (Type II) from the *HST* Space Telescope Imaging Spectrograph. Note that the Type I spectrum exhibits both broad and narrow emission lines as both the BLR and NLR are observed, where the Type II spectrum solely exhibits narrow lines. Fluxes are scaled by 10^{14} for NGC 4151 and 10^{15} for NGC 1068. Borrowed with permission (Revalski, 2019).

Koss et al., 2011, 2012), secular processes such as interactions with bar and/or spiral structures (Kormendy & Kennicutt, 2004; Athanassoula, 2008), or instabilities in the disk (Elmegreen et al., 2008; Dekel et al., 2009; Bournaud et al., 2010; Genzel et al., 2014). While the majority of SMBHs in the nearby universe are quiescent, extensive observational surveys in the radio (Sadler et al., 2002; Best et al., 2005; Mauch & Sadler, 2007), optical (Colless et al., 2001), and X-ray (Baumgartner et al., 2013) established the commonplace of low-level nuclear activity (compared to the high-level activity of quasars) in the local universe. These results yielded the expectation that all galaxies experience one or more AGN phases in their lifetime, and that the gas reservoir is large enough to fuel accretion onto the black hole for $\sim 10^7$ years (Martini, 2004).

The original observations of AGNs date back over 100 years ago (Fath, 1909; Slipher, 1917a,b; Campbell & Moore, 1918), with an intensive study of six of the brightest nuclei (NGC 1068, NGC

1275, NGC 3516, NGC 4051, NGC 4151, NGC 7469) conducted by Seyfert (1943). The spectra of these highly luminous nuclei revealed narrow, high-excitation emission and a number of extremely broadened emission lines (namely hydrogen and helium), examples of which are shown in Figure 1.3. The emission lines in Figure 1.3 are labeled by element and ionization state, where bracketed labels denote forbidden transitions of electrons (i.e., long transition lifetimes) and unbracketed labels denote permitted transitions (short transition lifetimes). The emission line broadening was originally theorized to be caused by large Doppler motion, and is now understood today to be Doppler motion of ionized gas deep within the gravitational potential well of the black hole. This gas absorbs and reprocesses the radiation from the accretion disk and composes the broad line region (BLR). Radiation from the accretion disk continues to ionize gas at distances of $\sim$1$-$1000 parsecs, too far from the central SMBH to induce the range of velocities observed in the BLR where the gravity of the SMBH dominates, thus emission from this region constitutes the narrow line region (NLR; Peterson 1997).

Further observations of AGNs revealed distinct types of nuclei. Those which displayed both broad and narrow lines came to be known as Type I AGNs, while those that solely exhibited narrow lines were denoted as Type II (Khachikian & Weedman, 1974). This dichotomy can be explained by a geometry shared by all AGNs which includes a toroidal-shaped region of thick gas and dust which surrounds the BLR. This torus obscures the SMBH, accretion disk, and BLR for certain observational lines of sight. Thus, a Type I AGN may be observed as long as the BLR is not obscured by the torus, and a Type II observed where it is obscured, with a transition point between the two types of $\sim$45$-$60 degrees (Marin 2014 and references therein). An example of this "unified model" (Antonucci, 1993; Urry & Padovani, 1995; Netzer, 2015; Padovani et al., 2017) is displayed in Figure 1.4.

1.3 *SMBHs and Their Host Galaxies*

As the prevalence of observations of both quiescent and active SMBHs has increased, it has become apparent that a symbiotic relationship exists between SMBHs and their host galaxies (see reviews

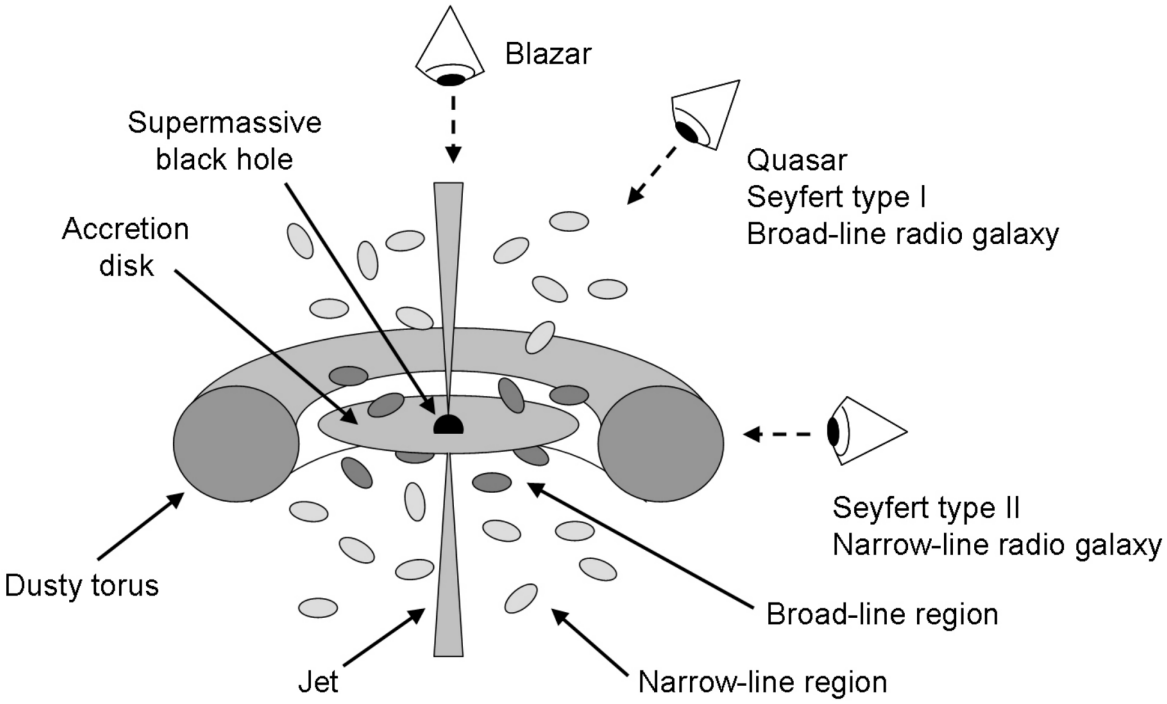

Figure 1.4: Example illustration of the AGN unified model (Zackrisson, 2005). Type I AGN are observed in an orientation such that the NLR and the BLR are unobscured by the torus, while Type II AGN are observed when the torus obscures the observer's line of sight to the BLR and accretion disk.

by Kormendy & Ho 2013 and Heckman & Best 2014). This discovery was highly unexpected given the enormous difference in spatial and dynamical scales, and the first indication of SMBH-galaxy connection was in the form of empirical scaling relationships between $M_{\rm BH}$ and large scale galaxy properties. These include the relation between black hole mass and bulge stellar velocity dispersion ($M_{\rm BH}-\sigma_\star$; Ferrarese & Merritt 2000; Gebhardt et al. 2000) and the relation between black hole mass and bulge luminosity ($M_{\rm BH}-L_{\rm BULGE}$; Kormendy & Richstone 1995), with evidence supporting SMBH mass scaling with the total gravitational mass of the host galaxy (Ferrarese, 2002).

The generally accepted interpretation of these empirical relations is that SMBH-galaxy growth is regulated by AGN activity (Silk & Rees, 1998; Bower et al., 2006; Ciotti et al., 2009; Fanidakis et al., 2011). In this interpretation, black holes grow by accreting or 'feeding' on cold gas which has flowed to the nucleus, and the subsequent radiation from the accretion disk (or 'feedback') is injected back into the galaxy, which can disrupt cooling flows of gas onto the galaxy and consume

and/or eject gas from the central bulge (Bower et al., 2006; Croton et al., 2006; De Lucia et al., 2006; Cattaneo et al., 2007; Lagos et al., 2008). With evidence for all galaxies hosting at least one AGN phase in their lifetime, it is clear that SMBHs play a role in galaxy evolution over cosmic time. Thus, it is important to obtain accurate measurements of both large scale galaxy properties and SMBH properties for understanding the physics of black hole-galaxy coevolution. We describe the galaxy and AGN properties of focus in this thesis below.

1.3.1 *Redshift*

Due to the universe's expansion, the majority of galaxies exhibit radial motion away from us, thus the observed wavelengths of emitted light are shifted towards larger values, or are redshifted. The redshift (z) of a galaxy may be measured by comparing the observed wavelength of one or more emission/absorption lines to the rest wavelength(s). Hydrogen emission lines are commonly employed, as hydrogen is the most abundant element in the universe (Payne, 1925). The electron and proton in a neutral hydrogen (HI) atom normally have aligned spins, a configuration of a higher energy state compared to misaligned spins. Thus, there is a probabilistic spin-flip of the electron, which in turn emits the hyperfine 21 cm radiation. The probability predicts one transition for one electron every $\sim$10 million years, however the significant presence of HI in gas-rich, late-type galaxies renders the emission easily detectable (e.g., Haynes & Giovanelli 1984 and references therein). Since the 21 cm-emitting gas is cold ($\sim$120 K) and nearly uniformly spread throughout the galaxy disk, it better reflects the overall kinematics of the disk as opposed to optical emission lines from gas at hotter temperatures (e.g., [O III]; Osterbrock & Pogge 1987). Higher-temperature gas can be influenced by processes other than the gross rotation of the galaxy, thus affecting the Doppler shifted velocity of the line and hence any redshift measurement based on it (e.g., Mirabel & Wilson 1984). Conversely, the central velocity of the emission profile of cold 21 cm emission provides one of the most reliable measurements of z for extragalactic sources.

One of the most common uses of a galaxy's redshift is distance estimation through the Hubble-Lemaître Law (Hubble, 1929), which states that the recessional velocity of a galaxy is equal to the

product of the galaxy's distance with the expansion rate of the universe (H_0). Thus, a measurement of recessional velocity through the redshift of one or more emission lines combined with an assumed value of H_0 yields a distance estimate. However, this method of estimating distance assumes a galaxy's recessional velocity is solely caused by expansion, or Hubble Flow, which ignores the velocity field generated by local gravitational interactions, or local peculiar velocity ($V_{\rm PEC}$). In the past decade, large compendiums of z-independent galaxy distances have allowed detailed study of the structure and dynamics of our local supercluster, namely the Cosmicflows programs (CF1, CF2, CF3; Tully et al. 2008, 2013, 2016). Removal of the contribution of Hubble Flow enables the local $V_{\rm PEC}$ field to be investigated and modeled (Shaya et al., 2017; Graziani et al., 2019), where the typical $V_{\rm PEC}$ in the local universe has been observed to be $\sim$500 km s^{-1} by CF1, with the larger catalogues of CF2 and CF3 including galaxies for which $V_{\rm PEC}$ is as large as $\sim \pm$4000 km s^{-1}. Thus, z-based distances carry significant uncertainty in areas with strong gravitational interactions (e.g., our inflowing motion towards the Virgo Cluster; Tully et al. 2008). Consequently, the accuracy of measurements of galaxy properties that are a function of distance (e.g., luminosity) is limited by using z-based distances for nearby galaxies

1.3.2 *Distance*

The distance to a galaxy is a fundamental yet difficult property to measure, and a myriad of galaxy properties are functions of it. Accurate distances to galaxies in the local universe have yielded a well-calibrated construction of what is commonly referred to as the comic distance ladder. One of the methods that sets the scale for nearly all extragalactic rungs of the ladder is Leavitt's Law (Cepheid period-luminosity relationship; Leavitt & Pickering 1912), which describes the correlation between the periods of pulsation of Cepheid variable stars and their intrinsic brightnesses. The second method applies to older stellar populations, where stars have nearly exhausted all their hydrogen fuel supply and move to the tip of the red giant branch (TRGB; Iben & Renzini 1983; Salaris & Cassisi 1997). These stars are standard candles in the infrared due to similar evolutionary tracks independent of mass and metallicity (Lee et al., 1993; Makarov et al., 2006; Madore et al.,

2008). Both of these methods require individual stars to be resolved, demanding high spatial resolution and thus are fundamentally limited to $\sim$40 Mpc (Riess et al., 2016).

Both the surface brightness fluctuation method (SBF; Tonry et al. 2001; Blakeslee et al. 2010), which utilizes the varying brightness between groups of unresolved, older stellar populations as a distance indicator, and Fundamental Plane method (Faber & Jackson, 1976; Djorgovski & Davis, 1987; Dressler et al., 1987), an empirical correlation between $\sigma_\star$, surface brightness, and intrinsic luminosity, are only applicable to early-type galaxies. However, the majority of optically bright AGNs in the local universe are hosted by spirals (see Kauffmann et al. 2003 and references therein) due to the necessity for a large gas reservoir to fuel the AGN. One of the most widely utilized distance measurement methods for late-type galaxies is the Tully-Fisher (TF) relation (Tully & Fisher, 1977), which is an empirical correlation between spiral galaxy rotational velocity and intrinsic luminosity. The mass of the galaxy is constrained by the maximum rotation rate (which can be traced by HI 21 cm emission), and light traces the galaxy mass, thus a measurement of the rotation rate yields the absolute magnitude, and comparison with apparent magnitude provides a distance constraint.

1.3.3 *Galaxy Mass*

The total gravitational mass of a late-type galaxy, or its dynamical mass ($M_{\rm DYN}$), can be broken down into three main contributors, namely gas ($M_{\rm GAS}$), stellar ($M_\star$), and dark matter mass ($M_{\rm DM}$). We describe the methods of constraining each below.

1.3.3.1 Gas

Integrating the total HI 21 cm emission profile yields an estimate of total atomic gas. For galaxies within the beam of the telescope, the integrated HI flux is directly related to the total number of neutral hydrogen atoms, and thus HI mass ($M_{\rm HI}$; Roberts 1962). The next significant mass contributor is helium, with its typical mass fraction with respect to hydrogen of $\sim$27% (Cox, 2000). Other phases of hydrogen and heavier elements are small fractions of the typical abundance of

atomic hydrogen in late-type galaxies (Young & Knezek, 1989; McGaugh & de Blok, 1997; Spitzer, 1998; Obreschkow & Rawlings, 2009). Thus, the total gas mass of a late-type galaxy may be estimated by $M_{\rm HI}$ with a scale factor to account for non-HI mass contributions, the vast majority of which is helium (McGaugh 2012 and references therein).

1.3.3.2 Stars

The stellar mass of a galaxy may be estimated from a measurement of its luminosity combined with a constraint on its stellar mass-to-light ratio (M/L). Stellar population models are commonly employed to constrain M/L (e.g., Bell et al. 2003; Portinari et al. 2004), which in turn are used to predict correlations between M/L and photometric color (e.g., Bell & de Jong 2001; Into & Portinari 2013). Thus, an observed color predicts M/L, and when combined with the integrated luminosity of the galaxy yields a constraint on $M_\star$. The total luminous mass, or baryonic mass ($M_{\rm BARY}$), is then simply calculated as the sum of $M_{\rm GAS}$ and $M_\star$.

1.3.3.3 Dark Matter

HI 21 cm emission is also widely used to trace late-type galaxy rotation rate, as neutral hydrogen extends far past the stellar disk, and resolved 21 cm studies provide the most precise method of measuring the maximum rotation rate ($V_{\rm mx}$) through rotation curves (e.g., Walter et al. 2008; Ott et al. 2012; Koribalski et al. 2018; Adams & van Leeuwen 2019; Koribalski et al. 2020; Maddox et al. 2021). For galaxies outside the reach of resolved studies, or for much larger samples, the rotational broadening of unresolved HI 21 cm emission may be used to estimate $V_{\rm mx}$ (Epstein, 1964; Roberts, 1969; Tully & Fouque, 1985). The large-scale velocity dispersion of 21 cm-emitting gas is also negligible relative to the rotational velocity (Tamburro et al., 2009; Ianjamasimanana et al., 2012), thus the emission line broadening is dominated by virial rotation, and the virial theorem describes the mass enclosed ($M_{\rm DYN}$) within a characteristic radius (R; in this case, the radial extent of the 21 cm-emitting gas) as $M_{\rm DYN} = RV_{\rm mx}^2/{\rm G}$, where G is the gravitational constant. The contribution of

dark matter within the luminous radius of a galaxy, then, may be estimated simply as the difference between $M_{\rm DYN}$ and $M_{\rm BARY}$.

1.3.4 *Black Hole Mass*

AGN activity provides one of the few mechanisms of direct black hole mass ($M_{\rm BH}$) measurement through reverberation mapping (RM; Blandford & McKee 1982; Peterson 1993; Cackett et al. 2021). The stochastic variability of the continuum emission (most likely arising from the accretion disk) is echoed through the variation in reprocessed flux emitted from the BLR. The delay in time (τ) between the driving continuum signal and BLR echo yields a measurement of the BLR radius ($R_{\rm BLR}$), which when combined with the velocity of the BLR gas allows a constraint on the total mass enclosed, the vast majority of which is contributed by the central black hole. In effect, RM relies on temporal resolution, as opposed to other direct $M_{\rm BH}$ measurement techniques that rely on spatial resolution and are thus limited to distances $\lesssim$100 Mpc (Gültekin et al., 2009).

One of the most important results of RM campaigns was the discovery of the relationship between $R_{\rm BLR}$ and the luminosity of the AGN ($R_{\rm BLR}-L_{\rm AGN}$; Koratkar & Gaskell 1991; Kaspi et al. 2000; Bentz et al. 2006, 2009b, 2013). This relation has enabled single-epoch SMBH mass estimates, where only one spectrum is required for a measurement of $L_{\rm AGN}$, which predicts $R_{\rm BLR}$, and broad emission line width, which measures BLR velocity (see Vestergaard & Peterson 2006). Thus, the $R_{\rm BLR}-L_{\rm AGN}$ relation provides an important shortcut for estimates of $M_{\rm BH}$ at any redshift without the significant time and resource investment required for RM (e.g., Jiang et al. 2007; Kurk et al. 2007, 2009; Willott et al. 2010).

The largest known uncertainty in the $R_{\rm BLR}-L_{\rm AGN}$ relation is the lack of accurate distances, producing uncertainties in the luminosity measurements of up to a factor of $\sim$3 (Bentz et al., 2013). Only nine galaxies in the complete RM AGN sample have z-independent distances, rendering the distances of galaxies in the local universe ($z \lesssim 0.1$) uncertain due to the unknown contribution of $V_{\rm PEC}$. As the reverberation sample serves as the basis for all secondary $M_{\rm BH}$ estimates in distant AGNs, accurate distances are essential for as many RM AGN hosts as possible.

1.3.5 *Broad Line Region Geometry and Kinematics*

BLRs have all long remained unresolved in even the nearest Seyfert 1 galaxies (with typical BLR sizes of $\sim$light days or angular sizes of $\sim$milliarcseconds), with the necessary spatial resolution to probe the outer BLR achieved only very recently for a handful of AGNs (Gravity Collaboration et al., 2020a,b, 2021a; Vermot et al., 2021; Gravity Collaboration et al., 2021b). However, one of the many powers of RM is the ability to probe the geometry and kinematics of a spatially-unresolved source (see Cackett et al. 2021 for an in-depth review). Traditional RM methods yield the average BLR size, thus require the order of unity scale factor $\langle f \rangle$ to account for the unknown structure and dynamics of the BLR. Recent RM programs, though, have begun to provide data of such high quality that the full geometry and kinematics of the BLR may be mapped out (Bentz et al., 2009b; Denney et al., 2009a; Denney et al., 2010; Barth et al., 2011a,b; Grier et al., 2013b; Du et al., 2016a; Pei et al., 2017), a goal included in the framework originally laid by Blandford & McKee (1982). Velocity-resolved RM, as it is now referred to, can thus provide constraints on the structure and dynamics of the BLR as well as $M_{\rm BH}$ independent of $\langle f \rangle$.

One of the main goals of these velocity-resolved RM studies is to recover the transfer function, which describes the behavior of τ as a function of line-of-sight velocity and thus possesses all the information about the geometry and kinematics of the BLR (Horne, 1994; Bentz et al., 2010; Grier et al., 2013b; Skielboe et al., 2015; Anderson et al., 2021). This can be treated as an ill-posed inverse problem (see Horne et al. 2021 for the most detailed recovery to date), or the analysis can be approached with direct, forward modeling by exploring parameter space and determining the set of models that best match the data (Brewer et al., 2011; Pancoast et al., 2011, 2012, 2014a,b; Li et al., 2013; Grier et al., 2017; Williams et al., 2018, 2020; Bentz et al., 2021).

1.4 *Overview of This Study*

The goal of this study is to provide accurate measurements of fundamental properties of RM AGN host galaxies. The parent sample consists of all Seyfert 1 galaxies with direct $M_{\rm BH}$ measurements

from the RM database of Bentz & Katz (2015). The host galaxies of these AGNs are nearly all late-type (morphological types ranging from S0 to Sc) within a redshift range of $z = 0.002 - 3.912$. We focus on measurements of redshift, distance, gas and baryonic masses, total galaxy gravitational masses, BLR geometry and kinematics, and black hole masses. We summarize here the three studies encompassed by this thesis, each of which focuses on a subset of these measurements.

1.4.1 *HI 21 cm Spectroscopy*

The first study explores the AGN host galaxy properties yielded by HI 21 cm emission and the rotational velocities to be later employed in TF distances. We selected RM AGNs hosted only by spirals (as required by the TF method) within $z \leq 0.1$, as the detection limit for 21 cm emission is $z \sim 0.1$ (Reyes et al., 2011). We thus targeted 44 AGN hosts for single-dish observations with the Robert C. Byrd Green Bank Telescope[1] (GBT), of which 31 were detected. In Chapter 2, we describe the observations of HI 21 cm emission and present measurements of the emission lines yielding profile widths (providing the projected rotational velocities), z, and HI 21 cm flux, as well as derived constraints on $M_{\rm HI}$ and $M_{\rm GAS}$. We also present explorations of the relationships between $M_{\rm BH}$ and $M_{\rm GAS}$, $M_{\rm BARY}$, and $M_{\star}$.

1.4.2 *Tully-Fisher Distances and Galaxy Dynamical Masses*

The broadening of the unresolved HI 21 cm emission profile may be used as a proxy for the maximum rotation rate required for TF-based distance measurements. The profile half width yields the line of sight velocity, thus an inclination correction is needed to recover the maximum velocity (Tully & Fisher, 1977). Additionally, the TF relation employs light as a mass tracer, necessitating accurate measurements of the galaxy starlight as it traces the stellar mass. AGNs have been shown to contribute up to $\sim$30% of the total galaxy brightness for low-luminosity Seyferts (Bentz et al., 2013), therefore the AGN contamination must be carefully removed from the host-galaxy brightness.

[1]The Green Bank Observatory is a facility of the National Science Foundation operated under cooperative agreement by Associated Universities, Inc.

In Chapter 3, we present TF distance determinations by first selecting the 24 HI 21 cm emission lines which exhibited the rotationally broadened dual-horned profile shape (as is needed to recover the disk velocities) out of the original 31 targeted for HI 21 cm spectroscopy. The half line widths of these emission lines provide the line of sight rotational velocities from which the maximum velocity may be recovered with an inclination correction. We then conducted two-dimensional surface brightness decompositions, separating the AGN from the host galaxy starlight, yielding galaxy-only fluxes, disk axis ratios which provide each galaxy's inclination, and galaxy radii. The inclination-corrected line widths predict each galaxy's absolute magnitude via the most recent calibrations of the TF relation (Tully et al., 2008; Tully & Courtois, 2012), and comparison with the AGN-free apparent magnitudes constrains each distance. Using our constraints on $V_{\rm mx}$ and radii, we also derive values of $M_{\rm DYN}$ and $M_{\rm DM}$, and investigate relationships between $M_{\rm DYN}$ and $M_{\rm DM}$ with respect to $M_{\rm BH}$.

1.4.3 *Direct Modeling of the Broad Line Region*

In Chapter 4, we describe forward modeling of velocity-resolved RM data (originally presented by De Rosa et al. 2018) and present preliminary models of the geometry and kinematics of five nearby Seyfert galaxies. These five Seyferts (Mrk 704, NGC 3227, NGC 3516, NGC 4151, NGC 5548) represent famous and well-studied AGNs, but these are the first BLR models for four of the five. We explore the resultant properties of the Hβ-emitting BLRs in addition to the high-ionization BLR probed through the He II λ4686 broad emission line for NGC 3227 and NGC 4151. Each set of models provides constraints on geometry, kinematics, velocity-dependent time delays, and new direct black hole masses for all five AGNs.

1.4.4 *Future Work*

In addition to the published and preliminary results presented here, we have identified several areas requiring further exploration. In Chapter 5, we describe these investigations in addition to recommendations for forthcoming analyses and observational strategies.

Chapter 2

HI Spectroscopy of Reverberation-mapped Active Galactic Nuclei[1]

2.1 *Introduction*

Hydrogen is the most abundant element in the universe (Payne, 1925), and is of fundamental importance in galactic and extragalactic studies. The spin-flip transition of electrons in neutral hydrogen (HI) atoms gives rise to the hyperfine 21 cm line radiation, which is easily detected from gas-rich galaxies (usually late-type galaxies, e.g. Haynes & Giovanelli 1984, and references therein).

The HI emission line provides a number of interesting details about the host galaxy. First, the Doppler-shifted recessional velocity yields one of the most reliable redshift measurements of extragalactic sources. Since the neutral gas is spread throughout the galaxy, it follows that the center velocity of the emission profile acts as a systemic velocity indicator. HI 21 cm emitting gas is also cold ($\sim$ 120 K), and reflects the overall motion of the disk as opposed to gas at hotter temperatures ($\sim$ 10,000 K) emitting in the optical (e.g. [O III]; Osterbrock & Pogge 1987). These higher temperature emission lines can be affected by the internal motion of the regions in which they emit, thus affecting the radial velocity and hence the redshift measurement (e.g., nuclear, optical emission lines reflecting net outflow motion; Mirabel & Wilson 1984).

Secondly, for inclined disk galaxies, the HI line width provides insight into their rotation speeds. The integrated emission profile is based on the distribution of radial velocities of the rotating disk, and correction for the disk's inclination provides a constraint on the maximum rotation rate (Fisher

[1]This chapter was originally published in the Astrophysical Journal, Volume 880, Pages 68-90 on 2019 July 26, under the title "HI Spectroscopy of Reverberation-mapped Active Galactic Nuclei" by Robinson et al. (2019). doi:10.3847/1538-4357/ab29f9.

& Tully, 1977). Inclination-corrected widths of observed HI profiles are thus related to the rotation curves of disk galaxies (Roberts, 1969; Epstein, 1964).

Finally, the total area under the integrated HI line provides an estimate of the total atomic gas content. For galaxies with angular extents smaller than the beam size of the telescope, the integrated HI flux is related to the total number of hydrogen atoms, and thus the mass in atomic hydrogen (M_{HI}; Roberts 1962). Atomic hydrogen is normally the dominant gas phase in disk galaxies, with molecular hydrogen (H_2) as the next significant component. HI has been observed to saturate and condense to H_2 above a threshold surface density of $\sim 10\,M_\odot\,pc^{-2}$ (Martin & Kennicutt, 2001; Wong & Blitz, 2002; Bigiel et al., 2008), and giant molecular clouds are the dominant locations for star formation in spiral galaxies (e.g., Leroy et al. 2008). There have been many studies aimed at estimating the molecular gas content of disk galaxies (e.g., Cortese et al. 2017), for example showing that M_{H_2}/M_{HI} scales as a function of morphology (Young & Knezek, 1989; McGaugh & de Blok, 1997). There is significant scatter in all of the distributions from Young & Knezek (1989), but the mean of their result for late-type spirals is $M_{H_2}/M_{HI} \sim 0.2 \pm 0.1$. Constraints on the solar helium abundance, the next most abundant element and significant gas mass contributor, place the M_{H_E}/M_{HI} fraction in the range of $0.274 \pm 6\%$ (Cox, 2000). The typical cosmic abundances of other elements such as carbon, nitrogen, and oxygen are only small fractions of the hydrogen abundance in spiral galaxies, including the Milky Way (e.g., Spitzer 1998; Obreschkow & Rawlings 2009). Yet, the mass contribution from non-HI gas is typically less than the uncertainty involved in constraining M_{HI}. So the total gas mass of a galaxy (M_{GAS}) is often estimated by simply applying a scale factor to M_{HI} to account for these contributions, the vast majority of which is helium (McGaugh 2012, and references therein).

The first significant HI study of galaxies hosting an active galactic nucleus (AGN) was an exploration of the relationship between the disk and the nucleus of Seyfert galaxies by Heckman et al. (1978). That initial study hinted that the host galaxies of AGNs have a relationship between UV excess outside of the nucleus and the ratio of atomic gas to galaxy luminosity (M_{HI}/L; luminosities from Heckman et al. 1978 are derived from the B-band magnitudes from de Vaucouleurs et al. 1976),

perhaps implying that feedback from nuclear activity triggers star formation in the larger galaxy disk. Heckman et al. (1978) also mention the tendency for Seyferts in their study with peculiar HI properties (e.g., HI absorption, abnormal M_{HI}/L) to have peculiar morphological characteristics (e.g., double nucleus, one spiral arm, faint disk). Peck & Taylor (1998) conducted an HI kinematic study near the active core of NGC 3984, finding that all the HI components were redshifted with respect to the stellar content of the galaxy, which they interpreted as the signature of central parsec-scale gas infalling and feeding the nucleus. Fabello et al. (2011) used the Arecibo[2] Legacy Fast ALFA (ALFALFA) Survey (Giovanelli et al., 2005) to search for trends in the fraction of M_{HI} to stellar mass (M_{STARS}) and black hole accretion rate. For galaxies with low star formation rates ($\log SFR / M_{STARS} < -11.0$), the accretion rate scaled with increasing M_{HI}/M_{STARS}.

Not all of the literature points to correlations between HI content and AGN activity, though. For galaxies with moderate star formation rates ($\log SFR / M_{STARS} > -11.0$) in the study by Fabello et al. (2011), no relationship was found between M_{HI}/M_{STARS} and accretion rate. Bieging & Biermann (1983) conducted HI studies of active and interacting galaxies and compared their HI fluxes to the Rieke (1978) survey of 10.6 μm emission from Seyfert nuclei and found no correlation. Their reasoning was that the infrared fluxes refer only to the nucleus as opposed to the HI flux which originates from the entire disk, therefore concluding no connection between gas and AGN luminosity. Finally, in their review of coevolution of black holes in AGNs and properties of their hosts, Heckman & Best (2014) conclude from a number of studies that HI is unlikely to reside within the central regions of AGN host galaxies. Heckman & Best (2014) also mention that HI surface density in all spiral galaxies, whether active or inactive, is usually lower or near zero at the center, and gas present near the central supermassive black hole (SMBH) is likely to be primarily molecular in the case of inactive galaxies, or ionized in the case of AGN. Thus, there seems to be no clear picture of how the overall gas content of a galaxy is related to AGN fueling.

However, we know that active galaxies have gas accreting onto their central SMBHs, and that the gas reservoir is large enough and/or replenished often enough to fuel the black hole for $\sim 10^7$

[2]The Arecibo Observatory is part of the National Astronomy and Ionosphere Center, which is operated by Cornell University under a cooperative agreement with the National Science Foundation.

years (Martini, 2004), perhaps multiple times in the history of the galaxy. The growth of the SMBHs in AGNs via accretion also appears to be related to the growth of the bulges of their host galaxies (see reviews by Heckman & Best 2014 and Kormendy & Ho 2013). The gas flows that fuel the accretion and growth of the SMBHs and bulges can be driven by mergers, with slower, gradual processes such as gravitational interactions with bar and spiral structures (Kormendy & Kennicutt, 2004; Athanassoula, 2008), or rapid, gas-rich disk instabilities (Genzel et al., 2014; Bournaud et al., 2010; Elmegreen et al., 2008; Dekel et al., 2009). Furthermore, over the past two decades it has become clear that galaxies and SMBHs have a symbiotic relationship, even though their typical size scales are different by orders of magnitude. Empirical scaling relationships between the central SMBH mass (M_{BH}) and the host galaxy itself have been the subjects of many studies (e.g., Ferrarese & Merritt 2000; Gebhardt et al. 2000; Kormendy & Ho 2013). It is therefore of interest to examine whether there is any relationship between M_{BH} and the gas properties of their host galaxies.

In this paper, we present the results of HI spectroscopy of 44 AGNs with direct M_{BH} measurements from the reverberation mapping database[3] of Bentz & Katz (2015). In Section 3.2, for those galaxies where HI emission is detected, we provide measurements of profile widths, recessional velocities and thus redshifts, and HI flux. In Section 2.3, we detail our derived quantities of M_{HI} and M_{GAS} from the raw measurements, as well as other characteristics of the host galaxies and central black holes. In Section 3.7, we explore the relationship between M_{BH} and M_{GAS}, and we test relationships between M_{BH} and baryonic mass (M_{BARY}), and M_{GAS} and M_{STARS}.

Throughout this work we adopt a ΛCDM cosmology of $H_0 = 72\,\mathrm{km\,s^{-1}\,Mpc^{-1}}$ (Freedman et al., 2001), Ω_M=0.3, and Ω_Λ=0.7 (Bennett et al., 2014).

[3] http://www.astro.gsu.edu/AGNmass/

Table 2.1:Target Observations

Target	RA	Dec	z	Session	Scans	Date	UT	LST	Hour	Back-
	(hh mm ss.s)	(dd mm ss)		Number		(yyyy-mm-dd)	(hh mm ss)	(hh:mm:ss)	Angle	end
(1)	(2)	(3)	(4)	(5)	(6)	(7)	(8)	(9)	(10)	(11)
Mrk 1501	00 10 31.0	+10 58 30	0.08934	2	6-52	2013-02-05	22 57 55.0	02 43 24.8	2.90	G
				4	6-162	2013-02-08	21 14 15.0	02 11 00.5	1.01	G
				9	6-23	2013-02-15	18 06 40.0	22 30 56.7	-1.64	G
				54	6-43	2013-06-30	09 07 41.0	22 22 31.8	-1.74	G
				55	6-33	2013-07-01	09 52 59.0	23 11 57.8	-0.92	G
				62	6-19	2013-08-10	05 53 18.0	21 49 25.4	-2.31	G
				64	6-22	2013-08-12	05 16 04.0	21 19 57.3	-2.83	G
Mrk 1044	02 30 05.5	-08 59 53	0.01645	38	6-132	2018-09-06	09 06 28.5	02 48 47.0	0.31	V
				44	6-139	2018-09-16	06 59 59.5	01 21 22.7	-1.15	V
3C120	04 33 11.1	+05 21 16	0.03301	20	7-106	2013-03-13	01 37 35.0	06 45 10.8	2.21	G
				23	6-90	2013-03-27	23 10 33.0	06 13 09.1	1.67	G
				27	1-52	2013-04-03	21 28 57.0	04 58 58.4	0.44	G
				59	6-25	2013-07-27	18 18 09.0	09 21 04.7	4.83	G
				65	6-20	2013-08-30	17 19 56.0	10 36 46.1	-8.01	G
				69	6-96	2013-09-03	11 16 53.0	04 48 00.1	0.26	G
Ark 120	05 16 11.4	-00 08 66	0.03271	45	146-277	2018-09-16	12 38 53.5	07 01 12.4	1.75	V
				52	6-135	2018-10-16	09 20 48.5	05 40 51.4	0.41	V
MCG+08-11-011	05 54 53.6	+46 26 22	0.02048	46	6-135	2018-09-20	08 15 37.5	02 52 59.3	-3.03	V
				53	6-129	2018-10-17	09 19 05.5	05 43 04.7	-0.20	V
Mrk 6	06 52 12.2	+74 25 37	0.01881	6	6-105	2013-02-26	02 26 11.0	07 34 35.3	1.88	G
				10	6-91	2013-02-21	04 36 55.0	09 22 25.2	2.52	G
				12	6-48	2013-02-26	23 09 41.0	04 18 05.3	-2.53	G
Mrk 374	06 59 38.1	+54 11 48	0.04263	32	6-137	2018-09-01	09 22 29.5	02 45 07.8	-4.24	V
				35	6-84	2018-09-04	16 52 10.5	10 27 52.4	3.47	V
				36	6-50	2018-09-05	11 05 51.5	04 44 33.0	-2.25	V
Mrk 79	07 42 32.8	+49 48 35	0.02219	3	32-53	2013-02-07	06 33 43.0	10 24 32.6	2.72	G
NGC 2617	08 35 38.8	-04 05 18	0.01421	51	6-133	2018-10-15	12 23 45.5	08 40 21.9	0.08	V
				55	6-135	2018-10-25	13 22 04.5	10 18 16.0	1.71	V
Mrk 704	09 18 26.0	+16 18 19	0.02923	37	56-181	2018-09-05	14 47 00.5	08 26 18.3	-0.87	V
				49	6-135	2018-10-14	12 13 26.5	08 26 04.6	-0.87	V
				68	8-135	2019-01-02	05 18 08.5	06 45 02.8	-2.56	V
				71	6-59	2019-01-08	08 51 54.5	10 43 03.3	1.27	V
Mrk 110	09 25 12.9	+52 17 11	0.03529	31	142-275	2018-08-31	11 17 01.5	04 36 02.1	-4.82	V
				33	143-270	2018-09-01	14 42 26.5	08 05 57.4	-1.32	V
NGC 3227	10 23 30.6	+19 51 54	0.00386	8	6-13	2013-02-15	05 56 56.0	10 19 14.6	-0.05	G

Table 2.1:Target Observations

Target	RA	Dec	z	Session	Scans	Date	UT	LST	Hour	Back-
	(hh mm ss.s)	(dd mm ss)		Number		(yyyy-mm-dd)	(hh mm ss)	(hh:mm:ss)	Angle	end
(1)	(2)	(3)	(4)	(5)	(6)	(7)	(8)	(9)	(10)	(11)
Mrk 142	10 25 31.3	+51 40 36	0.04494	5	6-147	2013-02-09	04 00 06.0	11 55 48.0	0.27	G
				11	6-91	2013-02-23	06 16 32.0	11 10 10.6	0.83	G
NGC 3516	11 06 47.5	+72 34 07	0.00884	3	22-31	2013-02-07	05 53 49.0	09 44 34.4	-1.35	G
				53	6-76	2013-06-24	02 08 21.0	14 58 25.5	3.87	G
				41	6-137	2018-09-09	02 36 23.5	20 29 27.6	9.38	V
				43	142-274	2018-09-11	02 48 40.5	20 49 39.7	9.71	V
				61	6-119	2018-12-21	02 15 07.5	02 54 13.1	-8.65	V
				62	6-75	2018-12-21	07 35 51.5	08 15 49.7	-3.29	V
				63	6-161	2018-12-22	00 07 18.5	00 49 59.6	-10.28	V
				64	6-81	2018-12-22	21 28 52.5	22 15 04.2	11.14	V
				65-66	6-138	2019-01-01	01 19 46.5	02 42 05.1	-8.86	V
				69	6-99	2019-01-03	23 34 38.5	01 08 29.5	-10.42	V
				70	6-73	2019-01-05	22 07 14.5	23 48 44.3	-11.30	V
				72	7-32	2019-01-08	10 41 31.5	12 32 58.3	0.99	V
SBS 1116+583A	11 18 57.7	+58 03 24	0.02787	29	6-84	2013-04-05	01 46 15.0	08 24 36.5	-2.91	G
				36	6-93	2013-05-06	22 28 41.0	08 08 51.4	-3.15	G
				39	6-69	2013-05-09	21 26 51.0	07 18 47.8	-3.74	G
Arp 151	11 25 36.2	+54 22 57	0.02109	31	66-243	2013-04-30	04 02 57.0	13 16 01.1	1.85	G
NGC 3783	11 39 01.7	-37 44 19	0.00973	50	6-76	2013-06-01	01 07 14.0	11 30 14.5	-1.47	G
UGC 06728	11 45 16.0	+79 40 53	0.00652	29	6-284	2018-08-16	09 54 44.5	02 14 23.3	-9.52	V
Mrk 1310	12 01 14.3	-03 40 41	0.01956	59	26-98	2013-07-27	20 50 37.0	11 53 52.0	-1.48	G
				60	36-96	2013-07-29	01 40 05.0	16 39 50.4	3.04	G
NGC 4051	12 03 09.6	+44 31 53	0.00234	3	6-13	2013-02-07	05 18 08.0	09 18 48.4	-2.98	G
				46	36-119	2013-05-23	00 15 46.0	10 59 19.0	-2.72	G
				47	6-95	2013-05-25	23 36 13.0	10 31 28.2	-3.29	G
				49	2270-2352	2013-05-27	23 52 16.0	10 55 28.1	-2.78	G
NGC 4151	12 10 32.6	+39 24 19	0.00332	3	14-21	2013-02-07	05 33 14.0	09 23 57.6	-2.78	G
NGC 4253	12 18 26.5	+29 48 46	0.01293	45	6-241	2013-05-22	01 52 39.0	12 32 47.8	0.24	G
				49	2240-2269	2013-05-27	21 36 54.0	08 40 00.1	-3.64	G
				47	6-109	2018-09-25	12 18 27.3	09 20 27.3	-2.97	V
Mrk 50	12 23 24.1	+02 40 45	0.02343	48	6-133	2018-10-12	14 51 38.5	10 56 49.5	-1.44	V
				50	142-271	2018-10-14	17 51 50.5	14 05 24.2	1.70	V
PG 1229+204	12 32 03.6	+20 09 28	0.06301	17	6-15	2013-03-05	03 59 27.0	09 32 25.6	-2.99	G
				42	6-81	2013-05-19	00 52 09.0	11 20 18.2	-1.20	G
				43	6-99	2013-05-20	03 06 54.0	13 39 21.9	1.12	G
				46	6-35	2013-05-22	22 00 35.0	08 44 02.2	-3.80	G

Table 2.1:Target Observations

Target	RA	Dec	z	Session	Scans	Date	UT	LST	Hour	Back-
	(hh mm ss.s)	(dd mm ss)		Number		(yyyy-mm-dd)	(hh mm ss)	(hh:mm:ss)	Angle	end
(1)	(2)	(3)	(4)	(5)	(6)	(7)	(8)	(9)	(10)	(11)
NGC 4593	12 39 39.4	-05 20 39	0.00900	38	6-77	2013-05-09	03 06 56.0	12 56 01.8	0.27	G
				41	6-116	2013-05-18	01 07 31.0	11 31 46.1	-1.13	G
NGC 4748	12 52 12.4	-13 24 53	0.01463	7	6-87	2013-02-14	07 27 03.0	11 45 41.2	-1.11	G
				37	10-93	2013-05-08	03 56 07.0	13 41 24.3	0.82	G
				44	6-36	2013-05-21	01 21 09.0	11 57 16.0	-0.92	G
				47	96-147	2013-05-26	02 29 44.0	13 25 45.1	0.56	G
MCG-06-30-015	13 35 53.7	-34 17 44	0.00775	8	14-27	2013-02-15	06 27 25.0	10 49 49.9	-2.77	G
				59	99-151	2013-07-27	23 13 36.0	14 17 27.9	0.69	G
				60	6-35	2013-07-28	23 19 44.0	14 27 33.5	0.86	G
				61	6-117	2013-08-03	22 35 46.0	14 07 07.6	0.52	G
MCG-05-33-019	13 49 19.2	-30 18 34	0.01514	24	6-86	2013-04-01	07 19 54.0	14 39 52.3	0.84	G
				30	6-87	2013-04-29	05 24 26.0	14 34 28.8	0.79	G
				48	6-69	2013-05-27	01 59 39.0	12 59 31.7	-0.83	G
Mrk 279	13 53 03.4	+69 18 31	0.03045	13	31-82	2013-03-01	00 55 27.0	06 12 09.1	-7.68	G
				14	6-99	2013-03-02	23 49 04.0	05 13 28.3	-8.66	G
				22	6-75	2013-03-24	12 08 09.0	18 57 22.3	5.07	G
				25	6-64	2013-04-01	10 24 57.0	17 45 25.7	3.87	G
				31	6-65	2013-04-29	10 34 25.0	19 45 18.7	5.87	G
NGC 5548	14 17 59.5	+25 08 12	0.01718	28	6-102	2013-04-04	09 46 21.0	17 18 33.1	3.01	G
				33	6-75	2013-05-01	07 38 06.0	16 56 23.9	2.64	G
				37	94-161	2013-05-08	06 55 11.0	16 40 57.7	2.38	G
PG 1426+015	14 29 06.6	+01 17 06	0.08657	58	6-133	2018-11-26	13 52 30.5	12 54 56.7	-1.57	V
				59	6-133	2018-11-27	16 24 05.5	15 30 53.2	1.03	V
				67	6-123	2019-01-01	14 37 48.5	16 02 18.2	1.42	V
Mrk 817	14 36 22.1	+58 47 39	0.03146	32	7-113	2013-04-30	09 56 12.0	19 10 56.0	4.58	G
				35	7-66	2013-05-06	10 06 48.0	19 45 13.1	5.15	G
				40	6-98	2013-05-11	07 41 23.0	17 39 06.9	3.05	G
				56	9-54	2013-07-07	18 22 10.0	08 06 22.9	-6.50	G
Mrk 478	14 42 07.5	+35 26 23	0.07906	42	6-135	2018-09-10	21 23 08.5	15 23 14.2	0.69	V
				54	6-139	2018-10-17	14 48 36.5	11 13 29.8	-3.48	V
NGC 5940	15 31 18.1	+07 27 28	0.03393	57	6-137	2018-11-07	20 06 12.5	17 54 45.6	2.39	V
				60	6-135	2018-11-28	15 17 07.5	14 27 40.7	-1.06	V
Mrk 290	15 35 52.3	+57 54 09	0.02958	1	6-177	2013-02-05	13 44 31.0	17 28 42.2	1.88	G
				17	16-51	2013-03-05	04 54 53.0	10 28 00.7	-5.13	G
Mrk 493	15 59 09.6	+35 01 47	0.03133	34	6-131	2018-09-02	20 54 26.5	14 22 55.0	-1.60	V
				56	6-139	2018-10-30	14 48 53.5	12 05 02.0	-3.90	V

Table 2.1:Target Observations

Target	RA	Dec	z	Session	Scans	Date	UT	LST	Hour	Back-
	(hh mm ss.s)	(dd mm ss)		Number		(yyyy-mm-dd)	(hh mm ss)	(hh:mm:ss)	Angle	end
(1)	(2)	(3)	(4)	(5)	(6)	(7)	(8)	(9)	(10)	(11)
3C390.3	18 42 09.0	+79 46 17	0.05610	13	6-25	2013-02-28	23 15 04.0	04 31 29.6	9.82	G
				26	6-64	2013-04-01	11 30 26.0	18 58 58.6	0.28	G
				52	6-70	2013-06-23	13 39 28.0	02 27 42.7	7.76	G
				60	97-108	2013-07-29	03 29 26.0	18 37 56.5	-0.07	G
				63	6-21	2013-08-10	21 53 39.0	13 52 29.5	-4.83	G
				66	6-33	2013-08-31	04 07 46.0	21 26 29.1	2.74	G
				67	6-12	2013-09-01	17 54 36.0	11 19 31.4	-7.38	G
				68	6-19	2013-09-02	21 10 18.0	14 39 42.1	-4.04	G
Zw 229-015	19 05 25.9	+42 27 40	0.02788	30	6-135	2018-08-31	05 52 11.5	23 10 18.7	4.08	V
				39	6-132	2018-09-08	00 39 51.5	18 28 39.9	-0.61	V
PGC 090334	19 37 33.0	-06 13 05	0.01031	18	6-79	2013-03-10	15 31 13.0	21 25 48.0	1.80	G
NGC 6814	19 42 40.6	-10 19 25	0.00521	40	6-55	2018-09-08	04 43 35.5	22 33 03.9	2.84	V
				21	6-11	2013-03-18	14 15 20.0	20 41 14.9	1.06	G
PG 2130+099	21 32 27.8	+10 08 19	0.06298	15	6-87	2013-03-03	15 52 47.0	21 19 49.6	-0.21	G
				16	6-35	2013-03-04	13 55 03.0	19 25 42.8	-2.11	G
				19	6-113	2013-03-11	13 51 23.0	19 49 38.1	-1.71	G
				58	6-37	2013-07-22	04 20 43.0	19 01 46.0	-2.51	G
NGC 7469	23 03 15.6	+08 52 26	0.01632	28	105-204	2013-04-04	13 51 10.0	21 24 02.3	-1.65	G

Note. — Columns (1-3): Galaxy names in increasing right ascension. Column (4): Listed redshift value from literature. Column (5): Session number of observation during observing block. Column (6): Scan number range of a given observation session. Column (7): Date. Columns (8-10): Universal time, local standard time, and hour angle values at the midpoint of the observation on each date. Column (11): Backend of instrument used for observation, G denotes GBT Spectrometer, V denotes VEGAS.

2.2 *Data*

2.2.1 *Target Selection and Observations*

Our ultimate goal for these observations is to employ the Tully-Fisher distance measurement method (Tully & Fisher, 1977) to provide a significant number of distances for galaxies in the reverberation mapping sample. In this paper, however, we focus on the HI properties of the galaxies. We began with the database of all broad-lined AGNs with black hole masses derived from reverberation mapping (Bentz & Katz, 2015). Because the Tully-Fisher method requires spiral galaxies, the AGNs hosted by elliptical galaxies were removed from the sample. Potential targets were then removed if they were at $z > 0.1$, and therefore likely outside the reach of the Tully-Fisher method (Reyes et al., 2011). Finally, the large, unblocked 100 m dish of the Robert C. Byrd Green Bank Telescope[4] (GBT) and its access to a large fraction of the sky make it ideal for sensitive 21 cm observations, therefore any remaining sources that were outside the pointing limits of the GBT were removed from the sample. The final selection consisted of 27 active galaxies observed in the spring of 2013 (project ID GBT13A-468; PI: Ou-Yang) and 17 active galaxies observed in the fall/winter of 2018-2019 (project ID GBT18B-258; PI: Robinson).

The GBT Spectrometer backend was used for GBT13A-468 and employed a 12.5 MHz bandwidth and 8,192 channels with velocity resolution of 0.3 km s^{-1} channel^{-1}. The GBT Spectrometer has since been retired, so we employed the VErsatile GBT Astronomical Spectrometer (VEGAS) for GBT18B-258. The VEGAS mode we employed has an 11.72 MHz bandwidth, 32,768 channels, and velocity resolution of 0.08 km s^{-1} channel^{-1}. The large $9\farcm1$ GBT L-Band beamwidth, defined as the full-width at half-maximum of the beam, encompassed even the largest optical angular sizes of our target galaxies.

Targets were observed in position-switched mode in pairs of equal on-off exposures, which were typically 60 second scans for GBT13A-468 and 120 second scans for GBT18B-258. All of the scans were divided into individual integrations of 3 seconds, so that if radio frequency interference (RFI)

[4]The Green Bank Observatory is a facility of the National Science Foundation operated under cooperative agreement by Associated Universities, Inc.

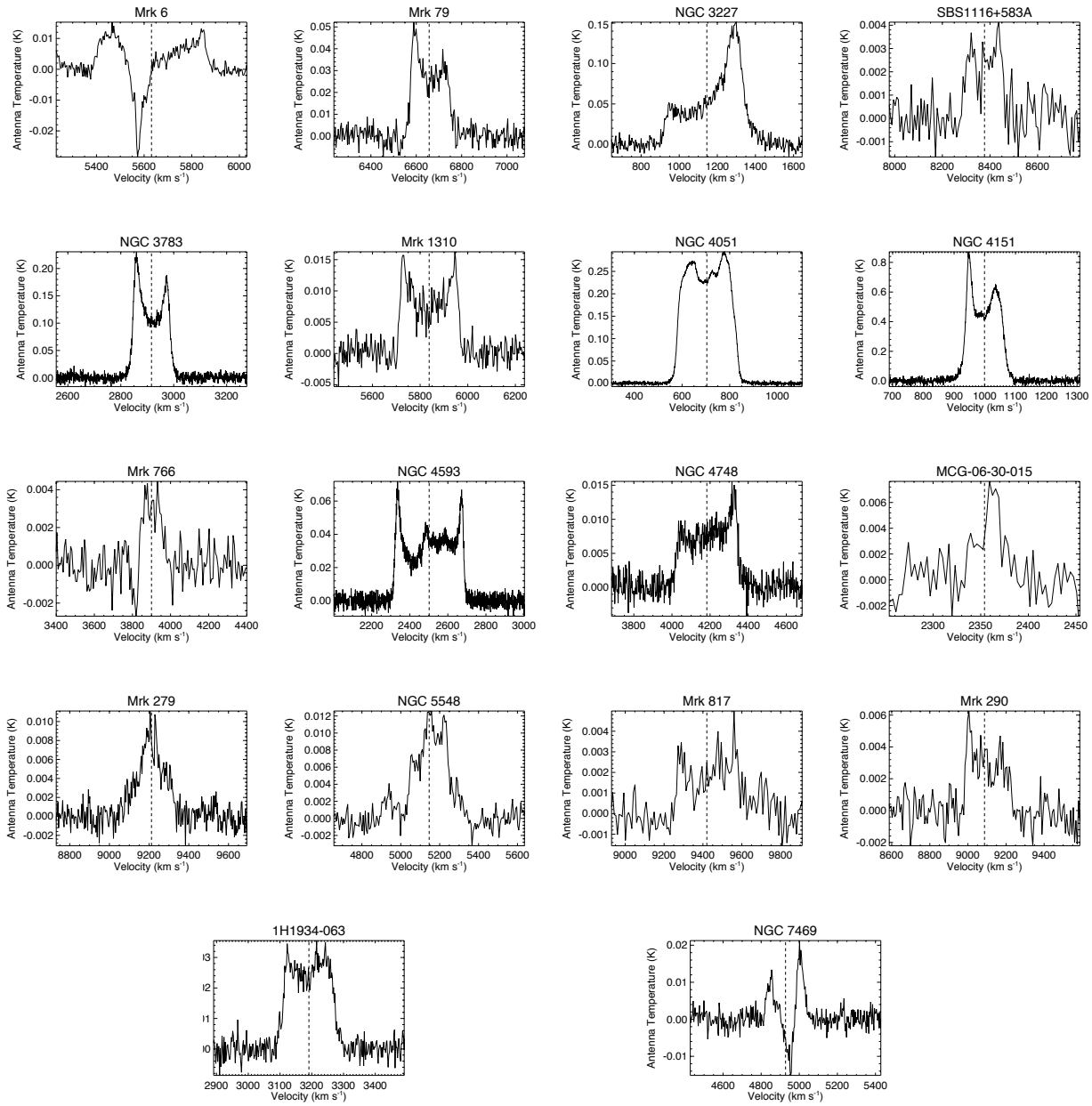

Figure 2.1: HI emission line spectra from GBT13A-468 after reduction, baseline subtraction, and smoothing with GBTIDL v2.8. Hanning smoothing was applied to all profiles, and further smoothing was dependent on the S/N (see Sec. 2.2.2). Note that Mrk 6 and NGC 7469 exhibit central absorption features. The vertical dashed lines indicate V_R measurements from `gmeasure`.

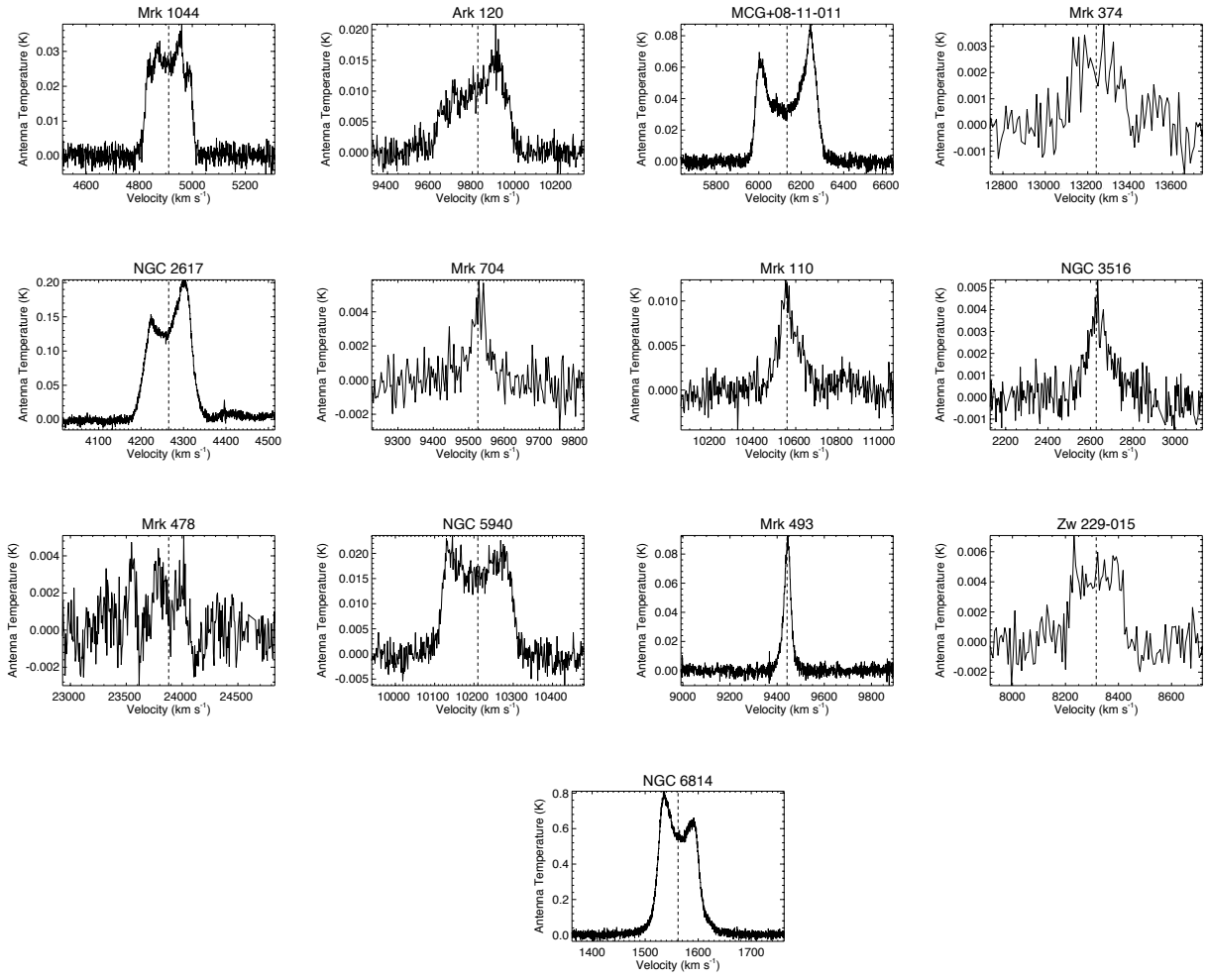

Figure 2.2: HI emission line spectra from GBT18B-258 after reduction, baseline subtraction, and smoothing with GBTIDL v2.10.1. Hanning smoothing was applied to all profiles, and further smoothing was dependent on the S/N (see Sec. 2.2.2). The vertical dashed lines indicate V_R measurements from `gmeasure`.

appeared, we could discard only the affected integrations rather than the whole scan. Off-source sky observations allowed for the removal of the frequency structure of the raw bandpass and an improvement in the signal-to-noise ratio (S/N). Total on-source exposure times were estimated from the expected gas content of the galaxy (based on its morphological type), its expected distance (based on redshift), and a goal of achieving S/N=10 in the peak flux of the HI emission line. We capped our initial time requests at 9 hours per source, but for a few weak yet promising targets, we requested and received additional time to improve the S/N. In total, our observations covered 184 hours for GBT13A-468 and 208.25 hours for GBT18B-258, with total on-source exposure times ranging from $\sim$ 6 minutes to 16 hours. Table 2.1 lists the targets and the details of their observations.

2.2.2 *Reduction*

Data reduction was carried out with GBTIDL (Marganian et al., 2006) v2.8 for GBT13A-468 and v2.10.1 for GBT18B-258. The updated software includes the ability to reduce spectra taken with the VEGAS backend, as well as bug fixes. Individual scans were visually inspected, and those which contained significant saturation from RFI were removed. The `getps` GBTIDL procedure retrieved the on-source and corresponding off-source data for each scan pairing and performed the (ON-OFF)/OFF operation. Scans were then accumulated and averaged over for each target. Weaker RFI spikes were manually removed by interpolating over the interference in the accumulated spectra. Targets that required several hours of exposure time were generally observed in separate blocks across a few days. Scans from separate observing sessions were managed in the same way; all scans from each observation block of the same source were accumulated and averaged at once into a single spectrum.

We fit a low-order polynomial (typically order 3) to the remaining baseline in each combined spectrum and subtracted it. Hanning smoothing (Hann, 1903) was then applied to all spectra after accumulation and baseline subtraction. Hanning smoothing is a running mean across the spectrum that aids in reducing the ringing produced by strong RFI sources and reduces the spectral resolution

Table 2.2. Spectral Characteristics

Target	Exp Time (s)	S/N	RMS (K)	Final Resolution (km s^{-1} $chan^{-1}$)	Backend
(1)	(2)	(3)	(4)	(5)	(6)
Mrk 1044	14720.6	15.7	0.0021	1.1	V
Ark 120	12684.7	9.8	0.0015	2.4	V
MCG+08-11-011	14405.1	23.4	0.0026	0.8	V
Mrk 6	12904.6	8.2	0.0014	3.0	G
Mrk 374	14163.8	4.7	0.0008	8.8	V
Mrk 79	1261.4	10.4	0.0038	3.0	G
NGC 2617	14843.2	45.4	0.0036	0.3	V
Mrk 704	20883.8	6.5	0.0009	3.2	V
Mrk 110	14160.4	8.9	0.0014	3.2	V
NGC 3227	458.6	13.1	0.0062	3.0	G
NGC 3516	56214.1	8.8	0.0006	4.0	V
SBS1116+583A	12445.8	4.0	0.0009	6.0	G
NGC 3783	4013.1	28.5	0.0059	0.6	G
Mrk 1310	7282.3	8.1	0.0017	3.0	G
NGC 4051	14965.0	112.0	0.0024	0.6	G
NGC 4151	344.1	42.0	0.0151	0.6	G
Mrk 766	15252.1	5.1	0.0008	6.0	G
NGC 4593	10204.7	19.1	0.0031	0.6	G
NGC 4748	14160.5	8.9	0.0013	1.8	G
MCG-06-30-015	12096.8	3.4	0.0015	3.0	G
Mrk 279	14739.9	8.4	0.0013	3.0	G
NGC 5548	13415.8	10.0	0.0011	4.8	G
Mrk 817	13879.6	5.8	0.0007	7.2	G
Mrk 478	13437.6	3.4	0.0012	5.6	V
NGC 5940	13917.5	10.2	0.0020	1.3	V
Mrk 290	11126.6	5.4	0.0009	6.0	G
Mrk 493	13051.6	38.9	0.0024	0.8	V
Zw 229-015	12750.2	6.8	0.0009	6.4	V
1H1934-063	4586.8	11.5	0.0027	1.8	G
NGC 6814	2812.5	81.0	0.0080	0.5	V
NGC 7469	4243.3	4.9	0.0022	3.0	G

Note. — Column (2) lists the total time spent on source after removal of contaminated scans. Column (3) lists approximate S/N, and the values were calculated as either a) the average value of the peak fluxes of the horns and mid-profile peak fluxes divided by the RMS of the noise or b) the peak value of the Gaussian-shaped profile divided by the RMS of the noise. Column (4) lists values for the root mean square of the noise in each spectra. Column (5) denotes the final velocity resolution per channel after spectral smoothing was applied (other than initial Hanning smoothing). Column (6) lists the backend of instrument used for observation, G denotes GBT Spectrometer, V denotes VEGAS. The default velocity resolutions of the GBT Spectrometer and VEGAS are 0.3 and 0.08 km s^{-1} $channel^{-1}$, respectively.

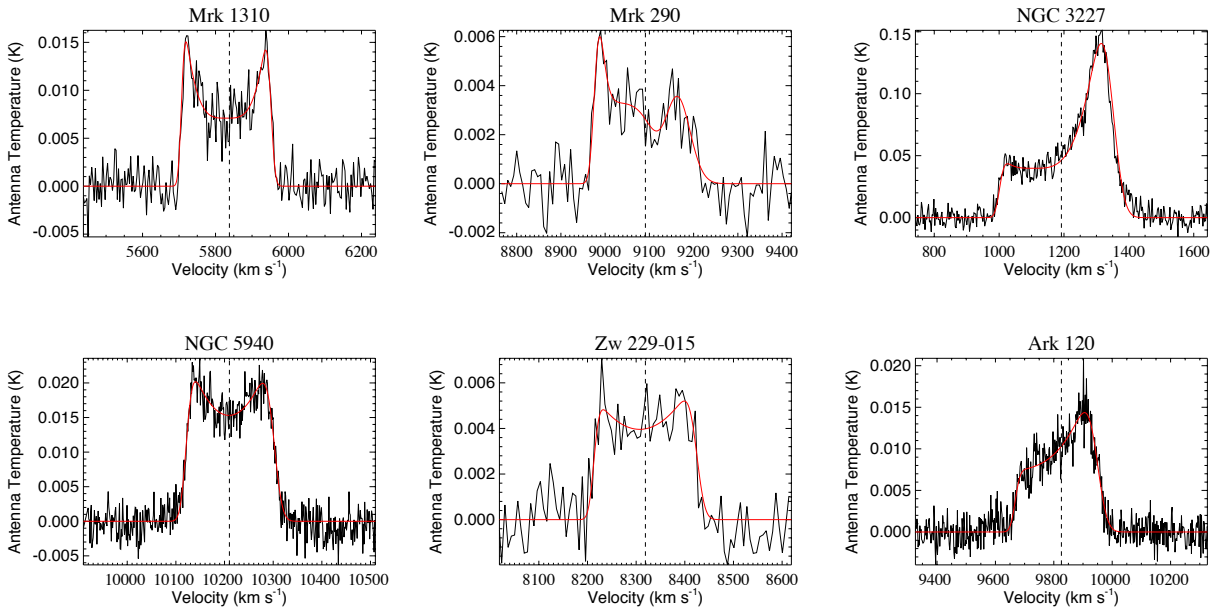

Figure 2.3: Example BUSYFIT (Westmeier et al., 2014) profiles for representative galaxies in our sample. The data is in black, the model fit is the solid red curve. The top row are profiles from GBT13A-468, the bottom are profiles from GBT18B-258. The vertical dashed lines indicate V_R measurements from BUSYFIT.

by a factor of 2. Higher order smoothing was then applied to spectra with low apparent S/N to aid in the measurement of the emission line properties.

We detected HI 21 cm emission in 18 of the 27 targets from GBT13A-468 and in 13 out of 17 for GBT18B-258. Some of the more distant objects in the sample with $z > 0.05$ resulted in non-detections within the allotted exposure time. Figs. 2.1 and 2.2 show the reduced, smoothed, and baseline subtracted spectra for targets where HI emission was detected from programs GBT13A-468 and GBT18B-258, respectively. We report in Table 3.3 the total resulting on-source exposure times after removal of contaminated scans, an approximate S/N for all spectra, values for the root-mean-square (RMS) of the noise in each spectrum, the final velocity resolution after smoothing, and the corresponding backend. For dual-horned profiles, approximate S/N values were calculated first by taking the average of the peak fluxes in each horn. We then averaged that with the mid-profile peak flux, and divided by the RMS of the noise to produce the approximate S/N. For Gaussian profiles, the approximate S/N was calculated as the peak flux value divided by the RMS of the noise.

2.2.3 *Analysis and Measurements*

Measurements of the emission-line widths, center-line recessional velocities (V_R), and integrated line fluxes were determined with two methods. The first method utilized the `gmeasure` procedure available within GBTIDL, which calculates line widths, fluxes, and recessional velocities directly from the data. For width measurements, the `gmeasure` procedure determines the edges of an emission profile by linear interpolation over channels containing the profile until the data are greater than the provided threshold. The threshold is normally 50% or 20% times the mean flux over the range of channels containing the HI signal. W_{50} and W_{20} values (line widths at 50% and 20%, respectively) as well as V_R values are provided in km s^{-1}. We choose the mean flux, rather than the peak flux, for determination of W_{50} and W_{20} because it is less sensitive to the noise level, especially when a profile consists of significantly asymmetric peak horn fluxes. Calculated line fluxes are given in terms of antenna temperature (T_L; see Section 2.3) in K km s^{-1}. Uncertainties on the `gmeasure` measurements were achieved using a bootstrap method. We began by defining beginning and ending spectral channel windows on either side of the line profile. The designated range of channels for each window on each side was unique to each profile and was mainly dependent on the noise properties (see Table 3.3), but was typically $\sim$ 50 channels in width. We then performed 100,000 iterations in which a starting and ending wavelength were randomly drawn from the defined windows, and a line width, flux, and central velocity were calculated using `gmeasure`. A distribution of each measurement was built up in this way, and we report the median of the distribution as the measurement value and the measurement uncertainty as the 1-σ deviation from the median on each side of the distribution, allowing for asymmetric distributions.

The second method employed the BUSYFIT software (Westmeier et al., 2014). For well-defined profiles, BUSYFIT is able to automatically determine the best-fit parameterization, but for noisy or poorly-defined profiles, additional user intervention is necessary. Measurements of W_{50} and W_{20}, (which in this case are defined as line widths at 50% and 20% of the peak flux density, which differs slightly from the definition employed by `gmeasure`), T_L, and V_R are derived from the BUSYFIT profiles. For both methods, we define V_R in the optical convention ($c(\lambda-\lambda_0)/\lambda_0$). The fitting function

has the form

$$B(x) = \frac{a}{4} \times (erf[b_1\{w+x-x_e\}]+1) \times (erf[b_2\{w-x+x_e\}]+1) \times (c|x-x_p|^n+1) \tag{2.1}$$

where x denotes the spectral axis input, a is the amplitude scaling factor, the error functions fit the sides of the HI profile (flanks), b_1 and b_2 are the independent slopes of the flanks allowing for asymmetric shapes of the lines to be fit, w is the half-width of the HI profile, x_e and x_p are separate offsets also aiding in fitting asymmetric profile shapes, and c denotes the amplitude of the central trough of the profile relative to the flanks which is fit with a polynomial of degree n.

The majority of the dual-horned profile fits converged without the need to hold any free parameter values fixed. Most well-defined, Gaussian-shaped profiles also achieved convergence in the fit. For these, BUSYFIT automatically fixes the parameters included in the central trough factor of the fitting function (c, x_p, and n) at 0. We found it common that low S/N or weakly defined dual-horned profiles required holding the c and n values fixed because the initial fits often converged to Gaussian shapes. We also found common that narrow, low S/N Gaussian profiles required holding at least one of the flank slopes fixed as the initial fits resulted in either extremely high uncertainties in these parameters or did not reach convergence. Generally in the cases which necessitated parameters to be held fixed, we inferred the values from the fits for well-defined profiles which converged automatically. We assessed by eye the accuracy of the shape of the fit relative to the inherent shape of the emission line, and we estimate the following additional uncertainties on each parameter: n: $\pm$15%, c: $\pm$29%, w: $\pm$4%, b_1: $\pm$21%, b_2: $\pm$22%, x_p: $\pm$8.5%.

BUSYFIT offers a number of methods for determining uncertainties. We employed the Monte Carlo method which generates 10,000 best fits by randomly varying the free parameters in each iteration. The variations are dependent on the covariance matrix of the values of the free parameters, with each parameter's random distribution centered on the initial fit value and standard deviation derived from the square root of the diagonal elements of the covariance matrix. The uncertainties are assumed to be symmetric and are reported as the standard deviation from the mean of the

resulting measurement distribution. For uncertainty determinations on fits in which parameters were held fixed, there is a tendency for underestimations due to the fixed parameters not contributing to uncertainty propagation. To account for this, we conducted best fits on SBS1116+583A (the lowest S/N HI profile in which no parameters were held fixed for the reported BUSYFIT measurements), fixing each free parameter and each combination of fixed free parameters to calculate the differences in resulting uncertainties from the initial fit's uncertainties. We then inflated the measurement uncertainties by a corresponding amount to match the differences on SBS1116+583A for objects with parameters that were held fixed in the fitting process.

Fig. 2.3 displays the best-fit BUSYFIT profiles overlaid on the HI spectra for a few representative galaxies. Profiles from GBT13A-468 are displayed in the top row, and profiles from GBT18B-258 in the bottom row. Table 2.3 reports the measured values of T_L, W_{50}, W_{20}, and V_R from `gmeasure` and from BUSYFIT. Comparisons between all measurements from `gmeasure` and BUSYFIT are shown in Fig. 2.4. Measurements from GBT13A-468 are shown in solid black circles, and GBT18B-258 are show in open blue circles. A line of unity is shown in each panel, and the differences between the two methods' measurements are shown below each panel. The results are generally in close agreement even though the definitions of the line widths are slightly different, with only a few objects showing large discrepancies. NGC 3227, in particular, has a highly asymmetric line profile with a low central trough and blueshifted horn. This makes the determination of W_{50} quite sensitive to the noise in the spectrum, and whether 50% of the peak flux is below or above the blueshifted horn. If we choose the peak flux definition for `gmeasure`'s W_{50} measurement, we find a more consisent value with BUSYFIT. Both MCG-06-30-15 and Mrk 478 show some disparities in their line widths due to the low S/N in their spectra. And for Gaussian-shaped profiles, like those seen in Mrk 279, NGC 5548, Mrk 704, Mrk 110, NGC 3516, and Mrk 493, the two methods are more likely to disagree due to the difficulty in determining the true edges of the profiles. We also note that three of our spectra (NGC 4051, NGC 4593, NGC 5548) exhibit the surprising feature of excess HI emission at or near the systemic velocity. For the remaining analysis, we prefer

the measurement values from `gmeasure` due to their asymmetric distributions more accurately reflecting the asymmetric nature of the majority of the profiles.

2.2.4 *Notes on Individual Objects*

Of the 31 galaxies with HI detections in our sample, 12 have not been previously studied in HI. For the remaining objects, we have tabulated their previous measurements for comparison with our own in Table 4.3. Below, we include a short discussion of the different measurements for each object. We also include discussion on the best-fit models produced by BUSYFIT whenever user intervention was necessary.

Two of the objects in this study, Mrk 6 and NGC 7469 (see Fig. 2.1) exhibit a strong center-line absorption feature in their HI profiles. While the absorption does not affect their line widths or recessional velocities, it does affect the line flux. In order to estimate a reasonable range of values for the unabsorbed line flux, we used a bootstrapping interpolation method. We first determined the ratios of horn-height to mid-profile-height from all of the unabsorbed dual-horned profiles in our sample. We then designated the lowest and highest ratios (0.16 and 0.52, respectively) as the acceptable range of flux values for the underlying unabsorbed central trough in the line profiles of Mrk 6 and NGC 7469. We then linearly interpolated over the central absorption with 100,000 random draws between the minimum and maximum allowed trough height. For each iteration, the total line flux was recorded, thereby building up a distribution of likely unabsorbed line flux measurements. The median of the resulting distribution is reported as the final T_L value, and the uncertainties reflect the 1-σ deviation from the median on either side of the distribution.

While the optical angular extents of all galaxies with HI detections in our sample are encompassed by the $9'.1$ GBT beam, the total extent of the HI distribution of the closest objects may not be. We examined resolved HI maps to verify the angular HI extent of the nearest galaxies in our sample, whenever such maps were available in the literature.

Mrk 1044: The emission profile for this galaxy contains several flux peaks between the flanks (see Fig. 2.2). This caused the initial BUSYFIT model to fit the flank slopes while converging with

Table 2.3. HI Spectroscopic Measurements

Target	T_L gmeasure (K km s^{-1})	T_L BUSYFIT (K km s^{-1})	W_{50} gmeasure (km s^{-1})	W_{50} BUSYFIT (km s^{-1})	W_{20} gmeasure (km s^{-1})	W_{20} BUSYFIT (km s^{-1})	V_R gmeasure (km s^{-1})	V_R BUSYFIT (km s^{-1})	Backend
Mrk 1044	$4.95^{+0.06}_{-0.03}$	5.01 ± 0.05	$183.2^{+4.6}_{-2.9}$	172.2 ± 5.2	$196.2^{+4.3}_{-10.4}$	202.9 ± 3.0	$4910.77^{+0.69}_{-1.35}$	4912.00 ± 0.90	V
Ark 120	$3.43^{+0.15}_{-0.11}$	3.63 ± 0.76	$337.3^{+17.0}_{-13.1}$	315.9 ± 20.8	$344.4^{+18.4}_{-17.9}$	372.6 ± 10.3	$9806.38^{+9.22}_{-4.51}$	9826.00 ± 26.96	V
MCG+08-11-011	$14.71^{+0.32}_{-0.19}$	14.92 ± 1.93	$310.8^{+6.7}_{-5.1}$	293.0 ± 4.6	$327.3^{+12.6}_{-8.6}$	322.4 ± 3.9	$6133.26^{+1.31}_{-1.04}$	6141.00 ± 4.01	V
Mrk 6	$3.04^{+0.19}_{-0.19}$	3.18 ± 0.57	$435.8^{+6.4}_{-0.5}$	440.3 ± 2.8	$447.7^{+9.7}_{-12.9}$	463.7 ± 3.4	$5631.35^{+0.48}_{-2.98}$	5621.00 ± 5.12	G
Mrk 374	$0.59^{+0.02}_{-0.01}$	0.57 ± 0.27	$263.8^{+0.9}_{-1.0}$	252.3 ± 59.9	$276.3^{+6.6}_{-0.9}$	272.8 ± 31.1	$13250.00^{+0.07}_{-0.06}$	13240.00 ± 15.18	V
Mrk 79	$5.02^{+0.34}_{-0.33}$	5.51 ± 0.85	$154.4^{+9.7}_{-4.5}$	159.6 ± 4.2	$160.3^{+12.9}_{-14.3}$	182.8 ± 3.5	$6657.41^{+4.76}_{-3.88}$	6656.00 ± 2.82	G
NGC 2617	$18.27^{+0.65}_{-0.31}$	18.51 ± 0.58	$126.3^{+5.9}_{-4.2}$	111.6 ± 0.5	$143.8^{+12.1}_{-9.7}$	134.9 ± 0.5	$4265.06^{+0.63}_{-0.28}$	4269.00 ± 0.33	V
Mrk 704	$0.19^{+0.02}_{-0.02}$	0.23 ± 0.05	$46.9^{+6.6}_{-3.2}$	52.2 ± 14.2	$57.8^{+12.8}_{-12.9}$	77.1 ± 21.1	$9525.87^{+1.60}_{-2.55}$	9530.00 ± 9.03	V
Mrk 110	$0.95^{+0.08}_{-0.07}$	1.14 ± 0.74	$127.2^{+16.6}_{-19.2}$	104.9 ± 8.6	$145.0^{+18.8}_{-18.5}$	171.2 ± 10.6	$10558.90^{+6.56}_{-9.49}$	10570.00 ± 5.83	V
NGC 3227	$28.51^{+0.53}_{-0.34}$	29.13 ± 5.35	$430.1^{+10.8}_{-2.8}$	135.9 ± 117.8	$441.2^{+12.9}_{-15.4}$	436.3 ± 3.8	$1144.74^{+4.33}_{-0.82}$	1192.00 ± 20.21	G
NGC 3516	$0.41^{+0.02}_{-0.02}$	0.46 ± 0.02	$143.4^{+5.4}_{-9.6}$	134.6 ± 7.4	$156.5^{+15.4}_{-12.5}$	183.9 ± 10.0	$2627.31^{+3.76}_{-4.67}$	2635.00 ± 4.25	V
SBS1116+583A	$0.38^{+0.03}_{-0.02}$	0.42 ± 0.19	$142.2^{+9.3}_{-10.5}$	145.1 ± 37.4	$148.2^{+12.9}_{-17.3}$	167.6 ± 18.8	$8376.82^{+7.62}_{-2.28}$	8378.00 ± 10.44	G
NGC 3783	$20.08^{+1.14}_{-0.48}$	20.34 ± 1.90	$145.9^{+9.5}_{-2.2}$	138.0 ± 1.7	$155.4^{+12.4}_{-9.3}$	152.5 ± 1.5	$2916.08^{+3.88}_{-0.64}$	2913.00 ± 0.92	G
Mrk 1310	$2.26^{+0.08}_{-0.03}$	2.30 ± 0.42	$243.2^{+8.0}_{-6.8}$	238.3 ± 2.1	$244.8^{+9.7}_{-10.0}$	250.5 ± 2.6	$5837.72^{+5.55}_{-2.50}$	5838.00 ± 1.27	G
NGC 4051	$60.69^{+0.83}_{-0.41}$	61.37 ± 0.17	$247.9^{+2.5}_{-1.1}$	236.3 ± 0.1	$264.5^{+9.5}_{-2.9}$	264.5 ± 0.1	$703.56^{+0.40}_{-0.08}$	703.40 ± 0.05	G
NGC 4151	$72.73^{+1.26}_{-0.82}$	72.57 ± 1.85	$134.1^{+1.7}_{-1.7}$	120.3 ± 0.5	$152.5^{+8.5}_{-0.7}$	139.6 ± 0.4	$998.56^{+0.14}_{-0.41}$	997.90 ± 0.32	G
Mrk 766	$0.37^{+0.02}_{-0.01}$	0.37 ± 0.23	$120.8^{+7.9}_{-1.9}$	104.2 ± 14.0	$138.6^{+10.1}_{-0.6}$	126.1 ± 13.9	$3899.68^{+0.42}_{-2.95}$	3904.00 ± 2.65	G
NGC 4593	$13.10^{+0.49}_{-0.17}$	13.20 ± 1.07	$361.5^{+11.7}_{-3.3}$	357.2 ± 1.8	$367.0^{+12.7}_{-13.6}$	367.6 ± 1.6	$2501.80^{+1.14}_{-5.46}$	2501.00 ± 1.57	G
NGC 4748	$2.61^{+0.09}_{-0.05}$	2.68 ± 0.33	$315.4^{+9.4}_{-2.0}$	306.9 ± 5.6	$323.3^{+12.2}_{-12.3}$	332.2 ± 3.6	$4183.19^{+3.60}_{-2.25}$	4196.00 ± 10.92	G
MCG-06-30-015	$0.14^{+0.04}_{-0.02}$	0.18 ± 0.16	$28.3^{+9.0}_{-6.5}$	18.6 ± 28.3	$29.0^{+6.4}_{-8.3}$	43.1 ± 16.1	$2353.53^{+4.15}_{-3.56}$	2358.00 ± 8.98	G
Mrk 279	$0.96^{+0.07}_{-0.08}$	1.23 ± 0.41	$146.1^{+18.1}_{-22.7}$	142.7 ± 12.0	$154.6^{+19.3}_{-19.3}$	219.5 ± 16.2	$9211.71^{+8.29}_{-6.49}$	9210.00 ± 4.94	G
NGC 5548	$1.77^{+0.07}_{-0.06}$	2.03 ± 0.93	$189.1^{+10.3}_{-3.0}$	197.5 ± 15.7	$197.3^{+11.8}_{-14.0}$	251.2 ± 9.3	$5145.78^{+5.15}_{-1.50}$	5159.00 ± 3.79	G
Mrk 817	$0.63^{+0.03}_{-0.02}$	0.67 ± 0.09	$293.5^{+7.8}_{-7.8}$	299.1 ± 54.5	$303.7^{+10.0}_{-7.8}$	331.0 ± 17.7	$9420.14^{+4.08}_{-3.91}$	9438.00 ± 14.24	G
Mrk 478	$0.64^{+0.03}_{-0.01}$	0.67 ± 0.27	$294.5^{+11.1}_{-10.6}$	296.8 ± 65.6	$296.9^{+13.6}_{-12.3}$	327.0 ± 53.7	$23879.90^{+5.54}_{-5.26}$	23870.00 ± 24.61	V
NGC 5940	$3.31^{+0.04}_{-0.02}$	3.30 ± 0.33	$188.8^{+0.7}_{-0.5}$	183.7 ± 1.9	$204.5^{+5.9}_{-6.5}$	201.8 ± 1.9	$10209.40^{+0.06}_{-0.08}$	10210.00 ± 0.65	V
Mrk 290	$0.70^{+0.02}_{-0.03}$	0.73 ± 0.04	$192.9^{+12.8}_{-3.0}$	194.3 ± 8.3	$219.0^{+12.9}_{-11.1}$	224.9 ± 7.4	$9087.17^{+1.33}_{-6.42}$	9091.00 ± 15.51	G
Mrk 493	$3.25^{+0.16}_{-0.10}$	3.20 ± 0.13	$54.6^{+6.5}_{-8.4}$	35.0 ± 10.5	$74.7^{+12.1}_{-10.9}$	55.0 ± 23.7	$9442.21^{+1.92}_{-0.31}$	9442.00 ± 3.85	V
Zw 229-015	$0.85^{+0.05}_{-0.04}$	0.92 ± 0.09	$195.7^{+13.0}_{-10.6}$	202.8 ± 21.7	$203.5^{+16.0}_{-15.5}$	219.9 ± 33.6	$8316.11^{+9.39}_{-2.12}$	8319.00 ± 13.78	V
1H1934-063	$4.39^{+0.08}_{-0.04}$	4.42 ± 0.45	$163.6^{+0.9}_{-0.6}$	160.3 ± 2.0	$186.4^{+8.6}_{-7.2}$	180.4 ± 1.9	$3191.42^{+0.06}_{-0.09}$	3192.00 ± 1.29	G
NGC 6814	$54.24^{+2.12}_{-1.15}$	54.42 ± 0.16	$89.0^{+4.2}_{-3.1}$	79.2 ± 0.1	$105.1^{+11.4}_{-8.4}$	96.2 ± 0.1	$1562.34^{+0.36}_{-0.16}$	1561.00 ± 0.04	V
NGC 7469	$1.91^{+0.31}_{-0.31}$	1.95 ± 0.59	$192.6^{+9.8}_{-13.9}$	184.6 ± 34.0	$196.2^{+12.7}_{-16.1}$	208.8 ± 16.9	$4927.87^{+4.99}_{-6.79}$	4939.00 ± 8.38	G

Note. — Spectroscopic measurements from gmeasure and BUSYFIT. Asymmetric error bars for the gmeasure measurements are the result of our bootstrap method discussed in Sec. 2.2.3. The last column lists the backend used for observation, G denotes GBT Spectrometer, V denotes VEGAS.

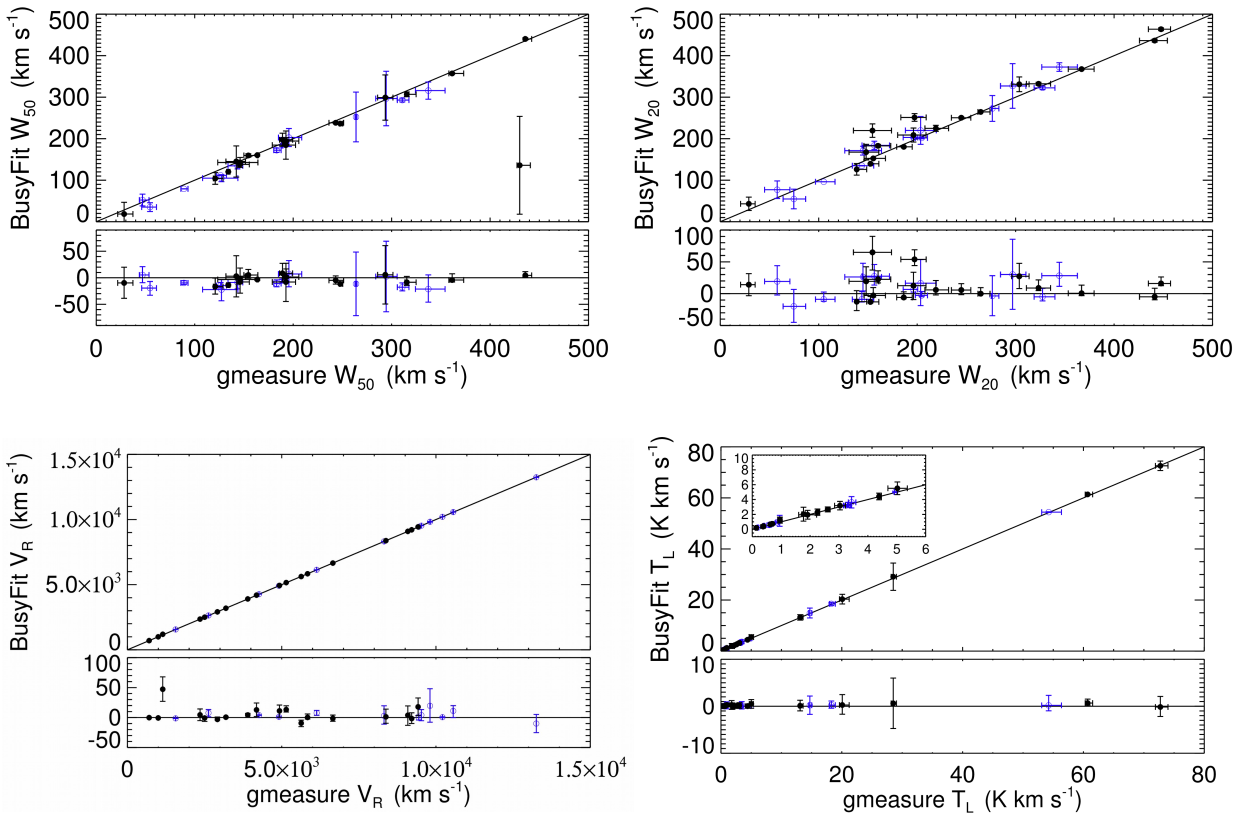

Figure 2.4: Comparison of the measurements from `gmeasure` and BUSYFIT: W_{50} (top left), W_{20} (top right), V_R (bottom left), and T_L (bottom right). The solid line in each panel is a line of unity, and BUSYFIT minus `gmeasure` is plotted below each panel. Measurements of profiles from GBT13A-468 are shown in solid, black circles, and measurements from GBT18B-258 are show in open, blue circles. The outlier in the top left plot is NGC 3227 (see Fig. 2.1, Sec. 3.5.4), which exhibits a lopsided profile, resulting in significant uncertainty in the W_{50} line width measurement due to the uncertainty on the exact value of 50% peak flux.

a value of 0 for the central trough amplitude. In order to fit a weak dual-horn signature, we held the trough amplitude (c) fixed at 0.0001, the trough offset (x_p) fixed at 235, and the polynomial degree (n) fixed at 2. For this object, Mirabel & Wilson (1984) employed the National Radio Astronomy Observatory (NRAO) 91 m telescope's 384 channel autocorrelation spectrometer with 11 km s^{-1} channel spacing and velocity resolution of 22 km s^{-1}. The spectrum reported by Mirabel & Wilson (1984) contains a noise spike close to the redshifted side of the HI profile. The inclusion of the noise spike as part of the HI profile, due to low S/N and low resolution, is the most probable cause for the large discrepancy between their W_{20} measurement of 489 km s^{-1} and ours of $196.2^{+4.3}_{-10.4}$ km s^{-1} and the slight offset in their V_R value of 4932 km s^{-1} compared to ours of $4910.77^{+0.69}_{-1.35}$ km s^{-1}. Measurements made by König et al. (2009) based on observations with the Effelsberg 100 m telescope's 8,192 channel autocorrelater are consistent with our measurements.

Ark 120: The profile of Ark 120 has a slightly skewed dual-horn shape (see Fig. 2.2). Theureau et al. (2005) conducted an observation using the Nançay 94 m telescope with an 8,192 channel autocorrelation spectrometer, which resulted in an HI detection with S/N=3.8. The low S/N in the Theureau et al. (2005) observations would make it difficult to fully characterize the weaker, blueshifted side of the line profile, and likely accounts for the discrepancies between their reported measurements and ours. Where they find values of W_{50}=194 $\pm$ 33 km s^{-1}, W_{20}=233 $\pm$ 50 km s^{-1}, and V_R=9807 $\pm$ 17 km s^{-1}, we report values of $W_{50}=337.3^{+17.0}_{-13.1}$ km s^{-1}, $W_{20}=344.4^{+18.4}_{-17.9}$ km s^{-1}, and $V_R=9806.38^{+9.22}_{-4.51}$ km s^{-1}. On the other hand, Ho et al. (2008a) report values of W_{20}=370.3 $\pm$ 6.8 km s^{-1} and V_R=9809.2 $\pm$ 3.4 km s^{-1} that are fairly consistent with our measurements within the uncertainties.

MCG+08-11-011: Mirabel & Wilson (1984) observed this target with the NRAO 91 m telescope, which was then reprocessed (Springob et al., 2005) for inclusion in the Extragalactic Distance Database (EDD; Tully et al. 2009a). Both V_R measurements (6146 and 6133 km s^{-1}, respectively) and the reprocessed width measurement (310$\pm$15 km s^{-1}) are consistent with our measurements of $V_R=6133.26^{+1.31}_{-1.04}$ and $W_{50}=310.8^{+6.7}_{-5.1}$ km s^{-1}.

Table 2.4. Previous Measurements

Target	Flux	W_{50} (km s^{-1})	W_{20} (km s^{-1})	V_R (km s^{-1})	S/N	Ref
Mrk 1044	...	...	489	4932	...	1
	$2.58 \pm 0.16^{[a]}$	193.9	...	4914	...	2
Ark 120	$1.51 \pm 0.71^{[a]}$	194 ± 33	233 ± 50	9807 ± 17	3.8	3
	$1.51^{[a]}$	97 ± 80	...	9740	2.1	4
	$1.965^{[a]}$	...	370.3 ± 6.8	9809.2 ± 3.4	...	5
MCG+08-11-011	...	...	...	6146	...	1
	$9.53^{[a]}$	310 ± 15	...	6133	8.5	6
Mrk 374	$8.54 \pm 1.94^{[a]}$	74 ± 16	121 ± 24	...	6.9	7
Mrk 79	$3.94^{[a]}$	169 ± 15	...	6657	8.5	6
	$3.95 \pm 0.46^{[a]}$	155 ± 7	...	6659 ± 5	12.1	6
NGC 2617	...	115.1	138.0	4208 ± 8	...	8
	$7.02^{[a]}$	120 ± 100	...	4267	10.1	9
	$9.3^{[a]}$	112.4	143.0	4265.2	...	10
	$9.3^{[a]}$	112.4	...	4264.0	...	11
Mrk 704	$0.2^{[a]}$	...	250	9510	...	12
NGC 3227	$15.495^{[a]}$	...	453.4 ± 6.8	1135.6 ± 3.4	...	5
	$13.1^{[a]}$	430	...	1050 ± 20	...	13
	...	103	437	1146 ± 5	...	14
	$10.5^{[b]}$	...	$234^{[c]}$	1284 ± 9	...	15
	$14^{[a]}$	...	...	1148	...	16
	...	...	...	1152 ± 25	...	17
	...	...	526	1146	...	1
	...	...	293 ± 442	1183	...	18
NGC 3783	$8.45^{[a]}$	145 ± 5	151 ± 30	2889	15.50	6
	...	145	159	2901 ± 20	...	6
	$8.83^{[a]}$	147 ± 13	...	...	10.2	9
	...	...	154 ± 7	2917	...	19
NGC 4051	$39.8^{[b]}$	...	$268^{[c]}$	706 ± 9	...	15
	$30.82^{[a]}$	246 ± 8	...	704	46.5	4
	...	...	267 ± 8	704 ± 7	...	20
NGC 4151	$46.0^{[b]}$	...	$156^{[c]}$	999 ± 9	...	15
	...	...	142 ± 6	996	...	21
NGC 4593	$11.1 \pm 1^{[a]}$	358 ± 10	378 ± 14	2499 ± 5	...	22
	$7.55 \pm 0.36^{[a]}$	355.5	...	2531	...	2
NGC 5548	$1.384^{[a]}$	...	321.1 ± 6.8	5169.8 ± 3.4	...	5
	...	110	...	5200 ± 20	...	13
	...	...	472	5142	...	1
	...	218 ± 25	...	5152	4.1	23
	$1.73 \pm 0.1^{[a]}$	303 ± 15	...	5093	9.6	24
Mrk 478	$0.48 \pm 0.07^{[a]}$	395 ± 26	477 ± 39	23406 ± 13	4.81	25
NGC 5940	$1.828^{[a]}$	187	240	10210 ± 3	9.3	26
	...	...	215	10205	...	1
	$1.729^{[a]}$	181.4	199.1	10211	11.6	27
	$1.80 \pm 0.08^{[a]}$	189 ± 3	...	10207	12.2	28
	$1.36^{[a]}$	183 ± 19	...	10214	3.4	6
	...	...	...	10203 ± 32	...	8
Mrk 493	...	...	60	9442	...	1
	$1.61^{[a]}$	67	...	9430	...	29
	$1.398^{[a]}$	35.7	59.8	9443	10.4	27
1H1934-063	...	...	...	3070 ± 7	...	8
NGC 6814	$29.5^{[a]}$	...	94	1565 ± 8	...	30
	...	...	134	1561	...	1
	$37.3 \pm 4.0^{[a]}$	82	105	1563 ± 2	...	31
	$33.68^{[a]}$	86 ± 8	...	1563	40.2	6
	...	...	124 ± 5	1562 ± 5	...	18
NGC 7469	$1.85 \pm 0.2^{[a]}$	306	...	4877	15.8	6
	$3.741^{[a]}$	...	525.1 ± 6.8	4899.5 ± 3.4	...	5
	...	570	...	5200 ± 20	...	13
	$1.90^{[a]}$	358 ± 100	...	4860	3.8	4
	...	515	583	4971 ± 41	...	32
	...	...	395	4916	...	1

Note. — References are as follows: 1. Mirabel & Wilson (1984), 2. König et al. (2009), 3. Theureau et al. (2005), 4. Tully et al. (2009b), 5. Ho et al. (2008a), 6. Springob et al. (2005), 7. Davoust & Contini (2004), 8. Paturel et al. (2003), 9. Theureau et al. (2006), 10. Meyer et al. (2004), 11. Doyle et al. (2005), 12. Hutchings (1989), 13. Biermann et al. (1979), 14. van Driel et al. (2001), 15. Dickel & Rood (1978), 16. Davis & Seaquist (1983), 17. Peterson (1979), 18. Huchtmeier & Richter (1989), 19. Theureau et al. (1998), 20. Fisher & Tully (1981), 21. Tifft & Cocke (1988), 22. Staveley-Smith & Davies (1987), 23. Stierwalt et al. (2005), 24. Haynes et al. (2013), 25. Teng et al. (2013), 26. Lewis (1983), 27. Lewis (1987), 28. Haynes et al. (2011), 29. Haynes & Giovanelli (1984), 30. Shostak (1978), 31. Koribalski et al. (2004) 32. Richter & Huchtmeier (1982).

Mrk 374: Mrk 374 has a relatively faint emission line (see Fig. 2.2) and we were only able to achieve a S/N of 4.7. The initial BUSYFIT profile converged into a box-shaped best fit with a value of 0 for the central trough amplitude. In order to generate a trough feature while keeping the slopes of the flanks accurate, we held fixed the initial best fits to the flank slopes (b_1 and b_2) at 0.8, 0.5, respectively. We then fixed the central trough amplitude (c) at 0.01 and polynomial degree (n) at 1.5, which allowed a double horned profile shape to converge. Mrk 374 was previously observed by Davoust & Contini (2004) with the 512 channel autocorrelator on the Nançay telescope. They defined their recessional velocities in the radio convention ($c(\lambda-\lambda_0)/\lambda$) instead of the optical convention ($c(\lambda-\lambda_0)/\lambda_0$), which we have used in this work. The recessional velocity reported for Mrk 374 by Davoust & Contini (2004) of 12780 $\pm$ 8 km s^{-1} is equivalent to 13349 km s^{-1} in the optical convention, as compared to our measurement of $13250.00^{+0.07}_{-0.06}$ km s^{-1} in the optical. They report a S/N of 6.9 with an integrated flux of 8.54 Jy km s^{-1}, which is equivalent to 17.08 K km s^{-1}, much higher than our flux of $0.59^{+0.02}_{-0.01}$ K km s^{-1}. Their width measurements also consist of significant discrepancies relative to ours; they list W_{50}=74$\pm$16 km s^{-1} and W_{20}=121$\pm$24 km s^{-1}, as opposed to our reported values of $W_{50}=263.8^{+0.9}_{-1.0}$ and $W_{20}=276.3^{+6.6}_{-0.9}$ km s^{-1}. However, their spectrum contains a strong Gaussian-shaped signal unlike the faint dual-horned profile which we report. Davoust & Contini (2004) discuss that observations at recessional velocities near $\sim$ 12500 km s^{-1} (in the radio convention) contained significant interference from radar signals, and that galaxies in their sample near those velocities are possibly unreliable. Therefore, it is possible that the target was misidentified in their work.

Mrk 79: Two previous observations of this object with the GBT are reported in the HI Digital Catalog of Springob et al. (2005). Each observation reports a W_{50} value (169$\pm$15, 155$\pm$7 km s^{-1}) and a recessional velocity (6657, 6659$\pm$5 km s^{-1}), and they are consistent with our measurements of $W_{50}=154.4^{+9.7}_{-4.5}$ and $V_R=6657.41^{+4.76}_{-3.88}$ km s^{-1} within the uncertainties.

NGC 2617: Previous observations include the Nançay telescope (Paturel et al., 2003) and the Parkes telescope including two measurements from the HI Parkes All Sky Survey Catalogue (Meyer et al., 2004; Doyle et al., 2005). The HI data for NGC 2617 was also reprocessed (Theureau et al.,

2006) for inclusion in the EDD. All previous reported measurements are in agreement with our measurements.

Mrk 704: Mrk 704 has a narrow Gaussian emission profile shape (see Fig. 2.2). The BUSYFIT central trough, offset, and polynomial parameters (c, x_p, and n) were thus automatically fixed at 0, and we also held the left flank slope (b_1) fixed at 0.15 to allow the profile to converge. The spectrum reported by Hutchings (1989) from observations with the Arecibo telescope contains a very low S/N emission line blended with a noise spike on the blueshifted side. The larger W_{20} value they report of 250 km s^{-1} compared to ours of $57.8^{+12.8}_{-12.9}$ km s^{-1} is possibly due to the nearby noise spike's inclusion in the profile measurement. This would also explain the slight offset in their V_R value of 9510 km s^{-1} compared to our measurement of $9525.87^{+1.60}_{-2.55}$ km s^{-1}.

NGC 3227: The blueshifted side of the profile of NGC 3227 is significantly weaker in flux than the redshifted side, resulting in a dramatically asymmetric shape (see Fig. 2.1). It is interacting with its neighboring galaxy NGC 3226 (Tonry et al., 2001), which is an elliptical galaxy, and in the resolved HI study by Mundell et al. (1995), they detected no HI emission from it. So while the interaction might be a possible explanation as to NGC 3227's skewed profile shape, NGC 3226 most likely does not contribute to the emission profile we have detected. The spectral resolution of the previously published spectra range from 6.6 km s^{-1} (Dickel & Rood, 1978) from observations which used the 91 m telescope at the NRAO to 30 km s^{-1} (Biermann et al., 1979) for observations with the 305 m Arecibo telescope. The V_R measurement of 1284 ± 9 km s^{-1} reported by Dickel & Rood (1978) presents the biggest discrepancy with our V_R measurement of $1144.74^{+4.33}_{-0.82}$ km s^{-1}. The baseline in their spectrum contains significant residual fluctuations and possible source confusion; it appears the S/N in their spectrum is too low for identification of the blueshifted side of the profile. Our spectral resolution of 3.0 km s^{-1} is higher than all previous spectra, and our higher S/N of 13.1 allows for clear identification of the entire profile. Our measurements of W_{20} and V_R are consistent with Ho et al. (2008a) within the uncertainties. Martin (1998) report a maximum HI angular diameter of NGC 3227 of 5′ based on the resolved study by Mundell et al. (1995), therefore the total 21 cm emission is most likely enclosed by the 9.′1 GBT beamwidth.

NGC 3516: This is the first HI spectrum for NGC 3516, a relatively nearby galaxy, due to the extreme faintness of its HI emission. The total on-source observing time spent on this object was longer than any of our other targets by a large margin ($\sim$ 15.6 hours). The HI profile of NGC 3516 exhibits a Gaussian shape, and as such the BUSYFIT model held the central trough amplitude, offset, and polynomial degree parameters (c, x_p, and n) fixed at 0. We also held the right flank slope (b_2) fixed at 0.1 to allow the profile fit to converge.

NGC 3783: Previous HI line widths are derived from observations with the Nançay telescope (Theureau et al., 2006) and reprocessed for inclusion in the EDD (Tully et al., 2009b). Our values for W_{50}, W_{20}, and V_R are consistent within the uncertainties.

NGC 4051: Our reported measurements of W_{50} and W_{20} are consistent with those of Fisher & Tully (1981), obtained from the NRAO 91 m telescope and reanalyzed for inclusion in the EDD. Dickel & Rood (1978), who used the same instrument as Fisher & Tully (1981), defined their profile widths as the half-width between points at one-quarter peak intensity corrected for the spectral resolution of the instrument of 6.6 km s^{-1}. Their reported value (doubled to achieve a full width at quarter intensity) of 268 km s^{-1} is consistent with our similar measurement of W_{20}=$264.5^{+9.5}_{-2.9}$ km s^{-1}. All previous V_R measurements are consistent with our measurements. The resolved HI study of Liszt & Dickey (1995) reveals the diameter of the major axis is similar to that of the optical diameter at 5′.2, therefore it is expected that all the HI emission is contained within the 9′.1 GBT beam.

NGC 4151: Our measurements of W_{50} and W_{20} are approximately consistent with the values reported by Tifft & Cocke (1988). The small discrepancies of $\sim 3-10$ km s^{-1} most likely come from the difference in spectral resolution, channel span, and channel spacing. For relatively flat baselines such as that present in our spectrum of NGC 4151, low-order polynomial fits can possibly introduce low-level sinusoidal structure in the baseline. This can affect subsequent measurements and/or fits to the emission profile, and can thus result in small discrepancies in reported measurements. The NRAO 91 m telescope employed by Tifft & Cocke (1988) produced a spectrum for NGC 4151 with a resolution of 11 km s^{-1} over 192 channels. As with NGC 4051, Dickel & Rood (1978) defined

their width as the half-width between points at quarter-intensity corrected for a spectral resolution of 6.6 km s^{-1}. Their reported value (doubled to match a full width) of 156 km s^{-1} is consistent with our measurement of W_{20}=152.5$^{+8.5}_{-0.7}$ km s^{-1}. The previous V_R measurements are consistent with our measurements. In their neutral hydrogen study of NGC 4151, Pedlar et al. (1992) report the extent of the spiral arms reach $\sim 6'$ from its center, and the reanalysis of the same study by Martin (1998) from their compiled catalog of HI maps report the largest angular extent of the neutral hydrogen as 10.′4. The 9.′1 beam of the GBT may not fully enclose the total extent of the HI emission from NGC 4151, but only a small fraction is likely to have been missed.

Mrk 766: Mrk 766 has a low S/N emission line (5.1; see Fig. 2.1) with a very faint dual-horn signature. With all eight BUSYFIT parameters free, the initial fit was Gaussian in shape. In order to fit the weak horns, the right flank slope (b_2) was held fixed at 0.45 in addition to the polynomial degree (n) which was fixed at 2. There are no previous measurements of the HI emission from this galaxy.

NGC 4593: Observations conducted by Staveley-Smith & Davies (1987) and König et al. (2009) employed the Jodrell Bank 76 m MklA radio telescope's 1024 channel autocorrelation spectrometer with a velocity resolution of 7.3 km s^{-1} and the Effelsberg 100 m telescope's 8,192 channel autocorrelator with a velocity resolution of 4.1 km s^{-1}, respectively. Our reported resolution is 0.6 km s^{-1}, and our width and velocity measurements are consistent with theirs. NGC 4593 is also composed of many morphological components including an outer ring and a bar, which is a possible explanation for the fluctuating HI emission between the horns of its profile.

MCG-06-30-015: The HI measurements in this work are the first reported for this galaxy. MCG-06-30-015 has one of the faintest emission lines that was detected (S/N=3.4) in our sample. To fit the asymmetric dual-horned profile, we held the central trough amplitude (c) fixed at 0.011, the half-width (w) fixed at 5, and the polynomial degree (n) fixed at 2.8.

NGC 5548: Within the uncertainties, our measurement of W_{50} is consistent with that of Stierwalt et al. (2005) based on observations with the Arecibo telescope, with a S/N of 4.1 and spectral resolution of 8.5 km s^{-1}. The spectrum reported by Biermann et al. (1979), also from Arecibo,

has a low resolution of 30 km s^{-1}, as opposed to our smoothed velocity resolution of 4.8 km s^{-1}, leading to significant ambiguity in identification of the edges of their profile and their subsequent W_{50} measurement of 110 km s^{-1}, compared to our W_{50} measurement of $189.1^{+10.3}_{-3.0}$ km s^{-1}. In the spectrum reported by Mirabel & Wilson (1984) from Arecibo, with a velocity resolution of 22 km s^{-1} and channel spacing of 11 km s^{-1}, the profile exhibits an extended, low-amplitude blueshifted wing, possibly leading to the discrepancy in their W_{20} measurement of 472 km s^{-1} in comparison to our W_{20} measurement of $197.3^{+11.8}_{-14.0}$ km s^{-1}. The same issue is present in the spectrum reported by Ho et al. (2008a) (velocity resolution of 5.15 km s^{-1}), leading to disagreement between their W_{20} measurement of 321.1 $\pm$ 6.8 km s^{-1} and our W_{20} measurement. After smoothing our spectrum to match the lower velocity resolution of 22 km s^{-1}, we arrive at a W_{20} measurement of 270 km s^{-1}, closer to the larger values of Mirabel & Wilson (1984) and Ho et al. (2008a). Our V_R value is within the range of reported values. The deep optical imaging of NGC 5548 by Tyson et al. (1998) reveals a low surface brightness arm wrapping around the galaxy, an extended tail, and ripples in the inner disk, all of which could contribute to the highly turbulent HI flux distribution present in our spectrum.

Mrk 478: There are multiple emission peaks near the expected location of HI emission from Mrk 478 (see Fig. 2.2), which is between 22484 – 23700 km s^{-1} (Richards et al., 2009; de Vaucouleurs et al., 1991) from recessional velocities measured from optical emission lines. The systemic velocity of Mrk 478 is not well constrained, and we do not detect emission at or near the low end of its range of optical velocities. We fit independent Gaussians to the three peaks present in our spectrum to compare to the systemic velocities of galaxies in the NASA/IPAC Extragalactic Database (NED) in a 9.′1 diameter neighbor search (equal to the GBT L-Band beam size). We measure the following velocities for each peak (from left to right): 23540$\pm$11, 23800$\pm$15, and 23980$\pm$4 km s^{-1}. The left peak's velocity is comparable to the nearby galaxy 2MASX J14415920+3527489 (V_R=23554 km s^{-1}; 2.′2 to the NW). Our V_R measurement for the center peak is near the reported velocities of neighboring galaxies 2MASX J14421361+3524459 (V_R=23738 km s^{-1}; 2.′3 to the SW) and 2MASX J14421426+3528139 (V_R=23763 km s^{-1}; 2.′3 to the NE). Lastly, within a 9.′1 diameter neighbor

search, there are no objects classified as galaxies near our measured velocity of the right peak. From the present information, it is unclear whether Mrk 478 exhibits a dual-horned shape, and it is also unclear as to which of the peaks represent emission from Mrk 478. Based on the similarity of the center and right peak's shape with that of the measured shapes of low S/N dual-horned profiles, as seen with other objects in our sample (SBS1116+583A, Mrk 817, Mrk 290), we have assumed the center and right peaks belong to the emission profile of Mrk 478. For analysis with BUSYFIT, we fixed the slope of the right flank (b_2) at 0.26, the half-width parameter (w) at 23, and the polynomial degree (n) at 3 in order to achieve a characteristic dual-horned fit. Teng et al. (2013) observed Mrk 478 with the 100 m GBT (identified as PG 1440+356 in their work), producing a spectrum with a resolution of ~ 6 km s^{-1} channel^{-1} and S/N of 4.81. The large absorption feature present in their spectrum at ~ 24000 km s^{-1} is absent from ours. Teng et al. (2013) note that the feature has a dramatic variability over short timescales and is also dependent on polarization, and their Figure 6 shows strong continuum fluctuations on month-long periods. They report measurements of W_{50}=395$\pm$26, W_{20}=477$\pm$39, and V_R=23406$\pm$13 km s^{-1}, which differ significantly from our values of $W_{50}=294.5^{+11.1}_{-10.6}$, $W_{20}=296.9^{+13.6}_{-12.3}$, and $V_R=23879.90^{+5.54}_{-5.26}$ km s^{-1}. It is possible that they assumed the left peak was part of the HI emission from Mrk 478, leading to the discrepancy between their measurements and our measurements. If we include all three peaks in our measurement, we find a W_{50} value of 476^{+12}_{-10} km s^{-1}, a W_{20} value of 477^{+12}_{-12} km s^{-1}, and a V_R value of 23752^{+6}_{-6} km s^{-1}, closer to those of Teng et al. (2013).

NGC 5940: All previous measurements for NGC 5940 originate from observations with the Arecibo telescope, including a reprocessed measurement for inclusion in the EDD. The measurements conducted by Lewis (1983) contain consistent W_{50} and V_R values with our values, however their W_{20} value of 240 km s^{-1} is slightly higher than ours of $204.5^{+5.9}_{-6.5}$ km s^{-1}. The lower resolution of their spectrum (~ 8.2 km s^{-1} compared to ours of 1.3 km s^{-1}) contributes to some of the discrepancy between the measurements, because we measure W_{20}=214 km s^{-1} when we smooth our spectrum to match their resolution. However, we expect that the lower S/N in their spectrum also contributes to the difference in W_{20}. The remaining measurements from Mirabel & Wilson (1984), Lewis

(1987), Haynes et al. (2011), Springob et al. (2005), and Paturel et al. (2003) are consistent with our measurements within the uncertainties.

Mrk 493: The HI profile of Mrk 493 exhibits a strong, narrow Gaussian shape (see Fig. 2.2). As standard for fitting a Gaussian-shaped profile, the BUSYFIT parameters controlling the central trough amplitude, offset, and polynomial degree (c, x_p, and n, respectively) were set to 0, and we found that we also needed to hold the half-width parameter (w) fixed at 10 to allow the profile fit to converge. All previous observations utilized the 305 m Arecibo telescope. The V_R reported by Haynes & Giovanelli (1984) is consistent with our measurement, and their W_{50} value agrees with our measurement at the $\sim 2\ \sigma$ level. Lewis (1987) also reports a consistent V_R value. They define their W_{50} measurement of 35.7 km s^{-1} as an un-smoothed width, which might account for the discrepancy, yet it is consistent with our W_{50} of $54.6^{+6.5}_{-8.4}$ km s^{-1} at the $\sim 2\ \sigma$ level. Values by Mirabel & Wilson (1984) are consistent with our measurements within the uncertainties.

1H1934-063: Paturel et al. (2003) report an HI line width of 248.4 $\pm$ 16.5 km s^{-1} from observations with the Nançay telescope. Their spectrum contains significant baseline fluctuations, causing a discrepancy both between our width measurement and theirs and their V_R measurement of 3070 $\pm$ 7 km s^{-1} compared to our value of $V_R = 3191.42^{+0.06}_{-0.09}$ km s^{-1}.

NGC 6814: Mirabel & Wilson (1984) observed this object with the NRAO 91 m telescope and the 192 channel autocorrelation spectrometer. The low spectral resolution of 22 km s^{-1} and channel spacing of 11 km s^{-1} possibly account for the slightly larger value of W_{20} that they report of 134 km s^{-1} compared to our value of $105.1^{+11.4}_{-8.4}$ km s^{-1}. All other previous measurements from Shostak (1978), Koribalski et al. (2004), Springob et al. (2005), Huchtmeier & Richter (1989) are consistent with our measurements. Liszt & Dickey (1995) estimate the HI diameter of NGC 6814 to be $\sim 7'$ based on their resolved HI map, thus it is likely that the $9\farcm1$ GBT beam encompassed the total HI distribution of NGC 6814.

NGC 7469: Our data for NGC 7469 contained large baseline fluctuations across the whole continuum in a significant amount of the scans which were not included in the final, accumulated spectrum. The absorption profile present in the HI spectrum of NGC 7469 (see Fig. 2.1) persists

throughout the literature, causing significant uncertainty in the line flux measurements. Richter & Huchtmeier (1982) utilized the Effelsberg 100 m telescope with spectral resolution of 13.2 km s^{-1} and channel spacing of 11 km s^{-1}, near insufficient to identify the emission profile separate from the noise level. Observations with the Arecibo telescope (e.g., Mirabel & Wilson 1984; Biermann et al. 1979; Ho et al. 2008a) all show self-absorption which is commented on in their analyses. Biermann et al. (1979), Richter & Huchtmeier (1982), and Mirabel & Wilson (1984) also comment on the galaxy companion IC 5283. NED lists the radial velocity of IC 5283 as 4804 km s^{-1}, very near the velocity of the blueshifted flank of NGC 7469, with an angular separation of only 1′.3 (well within the GBT L-Band beam). Thus it is likely that most previous studies have the emission from this companion galaxy blended with that of NGC 7469. When comparing our spectrum to those of Mirabel & Wilson (1984), Mirabel & Sanders (1988), and Ho et al. (2008a), we note that their higher S/N spectra show an emission bump on the blueshifted wing of the profile, while our spectrum does not. It is likely that this feature is lost in the noise since we had to reject a large number of scans for this object. Consequently, we find a significantly different width for NGC 7469 than these previous studies. Reported W_{50} measurements are as follows: 570 km s^{-1} (Biermann et al., 1979) and 515 km s^{-1} (Richter & Huchtmeier, 1982); previous W_{20} measurements consist of: 525.1±6.8 km s^{-1} (Ho et al., 2008a), 583 km s^{-1} (Richter & Huchtmeier, 1982), and 395 km s^{-1} (Mirabel & Wilson, 1984) We report measurements of $W_{50} = 192.6^{+9.8}_{-13.9}$ and $W_{20} = 196.2^{+12.7}_{-16.1}$ km s^{-1}. The previous V_R measurements are consistent with our values within the uncertainties.

The literature on radial velocities and redshifts for the remaining objects in the sample consist of measurement methods that do not rely on 21 cm spectroscopy. For example, MCG-06-30-015 has a previous radial velocity measurement of 2323 ± 15 km s^{-1} from the redshifting of infrared emission lines (Fisher et al., 1995). Based on the 21 cm emission, we report a measurement of $V_R = 2353.53^{+4.15}_{-3.56}$ km s^{-1}. Mrk 279 has measurements of V_R ranging from low estimates of 8904 ± 60 km s^{-1} from the redshift of the strongest optical emission lines (e.g., Hα, [O III]; Osterbrock & Pogge 1987), to high estimates of 9600 km s^{-1} from the redshift of the Hα emission line (Arakelian et al., 1971). Our measurement of $V_R = 9211.71^{+8.29}_{-6.49}$ km s^{-1} is contained within the wide range of

previous values. Similarly, Mrk 817 has a range of V_R measurements from 9275 km s^{-1} (Fouque et al., 1992) to 9430 $\pm$ 35 km s^{-1} (IRAS redshift survey; Strauss & Huchra 1988). Our measurement of $V_R = 9420.14^{+4.08}_{-3.91}$ km s^{-1} is in agreement with the higher end of these measurements. Table 2.5 lists the redshifts we have derived from our HI observations alongside previously published redshifts from a variety of observations and analysis methods.

2.3 *Distances and Masses*

With the detection of HI 21 cm emission from 31 AGN host galaxies, we can explore the gas properties of these galaxies compared to their stellar and central black hole properties. We also augmented our sample by including the dwarf Seyfert NGC 4395, as it should provide an interesting comparison as the lowest-mass AGN with a direct black hole mass constraint, hosted by a bulgeless low surface brightness galaxy. We describe here our adopted measurements and derived quantities for the baryonic properties of the galaxies.

2.3.1 *Distances*

Only five of the galaxies that we detected have distance measurements independent of their redshifts. The sources of the distances to NGC 3227, NGC 3783, NGC 4051, NGC 4151, and NGC 4593 are summarized in Bentz et al. (2013), but in brief, the measurements are generally the average of distances to galaxies within the same group, and were retrieved from the EDD. The exception is NGC 3227, which has an adopted distance that is the same as NGC 3226, with which it is interacting and which has a distance from the surface brightness fluctuation method (Tonry et al., 2001). These five galaxy distances have been recalibrated with a Hubble constant of H_0=72 km s^{-1} Mpc^{-1} for consistency with the Hubble Space Telescope (HST) Key Project (Freedman et al., 2001). Additionally, NGC 4395 has a distance from Cepheid variables (Thim et al., 2004) of 4.1 $\pm$ 0.4 Mpc.

Many of the galaxies in our sample were included in Bentz et al. (2013) and Bentz & Manne-Nicholas (2018). For those objects, we adopt the luminosity distances (D_L) reported in those works,

Table 2.5. z Comparisons

Target	z (HI) This Work	z (HI) Lit	Ref	z (Opt) Lit	z (IR) Lit	z (UV) Lit	Ref
(1)	(2)	(3)	(4)	(5)	(6)	(7)	(8)
Mrk 1044	0.01638	···	···	0.01621	···	0.01600	10,11
Ark 120	0.03271	0.03271	1	0.03312	···	···	12
MCG+08-11-011	0.02046	0.02046	2	0.02064	···	···	12
Mrk 6	0.01878	0.01881	3	0.01701 - 0.01975	···	···	13
Mrk 374	0.04420	0.04263	4	0.04385	···	···	14
Mrk 79	0.02221	0.02221	2	0.02192 - 0.02242	0.02220	···	13,15
NGC 2617	0.01423	0.01421	5	0.01432	···	···	13
Mrk 704	0.03177	···	···	0.02923 - 0.02991	0.02900	0.02900	16,12,15,11
Mrk 110	0.03522	···	···	0.03529	···	···	17
NGC 3227	0.00382	···	···	0.00371 - 0.00383	0.00400	···	18,19,15
NGC 3516	0.00876	···	···	0.00872 - 0.00884	0.00900	···	18,17,15
SBS1116+583A	0.02794	···	···	0.02788	···	···	20
NGC 3783	0.00973	0.00973	6	0.00851 - 0.01022	0.00970	···	13,15
Mrk 1310	0.01947	···	···	0.01956 - 0.02000	···	···	21,22
NGC 4051	0.00235	0.00234	7	0.00209 - 0.00235	0.00200	···	18,19,15
NGC 4151	0.00333	0.00333	8	0.00319 - 0.00320	0.00300	···	23,18,15
Mrk 766	0.01301	···	···	0.01293 - 0.01300	0.01293 - 0.01300	···	24,22,25,15
NGC 4593	0.00835	···	···	0.00797 - 0.00900	0.00900	···	13,26
NGC 4748	0.01395	···	···	0.01463	0.01500	···	27,15
MCG-06-30-015	0.00785	···	···	0.00775	0.00775 - 0.00800	···	28,29,15
Mrk 279	0.03073	···	···	0.02970	0.03025 - 0.03045	0.03050	30,31,32,33
NGC 5548	0.01716	0.01699 - 0.01727	3	0.01645 - 0.01651	0.01700 - 0.01717	0.01720	34,35,20,15,31,33
Mrk 817	0.03142	···	···	0.03120	0.03100 - 0.03146	0.03130	30,15,32,33
Mrk 478	0.07965	···	···	0.07500 - 0.07906	0.07700	0.07700	36,12,37,11
NGC 5940	0.03405	0.03408	2	0.03369 - 0.03400		0.03400	38,39,11
Mrk 290	0.03031	···	···	0.03023 - 0.03040	0.03000 - 0.03062	0.02960	40,20,37,31,33
Mrk 493	0.03150	···	···	0.03131 - 0.03133	···	0.03100	12,16,11
Zw 229-015	0.02774	···	···	0.02660 - 0.02788	···	···	41,42
1H1934-063	0.01065	0.01025	5	0.01060	0.01059	···	43,26
NGC 6814	0.00521	0.00521 - 0.00522	9,2	0.00479 - 0.00503	0.00567	···	18,12,44
NGC 7469	0.01644	0.01627	3	0.01580 - 0.02000	0.01600	···	45,16,15

Note. — The uncertainties on the redshift measurements ranged from ∼0.002%-0.15%. Column (4) denotes the references for z from HI analysis and are as follows: 1. Theureau et al. (2005), 2. Springob et al. (2005), 3. Gallimore et al. (1999), 4. Davoust & Contini (2004), 5. Paturel et al. (2003), 6. Theureau et al. (1998), 7. Verheijen & Sancisi (2001), 8. Wolfinger et al. (2013), 9. Koribalski et al. (2004). Column (8) denotes the references for all other z values and are as follows: 10. Huchra et al. (1993), 11. Monroe et al. (2016), 12. de Vaucouleurs et al. (1991), 13. NED, 14. Rines et al. (2000), 15. Hernán Caballero (2012), 16. Falco et al. (1999), 17. Keel (1996), 18. Humason et al. (1956), 19. Hakobyan et al. (2012), 20. Oh et al. (2015), 21. Ho & Kim (2009), 22. Stocke et al. (1991), 23. Wong et al. (2008), 24. Ramella et al. (1995), 25. Smith et al. (1987), 26. Strauss et al. (1992), 27. Maza & Ruiz (1989), 28. Kaldare et al. (2003), 29. Fisher et al. (1995), 30. Osterbrock & Pogge (1987), 31. Mendoza-Castrejón et al. (2015), 32. Strauss & Huchra (1988), 33. Tilton et al. (2012), 34. Haynes et al. (2011), 35. Humason et al. (1956), 36. Richards et al. (2009), 37. Shi et al. (2014), 38. Rines et al. (2016), 39. Wu & Jia (2010), 40. Argudo-Fernández et al. (2015), 41. Smith et al. (2015), 42. Proust et al. (1995), 43. Panessa et al. (2011), 44. Riffel et al. (2013), 45. Joshi et al. (2012).

which are derived from the redshifts of each galaxy. Uncertainties of 500 km s^{-1} were adopted due to the typical range of peculiar velocities reported by Tully et al. (2008).

For Mrk 1044, MCG+08-11-011, Mrk 374, NGC 2617, Mrk 704, Mrk 478, NGC 5940, Mrk 493, and 1H1934-063, we use our redshift measurement from the HI emission line to estimate D_L. For consistency with the other objects in our sample, we adopt an uncertainty of 500 km s^{-1} to account for peculiar velocities that may affect the distance derived from the redshift. Adopted distances are listed in Table 2.6.

2.3.2 *HI and Total Gas Mass*

The integrated flux of the HI emission line allows the atomic gas mass to be estimated because the intensity from the spin-flip radiation of optically thin sources is related to the number of HI atoms in a 1 cm^2 cross-section column. The measured flux is thus directly related to the total number of HI atoms in the beam, and the mass is given by

$$\frac{M_{HI}}{M_{\odot}} = [1.2 \times 10^5 D^2] \sum_{i=1}^{n} T_L(i) \Delta v \tag{2.2}$$

(Roberts, 1962), where D is the distance in Mpc (see Table 2.6), the summation is over channels spanning the HI emission-line profile, and Δv is the channel width in km s^{-1}.

The HI mass of a galaxy is then related to total gas mass as

$$M_{GAS} = 1.4 M_{HI} \tag{2.3}$$

(Cox, 2000). The scale factor of 1.4 accounts for the amount of atomic helium gas in the galaxy assuming solar abundance. As stated previously, H_2 is the next most prevalent gas phase in disk galaxies. However, McGaugh (2012) revisited several molecular gas content estimation techniques (e.g., Young & Knezek 1989), and concluded that there is no compelling evidence for significant sources of baryonic matter in disk galaxies other than what can be directly detected through observations, and that the molecular gas contribution (in gas-rich spirals) is usually smaller than

the uncertainty in the M_{HI} calculation. The uncertainties on the gas masses are primarily set by the uncertainties on the galaxy distances, but a small contribution also comes from the uncertainty on the integrated HI line flux. The M_{GAS} data used in McGaugh (2012) included uncertainties between 0.05 - 0.41 dex, consistent with what we find. Therefore, we assume that HI and helium accounts for approximately all significant gas mass contributions, with other phases and molecular gas providing a negligible contribution.

We derived M_{GAS} for NGC 4395 using the HI flux available in the All Digital HI Catalog (Springob et al., 2005) with Equations 2.2 and 2.3. The 140-foot Green Bank telescope was used to observe NGC 4395 and produce the subsequent HI flux we have used here. The beam size of the 140-foot is $21'$, large enough to encompass the angular extent of NGC 4395, therefore allowing use of Equation 2.2.

2.3.3 *Stellar and Baryonic Mass*

In order to derive baryonic masses, we adopt the stellar masses determined by Bentz & Manne-Nicholas (2018) for the majority of our targets. In that study, images in the V and H passbands from HST and the WIYN High-Resolution Infrared Camera, respectively, were modeled with GALFIT to separate the two-dimensional surface brightness components of the galaxy from the background sky and the AGN point source. $V-H$ colors were derived from the fits to the galaxies and were used with the Bell & de Jong (2001) prescriptions to estimate the stellar mass-to-light (M/L) ratios, and therefore the stellar masses, of the galaxies. We adopt the stellar masses based on the Bell & de Jong (2001) prescriptions for the 22 galaxies in common between this work and that of Bentz & Manne-Nicholas (2018), and list them in Table 2.6.

For those objects in our sample that were not included in the Bentz & Manne-Nicholas (2018) study, we estimated the stellar masses based on in-hand data, magnitudes and colors taken from the literature, or a combination of the two. The stellar mass for NGC 5548 was determined from in-hand HST V-band and Apache Point Observatory[5] H-band images in the same manner as the

[5]Based in part on observations obtained with the Apache Point Observatory 3.5 m telescope, which is owned and operated by the Astrophysical Research Consortium.

Table 2.6. Mass Estimates

Target	Morphology	D_L (Mpc)	Ref	Log M_{BH} ($M_\odot$)	Ref	Log M_{STARS} ($M_\odot$)	Log M_{GAS} ($M_\odot$)	Log M_{BARY} ($M_\odot$)
(1)	(2)	(3)	(4)	(5)	(6)	(7)	(8)	(9)
Mrk 1044	SB(s)c[b]	69.1 ± 7.0	1	$6.71^{+0.12}_{-0.10}$	7	9.88 ± 0.51	$9.60^{+0.08}_{-0.08}$	10.06 ± 0.39
Ark 120	Sb pec[a]	139.6 ± 7.1	2	$8.07^{+0.05}_{-0.06}$	8	11.04 ± 0.23	$10.05^{+0.05}_{-0.04}$	11.08 ± 0.21
MCG+08-11-011	SBc[b]	86.5 ± 7.0	1	$7.43^{+0.15}_{-0.15}$	9	11.37 ± 0.50	$10.27^{+0.07}_{-0.07}$	11.40 ± 0.48
Mrk 6	Sb[b]	80.6 ± 7.1	2	$8.10^{+0.04}_{-0.04}$	8	10.68 ± 0.23	$9.52^{+0.07}_{-0.07}$	10.71 ± 0.22
Mrk 374	SBc[b]	190.2 ± 7.2	1	$7.30^{+0.31}_{-0.31}$	9	10.85 ± 0.50	$9.55^{+0.03}_{-0.03}$	10.87 ± 0.49
Mrk 79	SBb[a]	94.0 ± 7.2	2	$7.61^{+0.11}_{-0.14}$	8	10.69 ± 0.23	$9.87^{+0.07}_{-0.07}$	10.75 ± 0.21
NGC 2617	Sc[b]	59.9 ± 7.0	1	$7.49^{+0.14}_{-0.14}$	9	10.47 ± 0.51	$10.04^{+0.09}_{-0.09}$	10.61 ± 0.42
Mrk 704	SBab[b]	135.5 ± 7.1	1	$7.61^{+0.06}_{-0.06}$	10	11.10 ± 0.40	$8.77^{+0.06}_{-0.06}$	11.10 ± 0.40
Mrk 110	Sc[b]	150.9 ± 7.1	2	$7.29^{+0.10}_{-0.10}$	8	10.69 ± 0.23	$9.56^{+0.05}_{-0.05}$	10.72 ± 0.22
NGC 3227	SAB(s) pec[a]	16.1 ± 2.4	3	$6.78^{+0.08}_{-0.11}$	8	11.03 ± 0.23	$9.09^{+0.11}_{-0.11}$	11.04 ± 0.23
NGC 3516	(R)SB(s)[a]	37.1 ± 7.0	2	$7.40^{+0.04}_{-0.06}$	8	10.52 ± 0.25	$7.97^{+0.14}_{-0.14}$	10.52 ± 0.25
SBS1116+583A	SBc[b]	118.5 ± 7.1	2	$6.56^{+0.08}_{-0.09}$	8	10.38 ± 0.23	$8.96^{+0.06}_{-0.06}$	10.40 ± 0.22
NGC 3783	(R')SB(r)a[a]	25.1 ± 5.0	4	$7.37^{+0.08}_{-0.08}$	8	10.48 ± 0.24	$9.33^{+0.15}_{-0.15}$	10.51 ± 0.23
Mrk 1310	Sbc[b]	82.7 ± 7.0	2	$6.21^{+0.07}_{-0.09}$	8	9.98 ± 0.23	$9.41^{+0.07}_{-0.07}$	10.08 ± 0.19
NGC 4051	SAB(rs)bc[a]	9.8 ± 3.4	4	$6.13^{+0.12}_{-0.16}$	8	10.13 ± 0.25	$8.99^{+0.23}_{-0.23}$	10.16 ± 0.24
NGC 4151	(R')SAB(rs)ab[a]	13.9 ± 3.3	4	$7.56^{+0.05}_{-0.05}$	8	10.40 ± 0.25	$9.37^{+0.17}_{-0.17}$	10.44 ± 0.23
Mrk 766	SBc[b]	54.4 ± 7.0	2	$6.82^{+0.05}_{-0.06}$	8	10.18 ± 0.24	$8.27^{+0.10}_{-0.10}$	10.19 ± 0.24
NGC 4395	SA(s)m[a]	4.1 ± 0.4	5	$5.45^{+0.13}_{-0.15}$	8	9.08 ± 0.41	$9.21^{+0.08}_{-0.08}$	9.45 ± 0.23
NGC 4593	(R)SB(rs)b[a]	37.7 ± 7.5	4	$6.88^{+0.08}_{-0.10}$	8	10.83 ± 0.25	$9.50^{+0.15}_{-0.15}$	10.85 ± 0.24
NGC 4748	Sab[b]	61.6 ± 7.0	2	$6.41^{+0.11}_{-0.18}$	8	10.46 ± 0.24	$9.22^{+0.09}_{-0.09}$	10.48 ± 0.23
MCG-06-30-015	S0[b]	25.5 ± 3.5	4	$6.20^{+0.35}_{-0.35}$	8	10.02 ± 0.22	$7.17^{+0.15}_{-0.12}$	10.02 ± 0.22
Mrk 279	S0[a]	129.7 ± 7.1	2	$7.44^{+0.10}_{-0.13}$	8	11.07 ± 0.23	$9.43^{+0.05}_{-0.05}$	11.08 ± 0.23
NGC 5548	(R')SA(s)0/a[a]	75.0 ± 7.3	6	$7.72^{+0.02}_{-0.02}$	8	11.10 ± 0.23	$9.22^{+0.08}_{-0.08}$	11.11 ± 0.23
Mrk 817	SBc[a]	134.2 ± 7.1	2	$7.59^{+0.06}_{-0.07}$	8	10.97 ± 0.23	$9.28^{+0.05}_{-0.04}$	10.98 ± 0.23
Mrk 478	Sab[b]	351.6 ± 7.4	1	$7.40^{+0.18}_{-0.18}$	11	11.15 ± 0.50	$10.12^{+0.03}_{-0.02}$	11.19 ± 0.47
NGC 5940	SBc[b]	145.5 ± 7.1	1	$7.04^{+0.07}_{-0.06}$	12	11.06 ± 0.40	$10.07^{+0.04}_{-0.04}$	11.10 ± 0.37
Mrk 290	S0[b]	130.0 ± 7.3	6	$7.28^{+0.06}_{-0.06}$	8	10.52 ± 0.40	$9.30^{+0.05}_{-0.05}$	10.54 ± 0.38
Mrk 493	SB(r)c[b]	134.3 ± 7.1	1	$6.41^{+0.04}_{-0.09}$	7	10.44 ± 0.50	$9.99^{+0.05}_{-0.05}$	10.57 ± 0.41
Zw 229-015	(R)SBc[b]	120.2 ± 7.2	2	$6.91^{+0.08}_{-0.12}$	8	10.32 ± 0.23	$9.31^{+0.05}_{-0.05}$	10.36 ± 0.21
1H1934-063	Sbc[b]	45.2 ± 7.0	1	$6.40^{+0.17}_{-0.20}$	11	10.53 ± 0.21	$9.18^{+0.12}_{-0.12}$	10.55 ± 0.20
NGC 6814	SAB(rs)bc[a]	21.8 ± 7.0	2	$7.04^{+0.06}_{-0.06}$	8	10.34 ± 0.29	$9.64^{+0.22}_{-0.22}$	10.42 ± 0.26
NGC 7469	(R')SAB(rs)a[a]	68.8 ± 7.0	2	$6.96^{+0.05}_{-0.05}$	8	10.88 ± 0.23	$9.18^{+0.10}_{-0.10}$	10.89 ± 0.23

Note. — Mass estimates and morphologies for the AGNs in this study. Morphological classifications in column (2) are from NED or the B/T ratios from the results of the surface brightness decomposition parameters from Bentz et al. (2009a), Bentz et al. (2013), Bentz et al. (2016), and Bentz & Manne-Nicholas (2018). Classifications were assigned to the B/T values based on Figure 6 of Kent (1985) (see Sec. 2.4.1). Column (3) lists the distances employed for each galaxy and are described in Sec. 3.5. The references listed in column (4) are for the sources of the distance values and are as follows: 1. estimated from redshift of HI emission line; this work, 2. Bentz & Manne-Nicholas (2018), 3. Tonry et al. (2001), 4. Courtois et al. (2009b), 5. Thim et al. (2004), 6. Bentz et al. (2013). Column (5) lists the SMBH values of each galaxy and are discussed in Sec. 2.3.4. The references listed in column (6) are for the sources of the M_{BH} values and are as follows: 7. mass calculated with $\tau_{H\beta}$ by Hu et al. (2015), σ_{line} by Du et al. (2016b), and scaled with $\langle f \rangle = 4.3$, 8. the AGN Black Hole Mass Database (Bentz & Katz, 2015), 9. the virial mass from Fausnaugh et al. (2017) scaled with $\langle f \rangle = 4.3$, 10. the virial mass from De Rosa et al. (2018) scaled with $\langle f \rangle = 4.3$, 11. preliminary mass estimate from in-hand reverberation mapping data, 12. mass calculated from the σ_{line} by Barth et al. (2015), $\tau_{H\beta}$ by Barth et al. (2013), and scaled with $\langle f \rangle = 4.3$. M_{STARS} estimates are listed in column (7) and the calculations are described in Sec. 2.3.3. The calculations for M_{GAS} estimates listed in column (8) are described in Sec. 2.3.2. M_{BARY} values in column (9) were calculated as $M_{GAS} + M_{STARS}$.

Bentz & Manne-Nicholas (2018) sample. For MCG-06-30-015 and 1H1934-063, we estimated the stellar masses using the same method and prescription from Bell & de Jong (2001) with our in-hand HST V-band images combined with ground-based K-band images from the VISTA Hemisphere Survey[6] (VHS; McMahon et al. 2013).

The stellar masses for Mrk 704, NGC 5940, and Mrk 290 were estimated using the disk $B-V$ colors reported by Granato et al. (1993). The disk colors will not be affected by the central AGN; however, they will also be missing much of the color contributed by the bulge, which influences the total color and therefore the M/L ratio. Due to this limitation, we adopt an uncertainty of 0.28 mag on the colors. We then combined these colors with in-hand HST V-band magnitudes to estimate the stellar M/L ratios and thus stellar masses. We adopted a typical uncertainty of 0.2 mag for the HST V-band magnitudes, consistent with Bentz & Manne-Nicholas (2018).

The stellar masses for Mrk 1044, MCG-08-11-011, Mrk 374, NGC 2617, Mrk 478, and Mrk 493 were derived by first estimating the mean galaxy color based on their morphological types (Buta et al. 1994, Table 6). For MCG-08-11-011, Mrk 374, NGC 2617, and Mrk 478, we then combined the estimated color with in-hand HST V-band magnitudes to estimate the stellar M/L ratio using the Bell & de Jong (2001) prescriptions, and thus constrain the total stellar mass. In the cases of Mrk 1044 and Mrk 493, where we did not have V-band HST imaging in hand, we utilized the surface brightness decompositions of Wang et al. (2014) to determine the fraction of the AGN luminosity to the total galaxy luminosity. We then corrected the total V-band magnitudes of these galaxies reported by MacKenty (1990) for the estimated contributions of the central AGNs. Combined with the galaxy color estimated from the morphological type, we were able to estimate the stellar M/L and thus the total stellar mass. For the HST V-band magnitudes, we adopted a typical uncertainty of 0.2 mag. For the mean galaxy colors and magnitudes from MacKenty (1990), we conservatively adopted uncertainties of 0.35 mag and 0.25 mag, respectively.

We derived the stellar mass for NGC 4395 using the integrated B-band magnitude and $B-V$ color from Prugniel & Heraudeau (1998), and the stellar M/L ratio from Bell & de Jong (2001).

[6]Based on observations obtained as part of the VISTA Hemisphere Survey, ESO Progam, 179.A-2010 (PI: McMahon.)

The contamination from the AGN hosted by NGC 4395 is negligible, yet we conservatively adopt uncertainties of 0.28 mag for the color and 0.2 mag for the magnitude.

Finally, baryonic masses were calculated simply as

$$M_{BARY} = M_{STARS} + M_{GAS} \tag{2.4}$$

and are reported in Table 2.6.

2.3.4 *Black Hole Mass*

The parent sample for the galaxies in this study is the reverberation sample of AGNs with direct black hole mass constraints. Reverberation mapping (Blandford & McKee, 1982; Peterson, 1993) is a light-echo technique in which the radius of the spatially-unresolved broad line region (R_{BLR}) is measured. The BLR of an AGN is composed of optically thick gas moving at large Doppler velocities deep in the potential well of the black hole. The BLR gas is photoionized by the continuum emission source (likely the accretion disk) and gives rise to the characteristic broad emission lines seen in the spectra of Type 1 AGNs. Variations in the continuum flux drive variations in the broad emission line flux, but delayed in time from the observer's point of view due to the extra path length most of the BLR light must travel to the observer. This time lag value provides a direct measure of the BLR size. Combining R_{BLR} and the Doppler-broadened emission line width through the virial theorem yields a constraint on the total mass enclosed within the BLR, the vast majority of which is the mass of the SMBH.

The black hole masses adopted here are from the AGN Black Hole Mass Database (Bentz & Katz, 2015), which is a compilation of reverberation-based M_{BH} values. Thus, the masses are calculated as

$$M_{\rm BH} = f\frac{c\tau V^2}{G} \tag{2.5}$$

where $c\tau$ is the time delay for a broad emission line, V is the width of the line, and G is the gravitational constant. The f term is an order-unity scaling factor which accounts for the unknown

kinematics and geometry of the BLR gas in AGNs. It is generally derived by assuming that the AGN black hole mass - stellar velocity dispersion relationship ($M_{BH} - \sigma_{STARS}$; Ferrarese & Merritt 2000; Gebhardt et al. 2000) is the same as that of nearby galaxies with black hole masses from dynamical modeling. We adopt $\langle f \rangle = 4.3$ which was determined by Grier et al. (2013a).

A few of the AGNs in our sample are included in the in-progress updates to the AGN Black Hole Mass Database, and thus require a little more explanation. For MCG+08-11-011, Mrk 374, and NGC 2617, we employed the virial M_{BH} from Fausnaugh et al. (2017), but scaled to match our adopted $\langle f \rangle$ value. Similarly, we employed the virial M_{BH} for Mrk 704 from De Rosa et al. (2018) and rescaled it with our adopted $\langle f \rangle$ value. For Mrk 1044 and Mrk 493, we utilized the Hβ time delay ($\tau_{H\beta}$) measurement from Hu et al. (2015) and the width of the Hβ emission line in the variable, root mean square (rms) spectrum (σ_{line}) from Du et al. (2016b) together with our adopted $\langle f \rangle$ value to calculate M_{BH}. For NGC 5940 we utilized the σ_{line} value from Barth et al. (2015) and the $\tau_{H\beta}$ value from Barth et al. (2013) to determine a black hole mass.

We have adopted a preliminary black hole mass for Mrk 478 based on early analysis of in-hand reverberation-mapping data (de Rosa 2019, private communication). The black hole mass for 1H1934-063 is based on current work on in-hand reverberation-mapping data from Bentz et al. (2019, in prep).

2.4 *Discussion*

In the past two decades there has been a surge of studies focusing on scaling relationships between host galaxy and SMBH characteristics, and these relationships seem to suggest galaxy − black hole coevolution. Such empirical scaling relations include the relationship between M_{BH} and the luminosity of the bulge ($M_{BH} - L_{BULGE}$; Kormendy & Richstone 1995), the M_{BH} − stellar velocity dispersion relation (Ferrarese & Merritt, 2000; Gebhardt et al., 2000), and the most recent calibration of the $M_{BH} - M_{STARS}$ relation found by Bentz & Manne-Nicholas (2018). Many of these scaling relationships are used as inputs or constraints to cosmological galaxy simulations in an attempt to further understand the details of the symbiotic relationship between galaxies and black holes (e.g.,

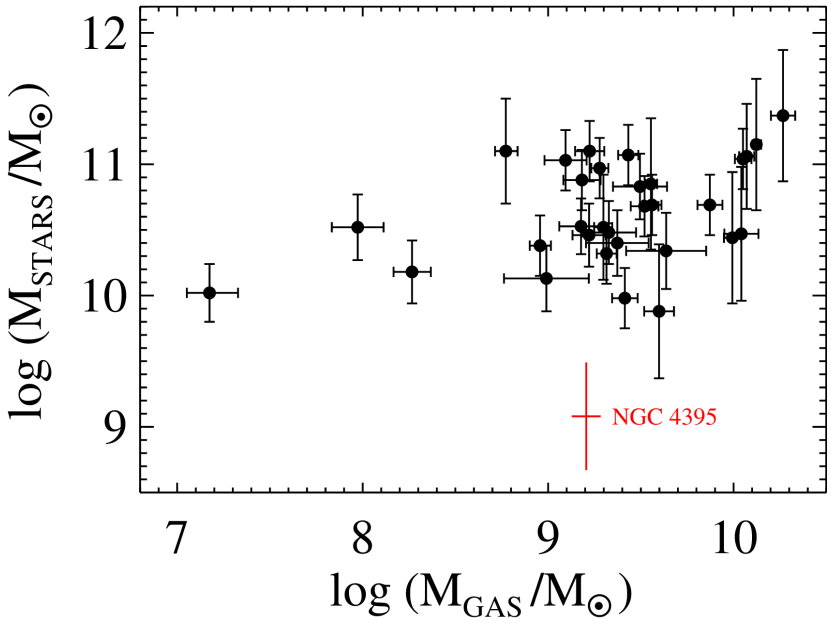

Figure 2.5: Comparison between M_{GAS} and M_{STARS}. There is a slight preference for gas mass to trace stellar mass, but the range of stellar masses is relatively small and the scatter is quite large.

Steinborn et al. 2015; Volonteri et al. 2016; Mutlu-Pakdil et al. 2018). Here, we explore potential scaling relationships that include M_{GAS}.

Linear regressions were carried out using the Bayesian method-based algorithm LINMIX_ERR (Kelly, 2007), which accounts for measurement uncertainties in both variables and includes an element of random scatter. We report the median and 1-σ deviations of large, random samples from the posterior probability distribution as the measurement and uncertainty for the slope, intercept, and scatter of each relationship.

2.4.1 *Gas Mass - Stellar Mass Relationship*

We first explored the relationship between M_{GAS} and M_{STARS} in our sample. We might expect to see smaller amounts of gas in galaxies with higher stellar mass if the gas content of these galaxies is not replenished as quickly as it is used up for star formation.

Fig. 2.5 displays M_{STARS} vs. M_{GAS}. There is a slight tendency for lower stellar mass to correspond to lower gas mass. The range of stellar and gas masses covered by our sample is fairly small,

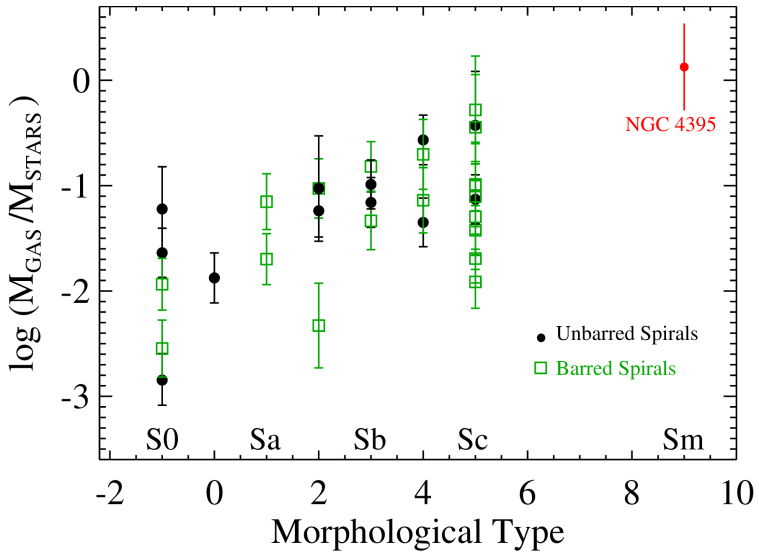

Figure 2.6: Gas fraction as a function of galaxy morphological type. Morphologies are either those listed in NED or from the derived B/T ratios, which were the results of the surface brightness fits carried out by Bentz et al. (2009a), Bentz et al. (2013), Bentz et al. (2016), and Bentz & Manne-Nicholas (2018) (see Sec. 2.4.1, Table 2.6). Morphologies based on B/T values were assigned according to the mean of the distributions in Figure 6 of Kent (1985). The black circles are unbarred spirals, the green squares are barred spirals.

however, given that most of the points are clumped together at $9 < \log(M_{GAS}/M_{\odot}) < 10$ and $10 < \log(M_{STARS}/M_{\odot}) < 11$, and the scatter is quite large.

We next examined whether the fraction of gas-to-stellar content in the galaxies, M_{GAS}/M_{STARS}, might serve as an indicator of morphological type. One might expect the gas content to change as a function of morphology, with lower M_{GAS} for early-type spirals, and higher values for later-types.

To explore this, we adopted galaxy morphologies from NED for those galaxies where previous ground-based data provided sufficient angular resolution to determine the morphology (most of the NGC objects, for example). For the more distant and compact galaxies, we determined the morphological type based on the bulge-to-total (B/T) luminosity ratio as follows. For most of the objects, the surface brightness decompositions of Bentz et al. (2009a), Bentz et al. (2013), Bentz et al. (2016), and Bentz & Manne-Nicholas (2018) were used to calculate B/T values, and these were compared to the distributions of B/T relative to galaxy morphology presented by Kent (1985) in their Figure 6. We then adopted the morphology associated with the mean B/T value that most

closely matched the B/T measured for each galaxy. For MCG+08-11-011 Mrk 374, NGC 2617, Mrk 704, Mrk 478, NGC 5940, and 1H1934-063, we calculated the B/T ratios from surface brightness decompositions of in-hand HST *V*-band images. Finally, for Mrk 1044 and Mrk 493, we used the surface brightness decompositions from Wang et al. (2014) in order to derive the B/T ratios.

Fig. 2.6 shows the gas-to-stellar fraction as a function of morphology. The black circles in Fig. 2.6 denote unbarred spirals, and the green squares denote barred spirals. The gas-to-stellar fraction appears to be approximately constant as a function of morphology for the barred spirals, albeit with a large scatter and with a lower typical M_{GAS}/M_{STARS} for SB0 galaxies. However the unbarred spirals show a slight preference for a higher gas fraction at later types, especially when the unbarred Sm galaxy NGC 4395 is included.

In addition, we explored the gas-to-stellar fraction as a function of M_{STARS}. If the gas reservoir of the galaxy is never refueled by accretion onto the disk, we might expect to see evidence of decreasing gas for galaxies of higher stellar content. However, there would be little evidence of this trend if accretion is ongoing and the reservoir is steadily refueled. In the left panel of Fig. 2.7 we plot the fraction M_{GAS}/M_{STARS} versus M_{STARS} and compare to several simple scenarios. The black dotted line shows the best formal fit to the data points and has the form

$$\log\frac{M_{GAS}}{M_{STARS}} = (-1.48 \pm 1.44)\log\left(\frac{M_{STARS}}{10^{11}M_{\odot}}\right) - (1.46 \pm 0.14) \tag{2.6}$$

with a scatter of (0.41 $\pm$ 0.24) dex. NGC 4395 is not included in our formal fit. The blue dot-dash line represents a "closed-box" relation, where there is a one-to-one correlation between the decrease in M_{GAS} and increase in M_{STARS}, therefore no cold gas accretion. The slope is slightly steeper than the trend of the data, suggesting that some refueling must be occurring on average for the galaxies in our sample. The red dot-dot-dot-dash line represents a constant M_{GAS} relation, where gas is assumed to be replenished at the rate that it is used up for star formation. The slope of this relationship is shallower than our formal fit (which has large uncertainties), suggesting that the average galaxy in this sample is replenishing its gas reservoir, but at a rate that is slower than the

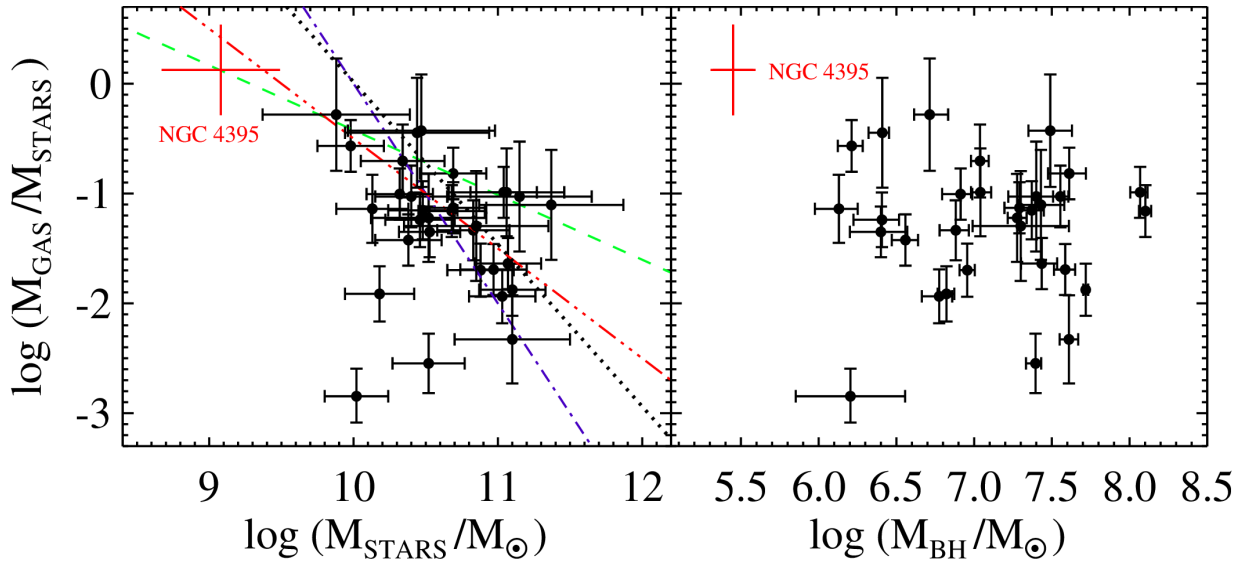

Figure 2.7: M_{GAS}/M_{STARS} as a function of M_{STARS} (left) and M_{BH} (right). The trend in the left plot shows decreasing mass fraction with increasing values of M_{STARS}. The black dotted line is our best fit with a scatter of (0.41 ± 0.24) dex. NGC 4395 is not included in the fit. The green dash line is the best-fit line found by Stewart et al. (2009) which characterizes the gas mass fraction of data from McGaugh (2005). The sample used by Stewart et al. (2009) is biased towards gas-rich spirals, while our sample is stellar-rich, which is a possible explanation to the data lying beneath the line. The blue dot-dash line shows a "closed box" relation that demonstrates direct conversion from M_{GAS} to M_{STARS}. The red dot-dot-dot-dash line shows a constant M_{GAS} relation, where M_{GAS} remains fixed at the approximate average value of our sample at $M_{GAS} \sim 10^{9.5}$ $M_{\odot}$ while M_{STARS} varies. On the right plot, there is no evidence of a trend for M_{GAS}/M_{STARS} as a function of M_{BH}.

gas is being used up. If NGC 4395 is included in the fit, we find a shallower slope of (-0.77 ± 0.42), much closer to that of the constant M_{GAS} relation.

McGaugh (2005) compiled a sample of galaxies with extended 21 cm rotation curves and derived gas and stellar masses for an in-depth baryonic Tully-Fisher relation study. Stewart et al. (2009), in their simulation of the baryonic content of galaxy mergers, assigned gas to the simulated galaxies by quantifying the relation between M_{GAS}/M_{STARS} as a function of M_{STARS} using the results from McGaugh (2005). Their M_{GAS}/M_{STARS} as a function of M_{STARS} at $z = 0$ is represented by the green dashed line in Fig. 2.7. The sample from McGaugh (2005) used by Stewart et al. (2009) is biased towards gas-rich galaxies, which explains why their relationship appears to serve as an upper limit

to our sample of galaxies. The general trend of decreasing gas fraction as M_{STARS} increases, however, is consistent between their sample and ours.

A recent study by Calette et al. (2018) included a large sample of early and late-type galaxies from the literature, attempting to homogenize their sample as much as possible, checking against potential biases in the process (i.e., selection effects, upper limits, distances which correct for peculiar motions). They found an overall decrease in M_{GAS}/M_{STARS} as a function of M_{STARS} similar to Stewart et al. (2009). However, their average slope from the single- and double-power law best fits is much shallower than ours and the sample of McGaugh (2005). Bradford et al. (2015) conducted a study of the baryonic content of galaxies selected from the Sloan Digital Sky Survey DR8 using isolated HI galaxy detections from the 40% ALFALFA survey (Haynes et al., 2011), which is a publicly available blind, drift-scan HI survey from the Arecibo Observatory. They also find a decreasing atomic-gas-to-stellar fraction as a function of stellar mass, with a break into a steeper slope at $M_{STARS} \approx 10^9$ $M_\odot$. The slope of the relationship they find after the break is very similar to our best-fit slope.

In addition, we have also explored M_{GAS}/M_{STARS} relative to M_{BH}, as shown in the right-hand panel of Fig. 2.7. We might expect M_{STARS} and M_{BH} to increase together, since the gas reservoir is used to create stars and fuel the growth of the SMBH. However, we find no evidence for a trend with this sample of AGNs. Instead, our sample demonstrates a relatively constant value of M_{GAS}/M_{STARS} as a function of M_{BH}, albeit with a large scatter. A formal fit finds a slope of (-0.02 ± 0.38), which is consistent with zero.

2.4.2 *Gas Mass - Black Hole Mass Relationship*

There have been many previous attempts to explore the connection between gas in galaxies and the central supermassive black hole. The vast majority of these studies have focused on AGN characteristics, such as luminosity or accretion rate, instead of the black hole mass itself. Such studies have included, for example, exploring correlations between Seyfert nucleus luminosity and HI emission peculiarities (Heckman et al., 1978), the link between the cold gas reservoir and AGN

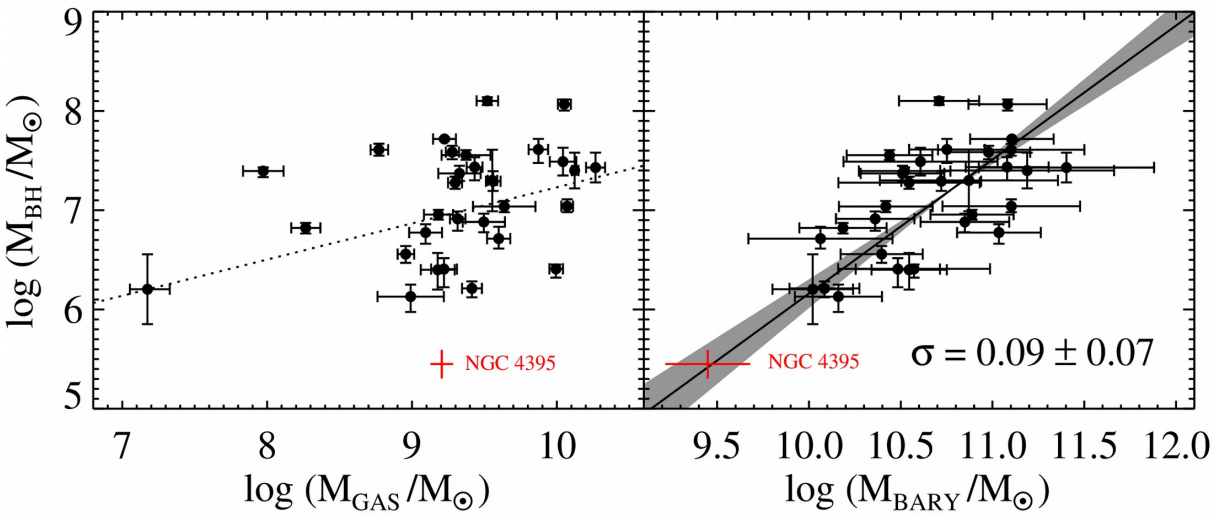

Figure 2.8: M_{BH} as a function of M_{GAS} (left) and M_{BARY} (right). For the data in the left plot, the formal fit for the M_{GAS}-M_{BH} relation includes a scatter of (0.32 $\pm$ 0.09) dex. On the right, the M_{BARY}-M_{BH} relation seems to exhibit a stronger correlation with less scatter. The red cross in the right panel is a derived baryonic mass for NGC 4395. NGC 4395 is not inluded in the fit to the black points, nevertheless it seems to follow the same relationship demonstrated by more massive galaxies.

accretion (van Gorkom et al., 1989; Peck & Taylor, 1998), and the connection between M_{HI}/M_{STARS} and black hole accretion rate (Fabello et al., 2011). The literature is inconclusive on these themes with other studies finding no evidence of mass transfer from the outer galactic regions to the central AGN when comparing gas content to near-infrared nuclear activity (Bieging & Biermann, 1983) and finding no discernable connection between global gas content and AGN presence (Ho et al., 2008b). However, even with the myriad of studies that do exist, it appears that no one has yet examined the relationship between gas mass and black hole mass.

The stellar content of galaxies seems to correlate with the black hole mass, for example the M_{BH} – L_{BULGE} (Kormendy & Richstone, 1995), $M_{BH} - \sigma_{STARS}$ (Ferrarese & Merritt, 2000), and M_{BH} – M_{STARS} (Bentz & Manne-Nicholas, 2018) relations. Here we explore whether the gas content also demonstrates a relation to M_{BH}.

We plot the reverberation-based black hole masses vs. the gas masses in Fig. 2.8. There is a weak correlation, with a slight preference for more massive black holes to live in galaxies with

larger gas reservoirs, but there is also a large scatter. A formal fit between M_{GAS} vs M_{BH} finds:

$$\log\frac{M_{BH}}{M_{\odot}} = (0.36 \pm 0.10)\log\left(\frac{M_{GAS}}{10^{9}M_{\odot}}\right) + (6.87 \pm 0.03) \tag{2.7}$$

with a scatter of (0.32 ± 0.09) dex. We also examined whether morphological type played a role in where objects fell in Fig. 2.8, but found no obvious trend.

2.4.3 *Baryonic Mass - Black Hole Mass Relationship*

Bentz & Manne-Nicholas (2018) recently calibrated the scaling relationship of M_{BH} to M_{STARS} for the AGN hosts in the reverberation sample. Their best fit based on the M/L ratio predictions of Bell & de Jong (2001) has a slope of (1.69±0.46) and an intercept of (8.05±0.18), with a scatter of (0.38±0.13) dex. In the right panel of Fig. 2.8, we show the relationship between M_{BH} and total baryonic masses for galaxies in our sample, many of which were included in the study by Bentz & Manne-Nicholas (2018). The best fit is given by:

$$\log\frac{M_{BH}}{M_{\odot}} = (1.35 \pm 0.18)\log\left(\frac{M_{BARY}}{10^{11}M_{\odot}}\right) + (7.51 \pm 0.04) \tag{2.8}$$

with a scatter of (0.09 ± 0.07) dex. The fits to both $M_{BH} - M_{BARY}$ and $M_{BH} - M_{STARS}$ are normalized at 10^{11} $M_{\odot}$, allowing for easier comparison. The stellar content accounts for the majority of the baryonic mass in these galaxies, so the slopes of the two relationships are formally indistinguishable. The typical fraction of M_{GAS}/M_{STARS} is about 10% for these galaxies, but reaches as high as 52% for Mrk 1044 and 134% for NGC 4395. The slight increase in baryonic mass over stellar mass accounts for the 0.5 dex shift in the intercept between the two relationships.

Interestingly, even though NGC 4395 has a significantly larger M_{GAS}/M_{STARS} than any of the other galaxies in our sample, it appears to follow the same relationship between black hole mass and baryonic mass as the other galaxies in our sample. NGC 4395 is not included in our fit to the rest of the data, but if we include it, we find a very similar slope of (1.34 ± 0.09). This initial

study suggests that the SMBHs of AGNs are not only correlated to their stellar content, but the total baryonic mass.

2.5 *Summary*

We present results from HI spectroscopy of 44 AGNs with reverberation-mapped black hole masses. We detect HI 21 cm emission in 31 of them, 12 of which are the first reported 21 cm detections. Measurements of the integrated HI fluxes, W_{50}, W_{20}, and V_R values are determined with two independent methods and are found to be generally consistent. From the HI fluxes, we determine M_{GAS} for each galaxy. Using the stellar masses provided by Bentz & Manne-Nicholas (2018) as well as derived M_{STARS} values from in-hand data and the literature, we also produce total M_{BARY} values for the galaxies in our sample.

We have explored a number of relationships involving M_{GAS}. We find no evidence for a correlation between M_{STARS} and M_{GAS}. We find a weak correlation between M_{BH} and M_{GAS}, albeit with a large scatter, and with no obvious trends based on morphological type. We find that the typical M_{GAS}/M_{STARS} value for our sample is $\sim 10\%$. For unbarred spirals, there is a slight preference for later morphological types to have larger M_{GAS}/M_{STARS}. For barred spirals, on the other hand, the gas fraction appears to be mostly constant as a function of morphology except for SB0 galaxies, where M_{GAS}/M_{STARS} is decidedly lower.

We find evidence of a trend of decreasing M_{GAS}/M_{STARS} as a function of M_{STARS}, consistent with findings by other groups, yet we detect no trend with M_{GAS}/M_{STARS} as a function of M_{BH}. Finally, we find a significant correlation between M_{BH} vs M_{BARY}, with similar slope to the recalibrated M_{BH} – M_{STARS} relation by Bentz & Manne-Nicholas (2018). The dwarf Seyfert NGC 4395 (which hosts the lowest reverberation-mapped black hole mass) is significantly more gas dominated than the other galaxies in our study, with $M_{GAS}/M_{STARS} = 134\%$, but it appears to follow the same trend in M_{BH} vs M_{BARY} defined by the other galaxies in our sample.

Chapter 3

Tully–Fisher Distances and Dynamical Mass Constraints for 24 Host Galaxies of Reverberation-mapped AGNs[1]

3.1 *Introduction*

It has become apparent in the past two decades that supermassive black holes (SMBHs) and their host galaxies have a symbiotic relationship (see reviews by Kormendy & Ho 2013 and Heckman & Best 2014), the discovery of which was unexpected given the vast difference in spatial and dynamical scales. The first indication of this was through empirical scaling relationships, for example the black hole mass – bulge velocity dispersion relation ($M_{\rm BH} - \sigma_\star$; Ferrarese & Merritt 2000, Gebhardt et al. 2000, Kormendy & Ho 2013) and the black hole mass – bulge luminosity relation ($M_{\rm BH} - L_{\rm BULGE}$; Kormendy & Richstone 1995; Kormendy & Ho 2013). To further understand and explore black hole-galaxy evolution, these scaling relations also provide observational evidence to constrain the parameters of large cosmological simulations of galaxy and SMBH growth (Steinborn et al., 2015; Volonteri et al., 2016; Mutlu-Pakdil et al., 2018). The generally accepted interpretation of these scaling relations and simulations is that black hole-galaxy growth is regulated by active galactic nucleus (AGN) feedback (Silk & Rees, 1998; Bower et al., 2006; Ciotti et al., 2009; Fanidakis et al., 2011), and thus SMBHs play an important role in galaxy evolution. It is therefore vital to obtain accurate measurements of both galaxy and black hole characteristics for investigating these relationships.

[1]This chapter was originally published in the Astrophysical Journal, Volume 912, Pages 160-185 on 2021 May 17, under the title "Tully–Fisher Distances and Dynamical Mass Constraints for 24 Host Galaxies of Reverberation-mapped AGNs" by Robinson et al. (2021). doi:10.3847/1538-4357/abedaa.

AGN activity not only affects galaxy evolution, it also provides a mechanism for directly constraining the mass of the central black hole through reverberation mapping (RM; Blandford & McKee 1982; Peterson 1993). Variability of the continuum emission is echoed through the variation in flux from the broad emission line region (BLR) gas. The time delay between the continuum signal and the BLR echo provides a measurement of the BLR radius ($R_{\rm BLR}$), which when combined with the velocity of the BLR gas yields a constraint on the enclosed mass, or $M_{\rm BH}$. In effect, RM relies on temporal resolution, as opposed to spatial resolution. Most other techniques that directly constrain $M_{\rm BH}$, such as dynamical modeling, rely on spatial resolution and therefore cannot be applied beyond $\sim$100 Mpc (Gültekin et al., 2009).

While RM measurements are effectively distance independent, they are both time consuming and resource intensive. However, the discovery of the relationship between $R_{\rm BLR}$ and the luminosity of the AGN ($R_{\rm BLR} - L_{\rm AGN}$; Koratkar & Gaskell 1991; Kaspi et al. 2000), calibrated with the RM method, has led to an important shortcut for estimating SMBH masses at any redshift (Vestergaard & Peterson, 2006; Jiang et al., 2007; Kurk et al., 2007, 2009; Willott et al., 2010). A single spectrum allows a measurement of $L_{\rm AGN}$ to predict $R_{\rm BLR}$, thus allowing $M_{\rm BH}$ to be estimated without investing months or years of spectroscopic monitoring.

The largest known uncertainty in the $R_{\rm BLR} - L_{\rm AGN}$ relation is the lack of accurate distances for AGN hosts, which produces uncertainties in the derived luminosities upwards of a factor of $\sim$3 (Bentz et al., 2013). Only 9 galaxies in the complete sample of RM AGN systems have distances independent of redshift. Since the sample is dominated by AGNs with $z \lesssim 0.1$, the majority of distances estimated from redshift may be heavily affected by the velocity field from local gravitational interaction, rather than dominated by Hubble flow. These peculiar velocities ($V_{\rm PEC}$) have been observed to be upwards of 500 km s^{-1} in the local universe (Tully et al., 2008, 2013), which causes significant uncertainty in distances derived solely from spectroscopic redshift. Measurements of galaxy properties that directly depend on distance (e.g., luminosity) and are relied on for SMBH-galaxy scaling relationships are thus hindered by z-based distances. The reverberation

sample serves as the basis for all secondary $M_{\rm BH}$ estimates in distant AGNs, so accurate distance determinations are crucial for a large number of RM AGN hosts.

Accurate distance measurements to galaxies in the local universe have allowed tight construction of what is commonly referred to as the cosmic distance ladder. The methods that set the scale for nearly all extragalactic rungs of the ladder are Leavitt's Law (Cepheid period-luminosity relationship; Leavitt & Pickering 1912) and the tip of the red giant branch (TRGB; Iben & Renzini 1983; Salaris & Cassisi 1997). Both of these methods require individual stars to be resolved, demanding high resolving power only achievable by a few instruments, thus limiting their reach to $\sim$40 Mpc (Riess et al., 2016). The surface brightness fluctuation (SBF; Tonry et al. 2001; Blakeslee et al. 2010) and Fundamental Plane (Faber & Jackson, 1976; Djorgovski & Davis, 1987; Dressler et al., 1987) methods are only applicable to early-type galaxies, but most of the optically bright AGNs in the local universe are hosted by spirals.

One of the most widely utilized distance methods for disk galaxies is the Tully–Fisher (TF) relation (Tully & Fisher, 1977). The TF relation is an empirical correlation between the rotational velocity of a late-type galaxy and its brightness. A galaxy's mass is constrained by its rotation rate, and its luminosity traces the mass. Therefore, measurement of the maximum rotation rate yields the absolute magnitude of the galaxy, and the difference between the absolute and apparent magnitudes constrains the distance. 21 cm emission from neutral hydrogen (HI), due to its overwhelming abundance in late-type galaxies and extension far past the stellar disk, is usually used to trace disk velocity. Resolved HI surveys (e.g., Walter et al. 2008; Ott et al. 2012; Koribalski et al. 2018; Adams & van Leeuwen 2019; Koribalski et al. 2020; Maddox et al. 2020) provide the most precise method for constraining maximum rotation rate (V_{mx}) through rotation curve analysis. For large samples of galaxies, the rotational broadening of unresolved, integrated HI emission may be used as a proxy for a rotation curve (Epstein, 1964; Roberts, 1969). The TF relation has traditionally been limited to $z \lesssim 0.1$ (Tully et al., 2008, 2013), even though HI has increasingly been detected at higher redshift (Jaffé et al., 2013; Catinella & Cortese, 2015; Fernández et al., 2016). Galaxies with $z \gtrsim 0.1$ are generally assumed to be within the Hubble flow.

We thus undertook a program to measure TF distances for as many RM AGN hosts as possible. In this paper, we use the HI emission lines from Robinson et al. (2019; hereafter Paper I) and present TF distance determinations for 24 Seyfert 1 galaxies. In Section 3.2, we briefly discuss the HI spectral observations (see Paper I) and describe the imaging of our sample. In Section 3.3, we describe the two-dimensional surface brightness modeling and separation of the central AGN from the host galaxy in the images. In Section 3.4, we describe the measurement methods for the calibrated galaxy magnitudes and HI 21 cm line widths. In Section 3.5, we detail our distance calculations and present the first calibration of the TF relation for the Johnson V band. In Section 3.6, we report derived values of galaxy dynamical mass ($M_{\rm DYN}$) and dark matter mass ($M_{\rm DM}$) within the HI radius. Finally, in Section 3.7, we explore the relationships between $M_{\rm DYN}$ and $M_{\rm DM}$ with $M_{\rm BH}$.

Throughout this work we adopt a ΛCDM cosmology of $\rm H_0 = 74\,km\,s^{-1}\,Mpc^{-1}$ (Riess et al., 2019), $\Omega_{\rm M}$=0.27, and Ω_{Λ}=0.73 (Bennett et al., 2014).

3.2 *Spectroscopy and Imaging*

In Paper I, we presented HI spectroscopy of 31 AGN hosts with direct $M_{\rm BH}$ measurements from the RM database of Bentz & Katz (2015), and constraints on gas mass ($M_{\rm GAS}$) and total baryonic mass ($M_{\rm BARY}$). Here we briefly summarize the 21 cm observations and describe the optical and near-infrared imaging of the AGN hosts.

3.2.1 *HI 21 cm Spectra*

Spectroscopy of the HI 21cm emission lines was acquired in 2013 (GBT13A-468; PI: Ou-Yang) and 2018/19 (GBT18B-258; PI: Robinson) with the Robert C. Byrd Green Bank Telescope[2] (GBT). The observational setups and instrument selections are detailed in Paper I. In brief, both data sets were observed in position-switched mode with equal on-off exposure pairs and typical exposures

[2]The Green Bank Observatory is a facility of the National Science Foundation operated under cooperative agreement by Associated Universities, Inc.

of 60 s scans for GBT13A-468 and 120 s scans for GBT18B-258. All scans were broken into 3 s integrations to aid in radio frequency interference removal.

Spectral reduction was carried out with the GBTIDL suite (Marganian et al., 2006) v2.8 for GBT13A-468 and v2.10.1 for GBT18B-258. Each on-off pair was combined with the standard (ON−OFF)/OFF procedure, and all exposures for one source were accumulated and averaged into a single spectrum. Low-order polynomials were fit to and subtracted from the baselines before spectral measurements were conducted.

While we detected HI emission lines from 31 of the 44 AGN host galaxies that were observed, we limit the analysis here to the 24 galaxies that exhibit a rotationally broadened dual-horned profile shape, as this is needed to recover the disk velocity information for use in TF distance determinations. Additionally, we note that although we limit this sample to dual-horned profiles, the galaxy inclinations tend to be oriented more face-on ($< 45°$) than the typical galaxies targeted for TF-based distances. The 24 galaxies are listed in Table 3.1.

3.2.2 *Optical and Near-Infrared Imaging*

Optical and near-infrared images of the AGN host galaxies have been compiled from several observatories, with the goal of separating the AGN contribution from the galaxy via 2-dimensional surface brightness decomposition (described in Sec. 3.3). For all ground-based data, images were reduced and combined in IRAF[3] following standard procedures.

3.2.2.1 Previous Observations

The majority of images used in this analysis were collected between 2003-2016 and have been previously described in publications. Table 3.1 lists observation dates, instrument setups, and exposure times.

HST: All 24 of our targets have medium-band V images obtained with the *Hubble Space Telescope* (*HST*). Galaxies were observed with either the Advanced Camera for Surveys (ACS)

[3]IRAF is distributed by the National Optical Astronomy Observatory, which is operated by the Association of Universities for Research in Astronomy (AURA) under a cooperative agreement with the National Science Foundation.

High Resolution Channel (HRC) through the F550M filter or the Wide Field Camera 3 (WFC3) through the F547M filter. The HRC has a field of view (FOV) of 29″ x 26″ and pixel scale of 0.″025 pixel^{-1}. The WFC3 observations utilized the UVIS channel, which has a 160″ x 160″ FOV and pixel scale of 0.″04 pixel^{-1}. In-depth descriptions of the *HST* observations and reductions are available in Bentz et al. (2009a, 2013); Bentz & Manne-Nicholas (2018).

Table 3.1:Optical and Near-IR Imaging

Target	RA (hh mm ss.s)	Dec (dd mm ss)	z	Date (yyyy-mm-dd)	Exp Time (s)	Obs. Setup
Mrk 1044	02 30 05.5	-08 59 53	0.01645	2011 Jan 10	725.0	HST WFC3 F547M
				2019 Dec 20	810.0	APO 3.5 m ARCTIC B
				2019 Dec 20	240.0	APO 3.5 m ARCTIC V
				2019 Sep 28	90.0	APO 3.5 m ARCTIC R
				2019 Sep 28	60.0	APO 3.5 m ARCTIC I
Ark 120	05 16 11.4	-00 08 66	0.03271	2006 Oct 30	2040.0	HST ACS HRC F550M
MCG+08-11-011	05 54 53.6	+46 26 22	0.02048	2016 May 21	2370.0	HST WFC3 F547M
Mrk 6	06 52 12.2	+74 25 37	0.01881	2014 Nov 06	2620.0	HST WFC3 F547M
				2020 Feb 12	60.0	APO 3.5 m ARCTIC V
				2012 Jan 13	720.0	WIYN WHIRC H
Mrk 374	06 59 38.1	+54 11 48	0.04263	2016 May 21	2420.0	HST WFC3 F547M
Mrk 79	07 42 32.8	+49 48 35	0.02219	2006 Nov 08	2040.0	HST ACS HRC F550M
				2003 Aug 12	1500.0	MDM 1.3 m Templeton B
				2003 Aug 12	1965.0	MDM 1.3 m Templeton V
				2003 Aug 12	1110.0	MDM 1.3 m Templeton R
				2012 Jan 13	4140.0	WIYN WHIRC H
NGC 2617	08 35 38.8	-04 05 18	0.01421	2016 May 21	2230.0	HST WFC3 F547M
				2020 Feb 17	1020.0	APO 3.5 m ARCTIC B
				2020 Feb 17	840.0	APO 3.5 m ARCTIC V
				2020 Feb 17	450.0	APO 3.5 m ARCTIC R
NGC 3227	10 23 30.6	+19 51 54	0.00386	2010 Mar 29	2250.0	HST WFC3 F547M
				2003 Aug 12	1800.0	MDM 1.3 m Templeton B
				2003 Aug 12	2280.0	MDM 1.3 m Templeton V
				2003 Aug 12	1575.0	MDM 1.3 m Templeton R
				2013 Apr 26	1470.0	WIYN WHIRC H
SBS 1116+583A	11 18 57.7	+58 03 24	0.02787	2010 Jun 06	2510.0	HST WFC3 F547M
NGC 3783	11 39 01.7	-37 44 19	0.00973	2011 Feb 09	2300.0	HST WFC3 F547M
				2015 Apr 23	960.0	SMARTS 0.9 m Tek2K B
				2015 Apr 23	960.0	SMARTS 0.9 m Tek2K V

Table 3.1:Optical and Near-IR Imaging

Target	RA (hh mm ss.s)	Dec (dd mm ss)	z	Date (yyyy-mm-dd)	Exp Time (s)	Obs. Setup
				2015 Apr 23	960.0	SMARTS 0.9 m Tek2K R
Mrk 1310	12 01 14.3	-03 40 41	0.01956	2009 Dec 02	2240.0	HST WFC3 F547M
				2015 Apr 23	960.0	SMARTS 0.9 m Tek2K B
				2015 Apr 23	960.0	SMARTS 0.9 m Tek2K V
				2015 Apr 23	960.0	SMARTS 0.9 m Tek2K R
				2013 Apr 27	4500.0	WIYN WHIRC H
NGC 4051	12 03 09.6	+44 31 53	0.00234	2010 Jul 17	2340.0	HST WFC3 F547M
				2003 Aug 12	1250.0	MDM 1.3 m Templeton B
				2003 Aug 12	795.0	MDM 1.3 m Templeton V
				2003 Aug 12	690.0	MDM 1.3 m Templeton R
				2013 Apr 26	3060.0	WIYN WHIRC H
NGC 4151	12 10 32.6	+39 24 19	0.00332	2010 Jul 03	2310.0	HST WFC3 F547M
				2003 Aug 12	1470.0	MDM 1.3 m Templeton B
				2003 Aug 12	1200.0	MDM 1.3 m Templeton V
				2003 Aug 12	1370.0	MDM 1.3 m Templeton R
				2019 May 26	1800.0	ARCSAT SurveyCam I
				2013 Apr 27	1005.0	WIYN WHIRC H
NGC 4593	12 39 39.4	-05 20 39	0.00900	2010 Jul 10	2240.0	HST WFC3 F547M
				2003 Aug 12	1650.0	MDM 1.3 m Templeton B
				2003 Aug 12	1860.0	MDM 1.3 m Templeton V
				2003 Aug 12	1380.0	MDM 1.3 m Templeton R
				2013 Apr 27	960.0	WIYN WHIRC H
NGC 4748	12 52 12.4	-13 24 53	0.01463	2010 Jun 28	2250.0	HST WFC3 F547M
				2015 Apr 23	960.0	SMARTS 0.9 m Tek2K B
				2015 Apr 23	960.0	SMARTS 0.9 m Tek2K V
				2015 Apr 23	960.0	SMARTS 0.9 m Tek2K R
				2013 Apr 27	3600.0	WIYN WHIRC H
NGC 5548	14 17 59.5	+25 08 12	0.01718	2010 Jul 15	2260.0	HST WFC3 F547M
				2003 Nov 17	4000.0	MDM 1.3 m Templeton B
				2003 Nov 17	2500.0	MDM 1.3 m Templeton V
				2003 Nov 17	1380.0	MDM 1.3 m Templeton R
Mrk 817	14 36 22.1	+58 47 39	0.03146	2003 Dec 08	1020.0	HST ACS HRC F550M
				2003 Nov 04	2530.0	MDM 1.3 m Templeton B
				2003 Nov 04	1530.0	MDM 1.3 m Templeton V
				2003 Nov 04	930.0	MDM 1.3 m Templeton R
				2013 Apr 26	3520.0	WIYN WHIRC H
NGC 5940	15 31 18.1	+07 27 28	0.03393	2016 May 28	2230.0	HST WFC3 F547M

Table 3.1:Optical and Near-IR Imaging

Target	RA (hh mm ss.s)	Dec (dd mm ss)	z	Date (yyyy-mm-dd)	Exp Time (s)	Obs. Setup
Mrk 290	15 35 52.3	+57 54 09	0.02958	2010 Jul 25	2520.0	HST WFC3 F547M
Zw 229-015	19 05 25.9	+42 27 40	0.02788	2014 Nov 13	2320.0	HST WFC3 F547M
1H1934-063	19 37 33.0	-06 13 05	0.01031	2016 May 27	2230.0	HST WFC3 F547M
				2015 Apr 23	960.0	SMARTS 0.9 m Tek2K B
				2015 Apr 23	960.0	SMARTS 0.9 m Tek2K V
				2015 Apr 23	960.0	SMARTS 0.9 m Tek2K R
NGC 6814	19 42 40.6	-10 19 25	0.00521	2010 May 06	2240.0	HST WFC3 F547M
				2019 Jun 23	1800.0	ARCSAT SurveyCam B
				2019 Jun 23	1800.0	ARCSAT SurveyCam V
				2019 Jun 23	1800.0	ARCSAT SurveyCam R
				2019 Jun 23	1800.0	ARCSAT SurveyCam I
				2011 Sep 20	1200.0	WIYN WHIRC H
NGC 7469	23 03 15.6	+08 52 26	0.01632	2009 Nov 11	2240.0	HST WFC3 F547M
				2003 Nov 13	1440.0	MDM 1.3 m Templeton B
				2003 Nov 13	1260.0	MDM 1.3 m Templeton V
				2003 Nov 13	1260.0	MDM 1.3 m Templeton R
				2019 Sep 28	70.0	APO 3.5 m ARCTIC I
				2011 Sep 19	300.0	WIYN WHIRC H

WIYN: Eleven galaxies in our sample were imaged with the 3.5 m WIYN telescope[4] (NOAO 2011B-0120; PI: Bentz; NOAO 2013A-0438; PI: Manne-Nicholas). The observations employed the High-Resolution Infrared Camera (WHIRC) and the H filter. WHIRC is a 2048 x 2048 Raytheon Virgo HgCdTe, with a FOV of 202″ x 202″ and a pixel scale of 0.″0986 pixel^{-1}. Each target was observed with multiple short exposures and large dither patterns to aid in the removal of strong fringing, cosmic rays, and bad pixels. A full description of the observations and reduction is available in Bentz & Manne-Nicholas (2018).

MDM: Eight galaxies were observed with the MDM Observatory 1.3 m McGraw-Hill Telescope. As described by Bentz et al. (2009b), objects were observed through Johnson B, V, and R filters

[4]The WIYN Observatory is a joint facility of the University of WisconsinMadison, Indiana University, the National Optical Astronomy Observatory and the University of Missouri.

with the Templeton CCD, which has 1024 x 1024 pixels, a pixel scale of $0\farcs5$ pixel^{-1}, and FOV of $8\farcm49$ x $8\farcm49$.

3.2.2.2 New Observations

New imaging of galaxies in our sample was conducted between 2015-2020. Dates, instrument selections, and exposure times are listed in Table 3.1.

APO: We obtained *B*, *V*, *R*, and *I*−band images of 4 galaxies in our sample with the 3.5 m Apache Point Observatory (APO) Astrophysical Research Consortium (ARC) telescope. The ARC Telescope Imaging Camera (ARCTIC) on the 3.5 m is a 4096 x 4096 pixel CCD with an FOV of $7\farcm85$ x $7\farcm85$ and a pixel scale of $0\farcs114$ pixel^{-1}. Because unbinned imaging tends to over sample the seeing, we employed 2 x 2 binning for all objects imaged by ARCTIC, which yields an effective pixel scale of $0\farcs228$ pixel^{-1}.

SMARTS: Optical images of 4 galaxies were obtained with the Cerro Tololo Inter-American Observatory/Small and Moderate Aperture Research Telescope System (CTIO/SMARTS) 0.9 m telescope. The 0.9 m utilizes a 2048 x 2048 pixel CCD with a FOV of $13\farcm6$ x $13\farcm6$ and pixel scale of $0\farcs401$ pixel^{-1}. Targets were observed through Tek 2K Set II Johnson-Cousins *B*, *V*, and *R* filters.

ARCSAT: Using the 0.5 m ARC Small Aperture Telescope (ARCSAT), we targeted galaxies which had not been observed with APO, MDM, or SMARTS or did not have *I*−band imaging. ARCSAT employs the SurveyCam CCD imager, which has 4096 x 4096 pixels, a FOV of $31\farcm1$ x $31\farcm1$, and pixel scale of $0\farcs465$ pixel^{-1}. For most observations, the large pixels and low spatial resolution caused the AGN and bulge to blend together in most images, eliminating the possibility of separation in the modeling process (see Sec. 3.3). The images for only 2 galaxies were found to be useful for surface brightness modeling; NGC 4151 and NGC 6814 were observed with Cousins *I* for the former and Johnson-Cousins *B*, *V*, *R*, and *I* for the latter. Dates and exposure times for these 2 galaxies are listed in Table 3.1.

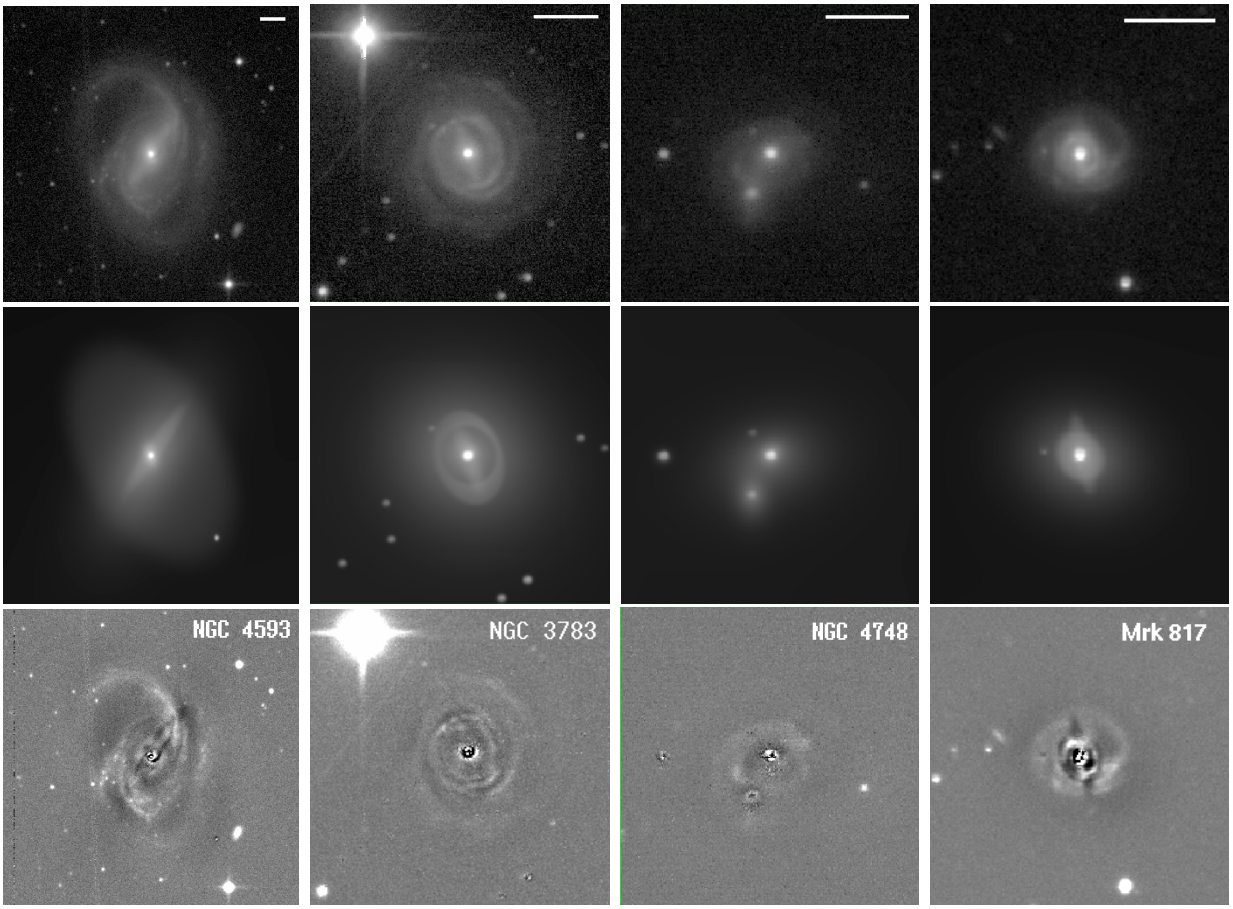

Figure 3.1: Selected ground-based B−band AGN host galaxy images (top), GALFIT models (center), and residuals (bottom). From left to right: NGC 4593, NGC 3783, NGC 4748, Mrk 817. The images and models are displayed with a logarithmic stretch, and the residuals are displayed with a linear stretch centered around zero counts. The scale bars in each row are 30″ in length. Due to the varying levels of compactness of each galaxy, the selected fits correspond to the quality range of the separation of the AGN and galaxy light, from good (NGC 4593, NGC 3783), to moderate (NGC 4748), to poor (Mrk 817). Higher uncertainties were assigned to galaxies with poor fits (see Sec. 3.4.1 for a quantitative explanation). Magnitudes were calculated as $m = -2.5\log(counts/s)+zpt$.

3.3 *Surface Brightness Modeling*

As demonstrated by Bentz et al. (2013), up to 30% of the total galaxy brightness of nearby active galaxies may be contributed by a central AGN. The TF relation uses galaxy light as a mass tracer, thus accurate measurements of the galaxy starlight (which traces the stellar mass) are needed. In order to remove the AGN contamination from the host galaxy brightness, we conducted two-dimensional surface brightness decompositions using GALFIT (Peng et al., 2002, 2010). For the vast majority of our targets, the decompositions of the $V-$band *HST* images have already been published (Bentz et al., 2009a, 2013; Bentz & Manne-Nicholas, 2018). We follow a similar procedure here in the modeling of the new ground-based images.

GALFIT allows a galaxy image to be modeled by a combination of analytical surface brightness components. These components are not always physically meaningful, although they may correspond to the morphological components of each spiral galaxy (i.e., disks, bulges, bars, rings, etc.). We utilized the general Sersic (1968) profile, which has the form

$$\sum(r) = \sum_e exp\left[-k\left(\left(\frac{r}{r_e}\right)^{1/n} - 1\right)\right] \tag{3.1}$$

where $\sum_e$ is the surface brightness of a pixel at an effective radius of r_e, n is the Sérsic index which dictates the profile's degree of curvature, and k is defined such that $\Gamma(2n) = 2\gamma(2n,k)$, where Γ and γ are the complete and incomplete gamma functions, respectively. The analytical profiles of the disks are extrapolated out to 0 counts. The integrated magnitude of each component is calculated as $m = -2.5\log(counts/s) + zpt$, where m is the magnitude and zpt is the zeropoint. A Sérsic index of $n = 1$ yields an exponential disk profile. Indices of $n = 0.5$ and $n = 4$ correspond to Gaussian and de Vaucouleurs (1948) profiles, respectively. Disks were modeled by holding the Sérsic index fixed at $n = 1$. Bulges are modeled with a typical index of $n > 1$, while bars are usually modeled by a shallower curvature of $n < 1$. For the few galaxies in our sample which displayed rings, we employed an exponential disk profile with the index fixed at $n = 1$ and truncation functions to remove the inner and outer regions of the profile.

Table 3.2. Galaxy Surface Brightness Parameters

Target	V_{galaxy} (HST) (mag)	B_{galaxy} (mag)	V_{galaxy} (mag)	R_{galaxy} (mag)	I_{galaxy} (mag)	$H_{-0.5,galaxy}$ (mag)	*Disk Radius* (arcsec)	q_d
(1)	(2)	(3)	(4)	(5)	(6)	(7)	(8)	(9)
Mrk 1044	14.20 ± 0.20	···	13.96 ± 0.20	13.71 ± 0.20	12.76 ± 0.20	···	12.09 ± 0.78 [a]	0.87
Ark 120	14.38 ± 0.20	···	···	···	···	11.85 ± 0.20	3.97 ± 0.56 [b]	0.81
MCG+08-11-011	11.80 ± 0.20	···	···	···	···	···	56.84 ± 10.15 [a]	0.62
Mrk 6	13.97 ± 0.20	···	13.74 ± 0.20	···	···	10.92 ± 0.20	29.45 ± 6.11 [a]	0.61
Mrk 374	14.34 ± 0.20	···	···	···	···	···	8.47 ± 0.85 [b]	0.58
Mrk 79	14.04 ± 0.20	14.22 ± 0.30	13.75 ± 0.20	13.25 ± 0.20	···	11.24 ± 0.20	31.68 ± 3.22 [a]	0.79
NGC 2617	12.66 ± 0.20	14.10 ± 0.30	12.80 ± 0.20	12.51 ± 0.20	···	···	23.80 ± 8.61 [a]	0.97
NGC 3227	11.00 ± 0.20	11.85 ± 0.20	10.87 ± 0.20	10.48 ± 0.20	···	8.22 ± 0.20	91.57 ± 18.72 [a]	0.42
SBS1116+583A	15.57 ± 0.20	···	···	···	···	13.65 ± 0.20	3.14 ± 0.44 [b]	0.87
NGC 3783	12.09 ± 0.20	12.89 ± 0.20	12.03 ± 0.20	11.50 ± 0.20	···	···	58.39 ± 6.58 [a]	0.96
Mrk 1310	14.93 ± 0.20	···	15.02 ± 0.20	14.40 ± 0.20	···	12.47 ± 0.20	11.67 ± 1.19 [a]	0.73
NGC 4051	10.11 ± 0.20	10.84 ± 0.20	10.21 ± 0.20	9.93 ± 0.20	···	8.57 ± 0.20	127.67 ± 7.22 [a]	0.58[c]
NGC 4151	10.80 ± 0.20	11.29 ± 0.20	10.63 ± 0.20	10.18 ± 0.20	9.73 ± 0.20	9.01 ± 0.20	64.12 ± 6.00 [a]	0.94[d]
NGC 4593	11.21 ± 0.20	12.05 ± 0.20	11.21 ± 0.20	10.70 ± 0.20	···	9.46 ± 0.20	89.44 ± 19.00 [a]	0.69[c]
NGC 4748	13.56 ± 0.20	14.43 ± 0.30	13.19 ± 0.30	12.54 ± 0.20	···	10.94 ± 0.20	24.46 ± 5.46 [a]	0.69
NGC 5548	12.72 ± 0.20	13.39 ± 0.20	12.58 ± 0.20	12.24 ± 0.20	···	···	36.03 ± 3.35 [a]	0.83
Mrk 817	14.30 ± 0.20	15.04 ± 0.30	13.99 ± 0.30	13.58 ± 0.30	···	11.76 ± 0.20	13.03 ± 2.12 [a]	0.81
Mrk 478	15.54 ± 0.20	···	···	···	···	···	3.39 ± 0.34 [b]	0.85
NGC 5940	13.35 ± 0.20	···	···	···	···	···	9.21 ± 0.92 [b]	0.86
Mrk 290	15.31 ± 0.20	···	···	···	···	···	4.12 ± 0.41 [b]	0.81
Zw 229-015	15.08 ± 0.20	···	···	···	···	12.77 ± 0.20	9.31 ± 1.33 [b]	0.60
1H1934-063	13.16 ± 0.20	14.47 ± 0.20	13.59 ± 0.20	13.08 ± 0.20	···	···	22.90 ± 3.12 [a]	0.85
NGC 6814	11.18 ± 0.20	12.16 ± 0.30	11.22 ± 0.20	10.62 ± 0.20	9.91 ± 0.20	9.80 ± 0.20	66.91 ± 15.75 [a]	0.98
NGC 7469	12.51 ± 0.20	13.05 ± 0.20	12.29 ± 0.20	12.10 ± 0.20	11.12 ± 0.20	9.84 ± 0.20	33.44 ± 2.03 [a]	0.81

Note. — Total calibrated galaxy magnitudes after removal of AGN contamination. Full decomposition information of the *HST* galaxy images is available in Bentz & Manne-Nicholas (2018). The majority of the surface brightness fits to the ground-based images were guided by the *HST*-based solutions (see Sec. 3.3). The B, V, R, and I magnitudes are total magnitudes, the $H_{-0.5}$ magnitude is calibrated for the aperture system of Aaronson et al. (1980). Disk axis ratios (q_d) are adopted from the *HST* decompositions of Bentz & Manne-Nicholas (2018) unless otherwise noted. Disk radii are either measured at the B–band 25th mag arcsec^{-2} isophote (R_{25}) or derived from the exponential disk radii (R_d) as noted. Uncertainties on the magnitudes were determined based on the quality of the surface brightness fits (see Sec. 3.4.1).

The AGN in each galaxy is an unresolved point source, therefore the brightness can be constrained with an accurate model of the point-spread-function (PSF) of each image. The PSF models were built by first selecting an isolated star in the field, and then modeling a small portion of the image centered on the star. The star itself was modeled with a set of Gaussians whose widths, magnitudes, axis ratios, and position angles were left as free parameters, and the background sky was modeled as a gradient. A PSF model was considered suitable when the residuals, after subtracting the model from the image, contained only random noise. Evidence of regular patterns such as a 'bulls-eye' signal the need for additional Gaussians. PSF models typically consisted of 3-4 Gaussian components. As we describe below, we fit several field stars in each image with the suitable PSF model in order to constrain the magnitude zeropoint. When fit, the residuals of the field stars were small, demonstrating that any changes in the PSF shape across the FOV were minimal for the images considered here.

Once the PSF model was constructed, the entire galaxy image was modeled. The background sky was again modeled as a gradient across the frame. The unresolved AGN was fit with the PSF model, and the galaxy was fit with bulge and disk components. The surface brightness decompositions of the *HST* images, due to the higher spatial resolution, lower sky levels, and no seeing effects, were used to guide the number and type of components included in the decompositions of the ground-based images. Additional morphological components, such as a bar or ring, were included when present in the *HST* decompositions. Most bulge characteristics were fixed to the parameters determined from the *HST* image. This included radii, Sérsic indices, and axis ratios, while the magnitudes were left as free parameters. For very compact galaxies (e.g., Mrk 79, 1H1934-063), bar and ring parameters were also held fixed to their *HST* values. Field stars that were superimposed on or near the galaxy were also fit with the PSF model to fully isolate the galaxy brightness. Any saturated stars in the field were masked out before the fitting process began.

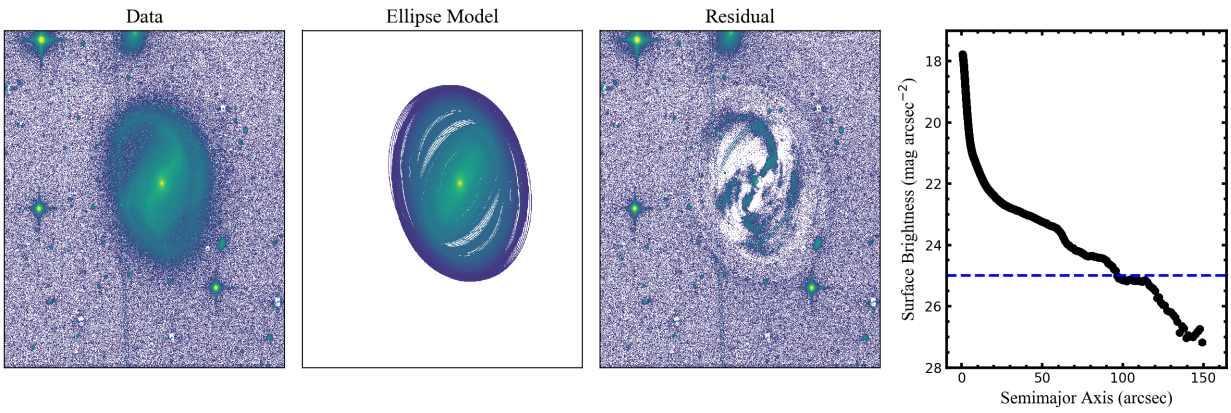

Figure 3.2: From left to right: original $B-$band image of NGC 4593, surface brightness isophotes from the ELLIPSE task in IRAF, data minus the model, and the surface brightness measurements as a function of semimajor axis in arcseconds. The 25 mag arcsec^{-2} surface brightness is indicated with the dashed blue line. East is up and north is right in the above images, and the FOV is 7′.78 x 8′.49.

3.4 *Measurements*

With the surface brightness modeling complete and HI spectral data in hand, we discuss here the measurements conducted for use in TF distance determinations. These include the AGN-free, calibrated galaxy magnitudes and constraints on maximum rotational velocities from the HI emission lines.

3.4.1 *Optical Galaxy Magnitudes*

The TF relation for the optical bandpasses requires total, integrated galaxy magnitudes. Thus, with acceptable surface brightness models determined for each image, the image zeropoints were then constrained in order to properly calibrate the model magnitudes. We achieved this by first modeling stars in the field which matched those in optical and near-infrared catalogs. The number of stars modeled was mainly dependent on how many were within the FOV, but was typically between $5-10$. For all of our B and $V-$band images, we drew stellar magnitudes from the AAVSO Photometric All-Sky Survey (APASS; Henden & Munari 2014; Henden et al. 2016), assuring none of the selected

stars were flagged as variable. For NGC 6814 and Mrk 817, we utilized the R and I−band field star magnitudes determined by Crimean Astrophysical Observatory imaging (Doroshenko et al., 2006).

For the remaining 12 galaxies in which data from the Crimean Observatory were not available, we collected r and i−band stellar magnitudes first from the Sloan Digital Sky Survey (SDSS) data release 16 (Ahumada et al., 2020), or we collected the r and i−band magnitudes from APASS. To transform the r and i magnitudes to R and I, we calculated synthetic photometry with the IRAF task SYNPHOT. We first estimated the spectral type of each star using the spectral classifications as a function of SDSS g–i (using g stellar magnitudes from either SDSS or APASS) color from Table 4 of Covey et al. (2007). Once the spectral type was assigned, we employed the corresponding stellar template from the Kurucz 1993 Atlas of Model Atmospheres (Kurucz, 1993), and used SYNPHOT to calculate the difference between magnitudes of the template through the SDSS and Johnson-Cousins throughputs. The color differences were small for R and r, $-0.05 < m_R - m_r < -0.26$, and slightly larger for I and i, $-0.06 < m_I - m_i < -0.76$.

We adjusted the zeropoint in GALFIT to minimize the difference between the measured and expected magnitudes of the field stars, thus calibrating the photometry of the galaxy components as well. Lastly, we combined all the host-galaxy surface brightness components to determine total galaxy magnitudes, which are listed in Table 3.2.

We determine a typical uncertainty of 0.2 mag for the integrated galaxy magnitudes, consistent with Bentz & Manne-Nicholas (2018) based on our previous experience using GALFIT as well as the level of agreement between fitting results to *HST* images of compact PG quasars (Veilleux et al., 2009). In some cases, poor seeing conditions or bright sky background induced higher uncertainty in the separation of AGN light from bulge light, or disk light from the sky contribution. For these cases, we assigned a slightly larger uncertainty 0.3 mag to the final galaxy magnitudes (Mrk 79, NGC 2617 NGC 4748, Mrk 817, NGC 6814). We were unable to separate the disk light from sky contribution in the B−band images of Mrk 1044 and Mrk 6. Additionally for Mrk 1310, the seeing conditions coupled with focusing offsets in the B−band image caused substantial blending of the

AGN and bulge light, thus we were unable to remove the AGN contamination. For these three galaxies, we omit the $B-$band data from our analysis.

Fig. 3.1 displays selected $B-$band galaxy images, surface brightness models, and residuals which show the range of quality in our surface brightness models of the ground-based images. For the most extended galaxies, like NGC 4593 and NGC 3783 (first and second column, respectively), we have good surface brightness models due to the larger size of the galaxy on the detector and, hence, easier separation of each surface brightness component in the modeling process. More compact galaxies like NGC 4748 (third column) had surface brightness models of moderate quality, and the most compact galaxies, such as Mrk 817 (fourth column), had relatively poor quality surface brightness models. The quality of our models was mainly determined by comparing our galaxy $V-$band magnitudes to their *HST* $V-$band magnitudes. Good models had excellent agreement, usually within $\sim 0.01-0.02$ mag. While moderate and poor models had larger discrepancies ($\sim 0.1-0.3$ mag), they are still in agreement within the larger uncertainties attributed to the compactness of the galaxy and the seeing conditions that complicated the modeling process of the ground-based images.

3.4.2 *H−band Aperture Photometry*

The TF relation for the $H-$band utilizes the $H_{-0.5}$ magnitude, which is calibrated for the aperture system $\log(A/D^i_{25}) = -0.5$, where A is the aperture through which the galaxy intensity is measured and D^i_{25} is the galaxy diameter at the $B-$band 25 mag arcsec^{-2} isophote, corrected for inclination (Aaronson et al., 1980). We employed the ELLIPSE task in IRAF to measure isophotes from our sky-subtracted, ground-based $B-$band images, with Galactic extinction corrections applied to the $B-$band magnitudes. We then fit an exponential disk function to the outer surface brightness profile to arrive at the semimajor axis in arcseconds at which the surface brightness reached 25 mag arcsec^{-2}. An example is shown in Fig. 3.2, where the blue dashed line indicates the 25th mag arcsec^{-2} surface brightness. For galaxies that had $H-$band imaging but did not have $B-$band images (Ark 120, SBS1116+583A, Zw 229-015), we utilized the relation between the radius at the 25 mag

Table 3.3. 21 cm Spectral Characteristics

Target	V_R (km s^{-1})	W_{m50} (km s^{-1})	S/N	Flux (Jy km s^{-1})	Resolution (km s^{-1})
(1)	(2)	(3)	(4)	(5)	(6)
Mrk 1044	4912.0	178.0 ± 8.0	20.4	4.98	1.1
Ark 120	9810.0	350.0 ± 13.0	10.1	3.63	2.4
MCG+08-11-011	6132.0	309.0 ± 8.0	28.7	14.97	0.8
Mrk 6	5632.0	477.0 ± 19.0	2.6	3.31	3.3
Mrk 374	13246.0	271.0 ± 18.0	4.6	0.60	9.0
Mrk 79	6661.0	178.0 ± 12.0	11.4	5.71	3.4
NGC 2617	4265.0	119.0 ± 8.0	41.7	18.62	0.3
NGC 3227	1148.0	428.0 ± 9.0	14.8	29.87	3.2
SBS1116+583A	8373.0	168.0 ± 18.0	3.8	0.43	6.8
NGC 3783	2916.0	147.0 ± 8.0	31.0	21.03	0.7
Mrk 1310	5838.0	258.0 ± 15.0	7.5	2.38	3.4
NGC 4051	703.0	245.0 ± 8.0	147.2	61.59	0.6
NGC 4151	999.0	131.0 ± 8.0	45.4	74.4	0.6
NGC 4593	2502.0	370.0 ± 9.0	15.4	13.52	0.7
NGC 4748	4184.0	332.0 ± 15.0	8.0	2.79	2.0
NGC 5548	5150.0	212.0 ± 15.0	8.2	2.12	5.3
Mrk 817	9438.0	353.0 ± 19.0	3.1	0.74	8.2
Mrk 478	23881.0	314.0 ± 23.0	1.9	0.73	8.8
NGC 5940	10209.0	186.0 ± 13.0	10.6	3.33	1.3
Mrk 290	9104.0	245.0 ± 18.0	3.8	0.76	6.8
Zw 229-015	8317.0	209.0 ± 17.0	5.2	0.94	6.4
1H1934-063	3191.0	165.0 ± 10.0	13.6	4.54	2.0
NGC 6814	1562.0	84.0 ± 8.0	60.4	55.92	0.2
NGC 7469	4930.0	215.0 ± 16.0	6.1	2.00	3.3

Note. — Columns (2) and (3) list the measured recessional velocity and W_{m50} values, respectively, with the updated HI line width measurement method described in Section 3.5. Columns (4) and (5) list the S/N and flux after spectral smoothing to the final spectral resolution, reported in column (6).

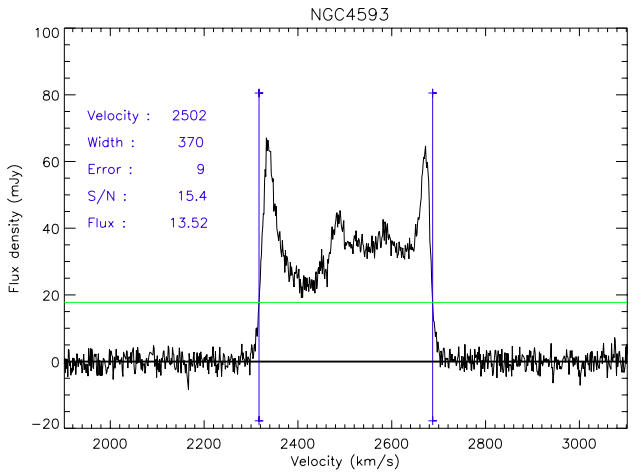

Figure 3.3: Example of the W_{m50} line width measurement method for the HI emission spectrum of NGC 4593. The blue vertical lines indicate the range of spectral channels which contain 90% of the HI flux, while the green horizontal line indicates 50% of the mean flux in this range. The integrated flux measurement is in units of Jy km s^{-1}, and the width and velocity measurements are in units of km s^{-1}. The error is the uncertainty on the width and in units of km s^{-1}.

arcsec^{-2} isophote (R_{25}) and the exponential disk scale length (R_d) of $R_{25} = 3.2R_d$ (Catinella et al. 2006; de Blok & Walter 2014) to estimate D_{25} from our exponential disk profile fits. Lastly, our inclination corrections to the diameters follow the formula from the Second Reference Catalog of Bright Galaxies (de Vaucouleurs et al. 1976, hereafter RC2):

$$D^i_{25} = D_{25}(a/b)^{-C} \tag{3.2}$$

where a/b is the ratio of major to minor axes, and Tully & Fouque (1985) determined $C = 0.22 \pm 0.03$ based on their best-fit to the deviations in $H-$band surface brightness as a function of galaxy inclination. $H_{-0.5}-$band magnitudes in addition to the galaxy radii and corresponding measurement method are listed in Table 3.2.

Aaronson et al. (1980) originally assumed a typical uncertainty of 0.1 mag for their $H_{-0.5}-$band values. However, the aperture photometry for our sample was conducted on galaxy images in which we removed the AGN contamination in the surface brightness modeling process, which induces additional uncertainty in the total galaxy magnitude. Therefore, we conservatively adopt 0.2 mag

uncertainty on all $H_{-0.5}$ magnitudes, consistent with our typical uncertainties on the AGN-free galaxy magnitudes for the optical bands.

3.4.3 *HI 21cm Line Widths*

The TF relation utilizes the width of the unresolved, rotationally-broadened HI 21 cm emission line from late-type galaxies, which is directly related to the maximum rotation rate (Epstein, 1964; Roberts, 1969). We follow the method originally described by Tully & Fouque (1985), with the updated definition of the HI line width (Courtois et al., 2009a) which includes corrections for instrumental and redshift broadening:

$$W^c_{m50} = \frac{W_{m50}}{(1+z)} - 2\Delta v\lambda \tag{3.3}$$

where z is the redshift of the HI line, Δv is the smoothed resolution of the spectrum, and λ is an empirically determined constant term given as $\lambda = 0.25$. We use the redshifts of the HI lines of our targets reported in Paper I. W_{m50} is defined as the width of the HI profile at 50% of the mean flux over the range of spectral channels which contain 90% of the HI flux. This new definition by Courtois et al. (2009a) is preferred as it employs the mean flux rather than the peak, which makes the width measurement independent of the strengths of the flanks. Excluding 5% of the flux on either side of the profile also aids in separation of the profile wings from the noise. The line widths reported in Paper I are widths calculated at 50% and 20% over 100% of the flux. Therefore, we have remeasured the widths of our HI profiles using the updated definition and we list them in Table 3.3. An example of this measurement for the HI emission from NGC 4593 is shown in Fig. 3.3.

The corrected, observed width is then adjusted to agree statistically with twice the maximum rotational velocity, as the width of the HI line includes both redshifted and blueshifted gas motions. The translation is given as

$$\begin{aligned} W^2_{mx} = (W^c_{m50})^2 + (W_{t,m50})^2[1-2e^{-(W^c_{m50}/W_{c,m50})^2}] \\ -2W^c_{m50}W_{t,m50}[1-e^{-(W^c_{m50}/W_{c,m50})^2}] \end{aligned} \tag{3.4}$$

where $W_{c,m50}$ = 100 km s^{-1} and $W_{t,m50}$ = 9 km s^{-1} are the values found by Courtois et al. (2009a) to produce the best match between maximum rotation rate and adjusted HI line width. The width is then deprojected to edge-on orientation by

$$W^i_{mx} = W_{mx}/sin(i) \tag{3.5}$$

where i is the inclination of the galaxy disk.

The inclinations were generally derived from the axis ratios of the galaxy disk, as listed in Table 3.2. For most of the galaxies, we adopted the axis ratios reported by Bentz & Manne-Nicholas (2018). For NGC 4051 and NGC 4593, where the disk extended beyond the FOV of the *HST* image, we adopted the axis ratios from our GALFIT models of the ground-based images. For NGC 4151, the spatially resolved HI study by Mundell et al. (1999) reveals the inclination of the HI disk to be 21°, much more face-on than the disk axis ratio that has been typically found in the optical based on the high surface brightness stellar distribution ($\sim$0.6; de Vaucouleurs et al. 1976, 1991; Bentz & Manne-Nicholas 2018; see Sec. 3.5.4). We therefore adopt 21° as the true inclination of the HI disk for NGC 4151. We follow the standard prescription from the photovisual analysis of Holmberg (1958) adopted by the main TF works in the literature (Tully & Fisher, 1977; Tully & Pierce, 2000; Tully et al., 2008, 2013):

$$cos(i) = [(q^2_d - q^2_{0,d})/(1 - q^2_{0,d})]^{1/2} \tag{3.6}$$

where $q_d = b/a$ is the disk axis ratio and $q_{0,d}$ is the intrinsic axial ratio of a disk galaxy viewed edge-on. Following Tully & Pierce (2000), we adopt $q_{0,d} = 0.2$ as the single, global value for the flattening. The uncertainties in the deprojected line widths increase as galaxy inclinations become more face-on. Consequently, the galaxies in this sample with the lowest inclination (NGC 2617, NGC 3783, NGC 6814) have the highest uncertainties in W^i_{mx}.

Table 3.4. Corrected HI line widths and Magnitudes

Target (1)	Morphology (2)	W^{i}_{mx} (3)	$m_V^{b,i,k}$ (*HST*) (4)	$m_B^{b,i,k}$ 5	$m_V^{b,i,k}$ (6)	$m_R^{b,i,k}$ (7)	$m_I^{b,i,k}$ (8)	$m_{H_{-0.5}}^{b,i,k}$ (9)
Mrk 1044	SB(s)c	329.89 ± 28.33	14.02 ± 0.20	···	13.79 ± 0.20	13.56 ± 0.20	12.65 ± 0.20	···
Ark 120	Sb pec	549.21 ± 33.78	13.82 ± 0.20	···	···	···	···	11.71 ± 0.20
MCG+08-11-011	SBc	360.16 ± 11.95	10.93 ± 0.20	···	···	···	···	···
Mrk 6	Sb	565.76 ± 25.94	13.19 ± 0.20	···	12.96 ± 0.20	···	···	10.78 ± 0.20
Mrk 374	SBc	295.93 ± 22.24	13.93 ± 0.20	···	···	···	···	···
Mrk 79	SBb	261.91 ± 21.85	13.74 ± 0.20	13.77 ± 0.30	13.45 ± 0.20	12.95 ± 0.20	···	11.15 ± 0.20
NGC 2617	Sc	445.10 ± 149.27	12.53 ± 0.20	13.93 ± 0.30	12.68 ± 0.20	12.38 ± 0.20	···	···
NGC 3227	SAB(s) pec	448.88 ± 10.74	10.38 ± 0.20	11.00 ± 0.20	10.25 ± 0.20	9.85 ± 0.20	···	8.13 ± 0.20
SBS1116+583A	SBc	301.51 ± 41.10	15.45 ± 0.20	···	···	···	···	13.58 ± 0.20
NGC 3783	(R')SB(r)a	480.53 ± 120.76	11.71 ± 0.20	12.38 ± 0.20	11.65 ± 0.20	11.17 ± 0.20	···	···
Mrk 1310	Sbc	347.49 ± 24.08	14.67 ± 0.20	···	14.76 ± 0.20	14.13 ± 0.20	···	12.40 ± 0.20
NGC 4051	SAB(rs)bc	282.83 ± 15.66	9.87 ± 0.20	10.45 ± 0.20	9.97 ± 0.20	9.61 ± 0.20	···	8.52 ± 0.20
NGC 4151	(R')SAB(rs)ab	342.95 ± 56.31	10.69 ± 0.20	11.14 ± 0.20	10.52 ± 0.20	10.09 ± 0.20	9.66 ± 0.20	8.98 ± 0.20
NGC 4593	(R)SB(rs)b	437.95 ± 23.30	10.81 ± 0.21	11.51 ± 0.20	10.81 ± 0.20	10.29 ± 0.20	···	9.39 ± 0.20
NGC 4748	Sab	429.70 ± 23.25	13.17 ± 0.20	13.89 ± 0.30	12.80 ± 0.30	12.17 ± 0.20	···	10.86 ± 0.20
NGC 5548	(R')SA(s)0/a	534.08 ± 30.90	12.49 ± 0.20	13.08 ± 0.20	12.35 ± 0.20	12.03 ± 0.20	···	···
Mrk 817	SBc	549.93 ± 40.97	14.09 ± 0.20	14.76 ± 0.30	13.78 ± 0.30	13.38 ± 0.30	···	11.67 ± 0.20
Mrk 478	Sab	516.02 ± 163.75	15.24 ± 0.22	···	···	···	···	···
NGC 5940	SBc	327.54 ± 32.79	13.13 ± 0.20	···	···	···	···	···
Mrk 290	S0	376.64 ± 34.87	15.08 ± 0.20	···	···	···	···	···
Zw 229-015	(R)SBc	234.32 ± 21.15	14.71 ± 0.20	···	···	···	···	12.66 ± 0.20
1H1934-063	Sbc	286.26 ± 25.28	12.29 ± 0.20	13.30 ± 0.20	12.72 ± 0.20	12.33 ± 0.20	···	···
NGC 6814	SAB(rs)bc	388.09 ± 195.55	10.66 ± 0.20	11.46 ± 0.30	10.69 ± 0.20	10.20 ± 0.21	9.62 ± 0.20	9.71 ± 0.20
NGC 7469	(R')SAB(rs)a	335.80 ± 30.96	12.19 ± 0.20	12.60 ± 0.20	11.97 ± 0.20	11.83 ± 0.20	10.92 ± 0.20	9.76 ± 0.20

Note. — The morphological classifications listed in Column (2) are consistent with those reported from Paper I. Column (3) lists the corrected HI line width in km s^{-1}, which is statistically equal to twice the maximum rotation rate, deprojected to edge-on orientation (see Sec. 3.4.3). Columns (4-8) list the observed magnitudes in each band corrected for Galactic extinction, inclination-dependent extinction, and redshift (see Sec. 3.5.1, 3.5.2).

3.5 *TF Distances*

With HI widths in hand and the AGN contamination removed from the galaxy brightness, we employed the TF method to constrain the distance to each AGN host.

3.5.1 *Current TF Calibrations*

The current calibrations for the B, R, $H_{-0.5}$ (Tully et al., 2008), and $I-$band (Tully & Courtois, 2012) TF relations are as follows:

$$M_B^{b,i,k} = -19.99 - 7.27(\log W_{mx}^i - 2.5) \tag{3.7}$$

$$M_R^{b,i,k} = -21.00 - 7.65(\log W_{mx}^i - 2.5) \tag{3.8}$$

$$M_I^{b,i,k} = -21.39 - 8.81(\log W_{mx}^i - 2.5) \tag{3.9}$$

$$M_{H_{-0.5}}^{b,i,k} = -22.17 - 9.55(\log W_{mx}^i - 2.5) \tag{3.10}$$

where b, i, and k are Galactic extinction, inclination, and redshift corrections, respectively, and the superscripts on the magnitudes indicate that the corresponding corrections have been applied. We estimate the extinction along the line of sight in each bandpass using the Schlafly & Finkbeiner (2011) recalibration of the Milky Way dust map of Schlegel et al. (1998).

The inclination correction is given by the expression $A_i^\lambda = \gamma_\lambda \log(a/b)$, originally formulated by Tully et al. (1998) and subsequently used by Tully et al. (2008) and Tully & Courtois (2012), where λ is the passband, a/b is the ratio of major to minor axes of the galaxy disk, and γ is defined as

$$\gamma_B = 1.57 + 2.75(\log W_{mx}^i - 2.5) \tag{3.11}$$

$$\gamma_R = 1.15 + 1.88(\log W_{mx}^i - 2.5) \tag{3.12}$$

$$\gamma_I = 0.92 + 1.63(\log W_{mx}^i - 2.5) \tag{3.13}$$

However, Tully et al. (1998) do not include a prescription for the $H_{-0.5}$ magnitudes. Sakai et al. (2000) approximated the correction as $A_i^{H_{-0.5}} = 0.5A_i^I$, however we adopt the original correction from Tully & Fouque (1985) of $A_i^{H_{-0.5}} = 0.1A_i^B$ as it was derived from measurements in the $H_{-0.5}$ band.

Finally, the $k-$corrections for the B, R, and I bands utilized in the TF calibrations of Tully et al. (2008) and Tully & Courtois (2012) are described in Tully & Pierce (2000) and Chilingarian et al. (2010) for the optical bands and near-infrared band, respectively, and are as follows:

$$A_k^B = (3.6 - 0.36T)z \tag{3.14}$$

$$A_k^R = [4.24(R-I) - 1.10]z \tag{3.15}$$

$$A_k^I = 0.302z + 8.768z^2 - 68.680z^3 + 181.904z^4 \tag{3.16}$$

where T is the galaxy morphological type (1, 3, 5, and 7 corresponding to Sa, Sb, Sc, and Sd) and z is the redshift. The $k-$corrections in this work utilize the morphological classifications reported in Paper I and are listed in Table 3.4. Once more the $H_{-0.5}$ band lacks a prescription from Tully & Pierce (2000), thus we adopt the original $k-$correction from Aaronson et al. (1980) as $A_k^{H_{-0.5}} = 1.9z$.

3.5.2 *V−band TF Calibration*

The TF relation has been calibrated for most optical and near-infrared bands (Tully et al., 2008; Tully & Courtois, 2012), and most recently for SDSS and WISE filters (Kourkchi et al., 2020). However, the Johnson V band has so far been neglected. We have therefore conducted the first calibration of the $V-$band TF relation.

Table 3.5:TF Distance and $V_{\rm PEC}$ Measurements

Target	Band	D (Mpc)	$V_{\rm PEC}$ (km s^{-1})	Flag
Mrk 1044	V (HST)	81.3 ± 13.0	···	···
	V	73.0 ± 11.7	···	···
	R	86.9 ± 14.0	···	···
	I	69.1 ± 12.2	···	···

Table 3.5:TF Distance and $V_{\rm PEC}$ Measurements

Target	Band	D (Mpc)	$V_{\rm PEC}$ (km s^{-1})	Flag
	Best Estimate	81.3 ± 16.3	-1275 ± 1212	a
Ark 120	V (HST)	161.2 ± 21.2	···	···
	$H_{-0.5}$	171.4 ± 25.6	···	···
	Best Estimate	161.2 ± 32.2	-1855 ± 2394	a
MCG+08-11-011	V (HST)	22.4 ± 4.5	4586 ± 335	c
Mrk 6	V (HST)	126.2 ± 14.7	···	···
	V	113.6 ± 13.2	···	···
	$H_{-0.5}$	117.9 ± 15.0	···	···
	Best Estimate	126.2 ± 25.2	-3625 ± 1873	b
Mrk 374	V (HST)	66.1 ± 13.2	8878 ± 981	c
Mrk 79	V (HST)	50.2 ± 7.9	···	···
	B	42.9 ± 7.9	···	···
	V	43.9 ± 6.9	···	···
	R	46.3 ± 7.3	···	···
	$H_{-0.5}$	32.2 ± 5.9	···	···
	Best Estimate	50.2 ± 10.0	3181 ± 743	b
NGC 2617	V (HST)	64.7 ± 33.6	···	···
	B	100.0 ± 50.7	···	···
	V	69.1 ± 35.9	···	···
	R	79.9 ± 41.7	···	···
	Best Estimate	64.7 ± 19.5	-183 ± 1446	a
NGC 3227	V (HST)	24.3 ± 2.4	···	···
	B	26.3 ± 2.6	···	···
	V	22.9 ± 2.3	···	···
	R	25.3 ± 2.5	···	···
	$H_{-0.5}$	22.4 ± 2.3	···	···
	Best Estimate	24.3 ± 4.9	-323 ± 364	a
SBS1116+583A	V (HST)	136.7 ± 31.1	···	···
	$H_{-0.5}$	129.0 ± 35.6	···	···
	Best Estimate	136.7 ± 27.3	-1393 ± 2030	a
NGC 3783	V (HST)	49.8 ± 19.6	···	···
	B	54.8 ± 20.7	···	···
	V	48.5 ± 19.1	···	···
	R	51.6 ± 20.4	···	···
	Best Estimate	49.8 ± 10.0	-427 ± 743	a
Mrk 1310	V (HST)	118.7 ± 16.7	···	···
	V	123.4 ± 17.3	···	···

Table 3.5:TF Distance and $V_{\rm PEC}$ Measurements

Target	Band	D (Mpc)	$V_{\rm PEC}$ (km s^{-1})	Flag
	R	122.7 ± 17.3	···	···
	$H_{-0.5}$	98.3 ± 15.8	···	···
	Best Estimate	118.7 ± 23.7	-2480 ± 1762	b
NGC 4051	*V* (*HST*)	9.5 ± 1.2	···	···
	B	10.4 ± 1.1	···	···
	V	10.0 ± 1.1	···	···
	R	11.2 ± 1.2	···	···
	$H_{-0.5}$	11.1 ± 1.3	···	···
	Best Estimate	9.5 ± 1.9	227 ± 141	a
NGC 4151	*V* (*HST*)	18.6 ± 5.0	···	···
	B	18.9 ± 4.8	···	···
	V	17.2 ± 4.6	···	···
	R	18.7 ± 5.0	···	···
	I	18.7 ± 5.7	···	···
	$H_{-0.5}$	19.9 ± 6.5	···	···
	Best Estimate	18.6 ± 3.7	-127 ± 275	a
NGC 4593	*V* (*HST*)	28.5 ± 3.6	···	···
	B	32.0 ± 3.3	···	···
	V	28.6 ± 3.0	···	···
	R	29.9 ± 3.1	···	···
	$H_{-0.5}$	38.2 ± 4.2	···	···
	Best Estimate	28.5 ± 5.7	756 ± 424	a
NGC 4748	*V* (*HST*)	82.2 ± 10.2	···	···
	B	93.2 ± 14.9	···	···
	V	69.3 ± 11.2	···	···
	R	68.7 ± 8.5	···	···
	$H_{-0.5}$	72.3 ± 10.0	···	···
	Best Estimate	82.2 ± 16.4	-1513 ± 1219	b
NGC 5548	*V* (*HST*)	83.6 ± 10.7	···	···
	B	88.0 ± 11.0	···	···
	V	78.4 ± 10.0	···	···
	R	90.0 ± 11.5	···	···
	Best Estimate	83.6 ± 16.7	-753 ± 1242	a
Mrk 817	*V* (*HST*)	182.8 ± 26.8	···	···
	B	198.9 ± 35.0	···	···
	V	158.7 ± 28.4	···	···
	R	175.0 ± 31.4	···	···

Table 3.5:TF Distance and $V_{\rm PEC}$ Measurements

Target	Band	D (Mpc)	$V_{\rm PEC}$ (km s^{-1})	Flag
	$H_{-0.5}$	168.8 ± 28.6	···	···
	Best Estimate	182.8 ± 36.6	-3770 ± 2721	c
Mrk 478	V (HST)	282.2 ± 139.4	4655 ± 10323	c
NGC 5940	V (HST)	53.4 ± 10.7	6687 ± 795	c
Mrk 290	V (HST)	162.3 ± 32.5	-2644 ± 2416	a
Zw 229-015	V (HST)	66.3 ± 11.0	···	···
	$H_{-0.5}$	52.2 ± 10.2	···	···
	Best Estimate	66.3 ± 13.3	3424 ± 989	c
1H1934-063	V (HST)	29.5 ± 4.8	···	···
	B	39.3 ± 6.2	···	···
	V	36.0 ± 5.9	···	···
	R	39.3 ± 6.4	···	···
	Best Estimate	29.5 ± 5.9	818 ± 439	a
NGC 6814	V (HST)	22.1 ± 17.1	···	···
	B	26.3 ± 19.6	···	···
	V	22.5 ± 17.4	···	···
	R	23.8 ± 18.5	···	···
	I	22.9 ± 20.4	···	···
	$H_{-0.5}$	35.1 ± 33.9	···	···
	Best Estimate	22.1 ± 8.0	-283 ± 593	a
NGC 7469	V (HST)	36.0 ± 6.1	···	···
	B	36.0 ± 5.9	···	···
	V	32.5 ± 5.5	···	···
	R	40.4 ± 6.8	···	···
	I	32.3 ± 6.0	···	···
	$H_{-0.5}$	27.3 ± 5.4	···	···
	Best Estimate	36.0 ± 7.2	1949 ± 535	c

Note. — TF Distance and $V_{\rm PEC}$ measurements for all bands. We quote the distance predicted from our V−band TF calibration of the HST decompositions as our adopted distance. For galaxies in which we were limited to $V(HST)$, we adopt the values that band predicts. We list the uncertainty on the Best Estimate distance as 20%, which is the typical uncertainty noted by CF1 and CF2 for TF-based distances. In cases where the uncertainty of the mean of all available TF distances for each galaxy is $> 20\%$, we list that value as the uncertainty. We have marked each galaxy with a quality flag for the distance based on comparison with literature, the mass distributions in the CF3 DVC, and peculiar velocities (see Sec. 3.4), a = best quality, b = moderate quality, c = poor quality.

[a]Adopted using the HI line width from Ho et al. (2008a)

We began by identifying the galaxies which were used to calibrate the most recent definitions of the optical TF relations (Tully et al., 2008). These included galaxies with distances determined from either Cepheid variable stars (26 galaxies), TRGB stars (13 galaxies), or SBF (7 galaxies). We then retrieved the $V-$band magnitudes for these galaxies from the Third Reference Catalogue of Bright Galaxies (de Vaucouleurs et al. 1991, hereafter RC3), the same source for the $B-$band magnitudes from the calibrations of Tully et al. (2008). These are purely observed magnitudes which have not been corrected for Galactic extinction, inclination-dependent extinction, or redshift. We followed Tully et al. (2008) and adopted the Schlegel et al. (1998) extinction corrections. We derived the inclination-dependent and redshift corrections in V following the same methods used to define them in B, R, and I. In-depth descriptions of the corrections and final calibration are available in Appendix A.

Tully et al. (1998) detailed the extinction corrections due to inclination in the B, R, and I bands. Following the same procedure and adopting the same formalism for the extinction parameter, $A_i^\lambda = \gamma_\lambda \log(a/b)$, where a/b is inverse of the disk axis ratio, we find

$$\gamma_V = (1.01 \pm 4.06) + (2.94 \pm 1.09)(\log W_{\rm R}^i - 2.5) \tag{3.17}$$

The method for deriving the $k-$corrections adopted by Tully & Pierce (2000) is not described, however they are quite similar to the $k-$corrections based on the analysis of Frei & Gunn (1994). We therefore adopt the Frei & Gunn (1994) methodology and find a $V-$band $k-$correction of

$$A_k^V = (2.23 - 0.22T)z \tag{3.18}$$

where T is the morphological type (1, 3, 5, and 7 again corresponding to Hubble types Sa, Sb, Sc, and Sd) and z is the redshift.

The extinction, inclination, and $k-$corrections were then applied to the apparent V magnitudes from RC3 of the Tully et al. (2008) calibrating sample. Using the accurate distances to these galaxies, which are based on Cepheids, TRGB, or SBF, we derived their absolute magnitudes. Finally, we

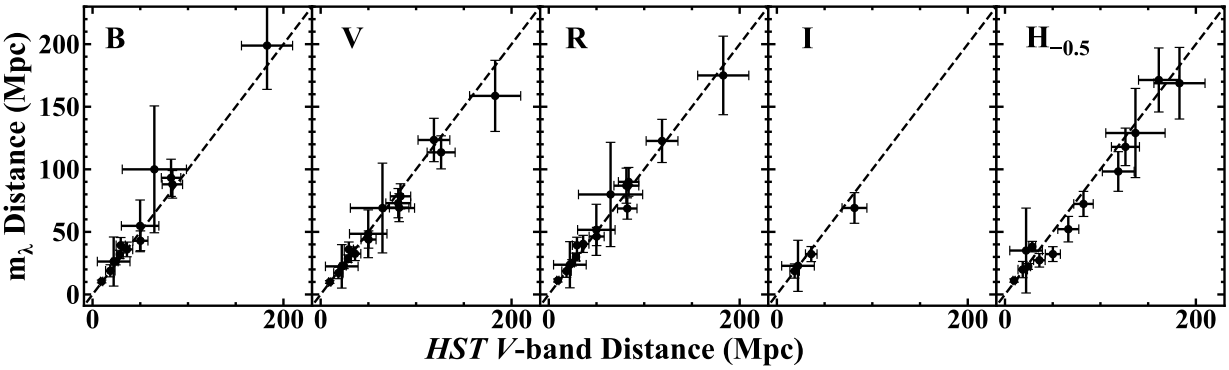

Figure 3.4: Comparisons between the TF distances determined by our calibration of the $V-$band relationship using our *HST* images to (from left to right) ground-based B, V, R, I, and $H_{-0.5}-$band distances. A line of unity is drawn in all panels. The error bars are the individual uncertainties of each distance calculation (see Table 3.5). We find good agreement for all calibrations within the uncertainties.

fit a linear relationship between the absolute magnitudes and the HI line widths, following the formalism adopted for the other bandpasses. Our best-fit result is:

$$M_V^{b,i,k} = (-20.39 \pm 0.03) - (7.62 \pm 0.15)(\log W_{mx}^i - 2.5) \tag{3.19}$$

We find a negligible change to the final result if we instead employ the updated Galactic extinction values from Schlafly & Finkbeiner (2011). When substituted, the slope and intercept shift slightly to -7.59 and -20.36, respectively. The calibrated relationship for the V band sits between the existing calibrated relationships for the B and R bands, and also agrees well with the recent TF calibrations of Kourkchi et al. (2020) for SDSS bands, especially when compared to g and r.

3.5.3 *Final Distances and Peculiar Velocities*

To constrain the TF distances, we utilized the deprojected HI line widths and calibrated TF relationships to derive absolute magnitudes for each galaxy in each available bandpass. We then calculated the distance moduli between our corrected apparent magnitudes and derived absolute magnitudes to constrain each distance. All corrected HI line widths and apparent magnitudes used in distance

calculations are listed in Table 3.4, and the distance measurements for all bands are tabulated in Table 3.5.

In Fig. 3.4, we compare the ground-based distances to the distances based on the $V-$band *HST* apparent magnitudes due to their superior spatial resolution and lack of seeing effects. Within the uncertainties, we generally find close agreement between the distances derived from the different photometric bands. In addition to the superior image quality of the *HST* data, the models of the ground-based images were guided by, and in some cases held fixed to, the parameters determined from the *HST* images. The axis ratios from the models of the *HST* images were used to derive the deprojected HI line widths in most cases, except for NGC 4051 and NGC 4593 as we described in Sec. 3.4.3. Therefore we prefer the distances based on the photometry derived from the *HST* images and quote them as our adopted TF distances in Table 3.5. We adopt a typical uncertainty of 20%, as used by CF1 and CF2 for TF-based distances. However, the ground-based photometry, especially when multiple bandpasses were available, can provide some additional insight into the uncertainties, so we list the uncertainty of the weighted mean as the final adopted uncertainty in cases where it was larger than 20% of the distance (3/24 galaxies). Though we employ the updated Galactic extinction values of Schlafly & Finkbeiner (2011), the calibrations of Tully et al. (2008) and Tully & Courtois (2012) utilize the previous values of Schlegel et al. (1998). We find a negligible change to our final distances if we instead employ the Schlegel et al. (1998) values, with a median fractional change of 0.4% for all galaxies in our sample.

Peculiar velocities relative to the Hubble Flow, or $V_{\rm PEC}$, can be calculated as a check on the reliability of the TF distances. Galaxies in the local universe are generally observed to have $V_{\rm PEC}$ values $\lesssim 500$ km s^{-1} (Tully et al., 2008), therefore larger values require additional scrutiny. We calculated the modified, cosmologically adjusted galaxy velocity $V_{\rm MOD}$, described in Tully et al. (2013, 2016) as

$$V_{MOD} = cz[1+0.5(1-q_0)z-(1/6)\left(1-q_0-3q_0^2+1\right)z^2] \tag{3.20}$$

where z is the redshift with respect to the Cosmic Microwave Background rest frame, $q_0 = 0.5(\Omega_M - 2\Omega_\Lambda)$, $\Omega_M = 0.27$, and $\Omega_\Lambda = 0.73$. This velocity includes relativistic corrections to the observed velocity assuming ΛCDM cosmology, which are small for galaxies with $z < 0.1$, like our sample.

V_{PEC} is then calculated as

$$V_{PEC} = V_{MOD} - H_0 D \tag{3.21}$$

where we adopt $H_0 = 74$ km s^{-1} Mpc^{-1} (Riess et al., 2019), and D is the adopted distance to the galaxy in Mpc.

3.5.4 *Notes on Individual Objects*

The TF distances we have determined are the first redshift independent distances for many of the galaxies in our sample. However, in a select few cases there are previously measured distances with which we can compare our results, primarily by Cepheid and SBF methods, and secondly the Cosmicflows programs (CF1, CF2, CF3; Tully et al. 2008, 2013, 2016). Previous TF measurements have been reported for 9 galaxies in our sample, mostly in the B band, yet none have taken into account the contamination of the predominantly blue AGN in the nucleus. As discussed in Sec. 3.3, the brightness contribution of an AGN can be significant and will bias the distance modulus towards smaller values, as we have found with the majority of TF distances discussed below. We have tabulated previous distance measurements with their respective methods in Table 4.3.

Mrk 1044: There are previously published distances for Mrk 1044 from the J, H, and $K-$band TF calibrations of Theureau et al. (2007) of 86.8 $\pm$ 18.4, 78.5 $\pm$ 17.0, and 68.5 $\pm$ 14.2 Mpc, respectively. We find a distance to Mrk 1044 of 81.3 $\pm$ 16.3 Mpc, which lies within the estimates of Theureau et al. (2007). Our surface brightness decomposition of the *HST* $V-$band image is mostly consistent with the decomposition of the same image from Wang et al. (2014), however we find a larger exponential disk radius of $21\farcs9$ compared to their value of $21\farcs2$.

NGC 3227: NGC 3227 is interacting with its neighboring elliptical galaxy NGC 3226, which has a SBF distance measurement of 23.7 ± 2.6 Mpc from Tonry et al. (2001), with a slight correction from Blakeslee et al. (2010). NGC 3227 also has two previously reported $B-$band TF distance

determinations: Bottinelli et al. (1984) report a $B-$band distance of 15.2 Mpc, and Tully & Fisher (1988) report an updated $B-$band distance of 20.6 ± 3.8. We report a distance of 24.3 ± 4.9 Mpc, which shows good agreement with the SBF measurement to its companion. The removal of the AGN contamination decreases the galaxy's apparent magnitude and results in the determination of a larger distance than both of the previous $B-$band TF determinations.

NGC 3783: NGC 3783 has a previous $B-$band TF estimate of 38.5 $\pm$ 14.2 Mpc (Tully & Fisher, 1988) based on the diameter-HI line width relation. We report a slightly larger distance of 49.8 $\pm$ 10.0 Mpc. However, NGC 3783 is one of the most highly inclined systems in our sample, with an axis ratio of 0.96. Near face-on systems cause large uncertainties in W^i_{mx}, and consequently a large uncertainty in the distance.

NGC 4051: There are numerous TF distance estimates for NGC 4051 with a large span of values, the most accurate of which is the recent Cepheids measurement by Yuan et al. (2020b) of 16.6 ± 0.3 Mpc. Sorce et al. (2014) report a 3.6μm TF distance of 8.8 ± 1.8 Mpc. $B-$band TF determinations span the range of $11.0-17.0$ Mpc (de Vaucouleurs et al., 1981; Bottinelli et al., 1984, 1985; Tully & Fisher, 1988; Tully et al., 2009a). Finally, CF3 reports an $I-$band measurement of 11.0 ± 2.0 Mpc. Our distance is 9.5 ± 1.9 Mpc, surprisingly smaller than the previous TF distances given the removal of AGN contamination. The original axis ratio used by CF1 (and subsequently by CF2 and CF3) for NGC 4051 is 0.66, which is slightly more face-on than our constrained axis ratio of 0.58 from the ground-based surface brightness modeling (see Sec. 3.4.3). The higher inclination used by CF1 would produce a larger deprojected HI line width and subsequently brighter absolute magnitude predicted by the TF relation, thus resulting in a slightly larger distance of 10.9 Mpc.

NGC 4151: NGC 4151 has been studied by numerous groups in an attempt to constrain its distance, finding values that range from 4.5 to 20.3 Mpc (de Vaucouleurs et al., 1981; Bottinelli et al., 1984, 1985; Tully & Fisher, 1988). The most accurate distance comes from a recent Cepheid study, which found 15.8 ± 0.4 Mpc (Yuan et al., 2020a). Almost all of the TF studies underpredict the distance, which seems to be caused by the adoption of an axis ratio of 0.6 when constraining the galaxy inclination. Resolved HI imaging of NGC 4151 (Mundell et al., 1999) suggests a much

Table 3.6. Previous Measurements

Target	Distance (Mpc)	Method	Ref
Mrk 1044	68.5 ± 14.2	TF K−band	1
	78.5 ± 17.0	TF H−band	1
	86.8 ± 18.4	TF J-band	1
NGC 3227	15.2	TF B−band	2
	20.6 ± 3.8	TF B−band	3
	23.7 ± 2.6[a]	SBF	4
NGC 3783	38.5 ± 14.2	TF B−band[b]	2
NGC 4051	8.8 ± 1.8	TF 3.6μm	5
	11.0 ± 1.0	TF B−band	6
	11.0 ± 2.0	TF I−band	7
	11.7 ± 1.6	TF B−band	8
	12.2 ± 2.0	CF2	9
	12.4 ± 2.3	TF B−band	10
	12.6 ± 1.5	TF B−band	3
	16.6 ± 0.3	Cepheids	11
	17.0 ± 3.1	TF B−band	12
NGC 4151	3.9 ± 0.6	CF1	13
	4.5 ± 0.8	TF B−band	10
	4.8 ± 1.0	TF B−band	8
	5.0 ± 0.7	TF B−band	3
	5.7 ± 1.2	TF K−band	1
	6.4 ± 1.4	TF H−band	1
	6.9 ± 1.5	TF J-band	1
	15.8 ± 0.4	Cepheids	14
	16.6 ± 1.1	SN 2018aoq	15
	20.0 ± 1.6	SN 2018aoq	15
	20.3 ± 3.7	TF B−band	11
NGC 4593	25.6 ± 5.30	TF K−band	1
	26.2 ± 5.7	TF H−band	1
	26.6 ± 5.6	TF J-band	1
	39.5 ± 14.5	TF B−band[b]	11
NGC 5548	34.0 ± 8.8	TF B−band	3
NGC 6814	8.6 ± 2.7	TF B−band	3
	21.65 ± 0.41	Cepheids	16
	22.8 ± 4.2	TF B−band	11
NGC 7469	35.6	TF B−band	3
	50.0 ± 10.4	TF K−band	1
	55.3 ± 12.0	TF H−band	1
	57.30 ± 2.11	SN 2008ec	17
	59.6 ± 12.7	TF J-band	1
	59.70 ± 4.57	SN 2008ec	17
	66.40 ± 6.23	SN 2008ec	18

Note. — References are as follows: 1. Theureau et al. (2007), 2. Tully & Fisher (1988), 3. Bottinelli et al. (1984), 4. Tonry et al. (2001), 5. Sorce et al. (2014), 6. Tully et al. (2013), 7. Tully et al. (2016), 8. Bottinelli et al. (1985), 9. Tully et al. (2009a), 10. de Vaucouleurs et al. (1981), 11. Yuan et al. (2020b), 12. Tully & Fisher (1988), 13. Tully et al. (2008), 14. Yuan et al. (2020a), 15. Tsvetkov et al. (2019), 16. Bentz et al. (2019), 17. Koshida et al. (2017), 18. Ganeshalingam et al. (2013)

Table 3.7. Final Adopted Distances and Mass Estimates

Target	Distance (Mpc)	Ref	$R_{\rm HI}$ (Kpc)	$M_{\rm BH}$ ($M_\odot$)	$M_\star$ ($M_\odot$)	$M_{\rm BARY}$ ($M_\odot$)	$M_{\rm DYN}$ ($M_\odot$)	$M_{\rm DM}$ ($M_\odot$)
(1)	(2)	(3)	(4)	(5)	(6)	(7)	(8)	(9)
Mrk 1044	81.3 ± 16.3	1	8.10 ± 1.87	$6.71^{+0.12}_{-0.10}$	10.02 ± 0.43	10.20 ± 0.32	10.71 ± 0.11	10.55 ± 0.22
Ark 120	161.2 ± 32.2	1	16.74 ± 4.39	$8.07^{+0.05}_{-0.06}$	11.13 ± 0.22	11.18 ± 0.21	11.47 ± 0.11	11.15 ± 0.27
MCG+08-11-011	84.2 ± 6.9	2	39.45 ± 8.60	$7.43^{+0.15}_{-0.15}$	11.10 ± 0.42	11.15 ± 0.39	11.47 ± 0.09	11.19 ± 0.38
Mrk 6	126.2 ± 25.2	1	30.63 ± 9.29	$8.10^{+0.04}_{-0.04}$	11.05 ± 0.22	11.08 ± 0.21	11.76 ± 0.12	11.65 ± 0.16
Mrk 374	185.3 ± 7.0	2	41.08 ± 5.81	$7.30^{+0.31}_{-0.31}$	10.84 ± 0.42	10.86 ± 0.41	11.32 ± 0.08	11.13 ± 0.28
Mrk 79	50.2 ± 10.0	1	13.10 ± 3.19	$7.61^{+0.11}_{-0.14}$	10.13 ± 0.22	10.19 ± 0.20	10.72 ± 0.11	10.56 ± 0.17
NGC 2617	64.7 ± 19.5	1	12.70 ± 6.10	$7.49^{+0.14}_{-0.14}$	10.54 ± 0.44	10.68 ± 0.36	11.17 ± 0.26	10.99 ± 0.37
NGC 3227	23.7 ± 2.6	3	17.89 ± 4.48	$6.77^{+0.08}_{-0.11}$	11.04 ± 0.20	11.05 ± 0.20	11.32 ± 0.10	10.99 ± 0.27
SBS1116+583A	136.7 ± 27.3	1	11.23 ± 2.94	$6.56^{+0.08}_{-0.09}$	10.48 ± 0.22	10.50 ± 0.22	10.77 ± 0.14	10.44 ± 0.32
NGC 3783	49.8 ± 10.0	1	23.98 ± 5.95	$7.37^{+0.08}_{-0.08}$	11.08 ± 0.21	11.11 ± 0.20	11.51 ± 0.19	11.29 ± 0.30
Mrk 1310	118.7 ± 23.7	1	11.41 ± 2.78	$6.21^{+0.07}_{-0.09}$	10.28 ± 0.22	10.38 ± 0.18	10.90 ± 0.11	10.75 ± 0.17
NGC 4051	16.6 ± 0.3	4	17.47 ± 1.94	$6.13^{+0.12}_{-0.16}$	10.10 ± 0.19	10.19 ± 0.16	10.91 ± 0.06	10.82 ± 0.09
NGC 4151	15.8 ± 0.4	5	8.35 ± 1.13	$7.56^{+0.05}_{-0.05}$	10.35 ± 0.19	10.41 ± 0.17	10.76 ± 0.13	10.50 ± 0.24
NGC 4593	28.5 ± 5.7	1	21.04 ± 6.45	$6.88^{+0.08}_{-0.10}$	10.58 ± 0.22	10.60 ± 0.22	11.37 ± 0.12	11.29 ± 0.15
NGC 4748	82.2 ± 16.4	1	16.58 ± 5.21	$6.41^{+0.11}_{-0.18}$	10.70 ± 0.22	10.73 ± 0.21	11.25 ± 0.12	11.09 ± 0.19
NGC 5548	83.6 ± 16.7	1	24.84 ± 5.96	$7.72^{+0.02}_{-0.02}$	11.19 ± 0.22	11.20 ± 0.22	11.61 ± 0.10	11.40 ± 0.20
Mrk 817	130.8 ± 6.9	2	14.04 ± 2.74	$7.59^{+0.06}_{-0.07}$	10.92 ± 0.19	10.93 ± 0.19	11.39 ± 0.10	11.21 ± 0.17
Mrk 478	342.7 ± 7.2	2	30.39 ± 4.19	$7.40^{+0.18}_{-0.18}$	11.13 ± 0.42	11.17 ± 0.40	11.67 ± 0.22	11.51 ± 0.34
NGC 5940	141.6 ± 6.9	2	34.15 ± 4.94	$7.04^{+0.07}_{-0.06}$	11.03 ± 0.29	11.07 ± 0.27	11.33 ± 0.10	10.98 ± 0.34
Mrk 290	162.3 ± 32.5	1	17.52 ± 4.24	$7.28^{+0.06}_{-0.06}$	10.79 ± 0.30	10.81 ± 0.29	11.16 ± 0.12	10.90 ± 0.29
Zw 229-015	115.5 ± 6.9	2	28.16 ± 5.07	$6.91^{+0.07}_{-0.12}$	10.26 ± 0.19	10.30 ± 0.18	10.95 ± 0.10	10.84 ± 0.13
1H1934-063	29.5 ± 5.9	1	5.57 ± 1.45	$6.40^{+0.17}_{-0.20}$	10.15 ± 0.21	10.17 ± 0.21	10.42 ± 0.12	10.07 ± 0.31
NGC 6814	21.6 ± 0.4	6	11.91 ± 3.03	$7.04^{+0.06}_{-0.06}$	10.33 ± 0.19	10.40 ± 0.16	11.02 ± 0.31	10.90 ± 0.38
NGC 7469	61.9 ± 3.3	7	17.06 ± 2.12	$6.96^{+0.05}_{-0.05}$	10.78 ± 0.19	10.81 ± 0.18	11.05 ± 0.09	10.67 ± 0.28

Note. — Final adopted distances and mass estimates for the AGN hosts in this study. The reference for each adopted distance in Column (3) is as follows: 1. TF distance; this work, 2. Redshift-based distances consistent with those reported in Paper I, adjusted for H_0 = 74 km s^{-1}, 3. SBF estimate to interacting companion NGC 3226 (Tonry et al., 2001), 4. Cepheids measurement (Yuan et al., 2020b), 5. Cepheids measurement (Yuan et al., 2020a), 6. Cepheids measurement (Bentz et al., 2019), 7. Average SN1a distance (Koshida et al., 2017; Ganeshalingam et al., 2013). The majority of black hole masses are from the reverberation-mapping database of Bentz & Katz (2015) (see Sec. 3.6.2). The calculations for $M_{\rm BARY}$ are detailed in Paper I, $M_{\rm DYN}$ and $M_{\rm DM}$ are described in Sec. 3.6.

more face-on orientation of $\sim 21^{\circ}$. Adopting this value constrains our TF estimate of the distance to 18.6 ± 3.7 Mpc, slightly larger than but consistent with the Cepheids distance.

NGC 4593: Theureau et al. (2007) measured J, H, and $K-$band TF distances to NGC 4593 of $\sim$26 Mpc, which agrees fairly well with our finding of 28.5 ± 5.7 Mpc. Tully & Fisher (1988) estimate a much larger distance of 39.5 ± 14.5 Mpc based on the HI line width-diameter TF relation. However, as shown originally by Tully & Fisher (1977) and noted by Bottinelli et al. (1983), the diameter relation is much less accurate than the luminosity-HI line width relationship.

NGC 5548: The previous $B-$band TF measurement from Bottinelli et al. (1984) places NGC 5548 at a distance of 34.0 ± 8.8 Mpc. We find a distance of 45.0 ± 3.8 Mpc with a large $V_{\rm PEC}$ of 2104 ± 288 km s^{-1}. However, the large predicted $V_{\rm PEC}$, in addition to the turbulent and low S/N HI profile, suggest this may not be a reliable distance. Ho et al. (2008a) collected a higher S/N HI spectrum with $W_{20} = 321.1 \pm 6.8$ km s^{-1}. Using this measurement predicts $D = 83.6 \pm 16.7$ Mpc with a more reasonable $V_{\rm PEC} = -753 \pm 1242$ km s^{-1}. We therefore adopt this distance for NGC 5548 and list it in Table 3.5.

NGC 6814: Bentz et al. (2019) recently reported a Cepheid-based distance to NGC 6814 of 21.6 ± 0.4 Mpc. There are also $B-$band TF estimates which range from $8.6-22.8$ Mpc (Bottinelli et al., 1984; Tully & Fisher, 1988). Even though NGC 6814 is almost perfectly face on (with an axis ratio of 0.98) and therefore has a large uncertainty, the TF distance we predict of 22.1 ± 8.0 Mpc is in good agreement with the Cepheids value.

NGC 7469: NGC 7469 was host to SN 2008ec, a type Ia supernova. Analysis of the supernova light curve by Koshida et al. (2017) and Ganeshalingam et al. (2013) constrained distances of $57.30-66.40$ Mpc. There are also multiple TF distance determinations to NGC 7469, including a $B-$band measurement of 35.6 Mpc (Bottinelli et al., 1984) and JHK measurements of $50.0-59.6$ Mpc (Theureau et al., 2007). However, in our analysis of the HI spectrum in Paper I, we commented on possible flux contribution to the blueshifted flank of NGC 7469 from companion galaxy IC 5283. Higher S/N emission line detections in the literature most likely include the flux contribution of the companion (Mirabel & Wilson, 1984; Mirabel & Sanders, 1988; Ho et al., 2008a), while our lower

S/N profile does not share the same signature. We have tested distances predicted using the W_{20} measurements (with the W_R^i definition) from the literature to compare to our result. If 525.1 km s^{-1} from Ho et al. (2008a) is used, we calculate 140 Mpc. If we use 395 km s^{-1} from Mirabel & Wilson (1984), the resulting distance is 91 Mpc. Using our width, our distance is 36.0 ± 7.2 Mpc with a V_{PEC} of 1949 ± 535 km s^{-1}. Due to the interaction of IC 5283 and uncertainty in the width of the emission line, resolved HI observations are necessary to both separate the interacting galaxies and improve on the current distance estimates which rely on the HI line width.

3.5.5 *Selection of Final Adopted Distances*

For all galaxies except Mrk 478, we are able to compare our distances to the distances predicted by the CF3 Distance-Velocity Calculator (Kourkchi et al. 2020, hereafter CF3 DVC) based on the velocity field from the Numerical Action Methods model (Shaya et al. 2017, $D < 38$ Mpc) and the Velocity and Density Field Model (Graziani et al. 2019, $D < 200$ Mpc). The CF3 DVC predicts a distance based on the Cosmicflows model of the local velocity field in a specific region of the sky. It also displays distances and velocities of known galaxy groups and clusters within the search region that define the local model, allowing us to analyze the density of matter in a particular region. The local gravitational interactions between a galaxy and its environment cause individual V_{PEC} values.

For Mrk 1044 ($V_{PEC} = -1275 \pm 1212$), Ark 120 ($V_{PEC} = -1855 \pm 2394$), SBS1116+583A ($V_{PEC} = -1393 \pm 2030$), NGC 4748 ($V_{PEC} = -1513 \pm 1219$), and Mrk 290 ($V_{PEC} = -2644 \pm 2416$), the V_{PEC} values we calculate agree with the range of peculiar velocities observed by CF1 within the large uncertainties. The peculiar velocities of Mrk 6 ($V_{PEC} = -3625 \pm 1873$), Mrk 79 ($V_{PEC} = 3181 \pm 743$), and Mrk 1310 ($V_{PEC} = -2480 \pm 1762$) are large, but still within those observed by the larger CF2 and CF3 catalogs (maximum observed V_{PEC} of $\sim$4000 km s^{-1}), and could be caused by the mass distributions near each galaxy's position on the sky present in the CF3 catalog. We confirmed that the CF3 DVC shows known, localized mass concentrations occupying distributions of either smaller or larger distances than those predicted by the DVC. These suggest local gravitational wells, and

the resultant blueshifts or redshifts would cause each galaxy to appear closer or farther, assuming the recessional velocities are equivalent to the Hubble flow.

For MCG+08-11-011, Mrk 374, Mrk 817, Mrk 478, NGC 5940, and Zw 229-015, however, we are unable to further check our TF distances with the CF3 DVC results (mostly due to the lack of clusters present in the CF3 catalog near the position of each galaxy) or any literature results. Within the uncertainties, these $V_{\rm PEC}$ constraints are all $>$1000 km s^{-1}, which we set as the cutoff for galaxies in which we were unable to analyze the local mass distribution. The same is true even if we adopt the uncertainty typically considered by Tully et al. of 20%. Our estimated distance for Mrk 478 is 282.2 Mpc, which is beyond the 200 Mpc limit of the CF3 DVC. Additionally, as previously discussed, any distance measurement which relies on current HI line width measurements of NGC 7469 is suspect. Thus, we have deemed the TF distances to these 7 galaxies as uncertain, and have assigned each with the poor quality flag 'c' in Table 3.5.

We note that the galaxy inclinations of the majority of this sample lie below the usual limit of 45° for TF studies in the literature, namely the Cosmicflows programs. Systems with tendencies towards face-on orientations cause large uncertainties in the deprojected HI line widths and, consequently, high uncertainties on distance and $V_{\rm PEC}$ constraints. We also note that the majority of the outliers in Fig. 3.5 have TF distance measurements far too small for their $V_{\rm MOD}$ given the Hubble flow for either value of H_0 we have displayed. The TF relation is calibrated with inactive galaxies, thus it is of interest to explore potential differences between active and inactive galaxies that could cause discrepancies in the predicted distances for this sample of AGN hosts.

The analysis of color-magnitude diagrams for mass-matched samples of AGN and non-AGN hosts from the Chandra Deep Field North and South surveys by Xue et al. (2010) found that the star formation rates in active galaxies are typically a factor of $\sim 2-3$ higher than quiescent galaxies for $0 < z < 1$. Increased star formation has been shown to lead to an increase in surface brightness (e.g., Graves & Faber 2010; Mould 2020), and a higher surface brightness would lead to a brighter apparent magnitude, thus causing a galaxy to appear closer than it is. Additionally, in their study of the *R*–band TF relation for close galaxy pairs, Barton et al. (2001) found that triggered star

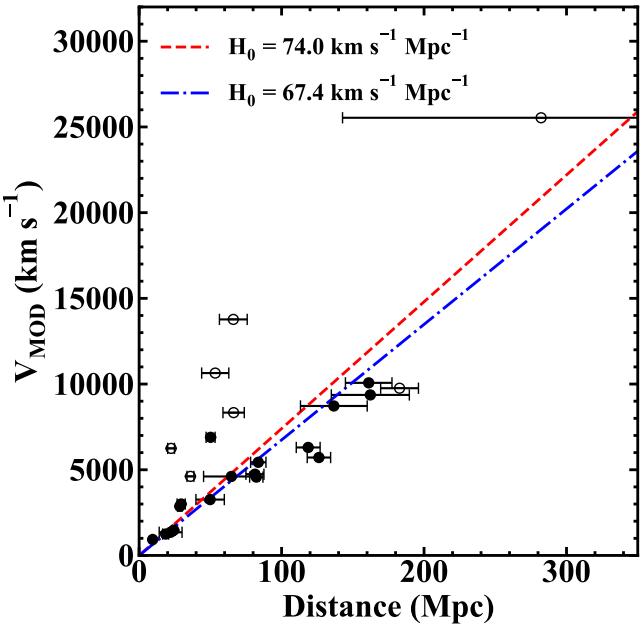

Figure 3.5: Hubble diagram exhibiting our TF distances vs their cosmologically-adjusted velocity $V_{\rm MOD}$. Points shown in open circles represent the 7 TF distances we have deemed as uncertain (see sec. 3.5.4), MCG+08-11-011, Mrk 374, Mrk 817, Mrk 478, NGC 5940, Zw 229-015, and NGC 7469. The closed points are our remaining, certain distance measurements. We compare these to the Hubble-Lemaître Law, with H_0 values of 74.0 km s^{-1} Mpc^{-1} determined by Riess et al. (2019) and 67.4 km s^{-1} Mpc^{-1} determined by Planck Collaboration et al. (2020).

formation is a significant contributor to the difference in slope from the TF relation. Whether higher star formation rates are caused by AGN activity or interactions, the observational effect would be consistent in that the galaxy would appear brighter than a comparable inactive or isolated galaxy, leading to a distance estimate that is biased low. Active galaxies might therefore be reasonably expected to show a larger scatter about the canonical TF relation.

All final TF distances are shown in the Hubble diagram in Fig. 3.5, where the aforementioned uncertain distances are open circles, and the rest are closed circles. For the remainder of this work, we apply the redshift-based distances for MCG+08-11-011, Mrk 374, Mrk 817, Mrk 478, NGC 5940, and Zw 229-015, consistent with those reported in Paper I. We employ the SBF distance to NGC 3226 as the adopted distance to NGC 3227 (Tonry et al., 2001; Blakeslee et al., 2010), the Cepheid distance measurements to NGC 4051, NGC 4151, and NGC 6814 (Yuan et al., 2020b,a; Bentz et al., 2019), and the average of the SN1a distances to NGC 7469 (Ganeshalingam et al., 2013; Koshida et al., 2017). Final adopted distances are tabulated in Table 3.7.

3.6 *Masses*

With distances and physical surface brightness details constrained, we are able to estimate the masses of the AGN hosts in our sample and explore their relationships to the central SMBH masses. Here we detail the methods of measurement for dynamical mass ($M_{\rm DYN}$) and dark matter mass ($M_{\rm DM}$) and adopted measurements of $M_{\rm BH}$.

3.6.1 *Dynamical and Dark Matter Mass*

Measurement of the maximum rotation rate (V_{mx}) of a disk galaxy allows the total enclosed mass of the system, or $M_{\rm DYN}$, to be measured. HI is one of the best tracers of galaxy rotational velocity at the outer extents of the disk, as its distribution usually extends much farther than the high surface brightness stellar component (i.e., Walter et al. 2008; Ott et al. 2012; Koribalski et al. 2018). V_{mx} is most precisely measured from the flat portion of HI rotation curves (i.e., de Blok et al.

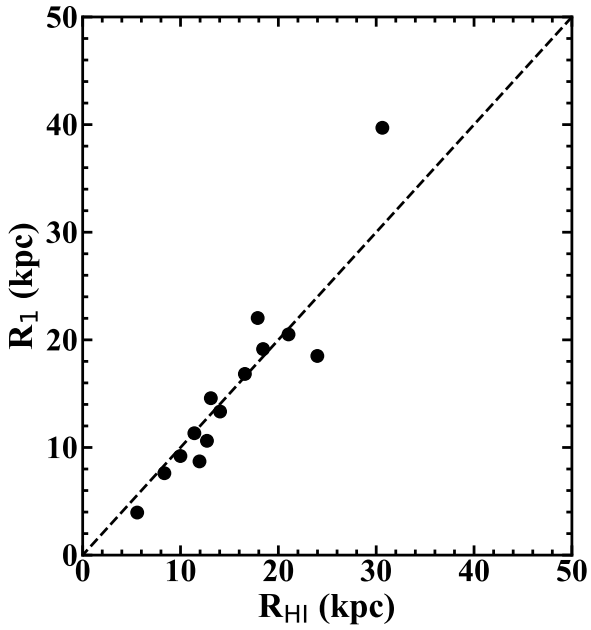

Figure 3.6: Comparison between $R_{\rm HI}$ and the radius at which the stellar mass density reaches 1 $M_\odot$ pc^{-2}, R_1, a proxy for the star formation threshold. We have followed the prescriptions from Trujillo et al. (2020) to convert the $B-$band surface brightness profiles of the galaxies in our sample to mass density profiles (see Sec. 3.6), after which R_1 was able to be measured. A line of unity is drawn, and we find good agreement between the two radii, with an average fraction of $R_{\rm HI}/R_1 \sim 1.1$.

2008), however the unresolved HI emission line is more commonly used as it requires far fewer observational resources to acquire.

The large scale velocity dispersion of HI is negligible, $\sim$10 km s^{-1} (Tamburro et al., 2009; Ianjamasimanana et al., 2012) relative to the rotational velocity. The broadening of the emission line is thus dominated by virial rotation, and the virial theorem describes the mass enclosed in the system as $M_{\rm DYN} = (RV_{mx}^2)/{\rm G}$, where R is a characteristic radius and G is the gravitational constant. In our case, R is the radial extent of the HI distribution, and V_{mx} is equivalent to $W_{mx}^i/2$, as Tully & Fouque (1985) have shown W_{mx} to be statistically equal to twice the maximum rotation rate.

There are multiple ways of estimating the HI radius in the literature. In their 21 cm study of 108 spiral galaxies, Broeils & Rhee (1997) found a relation between the HI radius and R_{25}. For galaxies where we have $B-$band images, we therefore adopt their relation of $R_{\rm HI} = (1.70 \pm 0.16)R_{25}$ with our R_{25} measurements from $B-$band isophote analyses (see Sec. 3.5). In the cases where $B-$band data are unavailable for the sample (Ark 120, Mrk 374, SBS1116+583A, Mrk 478, NGC 5940, Mrk 290,

Zw 229-015), we look to the collection of template disk galaxy rotation curves by Catinella et al. (2006) and de Blok & Walter (2014), and use the relation $R_{25} = 3.2R_d$, with the R_d measurements listed in Table 3.2. Combining these definitions yields $R_{\rm HI} = (5.4 \pm 0.5)R_d$, which agrees with the HI rotation curve analysis of de Blok & Walter (2014) that shows the maximum extent of all curves to be $\sim$5R$_d$. Therefore, for the remainder of the sample that do not have B–band data, we adopt $R_{\rm HI} = (5.4 \pm 0.5)R_d$.

Additionally, Wang et al. (2016) recalibrated the relation between the diameter of the HI disk and HI mass, resulting in an extremely tight relationship over 5 orders of magnitude in mass. With this calibrated relationship, the integrated 21 cm HI flux measurement may be employed to estimate $R_{\rm HI}$, as opposed to relying on the assumption of uniform scaling between the HI and optical sizes for all morphological types. We find a median fractional decrease of $\sim$18% in $R_{\rm HI}$ with this method compared to our adopted method of estimating $R_{\rm HI}$, which is within our typical uncertainty of $\sim$24%.

A recent study by Trujillo et al. (2020) sought to derive a physically motivated galaxy radius definition. Such a radius would correspond to a clearly measurable galaxy property, and they suggest the radius at which the star formation threshold is reached (R_1). The gas density for this threshold is usually estimated to be $\sim$3-10 M$_\odot$ pc^{-2} for gas-to-star transformation efficiencies of $\sim$100% (Schaye, 2004). However, Trujillo et al. (2020) argue that if the efficiency is less than 100%, a more reasonable estimation is 1 M$_\odot$ pc^{-2}, which corresponds to an efficiency of $\sim$10%. HI has been observed to condense to molecular hydrogen at a threshold of $\sim$10 M$_\odot$ pc^{-2} (Martin & Kennicutt, 2001; Wong & Blitz, 2002; Bigiel et al., 2008), and molecular clouds are the typical locations of star formation (e.g., Leroy et al. 2008). HI surface density should therefore be linked to star formation, and Trujillo et al. suggest that R_1 could be closely related to $R_{\rm HI}$. To investigate this, we follow the prescriptions of Trujillo et al. (2020), which were derived from SDSS colors and a Chabrier initial mass function (Chabrier, 2003), to transform the surface brightness profiles of the galaxies in our sample to stellar mass densities, and measure radii at 1 M$_\odot$ pc^{-2}. When compared to our $R_{\rm HI}$ estimates, we find an average ratio of $R_{\rm HI}$ to R_1 of $\sim$1.1, supporting the similarity between the two.

We display the comparison between the two measurements in Fig. 3.6. While we do not employ this method to estimate $R_{\rm HI}$, and while our sample is somewhat small and we employ estimates rather than measurements of $R_{\rm HI}$, the agreement between R_1 and $R_{\rm HI}$ may suggest a promising new avenue for constraining $R_{\rm HI}$ without resolved HI studies.

With $R_{\rm HI}$ estimates for all galaxies in our sample, the total enclosed mass $M_{\rm DYN}$ is calculated by

$$M_{DYN} = \left(\frac{R_{HI}(W^i_{mx}/2)^2}{G} \right) \tag{3.22}$$

with $R_{\rm HI}$ in units of kpc translated from the angular disk sizes by our adopted distances. The constraint on the amount of dark matter, then, is simply the difference between the total enclosed mass and luminous mass, $M_{\rm BARY}$, calculated as

$$M_{DM} = M_{DYN} - M_{BARY} \tag{3.23}$$

where our $M_{\rm BARY}$ values are the sum of the gas mass and the stellar mass ($M_\star$), or $M_{\rm BARY} = 1.4M_{\rm HI} + M_\star$. The factor of 1.4 on $M_{\rm HI}$ accounts for the contribution of helium. HI masses are adopted from Paper I, and the stellar masses are adopted from Bentz & Manne-Nicholas (2018) with a few additions in Paper I, both of which have been updated with our final adopted distances reported in this work. $M_\star$, $M_{\rm BARY}$, $M_{\rm DYN}$, and $M_{\rm DM}$ are reported in Table 3.7.

3.6.2 *Black Hole Mass*

All of the galaxies in this work belong to the sample of AGNs with direct black hole mass measurements from RM (Blandford & McKee, 1982; Peterson, 1993). RM measures the echo between the continuum variations of the nucleus, likely arising from the accretion disk, and the response of optically thick gas in the broad line region (BLR) moving at Doppler velocities. The time delay (τ) in the BLR variations is due to the extra path length travelled by the ionizing photons, and provides a measurement of the radius of the BLR ($R_{\rm BLR}$). When $R_{\rm BLR}$ is combined with the Doppler-broadened emission line width via the virial theorem, a constraint on the enclosed mass is

obtained, the majority of which is due to the SMBH. The mass is given by

$$M_{BH} = f\frac{c\tau V^2}{G} \tag{3.24}$$

where $c\tau$ is the effective radius, V is the width of the broad emission line, G is the gravitational constant, and f is an order-unity scale factor accounting for the unknown geometry and kinematics of the unresolved BLR. We adopt $\langle f \rangle = 4.3$ (Grier et al., 2013a).

The majority of $M_{\rm BH}$ values are adopted from the AGN Black Hole Mass Database (Bentz & Katz, 2015), and are the same as those used in our analysis in Paper I. For MCG+08-11-011, Mrk 374, and NGC 2617, we utilized the virial $M_{\rm BH}$ from Fausnaugh et al. (2017) and scaled them with $\langle f \rangle = 4.3$. For Mrk 1044, we used the Hβ time delay from Hu et al. (2015) and the rms Hβ line width from Du et al. (2016b) with our adopted $\langle f \rangle$ to arrive at an $M_{\rm BH}$ estimate. For NGC 5940, we adopt the rms line width from Barth et al. (2015) and time delay from Barth et al. (2013) to estimate $M_{\rm BH}$. Lastly, the black hole masses for Mrk 478 and 1H1934-063 are based on current work on in-hand RM data (G. de Rosa 2020, private communication; M. C. Bentz et al. 2020, in preparation). All $M_{\rm BH}$ values are listed in Table 3.7.

3.7 *Discussion*

With distances and derived masses in hand, we are able to place both in the context of other established and well-studied relationships. We first explore the most recent calibration of the Baryonic Tully-Fisher (BTF) relation (McGaugh et al., 2000), which can also be inverted to predict distance. Several scaling relations between $M_{\rm BH}$ and host galaxy characteristics have also been explored in the literature, and in the past two decades have strongly suggested a co-evolving relationship between black holes and their host galaxies. Such examples include the $M_{\rm BH} - \sigma_\star$ relation (Ferrarese & Merritt, 2000; Gebhardt et al., 2000; Kormendy & Ho, 2013), the $M_{\rm BH} - L_{\rm BULGE}$ relation (Kormendy & Richstone, 1995; Kormendy & Ho, 2013), and the $M_{\rm BH} - M_\star$ relation (Bentz & Manne-Nicholas, 2018), many of which are utilized as inputs to large cosmological

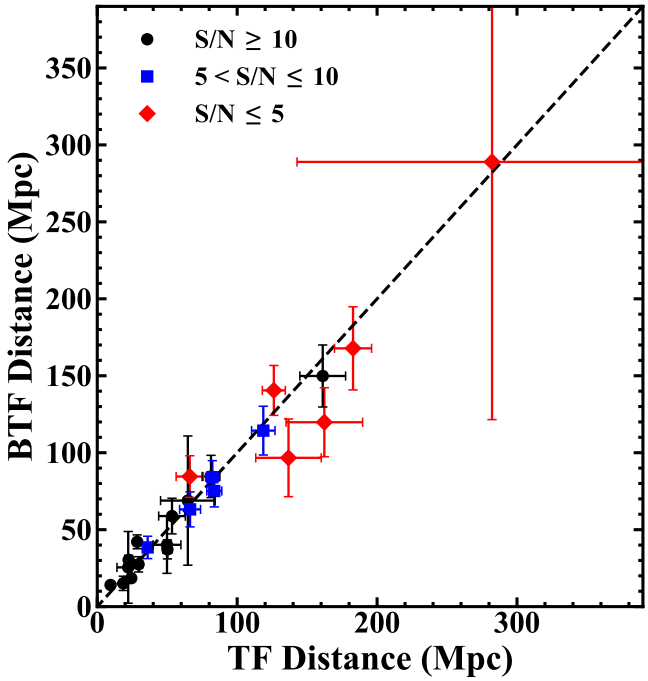

Figure 3.7: Comparison of our adopted distances (see Sec. 3.5.4) to those predicted by the BTF relation, using the W_{m50} calibration from Lelli et al. (2019). A line of unity is drawn. We display 3 HI emission line S/N thresholds (see Sec. 3.7.1), where black circles are $\geq$10, blue squares are $>$5 and $\leq$10, and red diamonds are $\leq$5, which may relate to the source of discrepancy for the few outliers.

simulations of galaxy evolution (e.g., Steinborn et al. 2015, Volonteri et al. 2016, Mutlu-Pakdil et al. 2018). Here, we investigate relationships between $M_{\rm BH}$ and $M_{\rm DYN}$, $M_{\rm DM}$, and galaxy halo mass ($M_{\rm HALO}$).

Linear regressions were carried out with LINMIX_ERR (Kelly, 2007), which is a Bayesian-based fitting algorithm that includes uncertainties in both variables in addition to a random scatter component. The slopes, intercepts, and scatter we report for each relationship are the medians of the respective large, random draws from the posterior probability distributions. The uncertainties are the 1-σ deviations of each distribution.

3.7.1 *The Baryonic Tully-Fisher Relation*

The past two decades have revealed that the most fundamental form of the TF relation is the BTF relation, which shows a tightly-correlated linear relation between rotational velocity and total

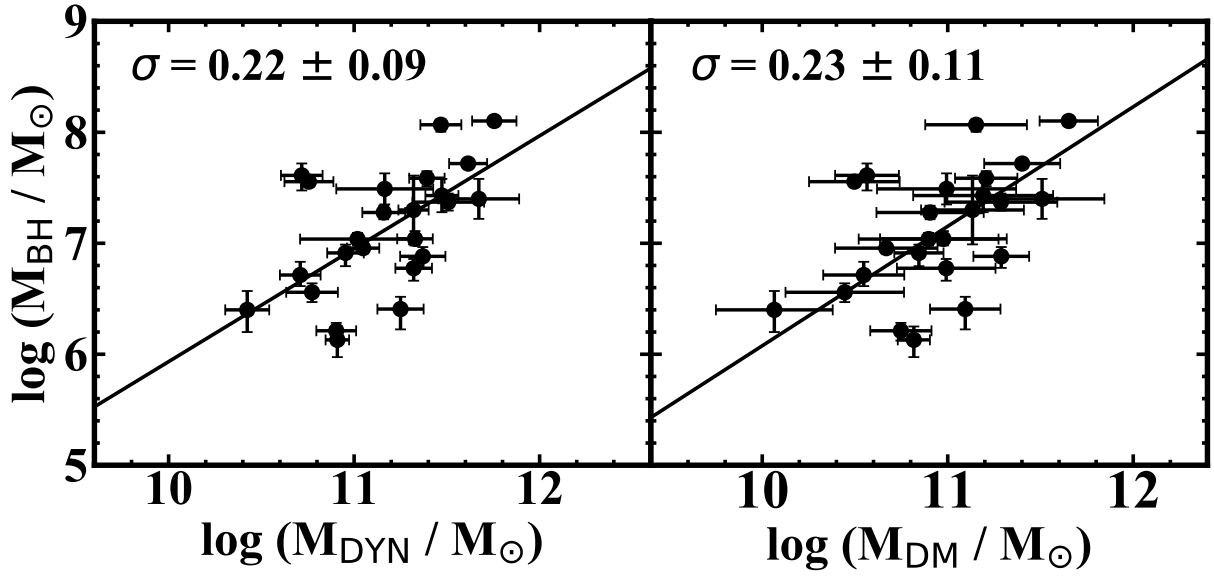

Figure 3.8: $M_{\rm BH}$ as a function of $M_{\rm DYN}$ (left) and $M_{\rm DM}$ (right). The best fits are displayed as solid, black lines in both panels. Uncertainties on the fits are displayed with gray shading around the best-fit lines. $M_{\rm DYN}$ values are calculated using $W^i_{mx}/2$ as the maximum rotation rate and $R_{\rm HI}$ as the enclosing radius. $M_{\rm DM}$ is calculated as $M_{\rm DYN} - M_{\rm BARY}$. $M_{\rm BARY}$ values were updated from those calculated in Paper I with the adopted distances in this work (see Sec. 3.6).

baryonic mass over 5 decades of mass (McGaugh et al., 2000; McGaugh, 2005; Lelli et al., 2015; Iorio et al., 2017). The mass contribution of gas in massive galaxies is small, therefore the BTF relation is equivalent to the classic TF relation on the high mass end. As calculations of both gas and stellar masses, which constitute $M_{\rm BARY}$, rely on distance, it is therefore of interest to compare our distances to those predicted by the BTF relation. Though some deviations from the relation have been observed, such as HI massive galaxies ($M_{\rm HI} \gtrsim 10^{10} M_\odot$; Courtois et al. 2015) and HI-rich ultra diffuse galaxies (Mancera Piña et al., 2019), the distances predicted by the BTF relation here are expected to be largely similar to those predicted by the TF relation, as the typical gas-to-stellar mass fraction for this sample is $\sim$13%. However, discrepancies may surface for a few galaxies with higher gas-to-stellar mass fractions (e.g., Mrk 1044, NGC 2617, Mrk 1310, Ark 120).

The BTF relation has been recently calibrated for several different definitions of rotational velocity measurement. We employ the calibration for our adopted velocity definition of W_{m50} from

Lelli et al. (2019), which has a slope of 3.62 ± 0.09 and an intercept of 2.33 ± 0.20. This agrees well with the examination of the BTF relation by Zaritsky et al. (2014) using the Spitzer Survey of Stellar Structure in Galaxies (Sheth et al., 2010), which found a slope of 3.5 ± 0.2. We employ the HI fluxes given in Table 3.3 for the HI mass estimates, with the scaling factor to convert HI mass to total gas mass of 1.33 for consistency with the BTF definition. We note that we use a scale factor of 1.33 here, rather than the value of 1.4 that we employ throughout the rest of this work, only to ensure that we calculate values in the same way as they were calculated in the calibration of the relation. Additionally, we note that the BTF relation employs the smaller scale factor of 1.33 as the helium contribution (which the scale factor accounts for) is assumed to be lower for the HI-rich calibrating sample of the BTF relation (McGaugh 2012 and references therein). We use the stellar mass-to-light ratios of Bell & de Jong (2001) to estimate $M_\star$. Comparison between the BTF distances and TF distances is shown in Fig. 3.7. A line of unity is drawn, and we find generally good agreement between the TF distances and those predicted by the BTF relation.

The points in Fig. 3.7 are labeled by HI emission line S/N, where profiles of S/N $\geq$ 10 are black circles, 5 $<$ S/N $\leq$ 10 are blue squares, and S/N $\leq$ 5 are red diamonds. Mrk 290 and SBS1116+583A lie below the unity line, along with Ark 120 and Mrk 817, which lie below the line but agree within the uncertainties. The HI emission lines of these outliers all have a S/N $<$ 5, which could result in underpredicting the flux and may be related to the cause of the discrepancies.

3.7.2 *Dynamical Mass - Black Hole Mass and Dark Matter Mass - Black Hole Mass Relations*

As described in Sec. 3.6, we utilize $R_{\rm HI}$ as the enclosing radius to estimate $M_{\rm DYN}$ for the galaxies in this sample. Here, we have examined the relationship between black hole mass and the total mass enclosed within the HI radius. The left panel of Fig. 3.8 displays a clear trend between $M_{\rm BH}$ and $M_{\rm DYN}$, with the best fit given by

$$\log\frac{M_{BH}}{M_\odot} = (1.02 \pm 0.35)\log\left(\frac{M_{DYN}}{10^{12}M_\odot}\right) + (6.95 \pm 0.12) \tag{3.25}$$

with a scatter of (0.22 ± 0.09).

Using the difference between the total enclosed mass and the luminous mass, we have also explored the relationship between $M_{\rm BH}$ and dark matter mass. We plot $M_{\rm BH}$ vs $M_{\rm DM}$ in the right panel of Fig. 3.8 and find a weaker, but still significant, correlation. The best fit to the relation is given by

$$\log\frac{M_{BH}}{M_{\odot}} = (1.08 \pm 0.49)\log\left(\frac{M_{DM}}{10^{12}M_{\odot}}\right) + (7.15 \pm 0.12) \tag{3.26}$$

with a scatter of (0.23 ± 0.11).

The average $M_{\rm DM}/M_{\rm DYN}$ fraction is $62 \pm 12\%$. However, we note that we are relying on the extent of the HI disk to measure $M_{\rm DYN}$ (and consequently $M_{\rm DM}$). The dark matter halo (DMH) is known to extend far beyond the visible radius, and thus we are probing only a fraction of the mass associated with each galaxy.

3.7.3 *Halo Mass - Black Hole Mass Relation*

We have also attempted to estimate the total enclosed mass within the halo radius, or $M_{\rm HALO}$. This includes estimates of the halo radius in relation to the HI radius and assumptions of the disk velocity at the halo radius ($V_{\rm HALO}$).

Kravtsov (2013) conducted a study relating R_{200} to several galaxy radius definitions. R_{200} is commonly treated as the radius of the DMH, and is the radius which encloses 200 times the critical density of the universe ($\rho_{\rm CR}(z)$). Halo radius hereafter is assumed to be equivalent to R_{200}. Through abundance matching of halo mass functions (Tinker et al., 2008; Klypin et al., 2011) and stellar mass functions (Bernardi et al., 2010; Papastergis et al., 2012), they first defined a relationship between stellar mass and the halo mass enclosed within R_{200}, or M_{200}. M_{200} was then estimated from $M_{\star} - M_{200}$ for a sample of galaxies with measured stellar masses that span 8 decades in $M_{\star}$ and all morphological types (Misgeld & Hilker, 2011; Leroy et al., 2008; Zhang et al., 2012). R_{200} was then estimated from M_{200}, where $M_{200} = (4\pi/3)200\rho_{\rm CR}(z)R_{200}^3$. Kravtsov (2013) found $R_{25} = 0.048R_{200}$, which when combined with $R_{\rm HI} = (1.70 \pm 0.16)R_{25}$ (Broeils & Rhee, 1997) yields $R_{200} \sim (12.3 \pm 1.2)R_{\rm HI}$.

Additionally, Lapi et al. (2018) derived global galaxy properties such as M_{200} and R_{200} for a sample of 546 nearby late-type galaxies (Persic & Salucci, 1995) by constructing templates of the rotation curve compilations of Persic et al. (1996), Catinella et al. (2006), and Yegorova et al. (2011). Templates were derived as a function of $I-$band luminosity. By modeling a DMH profile (Burkert, 1995), R_{200} was derived by extrapolating the rotation curve to where the halo density reached $\rho_{\rm CR}(z)$. They then explored the relation between R_{200} and the effective galaxy stellar radius R_e (assumed to be equivalent to $1.68R_d$). While they quote a polynomial form for the relationship, it is nearly linear within the sizeable scatter, except for a break in the trend towards smaller R_{200} at $R_e \sim 4$ kpc. Their best fit (approximated using solely the linear component) is $\log R_e = 0.73 \log R_{200} - 0.91$, which yields $R_{200} \sim (31.1 \pm 1.6) R_e$. Using their formula $R_e \sim 1.68 R_d$ and the relation $R_{\rm HI} \sim (5.4 \pm 0.5) R_d$ (Catinella et al., 2006; de Blok & Walter, 2014) yields $R_{200} \sim (9.7 \pm 1.0) R_{\rm HI}$. Given the numerous approximations in both studies, we adopt $R_{200} \sim (11 \pm 1) R_{\rm HI}$, the average of the results of Kravtsov (2013) and Lapi et al. (2018).

In regards to $V_{\rm HALO}$, if the DMH is assumed to have a constant density profile, it follows that the rotation curve would be flat out to R_{200}, thus $V_{\rm HALO} \sim W^i_{mx}/2$. This assumption is also adopted in the first derivation of a $M_{\rm BH} - M_{\rm HALO}$ relation by Ferrarese (2002). Though for any density profile other than a constant, the disk circular velocity would decrease out to R_{200}, in which case $W^i_{mx}/2$ would be an upper limit to $V_{\rm HALO}$ (as noted by Ferrarese 2002). The effect of the concentration parameter (the ratio of R_{200} to a characteristic inner radius) of the DMH on disk circular velocity was explored in the ΛCDM simulation of Bullock et al. (2001). The median of concentration parameters in the simulation showed an approximately flat rotation curve out to $\sim$40 kpc. Additionally, The HI Nearby Galaxy Survey (Walter et al., 2008) has measured flat rotation curves out to a maximum of $\sim$50 kpc, compared to the median R_{200} estimate of Lapi et al. (2018) of $\sim$ 150 kpc. Therefore, we assume a flat rotation curve out to R_{200}, and as follows $V_{\rm HALO} \sim W^i_{mx}/2$

We thus calculate the total enclosed mass $M_{\rm HALO}$ with the same formalism used to estimate $M_{\rm DYN}$. In Fig. 3.9 we explore the relationship between $M_{\rm BH}$ and $M_{\rm HALO}$. The best fit, which is

displayed with the solid line, is

$$\log\frac{M_{BH}}{M_{\odot}} = (1.07 \pm 0.37)\log\left(\frac{M_{HALO}}{10^{13}M_{\odot}}\right) + (7.97 \pm 0.31) \tag{3.27}$$

with a scatter of (0.22 ± 0.10) dex. The average fraction of dark matter within R_{200} is $97 \pm 1\%$. The typical $M_{\rm BH}/M_{\rm HALO}$ fraction is 10^{-5}, but shows a trend with less massive black holes making up a smaller fraction of the total mass of the system, similar to what was found for $M_{\rm BH}/M_{\star}$ by Bentz & Manne-Nicholas (2018).

To place the $M_{\rm HALO}$ estimates in context with other methods used to derive total enclosed galaxy mass, we first compare to the $M_{\rm HALO}$ estimates used to construct the globular cluster system mass − galaxy halo mass relation (Spitler & Forbes, 2009). In that study, halo masses were estimated using $M_{\star} - M_{\rm HALO}$ relations from weak gravitational lensing results (Hoekstra et al., 2005; Mandelbaum et al., 2006). The majority of the $M_{\rm HALO}$ estimates found by Spitler & Forbes (2009) fell within the range of $\sim 10^{10} - 10^{13}$ M$_{\odot}$ for a sample consisting of dE, E, S0, and S-type galaxies. Additionally, the E-MOSAICS simulation (Bastian et al., 2020) of the globular cluster system mass − galaxy halo mass relation found that the majority of $M_{\rm HALO}$ constraints ranged from $\sim 10^{11} - 10^{13}$ M$_{\odot}$. Comparatively, our sample of halo estimates span the right orders of magnitude for galaxies of similar morphological type.

We have compared our fit to several other estimates of the $M_{\rm BH} - M_{\rm HALO}$ relation. Ferrarese (2002) utilized $\sigma_{\star}$ measurements with the $M_{\rm BH} - \sigma_{\star}$ relation to constrain SMBH masses which spanned $\sim 10^{6} - 10^{9}$ M$_{\odot}$, along with several methods of estimating total gravitational mass, which fell within the range of $\sim 10^{11} - 10^{14}$ M$_{\odot}$. We plot the first derivation (equation 4 in Ferrarese 2002), which assumes $V_{\rm HALO} \sim W^{i}_{mx}/2$, as the red dashed line in Fig. 3.9. We find a shallower slope than Ferrarese (2002), even if we refit their relationship with their sample restricted to the same mass ranges we find. However, we employ direct measurements of $M_{\rm BH}$ while those in Ferrarese (2002) were estimated from the $M_{\rm BH} - \sigma_{\star}$ relation. Additionally, we constrain W^{i}_{mx} from unresolved HI line widths, while Ferrarese (2002) utilized V_{mx} measurements from rotation curves. The differences in

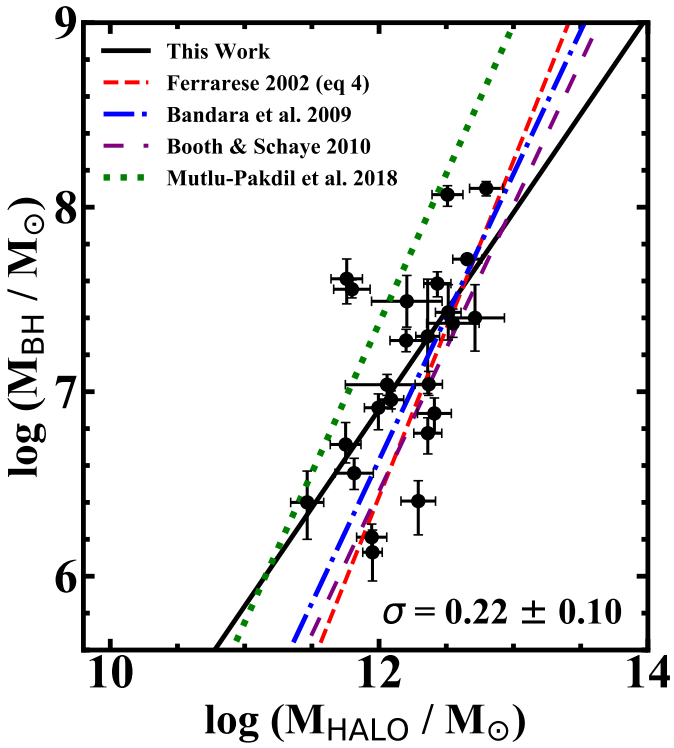

Figure 3.9: $M_{\rm BH}$ vs estimates of $M_{\rm HALO}$. We first use the average results of the relationships between observed radii and halo radii from Kravtsov (2013) and Lapi et al. (2018) to scale the $R_{\rm HI}$ values by (11 ± 1) to estimate R_{200}. We then assume a flat rotation curve out to R_{200} ($V_{\rm HALO} \sim W^i_{mx}/2$) to arrive at an approximation of $M_{\rm HALO}$. The solid black line is the formal fit to the data. The red dashed line is the first result from Ferrarese (2002), using the same assumption of a flat rotation curve. The blue dot-dashed line is the relationship of $M_{\rm BH}$ to total gravitational mass from Bandara et al. (2009), which utilized gravitational lens modeling to constrain $M_{\rm HALO}$. The purple dash-spaced line and green dotted line are the $M_{\rm BH} - M_{\rm HALO}$ relations from the simulations of Booth & Schaye (2010) and Mutlu-Pakdil et al. (2018), respectively.

both measurements are potential sources of discrepancy in the $M_{\rm BH}-M_{\rm HALO}$ relations. Ferrarese (2002) describes two other methods of estimating $M_{\rm HALO}$, however both assume nonconstant halo density profiles, and as such predict less massive DMHs and intercepts $\sim$0.5 dex and $\sim$1.5 dex smaller than what we find, respectively.

We also compare to the observationally-constrained relation from Bandara et al. (2009). Their $M_{\rm BH}$ values were derived using $\sigma_\star$ measurements and the $M_{\rm BH}-\sigma_\star$ relation, and total galaxy mass was estimated from strong gravitational lens modeling (Bolton et al., 2008). We plot their relation as the blue dot-dashed line in Fig. 3.9. We again find a slightly shallower slope in comparison (though the fits of our relation and Bandara et al. 2009 are statistically equivalent within the uncertainties). However, their study probes only the high mass end of both black hole and halo mass, with their sample spanning $\sim10^8-10^9$ M$_\odot$ in $M_{\rm BH}$ and $\sim10^{13}-10^{14}$ M$_\odot$ in $M_{\rm HALO}$.

Lastly, we have compared our results to those of large, hydrodynamical simulations. Booth & Schaye (2010) explored correlations between $M_{\rm BH}-M_\star$ and $M_{\rm BH}-M_{\rm HALO}$, which they define as the mass enclosed within a sphere of a mean density of $200\rho_{\rm CR}(z)$. Their result is plotted as the purple dash-spaced line in Fig. 3.9. The Illustris simulation also explored $M_{\rm BH}-M_{\rm HALO}$ (where the definition of $M_{\rm HALO}$ is the same as Booth & Schaye 2010), and we plot the result of Mutlu-Pakdil et al. (2018) as the green dotted line. The intercepts of their relations differ by a decade, most likely due to the difference in DMH density profiles between the simulations. Pillepich et al. (2014) reported that the halo density profile for the Illustris galaxies is well characterized by a negative power law, which would result in less massive haloes due to the quicker drop-off in density. Interestingly, galaxies in the the upgraded IllustrisTNG simulation (Lovell et al. 2018, which incorporated a larger volume, higher resolution, and new physics such as black hole-driven winds) are a much better match to observations, with flat rotation curves out to large radii ($\sim$60 kpc for $M_{200} = 10^{13}$ M$_\odot$). While the $M_{\rm BH}-M_{\rm HALO}$ relationship has not yet been reexamined for IllustrisTNG, the flatter rotation curves will result in a larger enclosed mass within R_{200} and may provide a better match to observationally-constrained relationships such as the one we present here.

3.8 *Summary*

We presented TF distance measurements for 24 AGN host galaxies with direct $M_{\rm BH}$ measurements from reverberation-mapping. We also presented the first calibration of the $V-$band TF relation. These are the first redshift independent distance determinations for 14 active galaxies. We utilized *HST* $V-$band and ground-based B, V, R, I, and $H-$band images to constrain multiple distance measurements for 19 galaxies. Removal of the bright nucleus via surface brightness modeling has allowed measurements of the distance moduli free of AGN contamination for the first time. Generally close agreement was found between distances derived from different photometric bandpasses within the uncertainties, and we found good agreement between the TF distances and those predicted by the BTF relation.

We collected available distance measurements from Cepheids (NGC 4051, NGC 4151, NGC 6814), SBF (NGC 3227), and SN1a (NGC 7469), z-based distances for 6 galaxies for which we deem the TF distances as uncertain (MCG+08-11-011, Mrk 374, Mrk 817, Mrk 478, NGC 5940, Zw 229-015), and the remaining 13 TF distances for estimates of galaxy dynamical and dark matter masses. We combined these with $W^i_{mx}/2$ and estimates of the HI radius to derive $M_{\rm DYN}$, which when compared to $M_{\rm BARY}$ allowed constraints on $M_{\rm DM}$. The typical fraction for our sample is $M_{\rm DM}/M_{\rm DYN}$ = 62%.

We also explored the relationships between $M_{\rm BH}$ and constraints on $M_{\rm DYN}$, $M_{\rm DM}$, and $M_{\rm HALO}$. We found significant correlations between $M_{\rm BH}-M_{\rm DYN}$ and $M_{\rm BH}-M_{\rm DM}$. To approximate $M_{\rm HALO}$, we assumed $R_{200} \sim (11 \pm 1)R_{\rm HI}$ and a flat rotation curve out to R_{200}. $M_{\rm HALO}$ estimates for this sample showed good agreement with the range of halo masses found by other observationally based methods and simulations (Spitler & Forbes, 2009; Bastian et al., 2020). Over the range of $M_{\rm BH}$ and $M_{\rm HALO}$ probed by this sample, we found good agreement between our $M_{\rm BH}-M_{\rm HALO}$ relation, the observationally-constrained relations of Ferrarese (2002) and Bandara et al. (2009), and the hydrodynamical simulations of Booth & Schaye (2010) and Mutlu-Pakdil et al. (2018).

Chapter 4

Dynamical Modeling of the Broad Line Regions of 5 Nearby Seyfert Galaxies

4.1 *Introduction*

Black holes have been featured as the centerpiece of several of some of the most imagination-capturing astrophysical achievements in the past $\sim$20 years. To focus on just a few, the first image of a supermassive black hole (SMBH) has been captured (Event Horizon Telescope Collaboration et al., 2019), the monitoring of individual stars around the Milky Way's central SMBH has yielded a precise, direct measurement of its mass and garnered the 2020 Nobel Prize in physics in the process (Ghez et al., 2000; Genzel et al., 2000; Ghez et al., 2008), and the most accurate depiction of an accreting black hole has even found its way onto the silver screen as a revolutionary, high-resolution simulation in 2014's *Interstellar* (James et al., 2015). Additionally, the past two decades have revealed that not only are SMBHs found at the centers of nearly every major galaxy, but they coevolve with the galaxies that host them (Kormendy & Ho, 2013; Heckman & Best, 2014), indicated by many empirical scaling relationships between SMBH mass and large-scale galaxy properties (e.g., Kormendy & Richstone 1995; Ferrarese & Merritt 2000; Gebhardt et al. 2000). Generally, the interpretation of these scaling relations is that SMBH and galaxy growth is regulated by feedback from the black hole when it enters a period of accretion and becomes an active galactic nucleus (AGN; Silk & Rees 1998; Bower et al. 2006; Ciotti et al. 2009; Fanidakis et al. 2011), and that SMBHs are important players in galaxy evolution over cosmic time. Therefore, accurate measurements of SMBH characteristics are essential for investigation of black hole-galaxy evolution.

There are several different methods by which to constrain black hole mass ($M_{\rm BH}$). Direct measurements can be achieved by modeling the bulk kinematics of gas or stars that are within the gravitational sphere of influence of a black hole. However, the sphere of influence must be spatially resolved in order to employ this technique, which has limits its application mostly to nearby bulge-dominated early-type galaxies (Tremaine et al., 2002; Marconi & Hunt, 2003; Ferrarese & Ford, 2005). Even for the most massive bulges, the spatial resolution required fundamentally confines gas and/or stellar dynamical modeling methods to a distance of $\sim$100 Mpc (Gültekin et al., 2009). Scaling relationships based on these direct measurements enable indirect estimates, whereby large-scale galaxy properties predicts $M_{\rm BH}$.

AGN activity provides another method of directly constraining $M_{\rm BH}$ through reverberation mapping (RM; Blandford & McKee 1982; Peterson 1993). The stochastic variability of the continuum emission (most likely from the accretion disk) is echoed through the variation in reprocessed flux from the broad emission line region (BLR) gas. The extra path length travelled by the reprocessed photons emitted by the BLR gas results in a time delay (τ) between the observed continuum and BLR flux variations (the recombination timescale is assumed to be negligible compared to the variation timescale; Blandford & McKee 1982) and provides a direct measure of the BLR radius ($R_{\rm BLR}$). The velocity of the BLR gas, obtained by measuring the line width of the broad emission line, combined with τ yields a constraint on the total enclosed mass within the BLR, the vast majority of which is contributed by the black hole. Thus, RM substitutes spatial resolution with temporal resolution, alleviating the distance limit of dynamical modeling methods. Additionally, distance is required in dynamical models in order to convert angular size to physical size, whereas RM is able to directly measure physical sizes.

The BLRs in even the nearest AGNs have long remained unresolved, with the GRAVITY instrument on the Very Large Telescope only very recently achieving the necessary spatial resolution to probe the outer regions of the BLR of a handful of AGNs (Gravity Collaboration et al., 2020a,b, 2021a; Vermot et al., 2021; Gravity Collaboration et al., 2021b). Additionally, because RM is a spectral and time-domain tool, traditional RM analyses yield an average BLR size with no

information regarding the detailed structure of the probed gas, and the resulting $M_{\rm BH}$ constraints require the order of unity scale factor $\langle f \rangle$ which accounts for the unknown kinematics and geometry of the BLR. Generally, an average $\langle f \rangle$ factor is employed, derived by assuming the black hole mass – bulge stellar velocity dispersion relation ($M_{\rm BH} - \sigma_\star$; Ferrarese & Merritt 2000; Gebhardt et al. 2000) is the same for both active and quiescent galaxies and finding the multiplicative scale factor for $M_{\rm BH}$ required to bring the active sample into agreement with the quiescent sample (Onken et al., 2004; Collin et al., 2006; Woo et al., 2010, 2013; Graham et al., 2011; Grier et al., 2013a; Batiste et al., 2017).

Recent high-quality RM data are able to reveal the behavior of τ as a function of line-of-sight velocity. These velocity-resolved analyses have exhibited variable behavior in individual parts of a broadened emission line, and have allowed some basic details of the geometry and kinematics of the BLR to be inferred (Bentz et al., 2009b; Denney et al., 2009a; Denney et al., 2010; Barth et al., 2011a,b; Grier et al., 2013b; Du et al., 2016a; Pei et al., 2017). The results of the majority of these studies are consistent with Keplerian orbits within a flattened geometry, with some also providing evidence for inflowing/outflowing gas motions (Bentz et al., 2009b; Denney et al., 2009b; Denney et al., 2010; Grier et al., 2013a; Du et al., 2016a).

One of the ultimate goals of velocity-resolved RM analyses is to recover the transfer function, which describes the distribution of time lags as a function line-of-sight velocity and is thus directly related to the geometry and kinematics of the BLR (Horne, 1994; Bentz et al., 2010; Grier et al., 2013b; Skielboe et al., 2015; Anderson et al., 2021). An alternative approach to this involves directly modeling RM data and producing a set of self-consistent BLR models which best match the observations (Brewer et al., 2011; Pancoast et al., 2011, 2012, 2014a,b; Li et al., 2013; Grier et al., 2017; Williams et al., 2018, 2020; Bentz et al., 2021). In addition to measuring $M_{\rm BH}$ independent of $\langle f \rangle$, these direct modeling results find key properties that are generally consistent between BLRs, namely that the Hβ-emitting gas is organized in thick disk geometries at low to moderate inclinations relative to the observer. The kinematics have been found to be largely comprised of near-circular elliptical orbits combined with evidence for inflow, consistent with previous velocity-

resolved RM studies. Investigations of BLR gas at higher ionization are more sparse, only recently modeled in detail by Williams et al. (2020) and Bentz et al. (2021), who (as expected) found that the high-ionization BLRs were more compact than the low-ionization regions. In general, the black hole masses derived from direct BLR modeling are in good agreement with previous RM measurements, even though traditional RM techniques are limited to a mean τ and require an $\langle f \rangle$ factor. The largest disparity arises when direct modeling derives a very low inclination to the observer's line of sight ($\lesssim$15°), which would produce smaller observed line of sight velocities from the BLR gas and would subsequently lead both the simpler RM measurements and masses from direct modeling to be biased low.

In this paper, we model the velocity-resolved RM data from the monitoring campaign of 5 bright Seyfert 1 galaxies during the first half of 2012 presented by De Rosa et al. (2018, hereafter dR18). The campaign targeted some of the most well-studied AGNs (Mrk 704, NGC 3227, NGC 3516, NGC 4151, and NGC 5548) with the intent of improving $M_{\rm BH}$ constraints and exploring the velocity-dependent time delays and resulting inferences on BLR geometry and kinematics. The BLR of NGC 5548 has been previously modeled by both Pancoast et al. (2014b) and Williams et al. (2020) from observations in 2008 and 2014 respectively, allowing an investigation of the properties and behavior of the BLR in NGC 5548 as a function of time. Additionally, NGC 3227 and NGC 4151 are among a small and critical sample of galaxies that have been targeted for SMBH mass measurement by both RM and gas/stellar dynamical modeling methods, allowing comparison between results of independent mass measurement techniques. We present here the constraints from direct modeling on the geometry and kinematics of the Hβ-emitting BLRs of the 5 Seyferts in this sample, including the high-ionization BLR probed through the He II λ4686 broad line for NGC 3227 and NGC 4151, and new direct constraints on the black hole masses in all 5 AGNs.

4.2 *Spectroscopy and Imaging*

Detailed descriptions of the target selection and spectroscopic and photometric monitoring data for all 5 AGNs investigated in this study are provided by dR18. We briefly describe the observations

and data processing here. NGC 3227 was the target for an additional, shorter campaign in 2014, also presented by dR18. However, the data are much more sparse than the 2012 observations causing both the continuum and emission line light curves to exhibit weak variation patterns, rendering the campaign inadequate for detailed modeling. We have thus chosen to omit this dataset from our analysis.

4.2.1 *Spectroscopy*

MDM. The majority of the spectroscopic observations were conducted with the MDM Observatory 1.3 m McGraw-Hill Telescope. The Boller and Chivens CCD spectrograph was employed for the monitoring campaign with a 350 mm^{-1} grating, dispersion of 1.33 Å pixel^{-1}, and wavelength coverage of 4400 − 5850 Å. The 5″.0 projected width of the slit resulted in a spectral resolution of 7.9 Å.

AAO. Additional spectroscopy for NGC 3227, NGC 4151, and NGC 5548 was obtained by the 1.22 m Galileo Telescope at the Asiago Astrophysical Observatory (AAO). A 300 mm^{-1} grating was employed on the Cassegrain Boller and Chivens spectrograph with a 5″.0 × 7′.75 long slit, covering a wavelength range of ∼3200–8000 Å with a dispersion of 2.3 Å pixel^{-1} and resolution of 10.5 Å.

CrAO. The Crimean Astrophysical Observatory (CrAO) was employed for supplemental spectroscopic observations of NGC 4151 and NGC 5548. The 2.6 m Shajn telescope was used with the Nasmith spectrograph and SPEC-10 CCD, with a 3″.0 slit, wavelength coverage of 3900–6100 Å, and dispersion of 1.85 Å pixel^{-1}.

WIRO. To cover planned gaps in the monitoring campaign, a small number of observations were conducted with the 2.3 m telescope at Wyoming Infrared Observatory (WIRO) and the WIRO Long Slit Spectrograph. A 5″.0 slit and 900 mm^{-1} grating were used, yielding a dispersion of ∼1 Å pixel^{-1} and wavelength coverage of 4400 − 5600 Å.

Spectra were reduced in IRAF[1] following standard procedures. An absolute flux calibration was conducted for the spectroscopic observations by using the narrow [O III] λ5007 emission line

[1]IRAF is distributed by the National Optical Astronomy Observatory, which is operated by the Association of Universities for Research in Astronomy (AURA) under a cooperative agreement with the National Science Foundation.

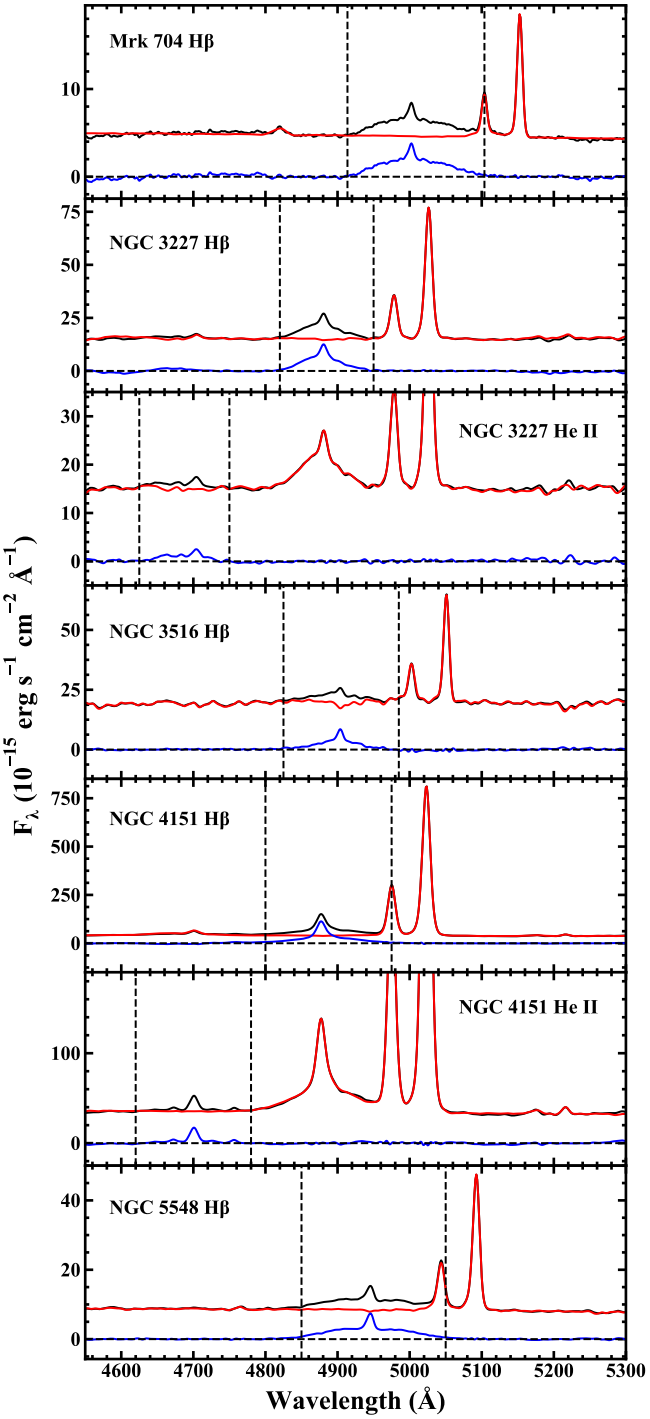

Figure 4.1: Examples of isolating the broad Hβ and He II emission lines from the continuum and [O III] $\lambda\lambda 4959, 5007$ doublet as described in Section 4.2.3. Spectra from single observations of each AGN are displayed in black. The preliminary fits to all other emission lines and the continuum is displayed in red, and the data minus the model is in blue. The vertical dashed lines represent window of wavelengths used for each respective BLR model.

Table 4.1. AGN Target Properties

Target	z	$N_{\rm epochs}$	Hβ Window (Å)	He II Window (Å)
(1)	(2)	(3)	(4)	(5)
Mrk 704	0.03177	83	4915–5100	···
NGC 3227	0.00382	90	4820–4950	4625–4750
NGC 3516	0.00876	89	4825–4985	···
NGC 4151	0.00333	85	4800–4975	4620–4780
NGC 5548	0.01716	92	4850–5050	···

Note. — Column (2) lists the redshift measurements from HI 21 cm spectra presented by Robinson et al. (2019). Column (3) lists the number of epochs of observation for each AGN, with typical observations per night of ∼7 for NGC 4151 and ∼3 for all other AGNs. Columns (4) and (5) list the wavelength ranges windowed for BLR modeling for the Hβ and He II emission lines, respectively.

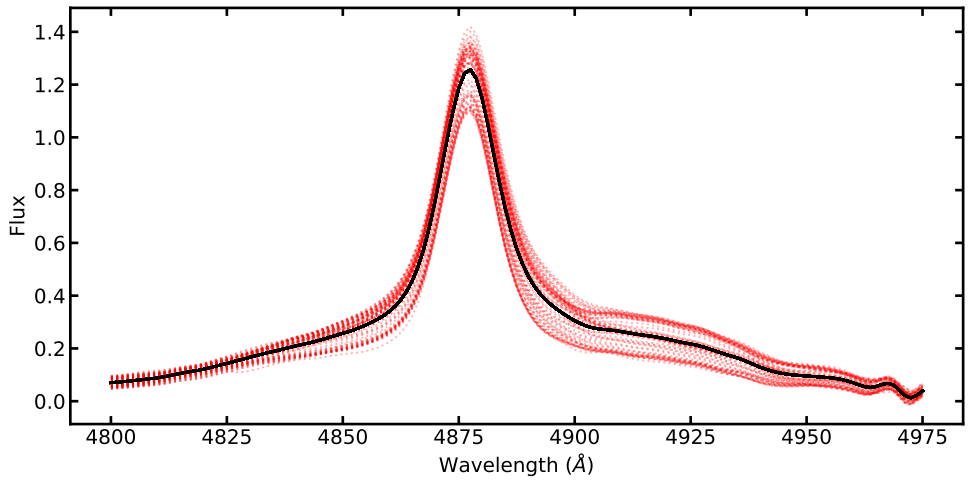

Figure 4.2: Example of all epochs of the isolated Hβ emission lines of NGC 4151. The mean emission profile is displayed in black, with all other epochs displayed as dotted red lines.

as the flux standard. While it has been observed that narrow lines can vary on timescales of years (Peterson et al., 2013), the flux is effectively constant on timescales of days to months. The [O III] λ5007 flux was measured for the highest quality spectra, and the adopted flux and uncertainty for each AGN were calculated as the mean and standard deviation of these measurements. A reference spectrum was then produced by combining the spectra with the highest signal-to-noise ratios (S/N). The reference spectrum was scaled to the adopted [O III] λ5007 flux, and each individual spectrum was then corrected for small wavelength shifts and differences in the flux and resolution compared to the reference spectrum.

4.2.2 *Imaging*

Spectroscopic observations were supplemented with photometry in the Johnson $V-$band for all of the following observatories.

*WC*18. The 0.5 m Centurian 18 telescope at Wise Observatory (WC18; Brosch et al. 2008) was employed with the STL-6303E CCD, which has a pixel scale of $1\farcs47$ and field of view (FOV) of $75' \times 50'$.

WMO. Photometry was also conducted with the 0.9 m telescope at West Mountain Observatory (WMO), which uses the Finger Lakes PL-3041-UV CCD with a $0\farcs61$ pixel scale and $21' \times 21'$ FOV.

ASAS−SN. Lastly, the All-Sky Automated Survey for Supernovae (ASAS-SN; Shappee et al. 2014) was also used for supplemental photometry. Data from ASAS-SN are from its first unit, Brutus, which in 2012 employed 2 14 cm Nikon telephoto lenses in the Faulkes Telescope North (Brown et al., 2013). The FLI ProLine CCDs in the Faulkes Telescope consist of Fairchild Imaging 2000×2000 pixel thinned CCDs, pixel scales of $7\farcs8$, and FOVs of 4.47×4.47 degrees.

4.2.3 *Light Curves*

Continuum light curves for each AGN were constructed from both photometric and spectroscopic data. The $V-$band AGN flux was isolated from the host galaxy contribution using the image subtraction package ISIS (Alard & Lupton, 1998; Alard, 2000) following the procedures of Shappee

Table 4.2. Broad Line Region Model Parameters

Parameter	Description	Mrk 704 Hβ	NGC 3227 He II	NGC 3227 Hβ	NGC 3516 Hβ	NGC 4151 He II	NGC 4151 Hβ	NGC 5548 Hβ
$\log_{10}(M_{\rm BH}/M_{\odot})$	Black hole mass	$7.38^{+0.57}_{-0.62}$	$5.86^{+0.30}_{-0.35}$	$6.04^{+0.36}_{-0.53}$	$7.28^{+0.10}_{-0.24}$	$5.60^{+0.45}_{-0.58}$	$6.48^{+0.24}_{-0.27}$	$6.97^{+0.22}_{-0.40}$
r_{mean} (light days)	Mean BLR radius	$4.45^{+8.79}_{-3.35}$	$0.50^{+0.55}_{-0.29}$	$2.75^{+3.35}_{-1.75}$	$12.13^{+2.69}_{-4.86}$	$0.98^{+1.62}_{-0.71}$	$5.05^{+2.14}_{-2.09}$	$5.65^{+2.91}_{-3.17}$
r_{median} (light days)	Median BLR radius	$3.67^{+9.00}_{-2.70}$	$0.43^{+0.50}_{-0.25}$	$2.16^{+2.38}_{-1.47}$	$11.22^{+2.53}_{-4.56}$	$0.37^{+0.61}_{-0.27}$	$2.67^{+1.45}_{-1.21}$	$3.53^{+1.84}_{-1.93}$
r_{min} (light days)	Minimum BLR radius	$1.26^{+3.91}_{-1.00}$	$0.08^{+0.21}_{-0.07}$	$0.24^{+0.58}_{-0.16}$	$0.91^{+1.10}_{-0.58}$	$0.05^{+0.08}_{-0.04}$	$0.29^{+0.26}_{-0.24}$	$0.89^{+0.75}_{-0.65}$
τ_{mean} (days)	Mean time delay	$2.39^{+6.24}_{-1.73}$	$0.47^{+0.52}_{-0.27}$	$2.53^{+1.76}_{-1.22}$	$5.82^{+1.34}_{-1.93}$	$0.58^{+1.09}_{-0.42}$	$3.36^{+1.49}_{-1.47}$	$4.51^{+4.55}_{-2.07}$
τ_{median} (days)	Median time delay	$2.16^{+5.47}_{-1.65}$	$0.37^{+0.40}_{-0.21}$	$1.35^{+1.38}_{-0.50}$	$3.41^{+0.92}_{-1.22}$	$0.16^{+0.33}_{-0.11}$	$1.37^{+0.92}_{-0.64}$	$2.16^{+2.55}_{-0.87}$
θ_i (degrees)	BLR inclination angle	$17.32^{+5.21}_{-6.43}$	$36.73^{+11.28}_{-9.36}$	$79.04^{+9.08}_{-33.94}$	$30.12^{+7.18}_{-8.04}$	$6.31^{+3.89}_{-3.15}$	$11.24^{+5.55}_{-4.62}$	$73.63^{+11.37}_{-19.39}$
θ_o (degrees)	BLR opening angle	$48.66^{+23.52}_{-16.64}$	$19.30^{+7.37}_{-5.09}$	$25.29^{+33.68}_{-16.63}$	$85.56^{+2.98}_{-8.87}$	$70.64^{+12.98}_{-14.97}$	$54.94^{+20.47}_{-13.54}$	$17.21^{+17.47}_{-8.70}$
θ_e (degrees)	Ellipse angle	$3.1^{+2.0}_{-1.9}$	$12.60^{+6.50}_{-7.40}$	$9.2^{+7.2}_{-6.9}$	$6.7^{+5.0}_{-3.7}$	$5.50^{+4.20}_{-3.30}$	$14.4^{+8.1}_{-8.0}$	$17.7^{+12.6}_{-12.1}$
σ_r (light days)	BLR radial extent	$2.23^{+7.96}_{-1.78}$	$0.28^{+0.69}_{-0.17}$	$4.53^{+6.90}_{-3.46}$	$21.61^{+8.13}_{-8.02}$	$18.71^{+28.01}_{-14.50}$	$28.27^{+19.58}_{-13.59}$	$15.55^{+10.02}_{-8.15}$
σ_{turb}	Turbulence	$0.014^{+0.017}_{-0.011}$	$0.01^{+0.02}_{-0.01}$	$0.066^{+0.027}_{-0.058}$	$0.021^{+0.024}_{-0.017}$	$0.01^{+0.04}_{-0.01}$	$0.020^{+0.049}_{-0.018}$	$0.054^{+0.024}_{-0.044}$
f_{ellip}	Fraction of elliptical orbits	$0.02^{+0.04}_{-0.02}$	$0.02^{+0.03}_{-0.02}$	$0.05^{+0.07}_{-0.03}$	$0.05^{+0.07}_{-0.04}$	$0.01^{+0.02}_{-0.01}$	$0.04^{+0.05}_{-0.03}$	$0.04^{+0.04}_{-0.03}$
f_{flow}	Inflow/outflow	$0.23^{+0.19}_{-0.16}$	$0.76^{+0.16}_{-0.17}$	$0.58^{+0.31}_{-0.33}$	$0.28^{+0.18}_{-0.19}$	$0.24^{+0.19}_{-0.17}$	$0.24^{+0.18}_{-0.16}$	$0.61^{+0.23}_{-0.43}$
β	BLR shape parameter	$0.77^{+0.34}_{-0.28}$	$0.73^{+0.30}_{-0.14}$	$1.14^{+0.13}_{-0.12}$	$0.96^{+0.09}_{-0.09}$	$1.92^{+0.06}_{-0.09}$	$1.60^{+0.13}_{-0.09}$	$1.49^{+0.07}_{-0.11}$
κ	Preferential emission direction	$0.01^{+0.30}_{-0.23}$	$-0.24^{+0.05}_{-0.08}$	$-0.47^{+0.96}_{-0.02}$	$0.38^{+0.07}_{-0.14}$	$0.38^{+0.08}_{-0.13}$	$0.12^{+0.14}_{-0.14}$	$-0.39^{+0.86}_{-0.07}$
γ	Preferential disk face emission	$1.44^{+0.38}_{-0.25}$	$1.75^{+0.19}_{-0.29}$	$1.44^{+0.45}_{-0.29}$	$1.88^{+0.08}_{-0.18}$	$1.94^{+0.04}_{-0.09}$	$1.87^{+0.10}_{-0.17}$	$1.32^{+0.49}_{-0.25}$
ξ	BLR midplane transparency	$0.05^{+0.05}_{-0.04}$	$0.06^{+0.08}_{-0.05}$	$0.60^{+0.28}_{-0.41}$	$0.33^{+0.11}_{-0.14}$	$0.86^{+0.10}_{-0.17}$	$0.49^{+0.10}_{-0.11}$	$0.69^{+0.20}_{-0.47}$

Note. — Median and 68% confidence intervals of the posterior PDFs of each respective BLR model parameter.

& Stanek (2011). The photometric light curves were then merged with the spectroscopic light curves, produced by measuring the flux-calibrated, scaled spectra at $5100 \times (1+z)$ Å. All data reduction and flux calibration was conducted by dR18. For the final continuum light curves used in this study, we binned data points within a cadence of 0.5 days.

The emission line light curves presented by dR18 were constructed by interpolating a linear continuum beneath the emission line and integrating the flux above the linear continuum. Here, we have constructed new light curves via isolation of the Hβ and He II λ4686 lines by modeling and subtracting the continuum, [O III] $\lambda\lambda$4959, 5007 doublet, and any other emission lines from each spectrum using the spectral fitting package ULySS (Koleva et al., 2009). We began by modeling the high S/N mean spectrum of each AGN with a continuum consisting of a power law (to isolate the AGN flux contribution to the continuum) and a Vazdekis model to the host-galaxy component (Vazdekis et al., 2010). Gaussian profiles were employed to fit the emission lines present in each mean spectrum, with $\sim$3−5 Gaussians required to fit each [O III] λ4959, [O III] λ5007, and Hβ emission line, and $\sim$1−2 Gaussians required to fit any other lines (i.e., He I λ4471, He II λ4686). We also investigated for evidence of Fe II emission, however dR18 found evidence of blended emission only with He II λ4686, which will be addressed in future work. Once the preliminary fit to the mean spectrum was achieved, each individual spectrum was fit by slightly adjusting the fit to the mean spectrum. The host-galaxy component was held fixed to the fit component for the mean spectrum but allowed to vary in flux, given the small differences in slit placement and seeing from night to night, while the power law and emission line components were left as free parameters with initial values consistent with those in the fit to the mean spectrum. Finally, the preliminary fit to the continuum, [O III] doublet, and remaining emission lines were subtracted from each individual spectrum.

Figure 4.1 displays examples of spectra from single observations for each AGN in black, the preliminary models to the continuum and any other emission features in red, and the residuals (data-model) highlighting the emission line of interest in blue. Spectra obtained within the same night were then averaged together. The broad emission line regions were windowed for BLR

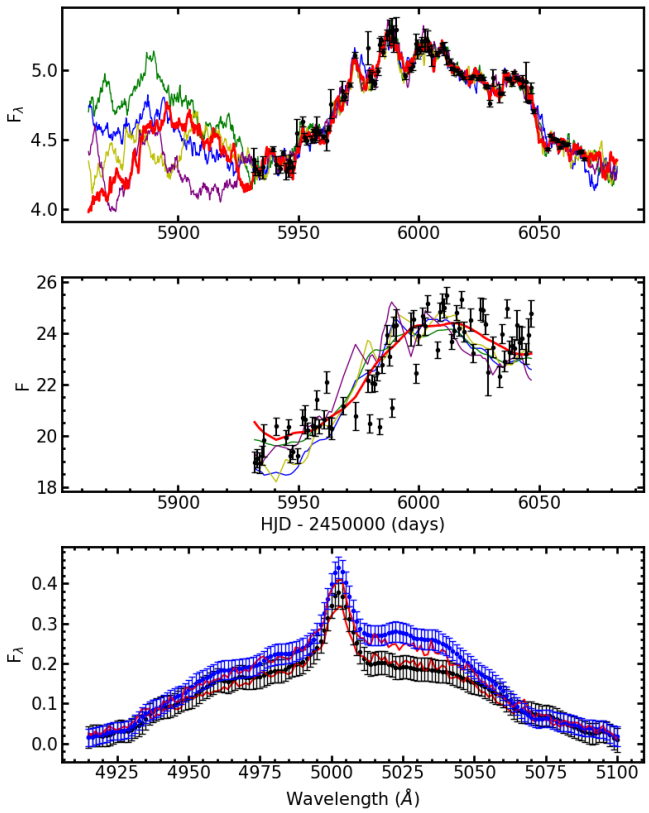

Figure 4.3: AGN continuum light curve (top panel), Hβ light curve (middle panel), and two examples of single observations of Hβ (bottom panel) for Mrk 704. The data in the top two panels are displayed in black, with the representative model to each light curve overplotted in bold red, and random models drawn from the posterior displayed with thinner lines of green, blue, yellow, and purple. The data in the bottom panel are displayed in black and blue with their respective models overplotted in bold red. The flux densities (F_λ) in the top and bottom panels are in units of 10^{-15} erg s^{-1} cm^{-2} Å^{-1}, and the integrated fluxes (F) in the middle panel are in units of 10^{-13} erg s^{-1} cm^{-2}.

modeling according to the wavelength ranges listed in Table 4.1, and are indicated by the vertical dashed lines in Figure 4.1. An example of the isolated Hβ emission lines for all epochs of NGC 4151 is shown in Figure 4.2.

4.3 *BLR Dynamical Modeling*

All BLR modeling was conducted with CARAMEL, a simply parameterized phenomenological code described in detail by Pancoast et al. (2014a). We give a brief overview of the main model components below.

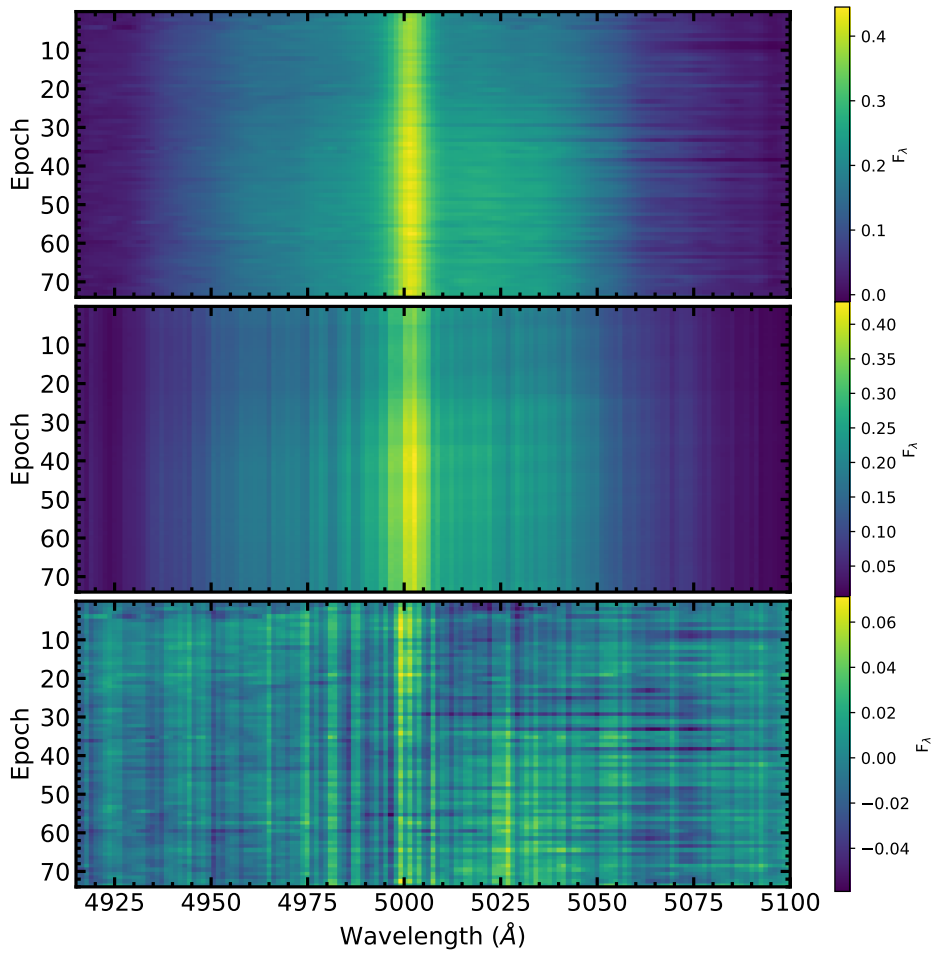

Figure 4.4: Hβ spectral time series for Mrk 704. The top panel displays the averaged spectra of all observations per night, with the middle panel displaying one possible model of Hβ for each night. The residual (data − model) is shown in the bottom panel.

The BLR is modeled as a distribution of massless point particles in position and velocity space surrounding a central, isotropically emitting continuum source. The source of ionizing photons surrounding the SMBH is assumed to be unresolved and is modeled as point-like, and the particles inhabit the region dominated by the gravity of the central black hole. The point particles receive the continuum emission after a delay in time depending on their position relative to the ionizing source and instantaneously process and re-emit some fraction of light towards the observer, thus they represent sites of BLR emission rather than a full distribution of all possible gas clouds. The wavelength of re-emitted light is equal to the rest wavelength of the emission line of interest (in this study, either Hβ or He II), with Doppler shifts dependent on the velocity distribution of the particles relative to the BLR's systemic velocity.

In addition to the BLR model, the continuum light curve is modeled in order to sample the driving light curve at any arbitrary point in time. Thus, with a model of the continuum and BLR particles, CARAMEL can produce a time series of emission spectra which may be directly compared to the observed emission-line profiles. The continuum light curve is modeled using Gaussian processes, which allows inclusion of the uncertainty from the interpolation and extrapolation in the uncertainties of the BLR model parameters in addition to extrapolation before and after the limits of the monitoring campaign to explore longer time lags.

The geometry of each BLR is parameterized by both radial and angular distributions. The radial positions of the particles are drawn from a Gamma distribution given by

$$p(x|\alpha,\theta) \propto x^{\alpha-1} \exp\left(-\frac{x}{\theta}\right) \tag{4.1}$$

where α is the shape parameter of the distribution and θ is the scale parameter. A shape parameter of $\alpha = 1$ yields an exponential profile, $\alpha > 1$ a Gaussian profile, and $\alpha < 1$ a cuspier profile. The particle distribution is then shifted away from the central black hole by a combination of the black hole's Schwarzschild radius ($R_s = 2GM_{BH}/c^2$) and a free parameter defining a minimum radius r_{min}. The maximum radius of the BLR, $r_{out} = c\Delta t_{data}/2$, is based on the time between the first modeled continuum light curve data point and the first emission line spectrum (Δt_{data}). The assumption in

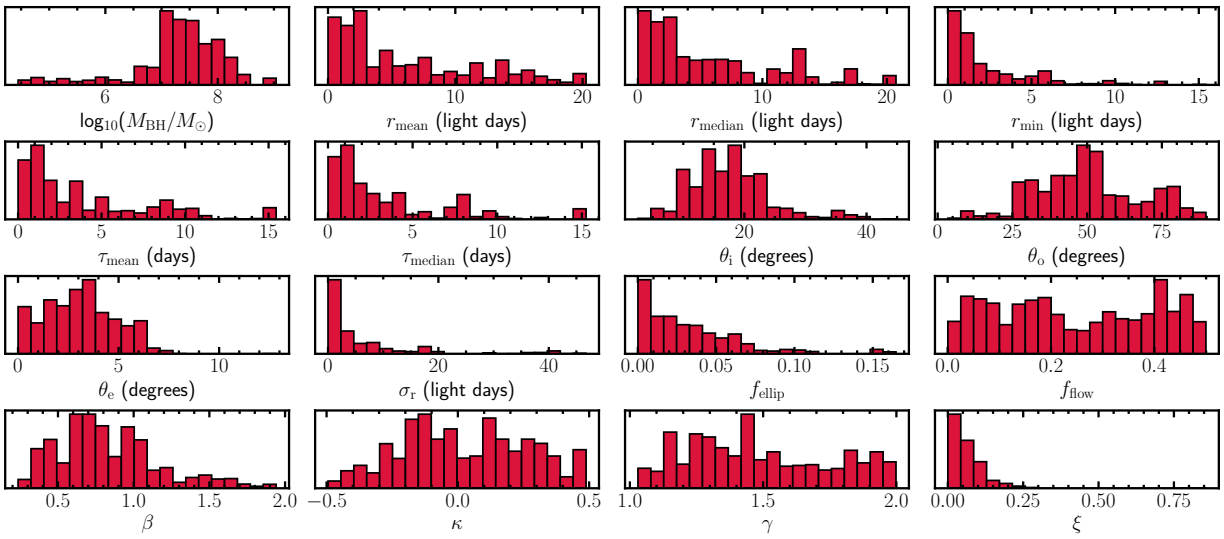

Figure 4.5: Histograms showing the full posterior PDFs for each of the Hβ-emitting BLR model parameters for Mrk 704.

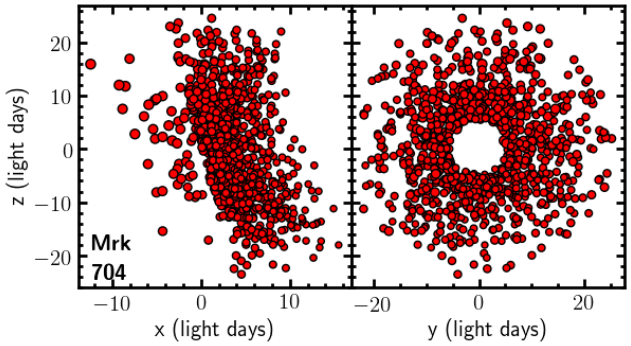

Figure 4.6: Representative geometric of the Hβ-emitting BLR in Mrk 704. The left panel displays the model along the y-axis, representing an edge-on orientation with the observer's viewpoint along the +x-axis. The right panel shows the model in a face-on orientation with respect to the observer. Each point represents a point particle in the BLR model, and the size of each point corresponds to the relative Hβ emission radiated from each particle.

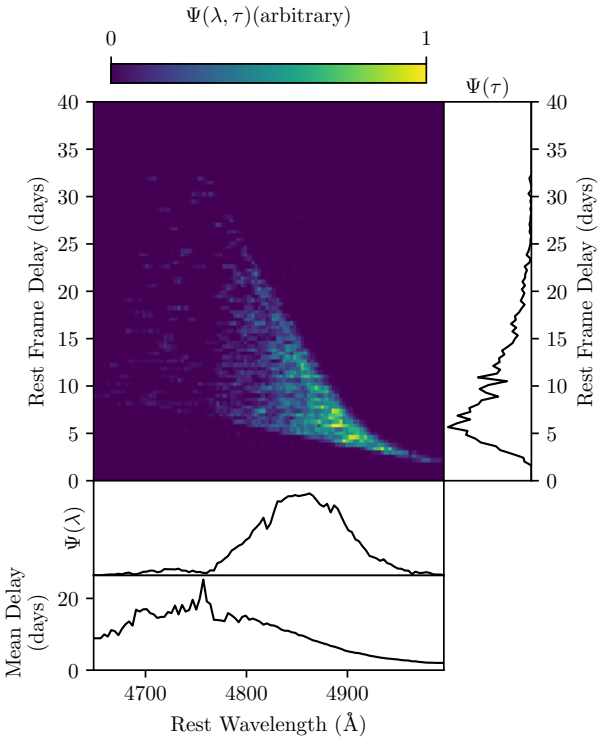

Figure 4.7: Representative transfer function for the Hβ-emitting BLR model for Mrk 704 shown in Figure 4.6. The right-hand panel shows the one-dimensional time lag profile Ψ_τ, found by integrating the transfer function over wavelength. The second panel from the bottom shows the variable emission profile, Ψ_λ, found by integrating the transfer function over time delay. The bottom panel displays the average time lag for each wavelength bin.

setting $r_{\rm out}$ is such that the monitoring campaign is sufficient in length to measure the reverberation signals across the whole of the BLR.

Next, a change of variables converts $(\alpha, \theta, r_{\rm min})$ to (μ, β, F), where μ is the mean radius of the BLR, β dictates the shape of the Gamma distribution, and F is $r_{\rm min}$ in units of μ. The change of variables is given by:

$$\mu = r_{\rm min} + \alpha\theta \tag{4.2}$$

$$\beta = \frac{1}{\sqrt{\alpha}} \tag{4.3}$$

$$F = \frac{r_{\rm min}}{r_{\rm min} + \alpha\theta} \tag{4.4}$$

The standard deviation of the radial profile of the BLR particles is now given by $\sigma_{\rm r} = (1-F)\mu\beta$.

The angular positions of the particles are then placed in a disk, the thickness (or angle between a particle and the disk midplane) of which is determined by an opening angle θ_o. A thin disk is modeled with opening angle $\theta_o = 0°$, while $\theta_o = 90°$ defines a sphere. The inclination of the disk relative to the observer's line of sight is defined by θ_i, where a face-on orientation is defined by $\theta_i = 0°$ and edge-on by $\theta_i = 90°$. Thus, the angle between a BLR particle and the disk midplane is given by:

$$\theta = \arccos(\cos\theta_{\rm o} + (1 - \cos\theta_{\rm o})U^{\gamma}) \tag{4.5}$$

where U is a random number drawn from uniform distributions between $0-1$. The γ parameter dictates any preferential broad-line emission from the faces of the disk and can range from 1, where the particles are distributed uniformly through the BLR model, to 2, where the particles are clustered near the face of the disk. Originally, γ ranged from 1 to 5, but has since been updated (Williams et al. 2022, in prep). An additional parameter, ξ, is added to account for any obscuration in emission

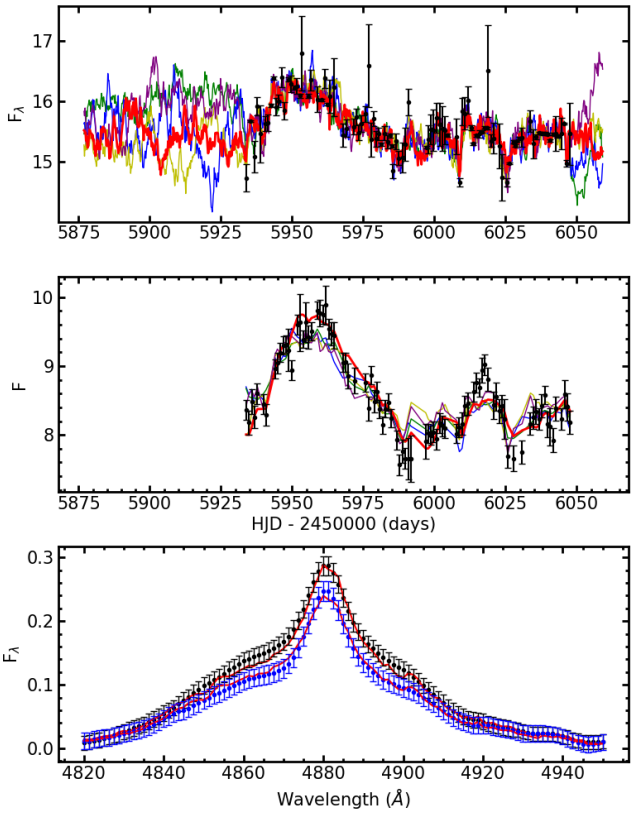

Figure 4.8: Same as Figure 4.3, but for Hβ in NGC 3227.

along the midplane of the disk. As ξ approaches 1, there is no midplane obscuration, while the limit as ξ approaches 0 yields complete obscuration of the half of the BLR behind the disk midplane.

The relative emission strength of each BLR particle is weighted by the asymmetry parameter

$$W(\phi) = \frac{1}{2} + \kappa \cos(\phi) \tag{4.6}$$

where W is the fraction of continuum flux re-emitted by a BLR particle as emission line flux, ϕ is the angle between the line connecting a particle to the ionizing source and the line connecting the observer's line of sight to the ionizing source, and κ defines preferential emission towards or away from the ionizing source. The value of κ can range from -0.5, where the BLR particles preferentially emit back towards the central SMBH, to 0.5, where the particles preferentially emit away from the SMBH. From an observer's point of view, $\kappa = -0.5$ would appear as preferential emission from the far side of the BLR, while $\kappa = 0.5$ would appear as preferential emission from the near side.

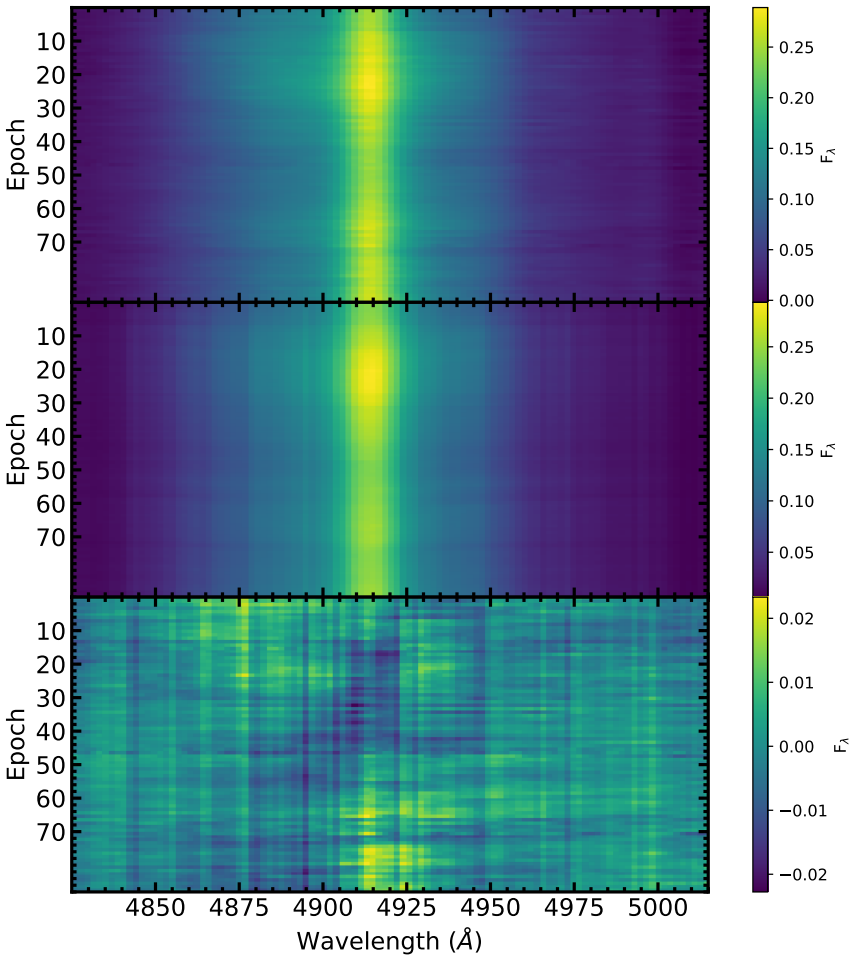

Figure 4.9: Same as Figure 4.4, but for Hβ in NGC 3227.

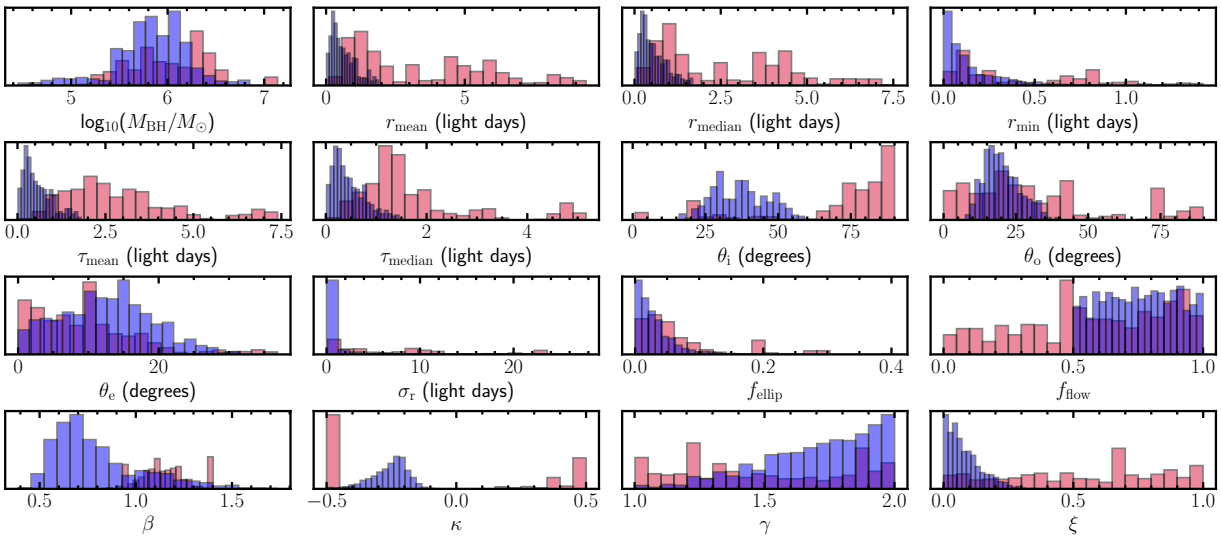

Figure 4.10: Same as Figure 4.5, but for the Hβ (red) and He II (blue) lines of NGC 3227.

Each BLR particle is assigned a velocity based on its radial position, its tangential position, and the black hole mass. A fraction of particles have near-circular orbits, given by $f_{\rm ellip}$, while the remaining particles exhibit flowing motion, $f_{\rm flow}$, where $0 < f_{\rm flow} < 0.5$ corresponds to inflowing motion towards the black hole and $0.5 < f_{\rm flow} < 1$ corresponds to outflowing motion away the black hole. The parameter $\theta_{\rm e}$ determines whether the orbits are generally bound or unbound. The angle $\theta_{\rm e}$ can range from 0° to 90°, where $\theta_e = 0°$ corresponds to a Gaussian distribution of particle velocities centered on the escape velocity of the black hole, and $\theta_e = 90°$ corresponds to a circular velocity-centered distribution. Thus, low values of $\theta_{\rm e}$ indicate preference towards orbits near the escape velocity, and high values indicate preference towards near-circular inflowing or outflowing orbits. Random contributions of macroturbulent velocities are also included in the velocity vectors of the BLR particles as

$$v_{\rm turb} = \mathcal{N}(0, \sigma_{\rm turb})|v_{\rm circ}| \tag{4.7}$$

where $v_{\rm circ}$ is a particle's circular velocity, $\mathcal{N}(0, \sigma_{\rm turb})$ is a Gaussian distribution centered about 0, and $\sigma_{\rm turb}$ is the standard deviation of the distribution.

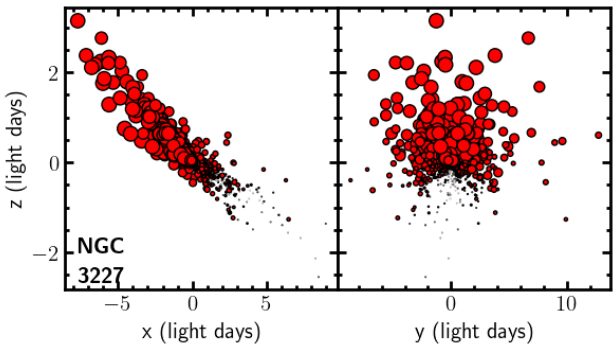

Figure 4.11: Same as Figure 4.6, but for Hβ in NGC 3227.

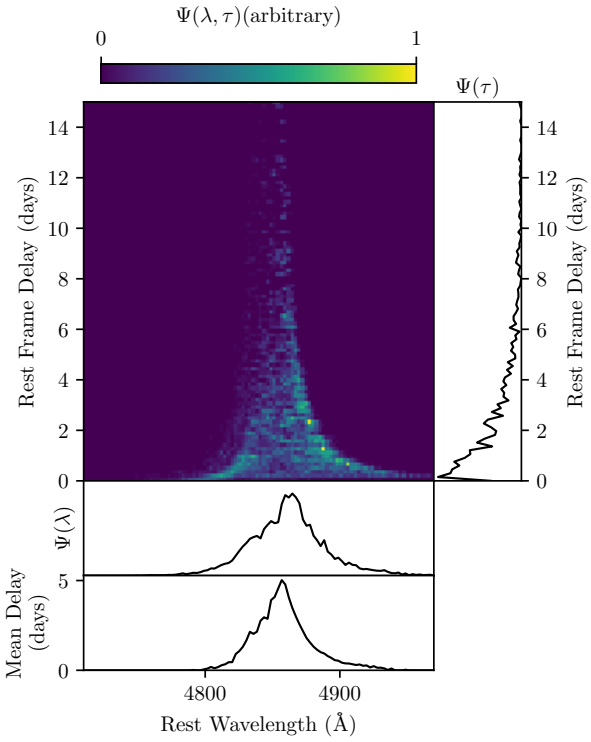

Figure 4.12: Same as Figure 4.7, but for Hβ in NGC 3227.

Combining the model for the AGN continuum light curve with the model of the geometry and kinematics of the BLR allows for emission line profiles to be generated. The amount of flux re-emitted by each particle from the continuum source is calculated, and the flux contribution from all particles is shifted in wavelength accordingly by each particle's line-of-sight velocity. Additionally, a nonvariable narrow-line component is included in the generated emission profiles to model the superimposed narrow emission, as it arises farther from the black hole than the BLR emission and is thus expected to exhibit reverberation only on timescales of several years (e.g., Peterson et al. 2013). The modeled spectra are then blurred to account for the varying observing conditions over the course of the monitoring campaign in addition to the inherent resolution of the instrument. The spectral blurring is conducted by comparing each observed [O III] λ5007 line width to its intrinsic width reported by Whittle (1992).

For each model, we designate 2000 point particles to represent the BLR. A Gaussian likelihood function is used to compare the observed, isolated Hβ spectra to the model-generated spectra, and adjusts the BLR model parameters to achieve a best fit. To efficiently explore each model's parameter space, CARAMEL employs the latest version of the diffusive nested sampling code DNEST4 (Brewer & Foreman-Mackey, 2018). To account for the systemic uncertainty in the BLR model and the data arising from any details in emission line variability not described by the simplified model, DNEST4 allows the likelihood function to be softened by a statistical temperature parameter T, which scales up the uncertainties by a factor of $\sqrt{T}$. The value of T for each model is determined in the post analysis, where we choose the highest value of T for which overfitting of the model hyperparameters does not occur and the parameter distributions are smooth and generally single-peaked.

Once a family of geometries and kinematics is achieved, the transfer functions, or maps of the time delays as a function of velocity, may be predicted from the models. These are interpreted in part by comparison to expected transfer function shapes assuming specific dynamics. Select examples presented by Horne et al. (2004) are shown in Figure 4.13, where theoretical velocity-delay maps are constructed from line-emitting clouds in a spherical distribution of circular orbits and a flat Keplerian disk in the top panels and a hydromagnetically driven wind in the bottom panel.

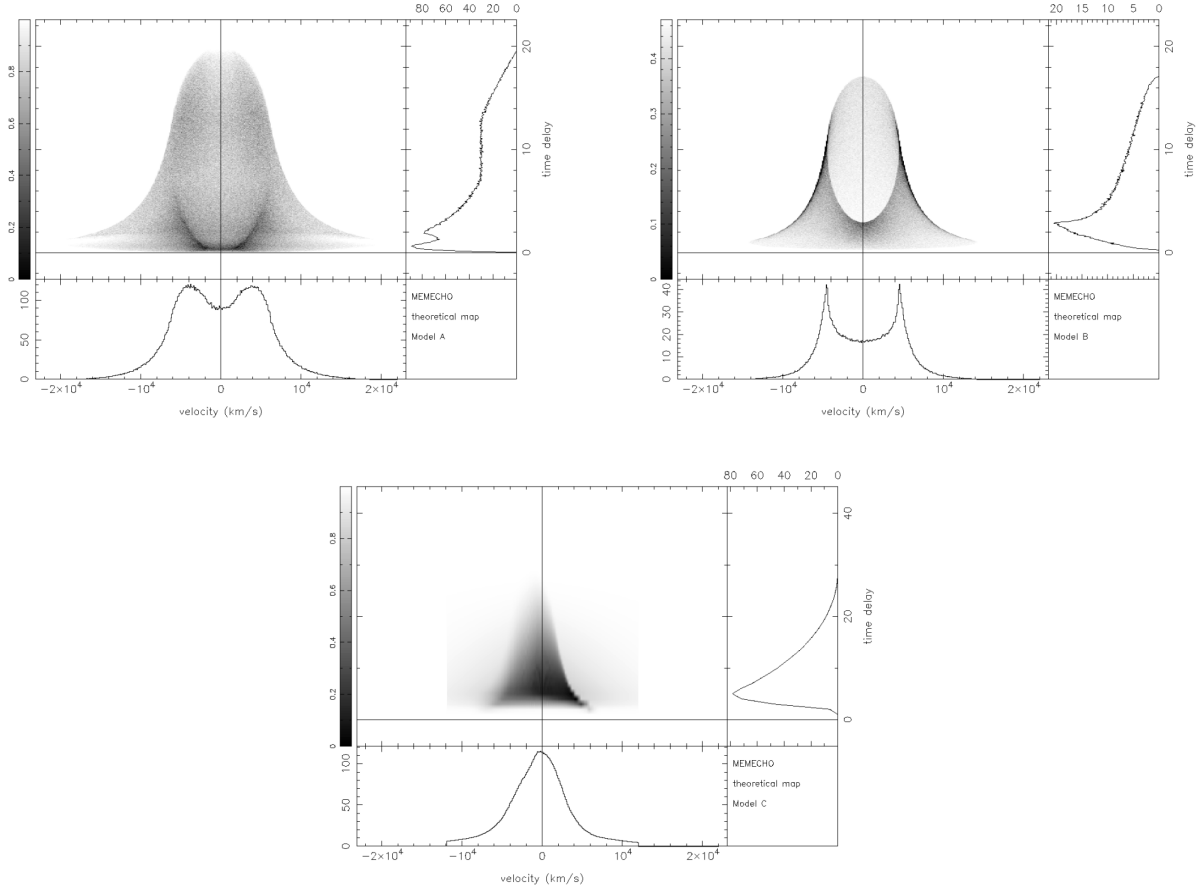

Figure 4.13: Select examples of theoretical transfer functions, $\Psi(v,\tau)$, presented by Horne et al. (2004). The top two panels from left to right exhibit $\Psi(v,\tau)$ from line-emitting clouds in a spherical distribution of circular Keplerian orbits and from a flat Keplerian disk, respectively. The bottom panel exhibits $\Psi(v,\tau)$ from a hydromagnetically driven wind. The projected responses, $\Psi(\tau)$ and $\Psi(v)$, are displayed to the right and bottom of each panel and are found by integrating $\Psi(v,\tau)$ over velocity and time delay, respectively.

4.4 *Preliminary Results*

We present here the preliminary results of modeling the Hβ-emitting, low-ionization BLRs for all 5 AGNs, and we also present models of the high-ionization He II-emitting BLR for NGC 3227 and NGC 4151. In Table 4.2 we list the median and 68% confidence intervals for the posterior probability distribution function (PDF) of each model parameter.

4.4.1 *Mrk 704*

The continuum and emission line light curves for Mrk 704 are displayed in the top and middle panels of Figure 4.3. The observed Hβ profiles, modeled profiles, and residuals for each epoch are shown in Figure 4.4. The model-generated emission lines are generally able to fit the main features of the observations, however the models exhibit more structure or noise as a function of wavelength than the observed profiles, which is most likely causing the vertical striping pattern seen in the residuals in the bottom panel of Figure 4.4. The emission line light curve model is able to fit the gross variation, however the emission line light curve in dR18 has a much clearer structure and an absence of the lower-flux outliers present in our light curve. We will thus carefully investigate the fits to the spectra as descried in Section 4.2.3. Additionally, the vertical striping should not be expected in the finalized models, and we discuss the underlying cause and future associated work in Sections 5.1.4.1 and 5.1.4.2. The models also required a likelihood softening of $T = 15$, equivalent to increasing the uncertainties by a factor of $\sqrt{T} \sim 4$.

The posterior PDFs of all model parameters for Mrk 704 are displayed in Figure 4.5. The characteristics of the geometry and dynamics of the Hβ-emitting BLR in Mrk 704 are less constrained than other AGNs in this study. The geometry is found to be a thick disk with an opening angle of $\theta_{\rm o} = 48.66^{+23.52}_{-16.64}$ degrees and relatively face-on inclination of $\theta_{\rm i} = 17.32^{+5.21}_{-6.43}$ degrees. The median radius of the disk is found to be $r_{\rm median} = 3.67^{+9.00}_{-2.70}$ lt-day, with a minimum radius away from the ionization source of $r_{\rm min} = 1.26^{+3.91}_{-1.00}$ lt-days and radial width of $\sigma_{\rm r} = 2.23^{+7.96}_{-1.78}$ lt-days. The radial positions of the BLR particles have a slight preference for a more Gaussian distribution ($\beta = 0.77^{+0.34}_{-0.28}$).

There is no clear preference for the particles to emit towards or away from the ionizing source ($\kappa = 0.01^{+0.30}_{-0.23}$), nor can the models discriminate preference for a uniform or clustering distribution of BLR particles ($\gamma = 1.44^{+1.44}_{-0.25}$). The amount of obscuration, though, is well constrained to be such that nearly all of the BLR behind the disk midplane is obscured ($\xi = 0.05^{+0.05}_{-0.04}$). A representative geometry of the Hβ-emitting BLR in Mrk 704 is displayed in Figure 4.6.

The dynamics in the BLR of Mrk 704 are dominated by inflowing orbits ($f_{\rm flow} = 0.23^{+0.19}_{-0.16}$), with minimal contribution of mactroturbulent velocities ($\sigma_{\rm turb} = 0.014^{+0.017}_{-0.011}$), and none of the full posterior PDF showing solutions for outflow. Few of the BLR particles exhibit near-circular orbits ($f_{\rm ellip} = 0.02^{+0.04}_{-0.02}$), and the velocities of the inflowing orbits are drawn from a distribution rotated only $\theta_{\rm e} = 3.1^{+2.0}_{-1.9}$ degrees away from radial escape velocity of the black hole. This suggests that the vast majority of particles are on unbound, inflowing orbits.

The models find a mean and median time delay of $\tau_{\rm mean} = 2.39^{+6.24}_{-1.73}$ days and $\tau_{\rm median} = 2.16^{+5.47}_{-1.65}$ days, much smaller than the average time delay reported by dR18 of $\tau_{\rm cent} = 12.65^{+1.49}_{-2.14}$ days. However, the time delays for these preliminary models of Mrk 704 are not well constrained, and delays of up to $\sim$15 days are not ruled out by the full posterior PDFs shown in Figure 4.5. The transfer function, $\Psi(\lambda, \tau)$, for a representative model for Mrk 704 is shown in Figure 4.7. We find a stronger responsivity of Hβ in the red wing than in the blue, and longer time delays in the blue wing. This behavior is generally in agreement with the velocity-resolved analysis of dR18, where the blueshifted velocities showed longer overall lags compared to the redshifted velocities. This signature can be interpreted as evidence for inflowing motions, which we have also found in the BLR model. Finally, $M_{\rm BH}$ is constrained to be $\log_{10}(M_{\rm BH}/M_{\odot}) = 7.38^{+0.57}_{-0.62}$.

4.4.2 *NGC 3227*

For NGC 3227, we were able to model both the Hβ and He II λ4686 emission lines, and describe the results of each below.

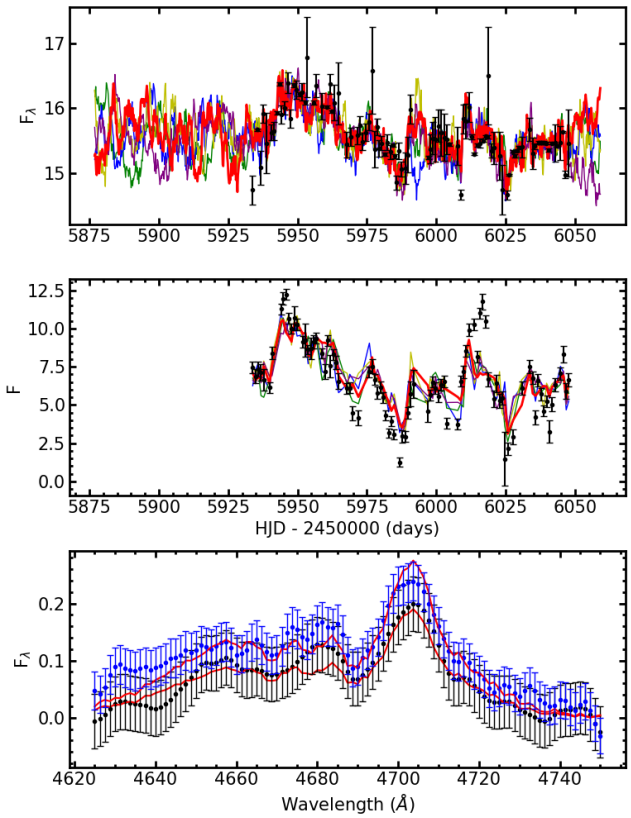

Figure 4.14: Same as Figure 4.3, but for He II in NGC 3227.

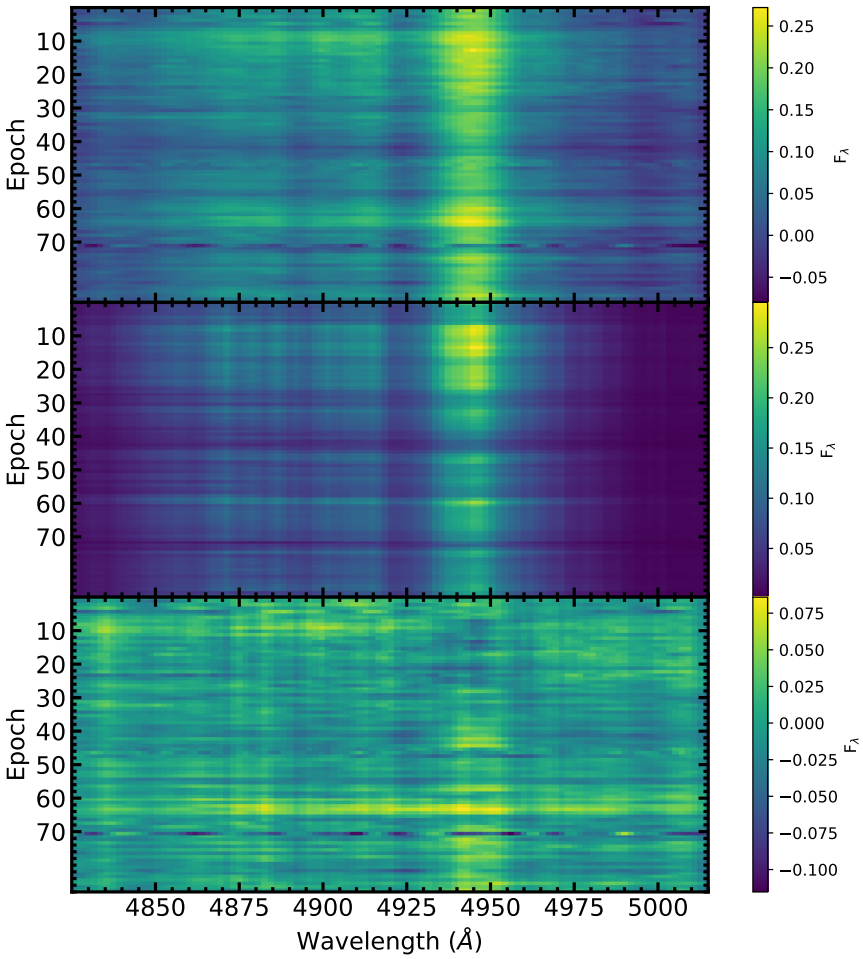

Figure 4.15: Same as Figure 4.4, but for He II in NGC 3227.

4.4.2.1 Hβ

The continuum and Hβ light curves for NGC 3227 are displayed in Figure 4.8, with the observed profiles and their associated models shown in Figure 4.9. The observed emission lines are generally well fit, with the gross variation captured by the model to the Hβ light curve in addition to the majority of the smaller variations. However, similar to Mrk 704, the preliminary models contain a higher amount of structure than the data, producing the same pattern in the residuals in the bottom panel of Figure 4.9, which will also require additional investigation. The models required a likelihood softening of $T = 10$, equivalent to increasing the uncertainties by a factor of $\sqrt{T} \sim 3$. In Figure 4.10, we display the posterior PDFs for all model parameters for both Hβ (red) and He II (blue).

The Hβ-emitting BLR geometry for NGC 3227 is found to be a thick disk, with relatively unconstrained opening and inclination angles of $\theta_o = 25.29^{+33.68}_{-16.63}$ degrees and $\theta_i = 79.04^{+9.08}_{-33.94}$ degrees. The inclination is surprisingly more edge-on than expected for a broad-lined AGN, however the uncertainties are rather large, especially on the low end. The models find a median BLR radius of $r_{\rm median} = 2.16^{+2.38}_{-1.47}$ lt-days, a minimum radial displacement from the central SMBH of $r_{\rm min} = 0.24^{+0.58}_{-0.16}$ lt-days, and radial width of $\sigma_r = 4.53^{+6.90}_{-3.46}$ lt-days. The radial positions of the particles prefer to be in a more cuspy distribution as opposed to Gaussian ($\beta = 1.14^{+0.13}_{-0.12}$). The models cannot discriminate between preferential emission towards and away from the central ionizing source ($\kappa = -0.47^{+0.96}_{-0.02}$) nor a preference between a uniform distribution of the particles or clustering towards the face of the BLR disk ($\gamma = 1.44^{+0.45}_{-0.29}$). There is, though, a constraint on a moderate amount of obscuration behind the BLR disk midplane ($\xi = 0.60^{+0.28}_{-0.41}$). A representative geometric model for the Hβ-emitting BLR for NGC 3227 is displayed in Figure 4.11.

The dynamics of the BLR in NGC 3227 are uncertain, with only $\sim$5% of the particles found to be on near-circular orbits ($f_{\rm ellip} = 0.05^{+0.07}_{-0.03}$) and an unclear preference for inflowing or outflowing orbits for the remaining particles ($f_{\rm flow} = 0.58^{+0.31}_{-0.33}$). The particle velocity distributions are rotated up to $\sim$30° toward the circular-velocity centered distribution, suggesting highly elliptical orbits

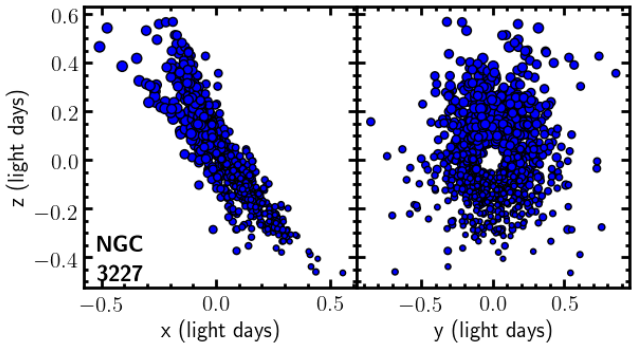

Figure 4.16: Same as Figure 4.6, but for He II in NGC 3227.

with a much higher fraction of bound orbits compared to Mrk 704. There is also a much higher contribution of macroturbulent velocities, with $\sigma_{\rm turb} = 0.066^{+0.027}_{-0.058}$.

The Hβ BLR models find a mean and median time delay of $\tau_{\rm mean} = 2.53^{+1.76}_{-1.22}$ days and $\tau_{\rm median} = 1.35^{+1.38}_{-0.50}$, in agreement with the mean time delay measured by dR18 of $\tau_{\rm cent} = 1.29^{+1.56}_{-1.27}$ days. The transfer function for a representative model is shown in Figure 4.12, which generally exhibits symmetric behavior in time delay around the line center, similar to the velocity-resolved analysis of dR18. The SMBH mass is found to be $\log_{10}(M_{\rm BH}/M_{\odot}) = 6.04^{+0.36}_{-0.53}$.

4.4.2.2 He II

The He II light curve for NGC 3227 is shown in Figure 4.14. The observed He II profiles, models generated from CARAMEL, and residuals are displayed in Figure 4.15. We again see the striping residual pattern which will be further investigated. Compared to the Hβ profiles, the S/N is much lower and the uncertainties are larger. Despite this, however, the modeled profiles are generally able to capture the gross variation trend in the light curve, including some of the smaller timescale variations. A likelihood softening of $T = 5$ was required, approximately doubling the uncertainties.

The geometry of the He II BLR is better constrained than that of the Hβ BLR model, and the disk is found to be slightly thinner than the Hβ-emitting region with an opening angle of $\theta_{\rm o} = 19.30^{+7.37}_{-5.09}$ degrees and inclination angle of $\theta_{\rm i} = 36.73^{+11.28}_{-9.36}$ degrees. As expected, the higher-ionization BLR is found to be more compact than the low-ionization Hβ BLR, with mean and median radii of $r_{\rm mean} = 0.50^{+0.55}_{-0.29}$ lt-days and $r_{\rm median} = 0.43^{+0.50}_{-0.25}$ lt-days. The disk has a minimum

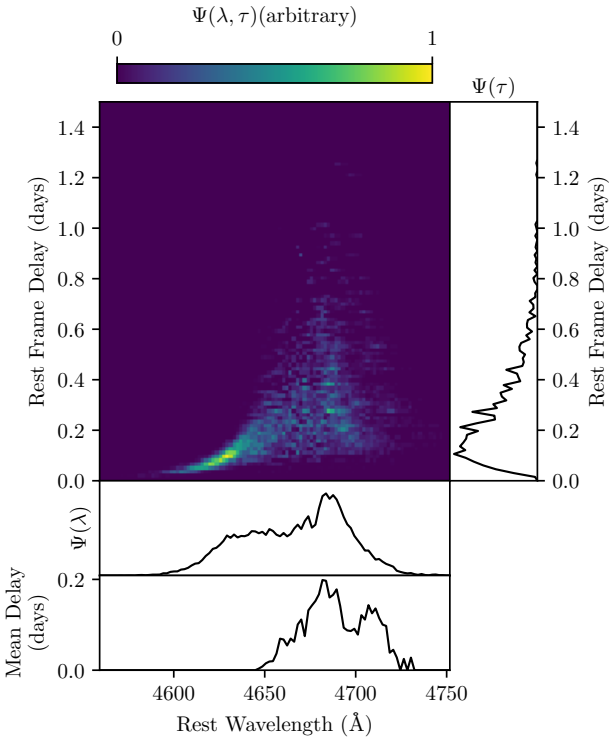

Figure 4.17: Same as Figure 4.7, but for He II in NGC 3227.

inner radius of $r_{\rm min} = 0.08^{+0.21}_{-0.07}$ lt-days, along with a width of $\sigma_{\rm r} = 0.28^{+0.69}_{-0.17}$ lt-days. While there is a strong preference for the particles to have radial positions drawn from a Gaussian distributions ($\beta = 0.73^{+0.30}_{-0.14}$), the posterior PDF shows solutions up to $\beta \sim 1.5$, which corresponds to a cuspy distribution. Preferential emission is well constrained to radiate back towards the central source ($\kappa = -0.24^{+0.05}_{-0.08}$) in addition to near total obscuration along the midplane ($\xi = 0.06^{+0.08}_{-0.05}$). There is a slight preference for a clustering of particles near the disk face ($\gamma = 1.75^{+0.19}_{-0.29}$). A representative geometric model for the He II-emitting BLR is shown in Figure 4.16.

The He II BLR dynamics in NGC 3227 seem to be largely comprised of outflowing motion ($f_{\rm flow} = 0.76^{+0.16}_{-0.17}$) with very few of the particles on near-circular orbits ($f_{\rm ellip} = 0.02^{+0.03}_{-0.02}$). The velocity distribution is rotated $\theta_{\rm e} = 12.6^{+6.5}_{-7.4}$ degrees towards circular velocities, suggesting that while most outflowing orbits are unbound, there is a significant fraction of bound outflowing motions. The models also find a near-negligible contribution from macroturbulent velocities ($\sigma_{\rm turb} = 0.009^{+0.018}_{-0.006}$).

The mean and median time delays for the He II BLR are constrained to be $\tau_{\rm mean} = 0.47^{+0.52}_{-0.27}$ days and $\tau_{\rm median} = 0.37^{+0.40}_{-0.21}$ days. We have previously been able to compare the time delays of our Hβ BLR models to those measured by dR18, however they did not explore the He II emission in their spectra. While our representative transfer function for Hβ was found to be generally symmetric, the representative He II transfer function (displayed in Figure 4.17) exhibits a stronger response and shorter time delays on the blueshifted side compared to the redshifted side. This signature is the opposite of what was seen in Hβ for Mrk 704, and is often interpreted as evidence for outflow. The black hole mass is constrained to be $\log_{10}(M_{\rm BH}/M_{\odot}) = 5.86^{+0.30}_{-0.35}$, consistent within the uncertainties with the mass predicted by the Hβ models.

4.4.3 *NGC 3516*

The continuum and Hβ light curves for NGC 3516 are shown in the top and middle panel of Figure 4.18, with two example observations and their models in the bottom panel. The modeled emission lines are able to fit the gross trend of the data, but are not able to capture the smaller-scale variations, as shown in the modeled profiles and residuals in the middle and bottom panels in Figure 4.19. Additionally, as with the previous targets, there is more structure in the modeled light curve than the data, most likely the cause for the striping pattern in the residuals. There is also more noise present here than in the light curve presented by dR18, which will require careful examination of the fits to the spectra described in Section 4.2.3. The continuum data (and continuum models) prefer an increase in flux towards the end of the observations, and the resultant emission line models are predicting a rise in flux as a response to the driving continuum model in disagreement with the last few measurements of Hβ emission. The models required a likelihood softening of $T = 35$, or an increase to the uncertainties by a factor of $\sqrt{T} \sim 6$, and the posterior PDFs for all model parameters are displayed in Figure 4.20.

These preliminary models prefer a BLR geometry closer to a sphere than a disk, with a large opening angle of $\theta_{\rm o} = 85.56^{+2.98}_{-8.87}$ degrees and moderate inclination of $\theta_{\rm i} = 30.12^{+7.18}_{-8.04}$ degrees. The BLR has a median radius of $r_{\rm median} = 11.22^{+2.53}_{-4.56}$ lt-days, inner radial displacement from the central black

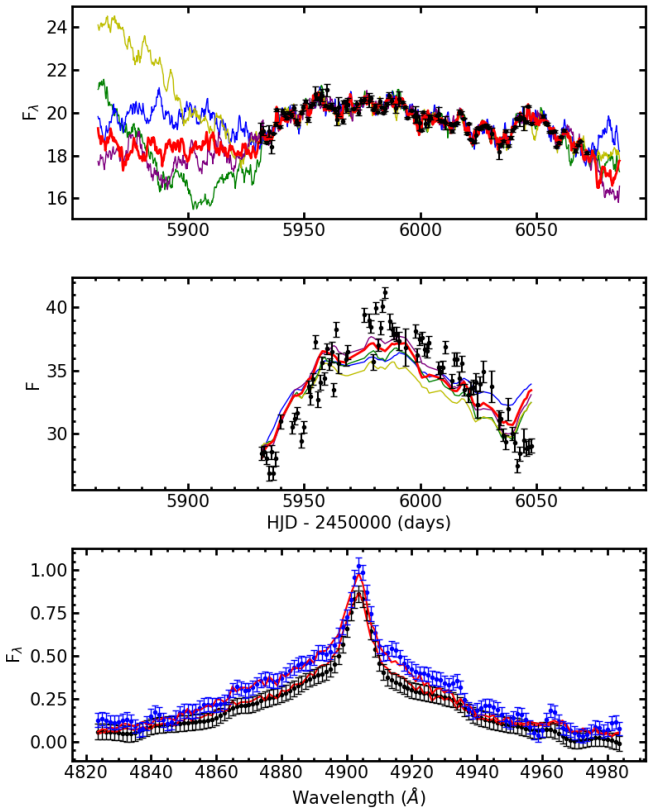

Figure 4.18: Same as Figure 4.3, but for Hβ in NGC 3516.

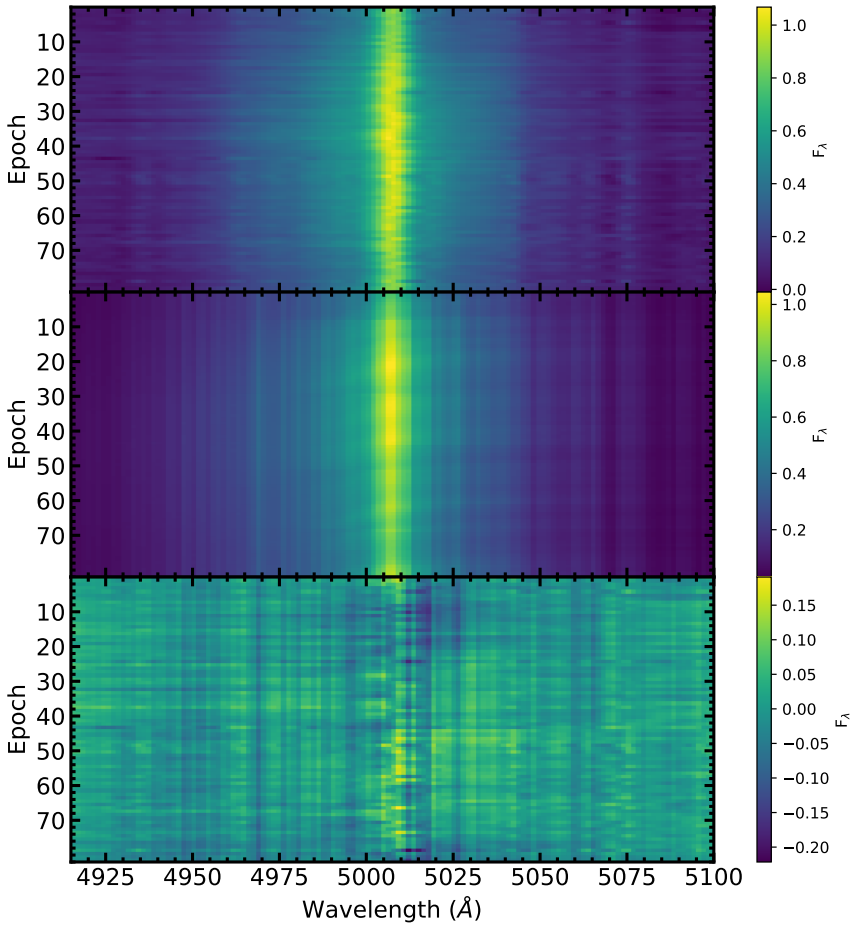

Figure 4.19: Same as Figure 4.4, but for Hβ in NGC 3516.

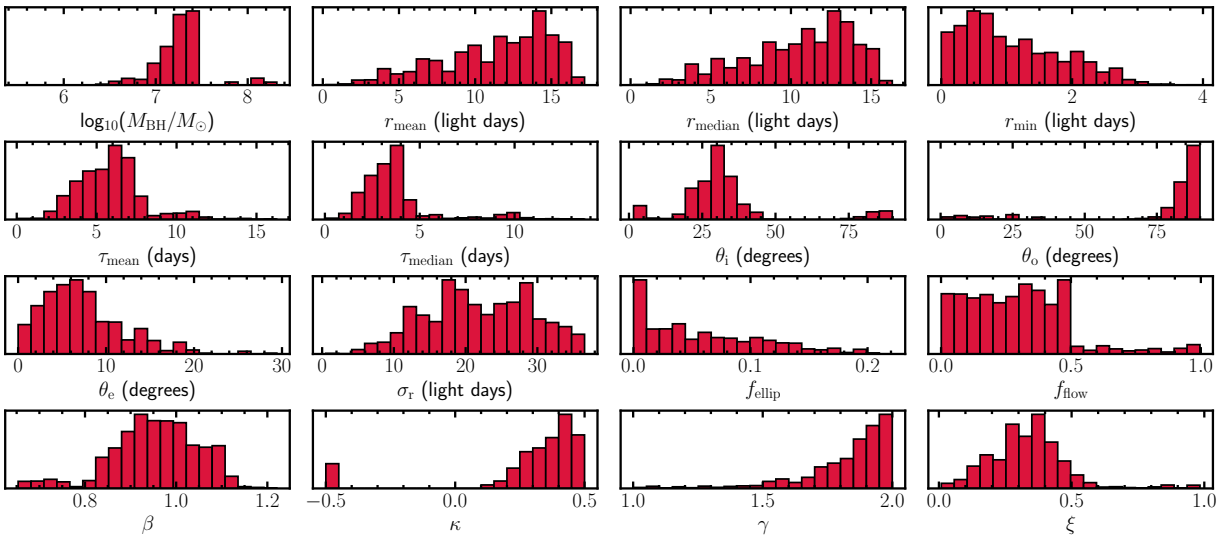

Figure 4.20: Same as Figure 4.5, but for Hβ in NGC 3516.

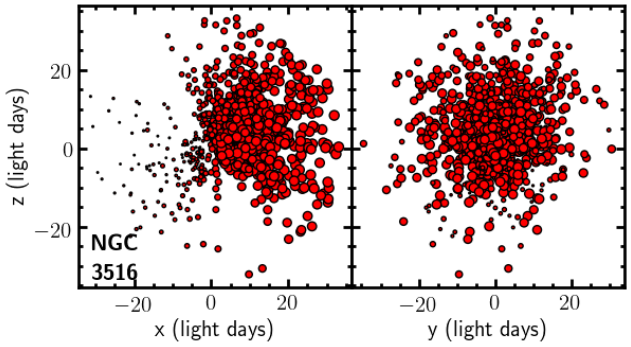

Figure 4.21: Same as Figure 4.6, but for Hβ in NGC 3516

.

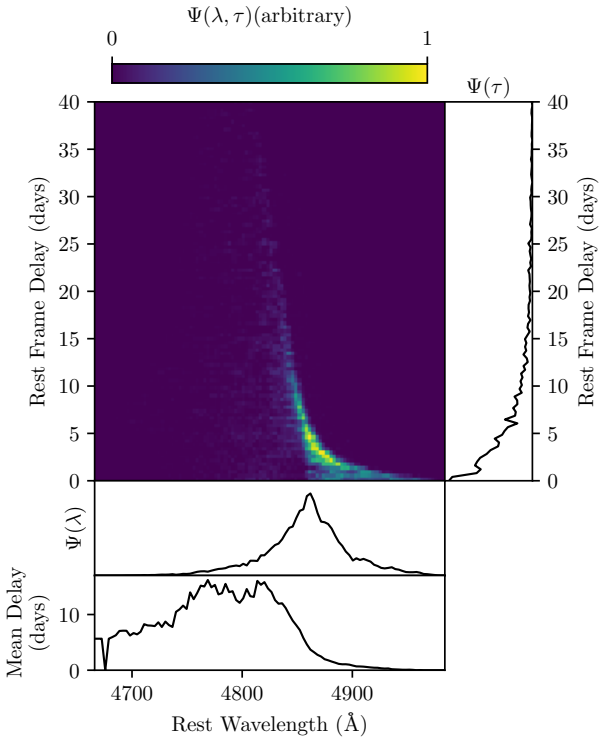

Figure 4.22: Same as Figure 4.7, but for Hβ in NGC 3516.

hole of $r_{\rm min} = 0.91^{+1.10}_{-0.58}$ lt-days, and radial width of $\sigma_{\rm r} = 21.61^{+8.13}_{-8.02}$ lt-days. The BLR particles have radial positions that are well constrained to be drawn from an exponential distribution ($\beta = 0.96^{+0.09}_{-0.09}$) and have a strong preference for clustering near the face of the disk ($\gamma = 1.88^{+0.08}_{-0.18}$). There is also a strong preference for the particles to emit away from the black hole, i.e. preferential emission from the near side of the BLR ($\kappa = 0.38^{+0.07}_{-0.14}$), and for moderate obscuration along the midplane of the disk ($\xi = 0.33^{+0.11}_{-0.14}$). A representative geometric BLR model for NGC 3516 is shown in Figure 4.21.

The dynamics constrained by the preliminary models find $\sim$5% of the particles in the BLR of NGC 3516 are on near-circular orbits, although solutions of up to $\sim$20% are not ruled out in the full posterior PDF. The remaining particles have a strong preference for inflowing motions ($f_{\rm flow} = 0.28^{+0.18}_{-0.19}$), with a modest contribution of macroturbulent velocities ($\sigma_{\rm turb} = 0.021^{+0.024}_{-0.017}$). The inflowing orbits have velocities drawn from a distribution rotated at a small angle of $\theta_{\rm e} = 6.7^{+5.0}_{-3.7}$ degrees away from escape velocity, though the full posterior PDF exhibits solutions of up to $\sim$20°, suggesting that most particles are on highly elliptical, unbound, inflowing orbits.

The mean and median time delays are relatively well constrained and found to be $\tau_{\rm mean} = 5.82^{+1.34}_{-1.93}$ days and $\tau_{\rm median} = 3.41^{+0.92}_{-1.22}$ days, which agree very well with the time lag measurement from dR18 of $\tau_{\rm cent} = 5.74^{+2.26}_{-2.04}$ days. A representative transfer function is displayed in Figure 4.22, and shows a heavier response and shorter time delays in the blue wing with a weaker response in the red wing. This lag signature appears to be the reverse of what was found by dR18, and will be carefully investigated. The black hole mass is constrained to be $\log_{10}(M_{\rm BH}/M_{\odot}) = 7.28^{+0.10}_{-0.24}$.

4.4.4 *NGC 4151*

As with NGC 3227, we were able to model the geometry and kinematics of the low and high-ionization BLRs in NGC 4151, and we discuss the results below.

4.4.4.1 Hβ

Both the continuum and emission-line light curves of NGC 4151 show the strongest variability over the course of the observing campaign compared to the other targets in this study. The light curves are shown in the top two panels of Figure 4.23, with two example spectra and the associated models in the bottom panel. Nightly Hβ observations, model profiles, and residuals are displayed in Figure 4.24. Generally, these preliminary models fit the overall trend of the light curve, though we again see the striping signature in the residuals, requiring further investigation. Similar to NGC 3516, we find a deviation of the models away from the Hβ data points at the end of and towards the midpoint of the observations. Because the spectral monitoring was conducted by several observatories, we investigated any significant change to the model results by limiting the spectroscopy to one observatory. We conducted a model run using only data from MDM, as it is the dominant contributor of the spectral data (73/112 total spectra), and found no significant changes. A likelihood softening of $T = 100$ was required for the modeling process, equivalent to applying a scale factor of $\sqrt{T} = 10$ to the uncertainties. The posterior PDFs for all the model parameters are displayed in Figure 4.25, with Hβ posteriors in red and He II posteriors in blue.

The preliminary models of the Hβ emission do not find a well-constrained geometry. The BLR exhibits a very thick disk, with an opening angle of $\theta_o = 70.64^{+12.98}_{-14.97}$ degrees, however the full posterior PDF includes solutions down to $\sim$30°. The models also find a very face-on inclination angle of $\theta_i = 11.24^{+5.55}_{-4.62}$ degrees. The radial width is largely unconstrained ($\sigma_r = 28.27^{+19.58}_{-13.59}$ lt-days), while there are slightly better constraints found for the minimum radius away from the central SMBH ($r_{min} = 0.29^{+0.26}_{-0.24}$lt-days), and median radius ($r_{median} = 2.67^{+1.45}_{-1.21}$lt-days). The BLR particles show a strong preference both for radial positions to be drawn from a cuspy profile ($\beta = 1.60^{+0.13}_{-0.09}$) and clustering towards the face of the BLR ($\gamma = 1.87^{+0.10}_{-0.17}$). There does not seem to be a strong indication of preferential emission towards or away from the central ionization source with $\kappa = 0.12^{+0.14}_{-0.14}$, while the models prefer small to moderate obscuration of the BLR along the disk midplane ($\xi = 0.49^{+0.10}_{-0.11}$). A representative geometric model for NGC 4151 is displayed in Figure 4.26.

The dynamics of the Hβ-emitting BLR are also generally unconstrained by the preliminary models. Roughly $\sim$5% of the particles are found to be on nearly circular orbits ($f_{ellip} = 0.04^{+0.05}_{-0.03}$). The remaining orbits are dominated by inflow, with few solutions found for outflowing motions ($f_{flow} = 0.24^{+0.18}_{-0.16}$). The distribution of inflowing orbits are found to be rotated $\theta_e = 14.4^{+8.1}_{-8.0}$ degrees away from the escape velocity of the black hole and towards a circular velocity-centered distribution, however the full posterior shows solutions to nearly $\sim$30 degrees. While most of the BLR particles might be on highly elliptical, inflowing orbits, the fraction of orbits that are bound is unclear.

The Hβ BLR models find mean and median time delays of $\tau_{mean} = 3.36^{+1.49}_{-1.47}$ days and $\tau_{median} = 1.37^{+0.92}_{-0.64}$ days, slightly shorter than the mean time delay found by dR18 from the cross-correlation measurement of $\tau_{cent} = 6.82^{+0.48}_{-0.57}$ days. However, the full posteriors PDFs show large ranges of solutions for the time delays, with the mean τ showing solutions up to $\sim$6 days. The representative transfer function is displayed in Figure 4.27, where the model finds a much stronger response in the red wing than in the blue wing, and also find a generally symmetric behavior of lags as a function of wavelength. This is inconsistent with the analysis of dR18, as the models prefer the majority of the particles to be on inflowing trajectories whereas dR18 found a clear virial-like pattern, suggesting

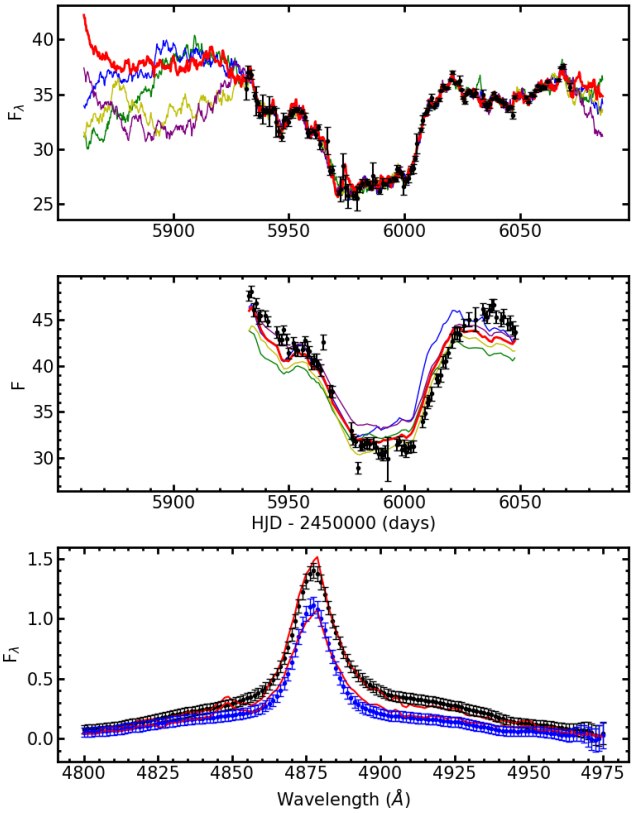

Figure 4.23: Same as Figure 4.3, but for Hβ in NGC 4151.

rotation as the dominant kinematic signature rather than inflow/outflow. The black hole mass is constrained to be $\log_{10}(M_{\rm BH}/M_\odot) = 6.48^{+0.24}_{-0.27}$.

4.4.4.2 He II

The He II light curve is displayed in Figure 4.28, while the observed profiles, generated models, and residuals are displayed in Figure 4.29. The preliminary models are generally able to capture the main variations of the observations, but the common striping pattern appears in the residuals here as well, requiring further examination. Similar to NGC 3227, the He II emission profiles for NGC 4151 have much lower S/N than the Hβ profiles. The models required a likelihood softening of $T = 165$, equivalent to increasing the uncertainties by a factor of $\sqrt{T} \sim 13$.

The geometry of the high-ionization BLR in NGC 4151 is indicative of a very thick disk, with an opening angle $\theta_{\rm o} = 70.64^{+12.98}_{-14.97}$ degrees and an extremely face-on orientation of $\theta_{\rm i} = 6.31^{+3.89}_{-3.15}$ degrees.

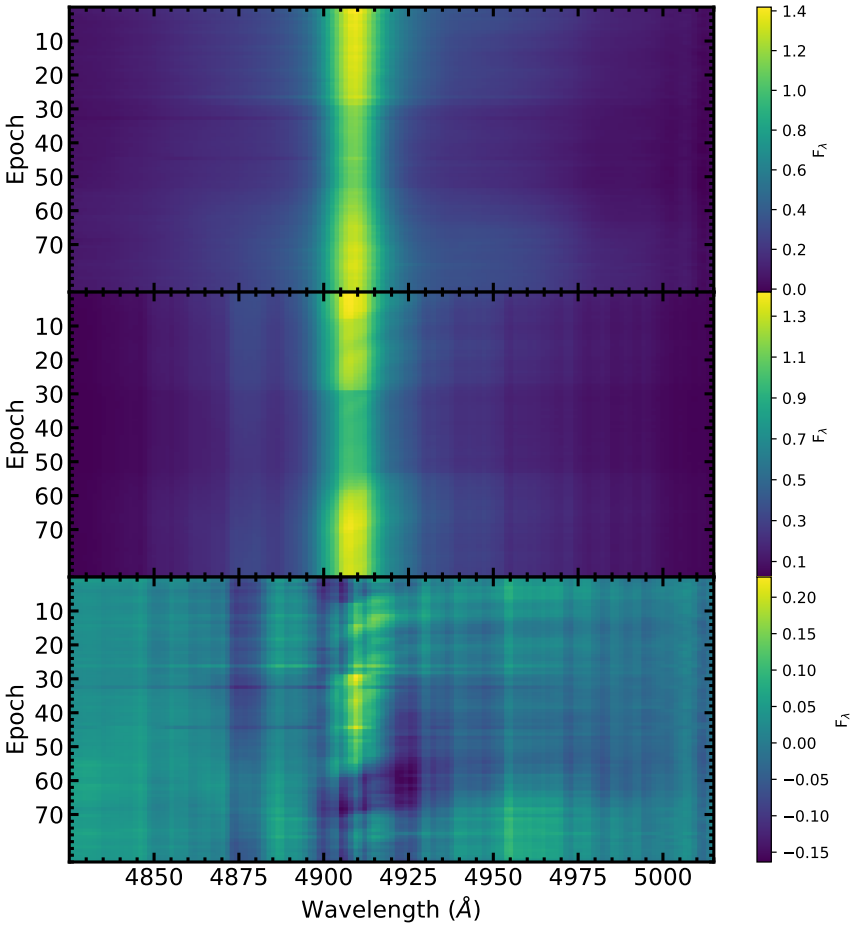

Figure 4.24: Same as Figure 4.4, but for Hβ in NGC 4151.

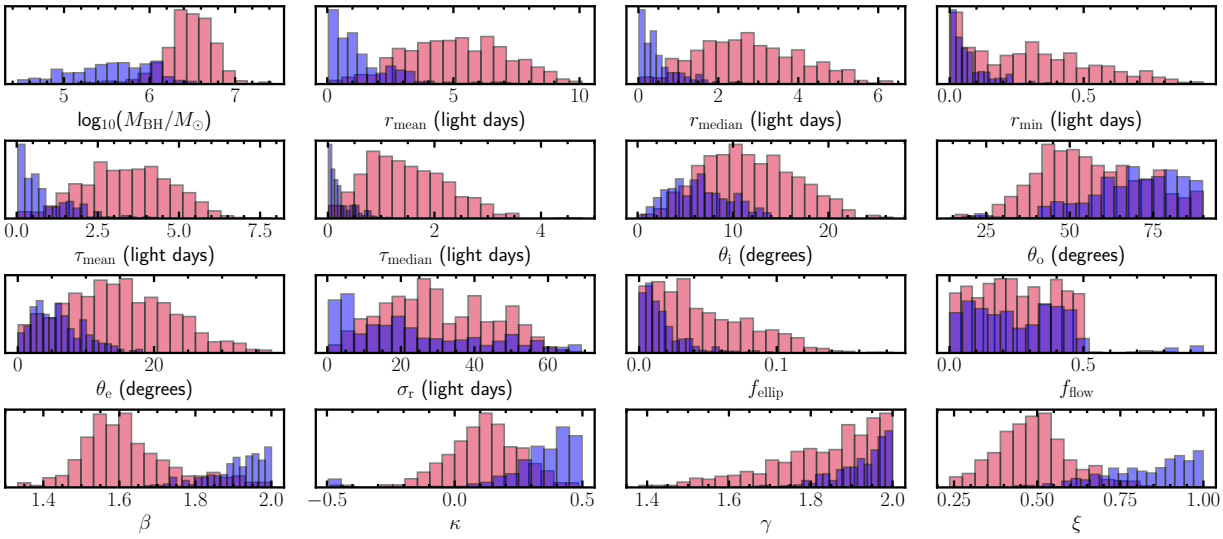

Figure 4.25: Same as Figure 4.5, but for the Hβ (red) and He II (blue) lines of NGC 4151.

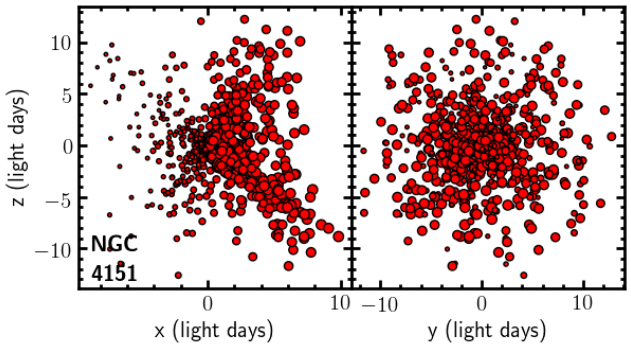

Figure 4.26: Same as Figure 4.6, but for Hβ in NGC 4151.

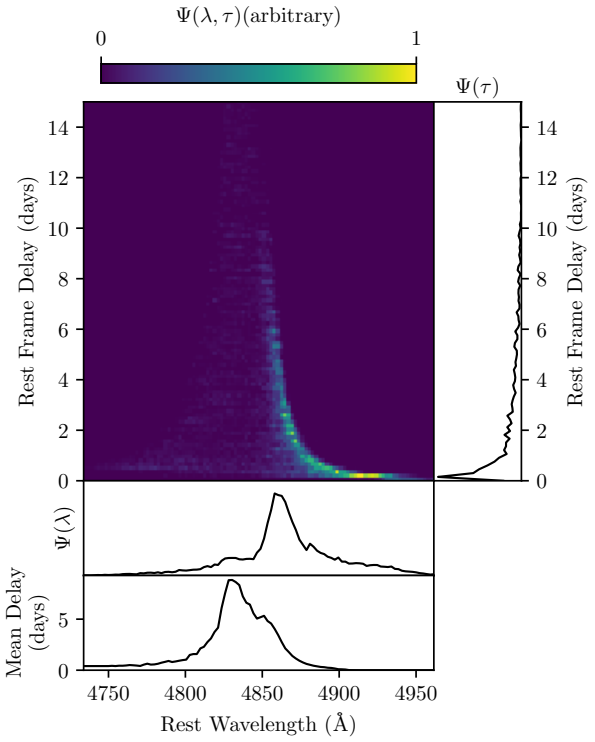

Figure 4.27: Same as Figure 4.7, but for Hβ in NGC 4151.

The He II-emitting BLR is found to be more compact than the Hβ-emitting region, as expected, with a median radius $r_{\rm median} = 0.37^{+0.61}_{-0.27}$, minimum inner radius of $r_{\rm min} = 0.05^{+0.08}_{-0.04}$, and a relatively unconstrained radial width of $\sigma_{\rm r} = 18.71^{+28.01}_{-14.50}$. There is a strong preference for the radial positions of the particles to be drawn from a cuspy distribution ($\beta = 1.92^{+0.06}_{-0.09}$) and for the direction of He II emission to be away from the central black hole (preferential emission from the near side of the BLR; $\kappa = 0.38^{+0.08}_{-0.13}$). The models also find preferential emission from the BLR face ($\gamma = 1.94^{+0.04}_{-0.09}$) and very little obscuration of the disk along the BLR midplane ($\xi = 0.86^{+0.10}_{-0.17}$).

The dynamics of the high-ionization BLR are well constrained by the preliminary models to be dominated by inflow ($f_{\rm flow} = 0.24^{+0.19}_{-0.17}$), with effectively none of the particles moving on near-circular orbits ($f_{\rm ellip} = 0.01^{+0.02}_{-0.01}$). The models also find a small but nonzero contribution of macroturbulent velocities, with ($\sigma_{\rm turb} = 0.010^{+0.035}_{-0.008}$). The velocities of the inflowing orbits, which appear to comprise the majority of orbits in the He II-emitting BLR, are found to be drawn from a distribution rotated only $\theta_{\rm e} = 5.5^{+4.2}_{-3.3}$ degrees away from the radial escape velocity of the central SMBH. This suggests

that the majority of particles are truly on inflowing orbital paths, rather than highly elliptical bound orbits.

The models to He II find a mean and median time delay $\tau_{\rm mean} = 0.58^{+1.09}_{-0.42}$ days and $\tau_{\rm median} = 0.16^{+0.33}_{-0.11}$ days. A representative transfer function is shown in Figure 4.31, where we find similar behavior to Hβ in a heavier response in the red wing than in the blue wing. The SMBH mass is found to be $\log_{10}(M_{\rm BH}/M_{\odot}) = 5.60^{+0.45}_{-0.58}$.

4.4.5 *NGC 5548*

The continuum and Hβ light curves for NGC 5548 are displayed in the top two panels of Figure 4.32, with two examples of observed emission line profiles with respective models overplotted. The averaged spectra for each night of observation, the model emission line profiles, and residuals are shown in Figure 4.33. In general, the observations are very well fit by the preliminary models to the Hβ light curve, with the gross variations captured as well as the handful of small-scale variations present in the data. However, like all previous objects, the preliminary models exhibit more structure or noise than the data, which is reflected in the striping pattern in the residual. The models required a likelihood softening of $T = 25$, or a scaling of the uncertainties by a factor of $\sqrt{T} = 5$, and the full posterior PDFs for all model parameters are shown in Figure 4.34.

The Hβ-emitting BLR geometry is found to be a thick disk with opening angle $\theta_{\rm o} = 17.21^{+17.47}_{-8.70}$ degrees and a surprisingly more edge-on inclination of $\theta_{\rm i} = 73.63^{+11.37}_{-19.39}$ degrees. Like NGC 3227, the uncertainties on inclination angle are rather large, specifically on the low end, with the full posterior PDF including solutions as low as $\sim$40°. The median radius is constrained to be $r_{\rm median} = 3.53^{+1.84}_{-1.93}$ lt-days, with a minimum radial displacement from the ionization source of $r_{\rm min} = 0.89^{+0.75}_{-0.65}$ lt-days, and a radial size of $\sigma_{\rm r} = 15.55^{+10.02}_{-8.15}$ lt-days. The models exhibit a strong preference for the radial positions of the particles to be drawn from a cuspy distribution profile ($\beta = 1.49^{+0.07}_{-0.11}$). However, the models cannot discriminate between preferential emission towards or away from the SMBH (where κ ranges from −0.46 to 0.47), preferential emission distributed uniformly or from the faces of the BLR disk ($\gamma = 1.32^{+0.49}_{-0.25}$), or the amount of obscuration along the midplane ($\xi = 0.69^{+0.20}_{-0.47}$), with the

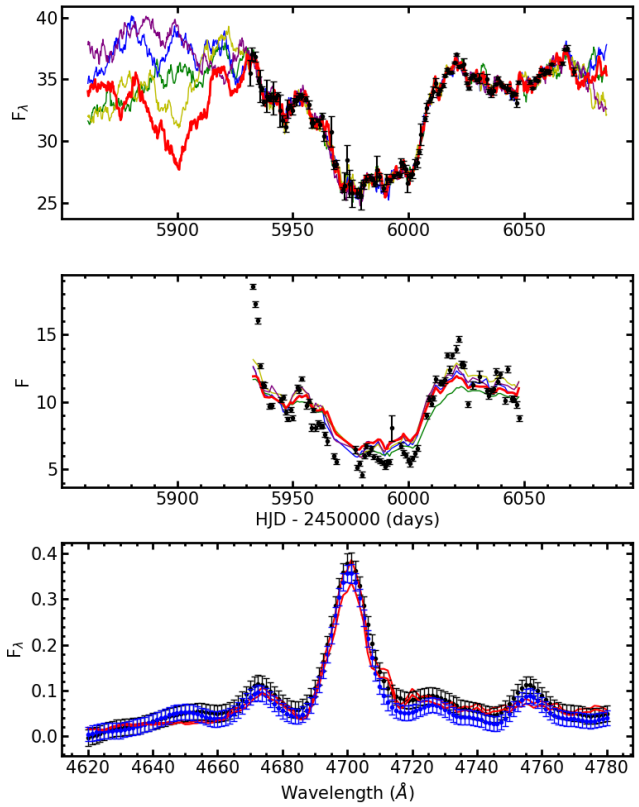

Figure 4.28: Same as Figure 4.3, but for He II in NGC 4151.

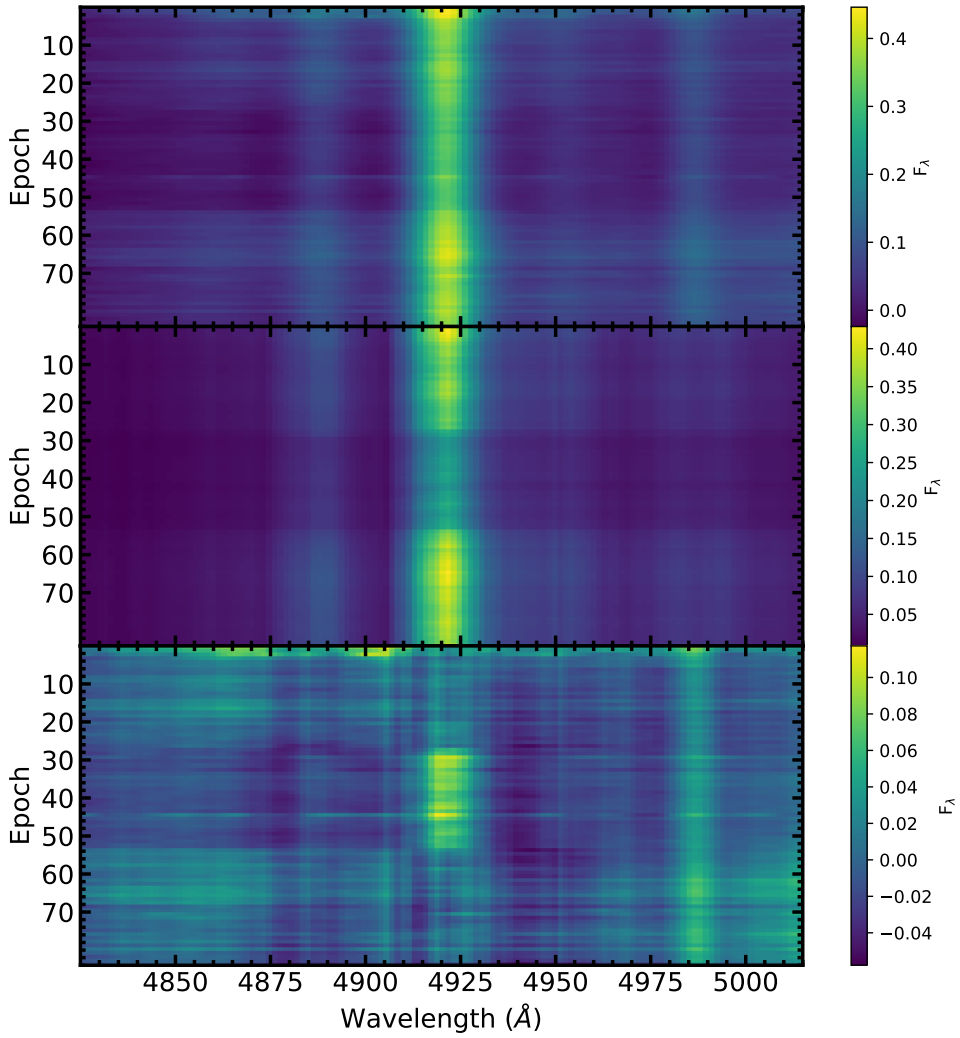

Figure 4.29: Same as Figure 4.4, but for He II in NGC 4151.

full posterior displaying solutions at all possible values of ξ. A representative geometry for the Hβ-emitting BLR of NGC 5548 is displayed in Figure 4.36.

The dynamics of the BLR of NGC 5548 are also not very well constrained in these preliminary models. Approximately 0-8% of the particles exhibit near circular orbits with the remaining fraction of particles showing a slight preference of outflowing motion ($f_{\rm flow} = 0.61^{+0.23}_{-0.43}$), however the posterior PDF shows solutions for both inflowing and outflowing orbits. The full posterior PDF also shows the orbital velocities of the particles being drawn from a distribution rotated between $\sim$0-45° away from the radial escape velocity and towards circular velocity. Whether the majority of the particle orbits are inflowing or outflowing, or whether they are bound or unbound, remains unclear from the results of these preliminary models.

Finally, the models constrain mean and median time lags of $\tau_{\rm mean} = 4.51^{+4.55}_{-2.07}$ days and $\tau_{\rm median} = 2.16^{+2.55}_{-0.87}$ days. The velocity-resolved RM analysis of dR18 measured a mean time lag of $\tau_{\rm cent} = 2.83^{+0.88}_{-0.96}$ days, consistent with our findings to within the large uncertainties. The transfer function for a representative model for NGC 5548 is shown in Figure 4.35. We find a generally symmetric responsivity and lag behavior as a function of wavelength, similar to the analysis of dR18. The black hole mass is constrained to be $\log_{10}(M_{\rm BH}/M_{\odot}) = 6.97^{+0.22}_{-0.40}$.

4.5 *Discussion*

With the preliminary models in hand, we can examine the results in light of previous findings. These include previous CARAMEL results in the case of NGC 5548, independent $M_{\rm BH}$ measurements for NGC 3227 and NGC 4151, and other works which sought to infer the inclinations of select AGNs in this study. We also compare the constraints on the low and high-ionization BLRs for NGC 3227 and NGC 4151, including joint constraints on $M_{\rm BH}$ and inclination angle. Finally, with the derived black hole masses, we can infer individual f factors for each AGN and place them in the context of the population average $\langle f \rangle$ yielded from the compilation of CARAMEL modeling results.

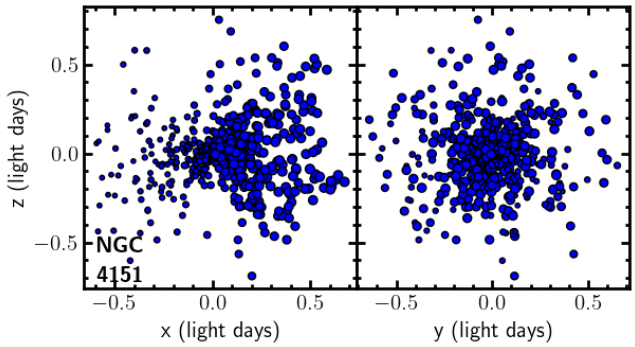

Figure 4.30: Same as Figure 4.6, but for He II in NGC 4151.

4.5.1 *Low and High Ionization BLRs*

The Hβ and He II emission lines for NGC 3227 and NGC 4151 are produced from the same respective nucleus, and though independent models were conducted for each emission line, a number of the derived parameters should agree. In particular, $M_{\rm BH}$ should be the same no matter the emission line. The inclination and opening angles might be reasonably expected to agree as well, as the emission is likely arising from different parts of a single large structure. We compare and contrast the model results of the low and high-ionization BLRs in both AGNs below.

4.5.1.1 NGC 3227

As expected, we find significant overlap in the solutions for $M_{\rm BH}$ from the Hβ and He II models, as shown in Figure 4.10. We follow the prescription of Williams et al. (2020) for calculating the joint inference on the mass. We approximated each posterior PDF with a Gaussian density kernel, then multiplied the two kernels together and normalized the final joint constraint. The result is shown in Figure 4.37, and the joint inference on $M_{\rm BH}$ is found to be $\log_{10}(M_{\rm BH}/M_{\odot}) = 5.86^{+0.40}_{-0.20}$.

Figure 4.38 shows representative models of the Hβ (red) and He II (blue) geometry plotted on the same scale. Although most of the geometric parameters of the low-ionization BLR are not well constrained, it is clear that the high-ionization BLR is significantly more compact and closer to the central ionization source than the low-ionization region. This agrees with the results of Williams et al. (2020) and Bentz et al. (2021), where the higher-ionization regions (probed by Lyα and C IV

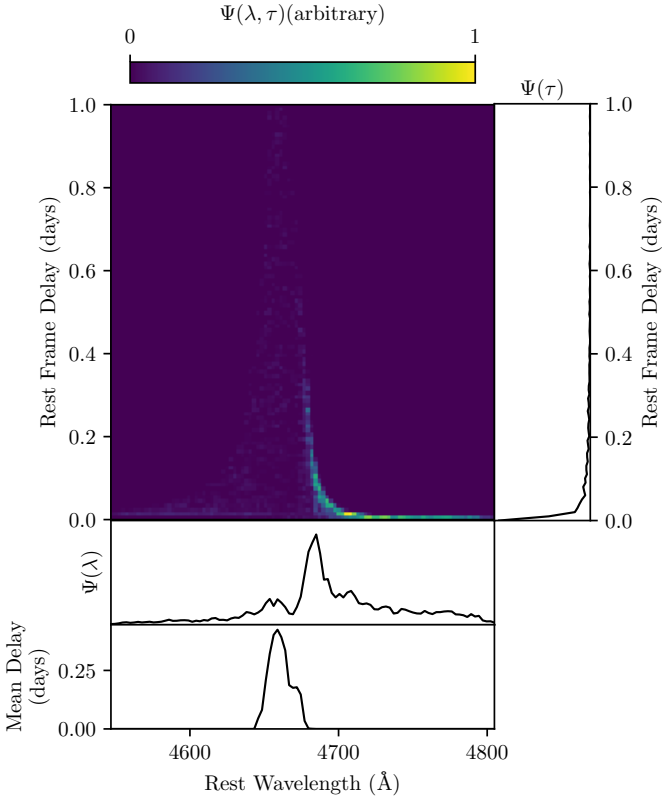

Figure 4.31: Same as Figure 4.7, but for He II in NGC 4151.

for the former and He II for the latter) were found to be more compact than the Hβ BLR. While there is overlap between the posterior PDFs of $r_{\rm mean}$, $r_{\rm median}$, and $r_{\rm min}$, the large uncertainties on the values for Hβ prevent the assertion of any true, physical overlap of the two regions. It is also unclear if there is a true difference in the opening angles between the two regions, as the higher ionization region is well constrained be a thinner disk with an opening angle of $\sim$20°, whereas the models to the low ionization region find solutions at a larger range of possible opening angles. Such a difference in opening angle could be indicative of a flared disk structure (see Figure 12 of Bentz et al. 2021). There is slight evidence for a misalignment between the two disks, where the He II region prefers a more face-on inclination angle than the Hβ region. However, the full posterior PDF of the inclination angle of the Hβ BLR shows solutions near $\sim$20°, and the formal uncertainties on $\theta_{\rm i}$ places the possible inclination between $\sim$45–90°, again hindering an inference on any true misalignment. The joint constraint on the inclination using both the low and high ionization constraints is found to be 30°, however it is possible that the inclinations of the two regions are truly different, as might be found for a warped disk, for example.

The models of the Hβ and He II-emitting regions predict nearly the same, small fraction of particles with near-circular orbits, and while there is no constraint on a preference for inflowing or outflowing orbits in the low ionization region, the high ionization region appears to be dominated by outflow, with no solutions found for inflowing orbits. This same behavior was found for NGC 3783 by Bentz et al. (2021) using the same emission lines, though Williams et al. (2020) found that the dominant direction of flowing motions in NGC 5548 probed through both the Lyα and C IV lines were largely undetermined.

4.5.1.2 NGC 4151

We find overlap in the posterior PDFs of $M_{\rm BH}$ constraints from the models to Hβ and He II, though only in the tails of the distributions as compared to NGC 3227, which exhibits significant overlap of the PDFs. We again follow the prescription of Williams et al. (2020) for estimating the joint

inference on the mass. The result is displayed in Figure 4.39, and the joint mass constraint is found to be $\log_{10}(M_{\rm BH}/M_{\odot}) = 6.16^{+0.20}_{-0.20}$.

Figure 4.40 displays the representative geometric models of Hβ (red) and He II (blue) plotted on the same scale. As we have discussed, the geometric parameters of the BLR in NGC 4151 are largely unconstrained. However, it is clear that the He II-emitting region is more compact than the lower ionization region, as expected and in agreement with the results of Williams et al. (2020) and Bentz et al. (2021). The He II-emitting region shows a slight preference to be more "puffed up" than the Hβ-emitting region, with a median opening angle of 70° compared to 60°, however, the opening angle of the low-ionization BLR is largely unconstrained. The inclinations of the two regions are also predicted to generally be the same ($\theta_{\rm i} \sim 11°$ for Hβ and $\theta_{\rm i} \sim 6°$ for He II), with a stronger preference of slightly more face-on inclinations for He II. A joint constraint on the inclination from both models gives $\theta_{\rm i} = 7.58^{+3.03}_{-2.73}$ degrees.

There seems to be fewer He II-emitting particles on near-circular orbits compared to Hβ, with the remaining particles dominated by inflowing motions through both the low and high-ionization regions. While the velocities of the Hβ-emitting particles are predicted to generally be drawn from a distribution centered between ∼0–30 degrees away from escape velocity, the He II-emitting particles exhibit a preference for velocities very near the escape velocity of the black hole. This suggests that the low-ionization BLR might be composed of more particles on highly elliptical but bound orbits, while the high-ionization region may be comprised of unbound inflowing orbits.

4.5.2 *Previous* CARAMEL *Results*

NGC 5548 is the only AGN in our sample that has previously been modeled with CARAMEL. Pancoast et al. (2014b, hereafter P14) modeled data from the Lick AGN Monitoring Project 2008 (LAMP; Bentz et al. 2009b), and Williams et al. (2020, hereafter W20) modeled data from the AGN Space Telescope and Optical Reverberation Mapping (AGN STORM; De Rosa et al. 2015; Fausnaugh et al. 2016) 2014 campaign. Both studies included modeling of the Hβ-emitting BLR in NGC 5548, with P14 employing Johnson $B-$ and $V-$bands as the driving continuum and W20 using

both the UV and $V-$band as the continuum light curve. We specifically compare our results to the $V-$band-based Hβ models of both studies.

P14 found the Hβ-emitting BLR in NGC 5548 to be a thick disk, constraining an opening angle of $\theta_{\rm o} = 27.4^{+10.6}_{8.4}$ degrees and inclination angle of $\theta_{\rm i} = 38.8^{+12.1}_{11.4}$ degrees. The mean radius was found to be $r_{\rm mean} = 3.31^{+0.66}_{0.61}$ lt-days, with minimum radial displacement away from the SMBH of $r_{\rm min} = 1.39^{+0.80}_{1.01}$ lt-days, and radial width $\sigma_{\rm r} = 1.50^{+0.73}_{0.60}$ lt-days. They found the radial positions of particles were drawn from a distribution between exponential and Gaussian ($\beta = 0.80^{+0.60}_{-0.31}$) and generally equal concentration of emission through the BLR disk ($\gamma = 2.01^{+1.78}_{-0.71}$, where γ could range from 1-5; Williams et al. 2022, in prep). Additionally, their models exhibited preference for moderate obscuration along the midplane ($\xi = 0.34^{+0.11}_{-0.18}$) and preferential emission back towards the source ($\kappa = -0.24^{+0.06}_{-0.13}$). The dynamics were found to be predominantly inflow, ($f_{\rm flow} = 0.25^{+0.21}_{0.16}$) with a moderate fraction of particles on near-circular orbits ($f_{\rm ellip} = 0.23^{+0.15}_{0.15}$) and only a small contribution from macroturbulent velocities ($\sigma_{\rm turb} = 0.016^{+0.044}_{0.013}$). The particles on inflowing orbits were found to be mostly bound, with velocities drawn from a distribution rotated $\theta_{\rm e} = 21.3^{+21.4}_{14.7}$ degrees towards circular velocities. Finally, the black hole was constrained to be $\log_{10}(M_{\rm BH}/M_{\odot}) = 7.51^{+0.23}_{0.14}$, which agrees well with the traditional RM measurement of $\log_{10}(M_{\rm BH}/M_{\odot}) = 7.39 \pm 0.14$ from dR18.

The modeling results of the Hβ-emitting BLR using the $V-$band continuum of W20 were found to be mostly consistent with those reported by P14. Specifically, the BLR was again found to be a thick disk ($\theta_{\rm o} = 38.6^{+14.0}_{13.5}$ degrees) inclined at an angle of $\theta_{\rm i} = 47.3^{+13.0}_{15.8}$ degrees. The mean and median BLR radii were constrained as $r_{\rm mean} = 8.0^{+4.3}_{-2.6}$ lt-days and $r_{\rm median} = 6.1^{+2.1}_{-3.7}$ lt-days, with the minimum radial displacement from the central black hole of $r_{\rm min} = 2.38^{+1.96}_{-0.99}$ lt-days. Preferences were shown for the radial positions of the particles to be drawn from a near-exponential profile ($\beta = 1.12^{+0.22}_{-0.18}$), isotropic emission of the BLR particles ($\kappa = 0.01^{+0.09}_{-0.07}$), and mild obscuration about the midplane ($\xi = 0.17^{+0.21}_{-0.12}$), however their spatial distribution was not well constrained ($\gamma = 3.0^{+1.3}_{-1.3}$). Approximately 30% of the particles were found to be on near-circular orbits ($f_{\rm ellip} = 0.29^{+0.18}_{-0.20}$), with the remaining particles exhibiting strong preference for outflow ($f_{\rm flow} = 0.73^{+0.18}_{-0.17}$), however most of the orbits were constrained to be bound. A small but nonzero contribution of macroturbulent

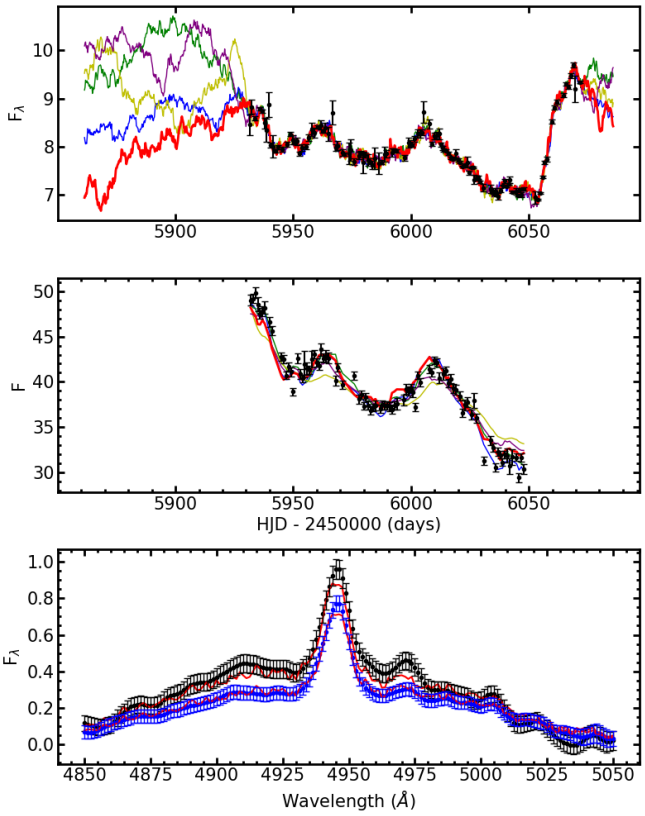

Figure 4.32: Same as Figure 4.3, but for Hβ in NGC 5548.

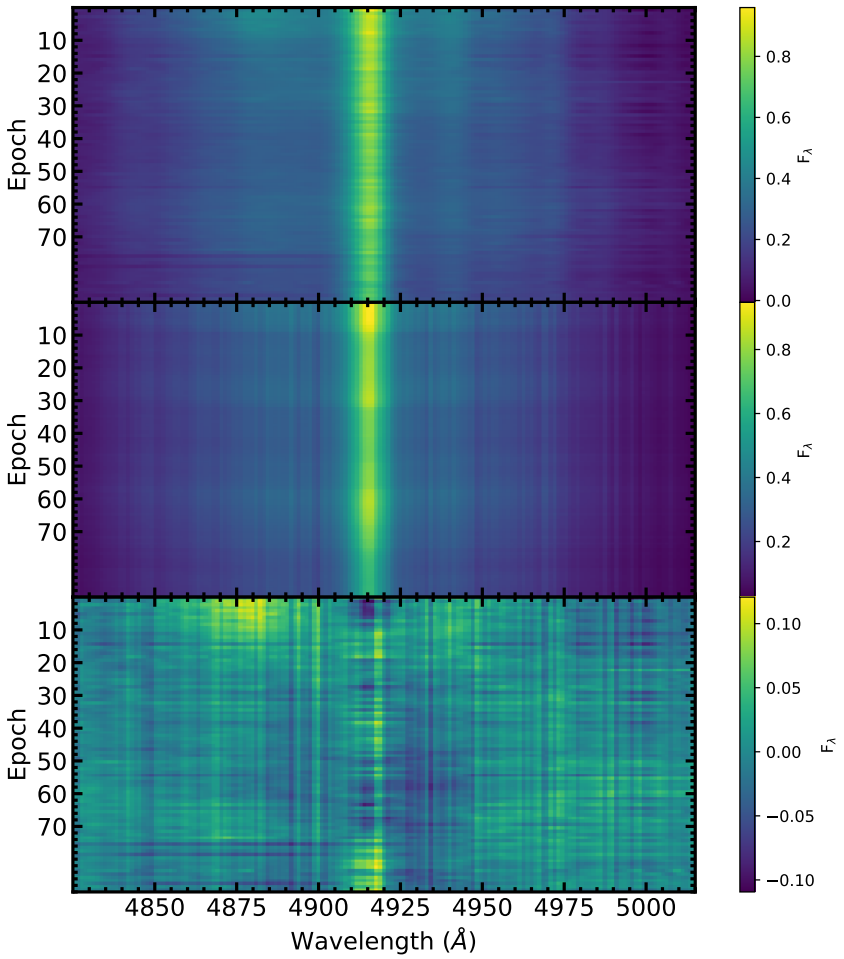

Figure 4.33: Same as Figure 4.4, but for Hβ in NGC 5548.

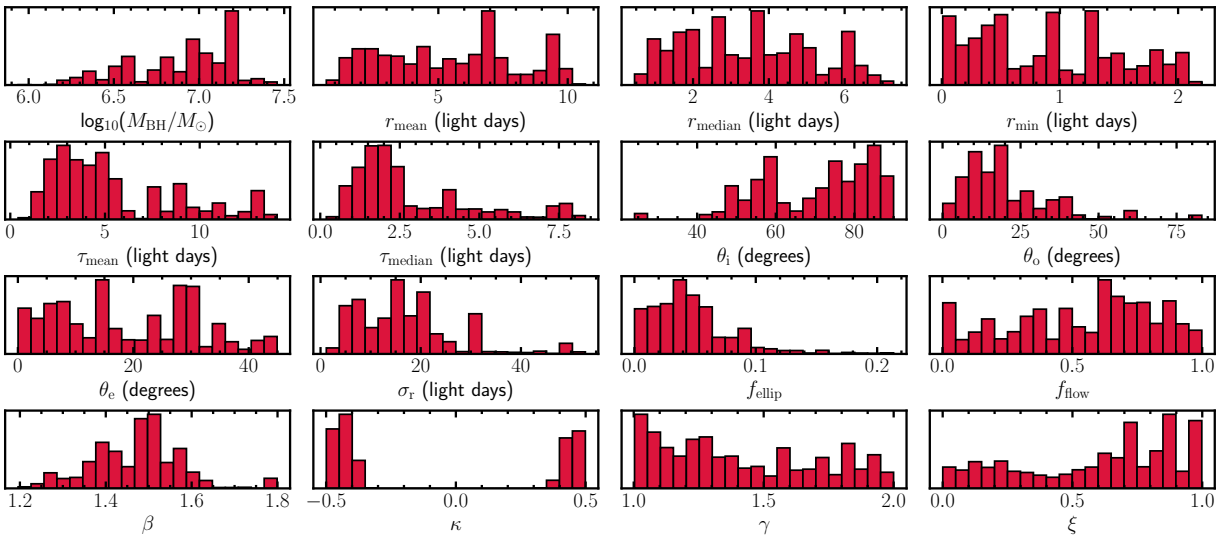

Figure 4.34: Same as Figure 4.5, but for Hβ in NGC 5548.

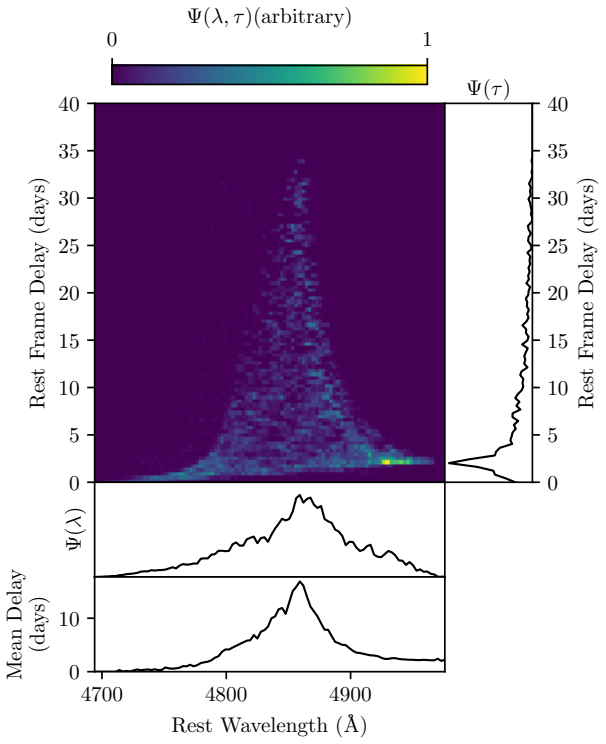

Figure 4.35: Same as Figure 4.7, but for Hβ in NGC 5548.

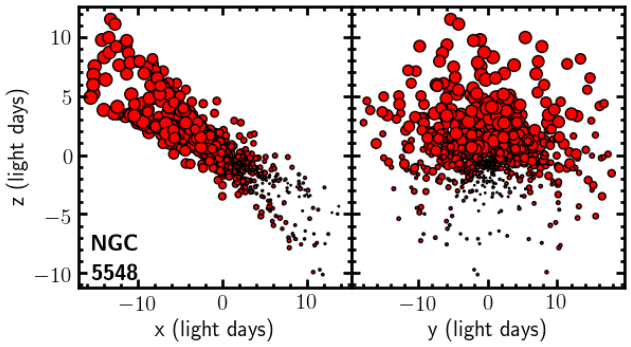

Figure 4.36: Same as Figure 4.6, but for Hβ in NGC 5548.

velocities was also present ($\sigma_{\rm turb} = 0.029^{+0.038}_{-0.026}$). The black hole mass reported by W20 (again using Hβ and the $V-$band driving continuum) is $\log_{10}(M_{\rm BH}/M_{\odot}) = 7.54^{+0.34}_{0.24}$, in excellent agreement with the findings of P14.

Figure 4.41 displays the constraints on the Hβ-emitting BLR parameters as a function of time from the 2008 LAMP campaign through observations in 2012 modeled in this work to the AGN STORM 2014 campaign. The mean radius of the BLR increases as a function of time, with the results of this study providing a glimpse at an intermediate point in time. As noted by W20, the nucleus of NGC 5548 was observed to show an increase in luminosity by a factor of $\sim$4 between 2008 and 2014 (Bentz et al., 2009b, 2013). A factor of $\sim$4 in luminosity would be expected to coincide with an increase in the BLR radius by a factor of $\sim$2 according to the relationship between AGN luminosity and BLR radius (Bentz et al., 2013), which is shown to be the case in Figure 4.41 within the uncertainties. The continuum luminosity measurements reported by Peterson et al. (2013) show that the nucleus had entered a low luminosity state near 2000, lasting through $\sim$2009, and nearly doubling in luminosity by 2012. Additionally, De Rosa et al. (2015) reported that by the time of the 2014 AGN STORM campaign, NGC 5548 had returned to the continuum luminosity exhibited in 1989, even brighter than what was observed in 2012. This suggests that from 2008 to 2014, the luminosity of this AGN was steadily increasing, which would in turn be expected to steadily increase the size of the photoionized BLR.

Another significant change in this time frame is the apparent turnover from inflowing to outflowing motions in the evolution of $f_{\rm flow}$, and the 2012 snapshot appears to bridge the gap between

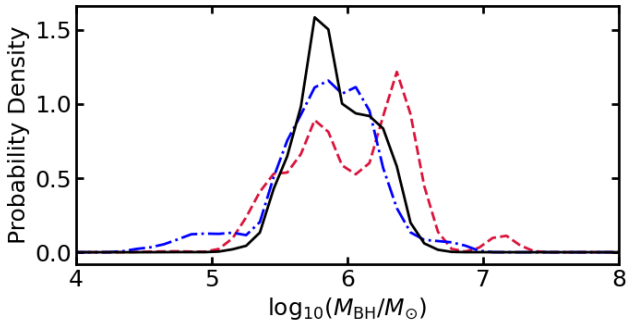

Figure 4.37: Joint inference on $M_{\rm BH}$ in NGC 3227 (black solid line) from the results of Hβ (red dashed line) and He II (blue dot-dashed line).

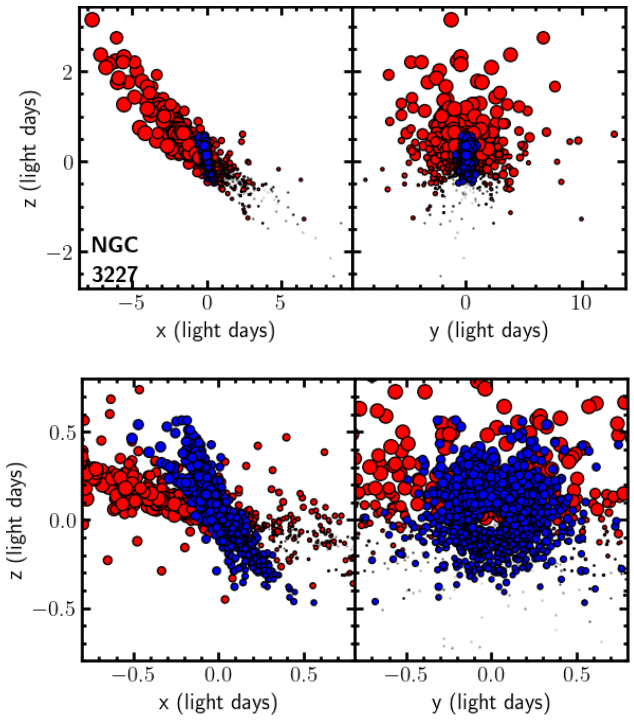

Figure 4.38: Representative geometric model of the combination of Hβ-emitting (red) and He II-emitting BLRs in NGC 3227. The orientations of the models in the left and right panels are the same as in Figure 4.6. The same geometries are present in all 4 panels, and the bottom two panels shows a closer distance scale.

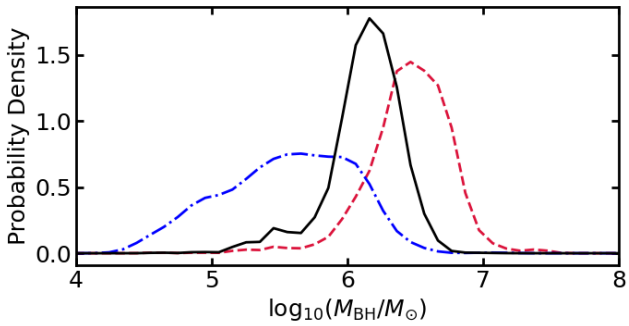

Figure 4.39: Same as Figure 4.37, but for the joint constraint on $M_{\rm BH}$ in NGC 4151.

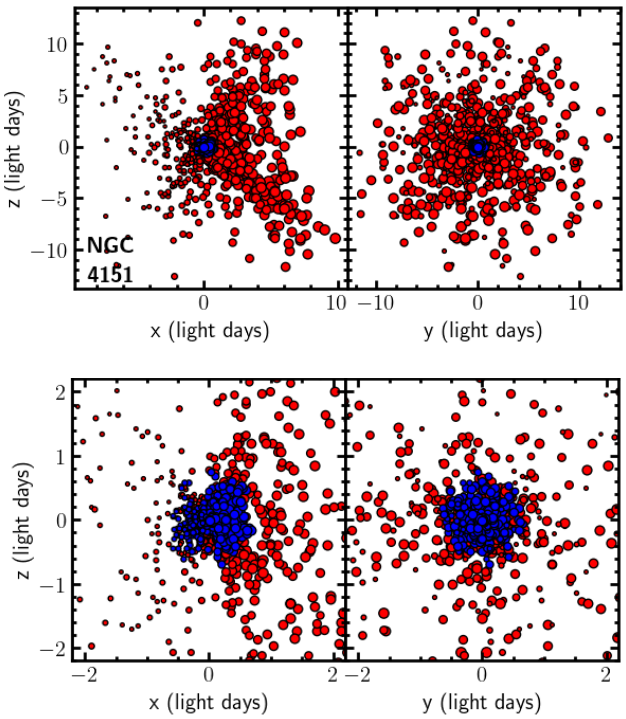

Figure 4.40: Same as Figure 4.38, but for the Hβ and He II-emitting BLRs in NGC 3227.

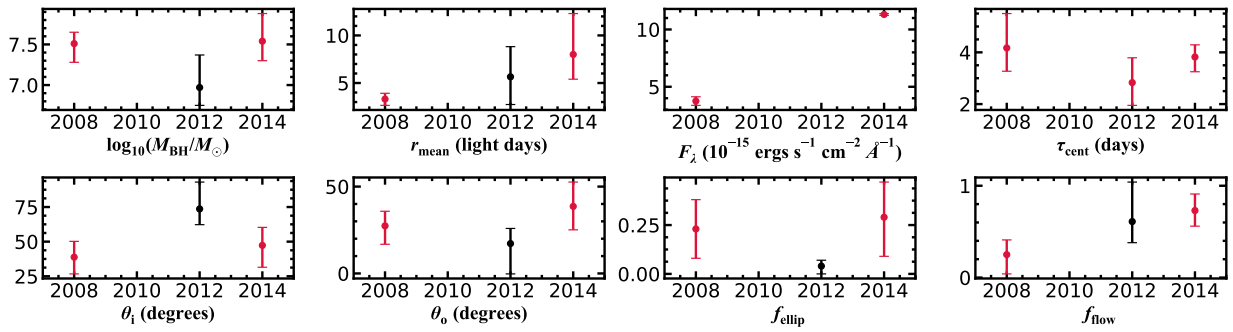

Figure 4.41: Comparisons of select Hβ-emitting BLR parameters in NGC 5548 constrained by CARAMEL modeling of the LAMP 2008 RM campaign (Pancoast et al., 2014b), this work, and the AGN STORM campaign in 2014 (Williams et al., 2020) in addition to observed luminosities and time delays. The points for the model parameters are the median values of each parameter, and the error bars indicate each respective 68% confidence level. The black points represent results from this work. Measurements of F_λ are from Bentz et al. (2013) for 2008 Pei et al. (2017) for 2014. Measurements of $\tau_{\rm cent}$ are from Bentz et al. (2009b) for 2008, dR18 for 2012, and Pei et al. (2017) for 2014.

the two kinematic signatures. W20 speculated that if this were truly a switch to net-outflowing gas motions, it might indicate significant impact on BLR kinematics from the increase in AGN luminosity. However, their high value of $\theta_{\rm e}$ is more suggestive of highly elliptical orbits rather than truly outflowing gas motions, and our models are much less constrained in this study than either the 2008 or 2014 studies.

Given the larger uncertainties of the model results we present here, the black hole mass remains consistent as well as the opening angle. As mentioned, the inclination angle is largely unconstrained by our models to the 2012 Hβ observations, however it is marginally consistent at the 2$-\sigma$ level.

4.5.3 *Previous Measurements*

We detail below the comparison between the results from the CARAMEL modeling in this work and other measurements in the literature, namely direct $M_{\rm BH}$ measurements (as opposed to indirect estimates from the $M_{\rm BH}-\sigma_\star$ relation or single epoch spectra) and any constraints on the inclination of the AGNs in this sample. We note that the AGN inclination is in no way expected to align with the host galaxy inclination, since it is set by the recent accretion and merger history of the black hole.

The time lags we compare to are those reported in dR18, which are measured in two ways. The first method is interpolated cross-correlation (Gaskell & Sparke, 1986; Gaskell & Peterson, 1987; White & Peterson, 1994; Peterson et al., 1998, 2004), and the second employs the modeling algorithm JAVELIN (Zu et al., 2011). A full discussion of the two methods is available in Fausnaugh et al. (2017). In brief, JAVELIN employs a damped random walk model. dR18 preferred the JAVELIN results because of their smaller measurement uncertainties. The cross-correlation results provide a model-independent measurement, albeit with more conservative uncertainties. We prefer the latter here.

4.5.3.1 Mrk 704

Within the large uncertainties, the mass we find for Mrk 704 of $\log_{10}(M_{\rm BH}/M_{\odot}) = 7.38^{+0.57}_{-0.62}$ agrees with the simpler reverberation measurement reported by dR18, who found $\log(M_{\rm BH}/M_{\odot}) = 7.58 \pm 0.13$ based on $\tau_{\rm cent}$, rms line width of Hβ, and an assumed $\langle f \rangle$ of 4.47 ± 1.25 (Woo et al., 2015). While there is agreement, we note that it is not necessarily expected given the more face-on orientation of the BLR in Mrk 704 found by the preliminary models in addition to the improvements to the models yet to be conducted.

4.5.3.2 NGC 3227

Several studies have attempted to constrain the inclination of the AGN in NGC 3227. Fischer et al. (2013) conducted three-dimensional models of the spatially-resolved narrow line region (NLR) bicone, and found a best-fit inclination of the bicone (and thus, a constraint on the inclination of the BLR and torus) in NGC 3227 of $15 \pm 5°$. The formal uncertainty of $\pm 5°$ is a lower limit as other inherent uncertainties, such as any asymmetries in the NLR geometry, kinematics not captured in their model, and offsets in inclination between the accretion disk and BLR/torus midplane, are not factored into their analysis. Zhao et al. (2020) later investigated the broadband X-ray spectra of the sample of Fischer et al. by fitting the spectra with XSPEC (Arnaud, 1996) and modeling through the radiative transfer code BORUS (Baloković et al., 2018). Zhao et al. found a lower limit of the AGN

Table 4.3. Previous $M_{\rm BH}$ Measurements

Target	$\log(M_{\rm BH}/M_\odot)$	Method	Ref
Mrk 704	$7.38^{+0.57}_{-0.62}$	This Work	···
	$7.58^{+0.13}_{-0.13}$	RM	1
NGC 3227	$5.86^{+0.40}_{-0.20}$	This Work[a]	···
	$6.32^{+0.35}_{-0.35}$	RM	1
	$7.27^{+0.17}_{-0.17}$	SD[b]	2
	$7.48^{+0.18}_{-0.08}$	GD[b]	3
NGC 3516	$7.28^{+0.10}_{-0.24}$	This Work	···
	$7.48^{+0.17}_{-0.17}$	RM	1
NGC 4151	$6.16^{+0.20}_{-0.20}$	This Work[a]	···
	$7.21^{+0.27}_{-0.27}$	SD	4
	$7.35^{+0.11}_{-0.11}$	RM	1
	$7.56^{+0.10}_{-0.24}$	GD[c]	3
NGC 5548	$6.97^{+0.22}_{-0.40}$	This Work	···
	$7.28^{+0.16}_{-0.16}$	RM	1
	$7.51^{+0.23}_{-0.14}$	CARAMEL	5
	$7.64^{+0.21}_{-0.18}$	CARAMEL[d]	6

Note. — Black hole masses are calculated from the measurements of $\tau_{\rm cent}$ and $\sigma_{\rm line}$ from dR18 assuming $\langle f \rangle = 4.47 \pm 1.25$. The method column refers to traditional reverberation-based measurements (RM), stellar dynamical modeling (SD), gas dynamical modeling (GD), and BLR modeling of RM data (CARAMEL). References are as follows: 1. dR18, 2. Davies et al. (2006), 3. Hicks & Malkan (2008), 4. Roberts et al. (2021), 5. Pancoast et al. (2014b), 6. Williams et al. (2020)

inclination to be $\sim$25° when left as a free parameter in the modeling process. While it is difficult to compare these results to the rather unconstrained inclination found by the preliminary models to the Hβ BLR in NGC 3227, we do find agreement between the joint constraint on inclination of $30.00^{+11.82}_{-5.45}$ degrees and the results of Zhao et al. (2020).

The joint inference on the black hole mass of $\log_{10}(M_{\rm BH}/M_{\odot}) = 5.86^{+0.40}_{-0.20}$ is significantly smaller than the traditional reverberation measurement by dR18 of $\log_{10}(M_{\rm BH}/M_{\odot}) = 6.57 \pm 0.13$ using the mean time delay and $\langle f \rangle = 4.47 \pm 1.25$. However, the time lag employed in their calculation of $M_{\rm BH}$ was measured using JAVELIN, which found a longer mean lag of $\tau_{\rm JAV} = 2.30^{+0.22}_{-0.20}$. If the cross-correlation based time lag measurement of $\tau_{\rm cent} = 1.29^{+1.56}_{-1.27}$ days is used, the black hole mass is found to be $\log_{10}(M_{\rm BH}/M_{\odot}) = 6.32 \pm 0.35$, which places it in better agreement with our constraint within the uncertainties. This agreement is expected if the inclination of the BLR is truly $\sim$20-30°, but not if the inclination is significantly higher or lower.

The central SMBH in NGC 3227 has also been the target of both stellar and gas dynamical modeling studies. Davies et al. (2006) used near-infrared integral field unit data to model the stellar kinematics within the gravitational sphere of influence of the black hole. Originally using the group-averaged distance of 17.0 Mpc to convert angular scales to physical scales, the black hole mass was constrained to be $\log(M_{\rm BH}/M_{\odot}) = 7.13 \pm 0.17$. However, a more accurate distance to NGC 3227 is available from a surface brightness fluctuation (SBF) measurement of the interacting galaxy to NGC 3227, NGC 3226 (Tonry et al., 2001). Assuming the distance of 23.5 ± 2.4 Mpc is the roughly the same for NGC 3227, the adjusted black hole mass is $\log(M_{\rm BH}/M_{\odot}) = 7.27 \pm 0.17$. An additional black hole mass measurement was derived by Hicks & Malkan (2008) through the dynamical modeling of the kinematics of molecular hydrogen from high resolution spectroscopic observations in the near-infrared, yielding a measurement of $\log(M_{\rm BH}/M_{\odot}) = 7.30^{+0.18}_{-0.08}$. Again, if we adjust the distance originally employed for their analysis (15.5 Mpc) to the SBF distance, $M_{\rm BH}$ becomes $\log(M_{\rm BH}/M_{\odot}) = 7.48^{+0.18}_{-0.08}$. With the joint inference of $\log_{10}(M_{\rm BH}/M_{\odot}) = 5.86^{+0.40}_{-0.20}$ that we find, the stellar and gas dynamics-based masses are approximately an order of magnitude larger than both the RM-based mass and the mass yielded from CARAMEL modeling.

4.5.3.3 NGC 3516

Nandra et al. (1997) observed broad Fe Kα emission in NGC 3516, and subsequently modeled the accretion disk of the central SMBH using the emission. Their Kerr model to the Fe Kα line constrained an inclination of the inner accretion disk to be 26^{+4}_{-3} degrees. We note that accretion disk modeling includes its own set of simplifications and assumptions that may affect any interpretations of these comparisons (i.e., accretion disks are assumed to be infinitesimally thin, the geometry of the corona is largely unknown, any radiation returned to the accretion disk from strong light bending is ignored, etc.; see review by Bambi et al. 2021). The inclination of the accretion disk and BLR midplane ($\theta_{\rm i} = 30.12^{+7.18}_{-8.04}$ degrees) are also close to the inclination of the host galaxy itself of $\sim$38° derived from the best-fit minor-to-major disk axis ratio of 0.79 from the two-dimensional image decomposition of Bentz & Manne-Nicholas (2018). The same general alignment of the rotation axes of the black hole out to the galaxy disk was found by Bentz et al. (2021) for NGC 3783, who suggested that the spin axis of the central SMBH has been stable for a significant amount of time, and that the recent evolution of the SMBH could be tied to secular processes in alignment with the host galaxy disk.

The black hole mass constrained by the BLR models of $\log_{10}(M_{\rm BH}/M_{\odot}) = 7.28^{+0.10}_{-0.24}$ is significantly smaller than the mass found by the traditional reverberation measurement reported by dR18 of $\log_{10}(M_{\rm BH}/M_{\odot}) = 7.63 \pm 0.13$. However, if we again employ the cross-correlation time lag ($\tau_{\rm cent} = 5.74^{+2.26}_{-2.04}$ days) in place of the delay measured by JAVELIN ($\tau_{\rm JAV} = 8.11^{+0.75}_{-0.58}$), the mass becomes $\log_{10}(M_{\rm BH}/M_{\odot}) = 7.48 \pm 0.17$, bringing the constraints into agreement within the uncertainties.

4.5.3.4 NGC 4151

The inclination of the AGN of NGC 4151 has been estimated from multiple methods. The NLR bicone model of Fischer et al. (2013) finds an inclination of the bicone of 45 ± 5 degrees. However, Nandra et al. (1997) observed Fe Kα emission in NGC 4151 as well, and the model of the SMBH accretion disk constrains the inclination to be a much more face-on 9^{+18}_{9} degrees. The analysis of

Fischer et al. (2013) probes spatial scales much larger than the inner parsecs of the AGN, and does not account for any offsets in orientation between the accretion disk, BLR, and NLR, which could contribute to the discrepancy. The joint inference on the inclination of BLR found by our models of $\theta_{\rm i} = 7.58^{+3.03}_{-2.73}$ degrees is in good agreement with the analysis of Nandra et al. (1997). However, a very low inclination in combination with a moderate opening angle seem incompatible with eclipses of the central X-ray source by BLR clouds, as has been observed by Puccetti et al. (2007).

The traditional RM analysis of dR18 find $\log_{10}(M_{\rm BH}/M_{\odot}) = 7.35 \pm 0.11$. Though the full posterior PDF of the black hole mass for NGC 4151 does show solutions up to $\sim \log_{10}(M_{\rm BH}/M_{\odot}) = 7$, it should be noted that the majority of model parameters (namely the inclination angle, radial size, and mean time delay) are not well constrained, and thus the black hole mass predicted by these models should be viewed with some skepticism. Normally, the low inclination of the BLR would suggest that the models would necessitate a larger black hole mass to maintain the observed line of sight velocities (e.g., Pancoast et al. 2014b), but this is not what we see in the case of NGC 4151. We also note again that there are discrepancies between the modeled Hβ light curve and the data, where the models prefer different behavior near the middle and end of the observing campaign likely due to the behavior of the driving continuum. While it is unclear how much of an effect this has on the derived parameters or discrepancy in mass, it may be a contributor.

4.5.3.5 NGC 5548

NGC 5548 was also among the targets of the Fe Kα study of Nandra et al. (1997), however they were not able to constrain the inclination of the inner accretion disk (10^{+80}_{10} degrees). The black hole mass constrained by the Hβ BLR models of $\log_{10}(M_{\rm BH}/M_{\odot}) = 6.97^{+0.22}_{-0.40}$ is slightly smaller than the simpler RM-based measurement by dR18 of $\log_{10}(M_{\rm BH}/M_{\odot}) = 7.39 \pm 0.14$. This mass again employs the mean time lag as measured by JAVELIN ($\tau_{\rm JAV} = 3.68^{+0.43}_{-0.52}$ days), and if we instead adopt the cross-correlation time lag of $\tau_{\rm cent} = 2.83^{+0.88}_{-0.96}$ days, the predicted mass becomes $\log_{10}(M_{\rm BH}/M_{\odot}) = 7.28 \pm 0.16$, which finds agreement with the mass we find to within the uncertainties. As described in Section 4.4.5, the previous CARAMEL models find $\log_{10}(M_{\rm BH}/M_{\odot}) = 7.51^{+0.23}_{-0.14}$ for Hβ from P14

Table 4.4. f Factors

Target	Estimated	Predicted
Mrk 704	$2.8^{+7.6}_{-8.9}$	$6.0^{+17.7}_{-18.3}$
NGC 3227	$1.5^{+3.0}_{-1.8}$	$2.5^{+14.0}_{-11.8}$
NGC 3516	$2.8^{+1.3}_{-2.3}$	$2.5^{+12.2}_{-12.5}$
NGC 4151	$0.3^{+0.2}_{-0.2}$	$11.8^{+25.6}_{-25.4}$
NGC 5548	$2.2^{+1.6}_{-3.4}$	$0.1^{+3.9}_{-4.6}$

Note. — Estimations of individual f factors were conducted using the $\tau_{\rm cent}$ and $\sigma_{\rm line}$ measurements from dR18. Predicted values are derived from the linear regression of f as a function of $\theta_{\rm i}$ from Williams et al. (2018).

and $\log_{10}(M_{\rm BH}/M_\odot) = 7.64^{+0.21}_{-0.18}$ from W20 based on the joint constraint for Hβ, Lyα, and C IV. Both of these are slightly larger than, but consistent with, the simpler RM measurement using $\tau_{\rm cent}$.

4.5.4 *Individual f Factors and Overall Modeling Results*

With black hole mass constraints from the models, we can now estimate individual f factors for each AGN in this sample. We employ the cross correlation-based mean time delay $\tau_{\rm cent}$ and the line dispersion measurements in the rms spectra $\sigma_{\rm line}$ from dR18, with the traditional RM-based black hole mass given by $(M_{\rm BH}/M_\odot) = \langle f \rangle c\tau\sigma^2/G$. Traditional RM-based $M_{\rm BH}$ measurements are reported in Table 4.3, and each estimate of f is reported in Table 4.4. In general, within the large uncertainties of the results of this study, the individual scale factors are in agreement with both the mean $\langle f \rangle$ found for the LAMP 2011 sample by Williams et al. (2018) of $\log_{10}(f) = 0.60 \pm 0.16$, or $\langle f \rangle = 3.98 \pm 1.77$, and the combined mean scale factor of the modeling results of Pancoast et al. (2014b), Grier et al. (2017), and Williams et al. (2018) of $\log_{10}(f) = 0.57 \pm 0.07$, or $\langle f \rangle = 3.72 \pm 0.65$. While it is true that the mean $\langle f \rangle$ for this sample ($\langle f \rangle \sim 2$) is lower than what is found for the larger

population, the large uncertainties and generally unconstrained nature of a significant portion of the modeling results we find prevent a more thorough investigation.

The above studies have also found that individual f factors are anticorrelated with $\theta_{\rm i}$. This is expected because, for a simple disk, as inclination approaches perfectly face-on angles, the observed line-of-sight velocities go to zero. We have thus compared our estimates of the scale factor to those predicted by the linear regression of f as a function of $\theta_{\rm i}$ reported by Williams et al. (2018), and also list the predicted values in Table 4.4. As expected, the AGNs with the lowest constrained inclinations in this work (Mrk 704, NGC 4151) have the highest predicted scale factors to account for the lack of observed line-of-sight velocities. We find general agreement between our estimates and the predicted f, although the near face-on orientations and large uncertainties for Mrk 704 and NGC 4151 cause the predicted scale factor to be largely unconstrained.

In comparison with previous results from CARAMEL modeling, we find more variety in both geometry and kinematics across the 5 AGNs in this study based on these preliminary models. The majority of previous investigations find the Hβ-emitting BLRs to be thick disks with relatively face-on orientations (e.g., Pancoast et al. 2014b; Williams et al. 2018; Bentz et al. 2021), while we find a range of thick disks to nearly spherical distributions at a range of inclinations. Most of the objects allow for the possibility of emission both towards and away from the central SMBH in addition to uniform emission through the disk or concentrated towards the BLR face. The obscuration of the midplane also varies from well-constrained preferences of near-total obscuration (Mrk 704) to all possibilities of transparency (NGC 5548). We do, however, find consistent results to W20 and Bentz et al. (2021) in the models to the He II-emitting BLRs in which the high-ionization BLR is much more compact than the low-ionization region and closer to the ionizing source.

We find an even greater deviation in the dynamics of our sample when compared to the larger collection of BLR models. Most studies have found the majority of particles to exhibit near-circular motions with moderate contributions of inflowing motions (e.g., Pancoast et al. 2014b; Grier et al. 2017). We find an almost uniform preference for low percentages ($\lesssim 5\%$) of circular orbits, with the remainder of particles usually on inflowing trajectories that are likely highly elliptical, unbound

orbits. We find slight evidence for outflowing motions in NGC 3227 (which was also suggested by Denney et al. 2009b) and NGC 5548 (also found by W20), however most of the model parameters are unconstrained and it is thus unclear if these are true representations of the dynamics in NGC 3227 and NGC 5548. We again stress that these are results from preliminary models, and any interpretations should be taken with a level of skepticism as further investigations into several previously discussed factors will be conducted and may significantly change these results.

Chapter 5

Conclusions and Future Work

We have presented measurements and derived quantities of HI 21 cm emission for 31 RM AGN host galaxies, 12 of which are the first reported. We have also provided TF distance determinations to 24 of those galaxies, 14 of which are the first reported distances independent of z, and the first calibration of the $V-$band TF relation. Finally, we described preliminary results of the models of the BLR models in five Seyfert 1 galaxies, four of which have not been previously explored with direct modeling. Our main conclusions are as follows:

- Chapter 2
  - We find a typical $M_{\rm GAS}/M_\star$ fraction of $\sim$10% for the 31 AGN hosts targeted for HI observations.
  - There is slight evidence for later-type unbarred galaxies to have a larger gas-to-stellar mass fraction than earlier-type spirals, however this trend is not seen for barred spirals.
  - We find evidence of decreasing $M_{\rm GAS}/M_\star$ as a function of $M_\star$, consistent with previous findings in the literature. The trend is steeper than that of a constant $M_{\rm GAS}$ relation but shallower than a "closed-box" expectation, suggesting that the average galaxy in this sample has had its gas reservoir replenished, albeit at a slower rate than the depletion of the reservoir.
  - There is a significant correlation between $M_{\rm BH}$ and $M_{\rm BARY}$, with a slope similar to the $M_{\rm BH}-M_\star$ relation presented by Bentz & Manne-Nicholas (2018).

- Chapter 3

  - Removal of the AGN from each galaxy via two-dimensional surface brightness modeling has yielded distance moduli free of AGN contamination for the first time, providing improvements over previous TF distances in the literature.
  - We find good agreement between distances derived from apparent galaxy magnitudes in several different filters and with distances predicted by the BTF relation within the uncertainties.
  - The typical $M_{\rm DM}/M_{\rm DYN}$ fraction for this sample within $R_{\rm HI}$ is found to be 62%.
  - We find significant correlations between $M_{\rm BH}-M_{\rm DYN}$ and $M_{\rm BH}-M_{\rm DM}$, suggesting that SMBHs are not only correlated with bulge properties or solely the galaxy stellar content, but the total mass enclosed within the luminous radius.
  - Our $M_{\rm HALO}$ estimates agree well with the range of halo masses constrained by both observations and simulations (Spitler & Forbes, 2009; Bastian et al., 2020)
  - Over the range of $M_{\rm BH}$ and $M_{\rm HALO}$ considered in this sample, we find good agreement between our $M_{\rm BH}-M_{\rm HALO}$ relation and that found by both observational constraints (Ferrarese, 2002) and hydrodynamical simulations (Booth & Schaye, 2010; Mutlu-Pakdil et al., 2018).

- Chapter 4

  We note that the conclusions presented here are drawn from the preliminary results discussed in Chapter 4, and thus require an additional level of scrutiny and may be subject to change after we have improved our data treatment and finalized the models.

  - We find a range of dynamics for this sample of BLRs. Though many parameters are unconstrained, there is uniform preference for low percentages of near-circular orbits, with most models preferring inflowing trajectories that are likely highly elliptical and unbound.

- We find geometries ranging from thin to very thick disks. Consistent with previous models of the high-ionization BLR (Williams et al., 2020; Bentz et al., 2021), we find the He-II emitting regions to be much more compact and closer to the central ionizing source than the Hβ-emitting regions. The inclinations of the BLRs we find also tend to agree with available accretion disk models of Fe Kα observations in the literature.
- Within the large uncertainties, $M_{\rm BH}$, $\theta_{\rm o}$, and $\theta_{\rm i}$ for NGC 5548 are generally found to be consistent between 2008 and 2014. We find further evidence of the Hβ BLR radius steadily increasing over this time frame, as expected with the luminosity of the AGN increasing over the same period of time. There is also slight evidence for a turnover in dynamics from inflowing to outflowing motions in agreement with W20.
- The time delays and the transfer functions of the representative BLR geometries are generally in agreement with the velocity-resolved RM analysis of dR18.
- The majority of black hole mass constraints agree with traditional RM measurements within the large uncertainties, although the preliminary models prefer systemically smaller masses compared to traditional RM results.
- We estimate individual f factors for each AGN. General agreement is found with the mean $\langle f \rangle$ factor calculated by Williams et al. (2018) for the full family of AGNs with direct modeling results within the large uncertainties. However, the mean $\langle f \rangle$ for this sample is lower than what is found for the larger population.

5.1 *Future Work*

With both the published and preliminary results presented in this manuscript, there are several areas where future investigations are recommended or necessary, and we detail each below.

5.1.1 *Baryonic Mass - Black Hole Mass Relationship*

While we find little to no correlations between black hole mass and gas-to-stellar mass fraction or black hole mass and gas mass, we do find a significant correlation between $M_{\rm BARY}$ and $M_{\rm BH}$ as discussed in Section 2.4.3. As the sample of AGN hosts for the work presented in Chapter 2 are far more stellar dominated than gas dominated, the relation is very similar to the $M_{\rm BH} - M_{\star}$ relation found by Bentz & Manne-Nicholas (2018). However the dwarf Seyfert NGC 4395, with a gas-to-stellar mass fraction of 134%, appears to follow the same trend as the other galaxies in the sample. The typical gas-to-stellar mass fraction in our sample is 10%, so it would be of interest to further explore the $M_{\rm BH} - M_{\rm BARY}$ relation with a larger sample consisting of more gas-rich systems to investigate whether the trend holds between SMBH mass and total baryonic content, thereby extending the investigations of SMBH-galaxy relationships that have historically been limited to central bulge properties (see Kormendy & Ho 2013).

5.1.2 *The TF Relation for Active Galaxies*

As discussed in Section 3.5.5 and displayed in Figure 3.5, a significant number of galaxies have TF distances far too small for their recessional velocities and, subsequently, far larger $V_{\rm PEC}$ than observed in any of the CF catalogs. While it is important to note that the inclinations of the majority of galaxies in this sample lie below the usual cutoff of 45° for TF distances conducted in the literature (thus requiring larger inclination corrections and inducing larger uncertainties in $V_{\rm PEC}$), the canonical TF relation avoids active galaxies in its calibrating samples. Star formation rates in AGN hosts have been found to be higher, on average, than quiescent galaxies in the nearby universe (Xue et al., 2010), which in turn has been shown to produce higher surface brightnesses (Graves & Faber, 2010; Mould, 2020) and could therefore bias many of the TF-based distances low among our sample. Triggered star formation from gravitational interaction has also been shown to contribute a difference to the slope of the $R-$band TF relation (Barton et al., 2001). This suggests that regardless of the cause of increased galaxy surface brightness, the canonical TF relation may not be applicable to AGN hosts and/or interacting galaxies. Thus, an independent calibration of the

relation for active galaxies is needed to explore the magnitude of any difference, and thus bias, in the predicted distance for active and quiescent galaxies.

5.1.3 *The Relation Between R_1 and $R_{\rm HI}$*

As discussed in Section 3.6.1, we compared our estimates of $R_{\rm HI}$ to the physically motivated radius definition of Trujillo et al. (2020), R_1, the radius at which the stellar mass density of 1 $M_\odot$ pc^{-2} is reached. We find an average ratio of $R_{\rm HI}/R_1 \sim 1.1$ (see also Figure 3.6). The radius proposed by Trujillo et al. (2020) corresponds to the star formation threshold assuming a gas-to-star transformation efficiency of $\sim$10% (as opposed to an efficiency of 100% which yields a star formation threshold of $\sim$3–10 $M_\odot$ pc^{-2}; Schaye 2004). As star formation is typically hosted by molecular clouds (e.g., Leroy et al. 2008), and HI has been observed to condense to molecular hydrogen at $\sim$10 $M_\odot$ pc^{-2} (Martin & Kennicutt, 2001; Wong & Blitz, 2002; Bigiel et al., 2008), HI surface density should be reasonably assumed to be linked to star formation, and hence $R_{\rm HI}$ and R_1 should be similar.

However, our comparison is based on our estimates of $R_{\rm HI}$ as opposed to direct measurements. Because the similarity between $R_{\rm HI}$ and R_1 could offer a new method of estimating the hydrogen radius without the usual requirement of resolved HI studies, it is therefore of interest to conduct a detailed investigation of the similarity between both radii. Such an investigation would necessitate a moderate number of galaxies spanning a representative range of sizes which have both $R_{\rm HI}$ measurements from spatially resolved 21 cm studies and multi-band optical photometry in order to measure R_1 from the surface brightness profiles.

5.1.4 *Preliminary BLR Models*

As discussed in Chapter 4, analyses of our preliminary BLR models have revealed areas which require further investigation, which we detail below.

5.1.4.1 Continuum Modeling and Subtraction

In Section 4.2.3, we discussed the differences between production of emission line light curves in this work compared to those presented in dR18. Namely, dR18 measured the integrated emission-line flux above an interpolated linear continuum, while we have produced models of each emission line and continuum that were then subtracted from each spectrum. It is clear that several of our emission line light curves (e.g. Mrk 704 and NGC 3516) contain a higher level of scatter and outlying flux measurements compared to the light curves of dR18. While dR18 comment that their measurement method is fairly crude, it nevertheless has few opportunities for introducing scatter or uncertainty into the measurements, so we should not expect discrepancies between our light curves and theirs on this scale. The issue likely arises from insufficiently accurate continuum modeling and/or subtraction, which we will carefully reexamine. We will also carefully investigate the modeling and subtraction of the [O III] λ4959 emission line, as it blends with the red wing of many of the Hβ lines and could significantly affect the model preferences for inflow, in addition to any Fe II contribution to the He II λ4686 or Hβ lines.

5.1.4.2 Spectral Blurring and Residual Patterns

In Section 4.4, we noted that the model emission line profiles for all AGNs in this study exhibit significantly more structure or noise as a function of wavelength than the observed spectra. This discrepancy is the most likely cause for the vertical stripe pattern persistent in all residuals between observed and modeled emission profiles. This will also be closely investigated at a later date, however preliminary tests suggest that the issue may lie in the spectral smoothing during the modeling process. As discussed in Section 4.3, the modeled emission profiles are blurred to account for the instrumental resolution and varying observing conditions over a monitoring campaign. This process is done by comparing the observed width of the [O III] λ5007 line to the intrinsic width reported by Whittle (1992). A preliminary investigation has revealed the conversion of the observed line widths to the values expected by the modeling to be incorrect, resulting in the blurred models assuming a much higher spectral resolution than the data. We have since corrected the conversion for

the NGC 4151 dataset, and the resultant CARAMEL models generate much smoother emission-line profiles, more similar to the observed emission-line profiles, and an absence of the striping residual pattern. The same method was applied to determine the smoothing values for all the objects in this study, and thus we will correct the smoothing and produce updated models for the other objects in our sample as well.

5.1.4.3 Discussion on Future Monitoring Campaigns

In our analyses of the preliminary modeling results, we included a number of remarks on the observations from the 2012 monitoring campaign. For specific AGNs (Mrk 704, NGC 3516), the continuum and spectroscopic light curves do not exhibit nearly as much variable behavior as other objects in our sample, which may be a significant contributor to the largely unconstrained results from the models. Subsequent observing campaigns that target these same galaxies and are fortunate enough to capture more favorable variability could provide improved model constraints. Additionally, the photometric and spectroscopic observations in the 2012 campaign began at the same time. However, other RM campaigns have initiated photometric continuum monitoring before the spectroscopic monitoring (e.g., Bentz et al. 2009b), which can ensure that variations at the start of the delayed emission line light curve may be compared to earlier variations in the continuum light curve. Such a strategy is an efficient way to make the most of the limited spectroscopic information without significantly increasing the resource cost of a monitoring program, and could have provided further model constraints for this study.

This thesis has provided measurements of some of the most fundamental properties of RM AGNs and their host galaxies, including distance, z, $M_{\rm GAS}$, $M_{\rm BARY}$, $M_{\rm DYN}$, and $M_{\rm BH}$. The $M_{\rm BH}-M_{\rm BARY}$, $M_{\rm BH}-M_{\rm DYN}$, and $M_{\rm BH}-M_{\rm DM}$ relations place SMBHs in a larger picture painted by an evolutionary connection between black holes and their host galaxies on increasingly larger scales. Our BLR models will be added to the unique, growing sample of BLRs with full geometric and kinematic maps in addition to direct $M_{\rm BH}$ measurements independent of any scale factor. This collection of

measurements serves as an important cog in an ever-evolving machine dedicated to understanding the behavior and evolution of supermassive black holes and the galaxies in which they reside.

Bibliography

Aaronson, M., Mould, J., Huchra, J., et al. 1980, ApJ, 239, 12

Adams, E. A. K., & van Leeuwen, J. 2019, Nature Astronomy, 3, 188

Ahumada, R., Allende Prieto, C., Almeida, A., et al. 2020, ApJS, 249, 3

Alard, C. 2000, A&AS, 144, 363

Alard, C., & Lupton, R. H. 1998, ApJ, 503, 325

Alonso, M. S., Lambas, D. G., Tissera, P., & Coldwell, G. 2007, MNRAS, 375, 1017

Anderson, M. D., Baron, F., & Bentz, M. C. 2021, MNRAS, 505, 2903

Antonucci, R. 1993, ARA&A, 31, 473

Arakelian, M. A., Dibay, E. A., Yesipov, V. F., & Markarian, B. E. 1971, Astrofizika, 7, 177

Argudo-Fernández, M., Verley, S., Bergond, G., et al. 2015, A&A, 578, A110

Arnaud, K. A. 1996, in Astronomical Society of the Pacific Conference Series, Vol. 101, Astronomical Data Analysis Software and Systems V, ed. G. H. Jacoby & J. Barnes, 17

Athanassoula, E. 2008, MNRAS, 390, L69

Baloković, M., Brightman, M., Harrison, F. A., et al. 2018, ApJ, 854, 42

Bambi, C., Brenneman, L. W., Dauser, T., et al. 2021, , 217, 65

Bandara, K., Crampton, D., & Simard, L. 2009, ApJ, 704, 1135

Barth, A. J., Nguyen, M. L., Malkan, M. A., et al. 2011a, ApJ, 732, 121

Barth, A. J., Pancoast, A., Thorman, S. J., et al. 2011b, ApJ, 743, L4

Barth, A. J., Pancoast, A., Bennert, V. N., et al. 2013, ApJ, 769, 128

Barth, A. J., Bennert, V. N., Canalizo, G., et al. 2015, ApJS, 217, 26

Barton, E. J., Geller, M. J., Bromley, B. C., van Zee, L., & Kenyon, S. J. 2001, The Astronomical Journal, 121, 625

Bastian, N., Pfeffer, J., Kruijssen, J. M. D., et al. 2020, Monthly Notices of the Royal Astronomical Society, 498, 1050

Batiste, M., Bentz, M. C., Raimundo, S. I., Vestergaard, M., & Onken, C. A. 2017, ApJ, 838, L10

Baumgartner, W. H., Tueller, J., Markwardt, C. B., et al. 2013, ApJS, 207, 19

Bell, E. F., & de Jong, R. S. 2001, ApJ, 550, 212

Bell, E. F., McIntosh, D. H., Katz, N., & Weinberg, M. D. 2003, ApJS, 149, 289

Bennett, C. L., Larson, D., Weiland, J. L., & Hinshaw, G. 2014, ApJ, 794, 135

Bentz, M. C., Cackett, E. M., Crenshaw, D. M., et al. 2016, ApJ, 830, 136

Bentz, M. C., Ferrarese, L., Onken, C. A., Peterson, B. M., & Valluri, M. 2019, ApJ, 885, 161

Bentz, M. C., & Katz, S. 2015, PASP, 127, 67

Bentz, M. C., & Manne-Nicholas, E. 2018, ApJ, 864, 146

Bentz, M. C., Peterson, B. M., Netzer, H., Pogge, R. W., & Vestergaard, M. 2009a, ApJ, 697, 160

Bentz, M. C., Peterson, B. M., Pogge, R. W., Vestergaard, M., & Onken, C. A. 2006, ApJ, 644, 133

Bentz, M. C., Williams, P. R., Street, R., et al. 2021, ApJ, 920, 112

Bentz, M. C., Walsh, J. L., Barth, A. J., et al. 2009b, ApJ, 705, 199

Bentz, M. C., Horne, K., Barth, A. J., et al. 2010, ApJ, 720, L46

Bentz, M. C., Denney, K. D., Grier, C. J., et al. 2013, ApJ, 767, 149

Bernardi, M., Shankar, F., Hyde, J. B., et al. 2010, Monthly Notices of the Royal Astronomical Society, 404, 2087

Best, P. N., Kauffmann, G., Heckman, T. M., et al. 2005, MNRAS, 362, 25

Bieging, J. H., & Biermann, P. 1983, AJ, 88, 161

Biermann, P., Clarke, J. N., & Fricke, K. J. 1979, A&A, 75, 19

Bigiel, F., Leroy, A., Walter, F., et al. 2008, AJ, 136, 2846

Blakeslee, J. P., Cantiello, M., Mei, S., et al. 2010, The Astrophysical Journal, 724, 657

Blandford, R. D., & McKee, C. F. 1982, ApJ, 255, 419

Bolton, A. S., Burles, S., Koopmans, L. V. E., et al. 2008, The Astrophysical Journal, 682, 964

Booth, C. M., & Schaye, J. 2010, MNRAS, 405, L1

Bottinelli, L., Gouguenheim, L., Paturel, G., & de Vaucouleurs, G. 1983, A&A, 118, 4

—. 1984, A&AS, 56, 381

—. 1985, A&AS, 59, 43

Bournaud, F., Elmegreen, B. G., Teyssier, R., Block, D. L., & Puerari, I. 2010, MNRAS, 409, 1088

Bower, R. G., Benson, A. J., Malbon, R., et al. 2006, MNRAS, 370, 645

Bradford, J. D., Geha, M. C., & Blanton, M. R. 2015, ApJ, 809, 146

Brewer, B. J., & Foreman-Mackey, D. 2018, Journal of Statistical Software, Articles, 86, 1

Brewer, B. J., Treu, T., Pancoast, A., et al. 2011, ApJ, 733, L33

Broeils, A. H., & Rhee, M. H. 1997, A&A, 324, 877

Brosch, N., Polishook, D., Shporer, A., et al. 2008, AP&SS, 314, 163

Brown, T. M., Baliber, N., Bianco, F. B., et al. 2013, Publications of the Astronomical Society of the Pacific, 125, 1031

Bullock, J. S., Kolatt, T. S., Sigad, Y., et al. 2001, MNRAS, 321, 559

Burkert, A. 1995, The Astrophysical Journal, 447

Burstein, D., & Heiles, C. 1984, ApJS, 54, 33

Buta, R., Mitra, S., de Vaucouleurs, G., & Corwin, Jr., H. G. 1994, AJ, 107, 118

Cackett, E. M., Bentz, M. C., & Kara, E. 2021, iScience, 24, 102557

Calette, A. R., Avila-Reese, V., Rodríguez-Puebla, A., Hernández-Toledo, H., & Papastergis, E. 2018

Campbell, W. W., & Moore, J. H. 1918, Publications of Lick Observatory, 13, 75

Cattaneo, A., Blaizot, J., Weinberg, D. H., et al. 2007, MNRAS, 377, 63

Catinella, B., & Cortese, L. 2015, MNRAS, 446, 3526

Catinella, B., Giovanelli, R., & Haynes, M. P. 2006, The Astrophysical Journal, 640, 751

Chabrier, G. 2003, Publications of the Astronomical Society of the Pacific, 115, 763

Chilingarian, I. V., Melchior, A.-L., & Zolotukhin, I. Y. 2010, Monthly Notices of the Royal Astronomical Society, 405, 1409

Ciotti, L., Ostriker, J. P., & Proga, D. 2009, ApJ, 699, 89

Colless, M., Dalton, G., Maddox, S., et al. 2001, MNRAS, 328, 1039

Collin, S., Kawaguchi, T., Peterson, B. M., & Vestergaard, M. 2006, A&A, 456, 75

Cortese, L., Catinella, B., & Janowiecki, S. 2017, ApJ, 848, L7

Courtois, H. M., Tully, R. B., Fisher, J. R., et al. 2009a, AJ, 138, 1938

—. 2009b, AJ, 138, 1938

Courtois, H. M., Zaritsky, D., Sorce, J. G., & Pomarède, D. 2015, MNRAS, 448, 1767

Covey, K. R., Ivezić, Ž., Schlegel, D., et al. 2007, The Astronomical Journal, 134, 2398

Cox, A. N. 2000, Allen's astrophysical quantities

Croton, D. J., Springel, V., White, S. D. M., et al. 2006, MNRAS, 365, 11

Davies, R. I., Thomas, J., Genzel, R., et al. 2006, ApJ, 646, 754

Davis, L. E., & Seaquist, E. R. 1983, ApJS, 53, 269

Davoust, E., & Contini, T. 2004, A&A, 416, 515

de Blok, W. J. G., & Walter, F. 2014, The Astronomical Journal, 147, 96

de Blok, W. J. G., Walter, F., Brinks, E., et al. 2008, The Astronomical Journal, 136, 2648

De Lucia, G., Springel, V., White, S. D. M., Croton, D., & Kauffmann, G. 2006, MNRAS, 366, 499

De Rosa, G., Peterson, B. M., Ely, J., et al. 2015, ApJ, 806, 128

De Rosa, G., Fausnaugh, M. M., Grier, C. J., et al. 2018, ApJ, 866, 133

Desai, V., Dalcanton, J. J., Aragón-Salamanca, A., et al. 2007, ApJ, 660, 1151

Dressler, A., Oemler, Augustus, J., Couch, W. J., et al. 1997, ApJ, 490, 577

de Vaucouleurs, G. 1948, Annales d'Astrophysique, 11, 247

de Vaucouleurs, G., de Vaucouleurs, A., Corwin, Jr., H. G., et al. 1991, , 82, 621

de Vaucouleurs, G., de Vaucouleurs, A., & Corwin, J. R. 1976, in Second reference catalogue of bright galaxies, Vol. 1976, p. Austin: University of Texas Press., Vol. 1976

de Vaucouleurs, G., Peters, W. L., Bottinelli, L., Gouguenheim, L., & Paturel, G. 1981, ApJ, 248, 408

Dekel, A., Sari, R., & Ceverino, D. 2009, ApJ, 703, 785

Denney, K. D., Peterson, B. M., Dietrich, M., Vestergaard, M., & Bentz, M. C. 2009a, ApJ, 692, 246

Denney, K. D., Peterson, B. M., Pogge, R. W., et al. 2009b, ApJ, 704, L80

Denney, K. D., Peterson, B. M., Pogge, R. W., et al. 2010, 721, 715

Dickel, J. R., & Rood, H. J. 1978, ApJ, 223, 391

Djorgovski, S., & Davis, M. 1987, ApJ, 313, 59

Doroshenko, V. T., Sergeev, S. G., Merkulova, N. I., et al. 2006, VizieR Online Data Catalog (other), 0160, J/other/Ap/48

Doyle, M. T., Drinkwater, M. J., Rohde, D. J., et al. 2005, MNRAS, 361, 34

Dressler, A., Lynden-Bell, D., Burstein, D., et al. 1987, ApJ, 313, 42

Du, P., Lu, K.-X., Hu, C., et al. 2016a, ApJ, 820, 27

Du, P., Lu, K.-X., Zhang, Z.-X., et al. 2016b, VizieR Online Data Catalog, 182

Einstein, A. 1905, Annalen Phys., 17, 891

Elmegreen, B. G., Bournaud, F., & Elmegreen, D. M. 2008, ApJ, 688, 67

Epstein, E. E. 1964, AJ, 69, 490

Event Horizon Telescope Collaboration, Akiyama, K., Alberdi, A., et al. 2019, ApJ, 875, L6

Fabello, S., Kauffmann, G., Catinella, B., et al. 2011, MNRAS, 416, 1739

Faber, S. M., & Jackson, R. E. 1976, ApJ, 204, 668

Falco, E. E., Kurtz, M. J., Geller, M. J., et al. 1999, PASP, 111, 438

Fanidakis, N., Baugh, C. M., Benson, A. J., et al. 2011, MNRAS, 410, 53

Fasano, G., Marmo, C., Varela, J., et al. 2006, A&A, 445, 805

Fath, E. A. 1909, Lick Observatory Bulletin, 149, 71

Fausnaugh, M. M., Denney, K. D., Barth, A. J., et al. 2016, ApJ, 821, 56

Fausnaugh, M. M., Grier, C. J., Bentz, M. C., et al. 2017, ApJ, 840, 97

Fernández, X., Gim, H. B., van Gorkom, J. H., et al. 2016, ApJ, 824, L1

Ferrarese, L. 2002, ApJ, 578, 90

Ferrarese, L., & Ford, H. 2005, , 116, 523

Ferrarese, L., & Merritt, D. 2000, ApJ, 539, L9

Fischer, T. C., Crenshaw, D. M., Kraemer, S. B., & Schmitt, H. R. 2013, ApJS, 209, 1

Fisher, J. R., & Tully, R. B. 1977, Comments on Astrophysics, 7, 85

—. 1981, ApJS, 47, 139

Fisher, K. B., Huchra, J. P., Strauss, M. A., et al. 1995, ApJS, 100, 69

Fouque, P., Gourgoulhon, E., Chamaraux, P., & Paturel, G. 1992, A&AS, 93, 211

Freedman, W. L., Madore, B. F., Gibson, B. K., et al. 2001, ApJ, 553, 47

Frei, Z., & Gunn, J. E. 1994, AJ, 108, 1476

Gallimore, J. F., Baum, S. A., O'Dea, C. P., Pedlar, A., & Brinks, E. 1999, ApJ, 524, 684

Ganeshalingam, M., Li, W., & Filippenko, A. V. 2013, MNRAS, 433, 2240

Gaskell, C. M., & Peterson, B. M. 1987, ApJS, 65, 1

Gaskell, C. M., & Sparke, L. S. 1986, ApJ, 305, 175

Gebhardt, K., Bender, R., Bower, G., et al. 2000, ApJ, 539, L13

Genel, S., Vogelsberger, M., Springel, V., et al. 2014, MNRAS, 445, 175

Genzel, R., Pichon, C., Eckart, A., Gerhard, O. E., & Ott, T. 2000, Monthly Notices of the Royal Astronomical Society, 317, 348

Genzel, R., Förster Schreiber, N. M., Lang, P., et al. 2014, ApJ, 785, 75

Ghez, A. M., Morris, M., Becklin, E. E., Tanner, A., & Kremenek, T. 2000, , 407, 349

Ghez, A. M., Salim, S., Weinberg, N. N., et al. 2008, The Astrophysical Journal, 689, 1044

Giovanelli, R., Haynes, M. P., Kent, B. R., et al. 2005, AJ, 130, 2598

Graham, A. W., Onken, C. A., Athanassoula, E., & Combes, F. 2011, MNRAS, 412, 2211

Granato, G. L., Zitelli, V., Bonoli, F., et al. 1993, ApJS, 89, 35

Graves, G. J., & Faber, S. M. 2010, The Astrophysical Journal, 717, 803

Gravity Collaboration, Dexter, J., Shangguan, J., et al. 2020a, A&A, 635, A92

Gravity Collaboration, Amorim, A., Bauböck, M., et al. 2020b, A&A, 643, A154

—. 2021a, A&A, 648, A117

—. 2021b, A&A, 654, A85

Graziani, R., Courtois, H. M., Lavaux, G., et al. 2019, MNRAS, 488, 5438

Grier, C. J., Pancoast, A., Barth, A. J., et al. 2017, ApJ, 849, 146

Grier, C. J., Martini, P., Watson, L. C., et al. 2013a, ApJ, 773, 90

Grier, C. J., Peterson, B. M., Horne, K., et al. 2013b, ApJ, 764, 47

Gültekin, K., Richstone, D. O., Gebhardt, K., et al. 2009, The Astrophysical Journal, 698, 198

Hakobyan, A. A., Adibekyan, V. Z., Aramyan, L. S., et al. 2012, A&A, 544, A81

Hann, J. v. 1903, New York, The Macmillan company, 1

Haynes, M. P., & Giovanelli, R. 1984, AJ, 89, 758

Haynes, M. P., Giovanelli, R., Martin, A. M., et al. 2011, AJ, 142, 170

—. 2013, VizieR Online Data Catalog, J/AJ/142/170

Heckman, T. M., Balick, B., & Sullivan, III, W. T. 1978, ApJ, 224, 745

Heckman, T. M., & Best, P. N. 2014, ARA&A, 52, 589

Henden, A., & Munari, U. 2014, Contributions of the Astronomical Observatory Skalnate Pleso, 43, 518

Henden, A. A., Templeton, M., Terrell, D., et al. 2016, VizieR Online Data Catalog, II/336

Hernán Caballero, A. 2012, MNRAS, 427, 816

Hicks, E. K. S., & Malkan, M. A. 2008, ApJS, 174, 31

Ho, L. C., Darling, J., & Greene, J. E. 2008a, ApJS, 177, 103

—. 2008b, ApJ, 681, 128

Ho, L. C., & Kim, M. 2009, The Astrophysical Journal Supplement Series, 184, 398

Hoekstra, H., Hsieh, B. C., Yee, H. K. C., Lin, H., & Gladders, M. D. 2005, ApJ, 635, 73

Holmberg, E. 1958, Meddelanden fran Lunds Astronomiska Observatorium Serie II, 136, 1

Hopkins, P. F., Hernquist, L., Cox, T. J., et al. 2006, ApJS, 163, 1

Hopkins, P. F., Hernquist, L., Cox, T. J., & Kereš, D. 2008, ApJS, 175, 356

Horne, K. 1994, in Astronomical Society of the Pacific Conference Series, Vol. 69, Reverberation Mapping of the Broad-Line Region in Active Galactic Nuclei, ed. P. M. Gondhalekar, K. Horne, & B. M. Peterson, 23

Horne, K., Peterson, B. M., Collier, S. J., & Netzer, H. 2004, PASP, 116, 465

Horne, K., De Rosa, G., Peterson, B. M., et al. 2021, ApJ, 907, 76

Hu, C., Du, P., Lu, K.-X., et al. 2015, ApJ, 804, 138

Hubble, E. P. 1926, ApJ, 64, 321

Hubble, E. 1929, Proceedings of the National Academy of Science, 15, 168

Huchra, J., Latham, D. W., da Costa, L. N., Pellegrini, P. S., & Willmer, C. N. A. 1993, AJ, 105, 1637

Huchtmeier, W. K., & Richter, O.-G. 1989, A General Catalog of HI Observations of Galaxies. The Reference Catalog., 350

Humason, M. L., Mayall, N. U., & Sandage, A. R. 1956, AJ, 61, 97

Hutchings, J. B. 1989, AJ, 98, 524

Ianjamasimanana, R., de Blok, W. J. G., Walter, F., & Heald, G. H. 2012, The Astronomical Journal, 144, 96

Iben, I., J., & Renzini, A. 1983, ARA&A, 21, 271

Into, T., & Portinari, L. 2013, MNRAS, 430, 2715

Iorio, G., Fraternali, F., Nipoti, C., et al. 2017, MNRAS, 466, 4159

Jaffé, Y. L., Poggianti, B. M., Verheijen, M. A. W., Deshev, B. Z., & van Gorkom, J. H. 2013, MNRAS, 431, 2111

James, O., von Tunzelmann, E., Franklin, P., & Thorne, K. S. 2015, Classical and Quantum Gravity, 32, 065001

Jiang, L., Fan, X., Vestergaard, M., et al. 2007, The Astronomical Journal, 134, 1150

Joshi, R., Chand, H., Wiita, P. J., Gupta, A. C., & Srianand, R. 2012, MNRAS, 419, 3433

Kaldare, R., Colless, M., Raychaudhury, S., & Peterson, B. A. 2003, MNRAS, 339, 652

Kaspi, S., Smith, P. S., Netzer, H., et al. 2000, ApJ, 533, 631

Kauffmann, G., & Haehnelt, M. 2000, MNRAS, 311, 576

Kauffmann, G., Heckman, T. M., Tremonti, C., et al. 2003, Monthly Notices of the Royal Astronomical Society, 346, 1055

Keel, W. C. 1996, AJ, 111, 696

Kelly, B. C. 2007, ApJ, 665, 1489

Kent, S. M. 1985, ApJS, 59, 115

Khachikian, E. Y., & Weedman, D. W. 1974, ApJ, 192, 581

Klypin, A. A., Trujillo-Gomez, S., & Primack, J. 2011, The Astrophysical Journal, 740, 102

Koleva, M., Prugniel, P., Bouchard, A., & Wu, Y. 2009, A&A, 501, 1269

König, S., Eckart, A., García-Marín, M., & Huchtmeier, W. K. 2009, A&A, 507, 757

Koratkar, A. P., & Gaskell, C. M. 1991, ApJ, 370, L61

Koribalski, B. S., Staveley-Smith, L., Kilborn, V. A., et al. 2004, AJ, 128, 16

Koribalski, B. S., Wang, J., Kamphuis, P., et al. 2018, MNRAS, 478, 1611

Koribalski, B. S., Staveley-Smith, L., Westmeier, T., et al. 2020, AP&SS, 365, 118

Kormendy, J. 2004, in Coevolution of Black Holes and Galaxies, ed. L. C. Ho, 1. astro-ph/0306353

Kormendy, J., & Ho, L. C. 2013, ARA&A, 51, 511

Kormendy, J., & Kennicutt, R. C. 2004, Annual Review of Astronomy and Astrophysics, 42, 603

Kormendy, J., & Richstone, D. 1995, ARA&A, 33, 581

Koshida, S., Yoshii, Y., Kobayashi, Y., et al. 2017, ApJ, 842, L13

Koss, M., Mushotzky, R., Treister, E., et al. 2012, ApJ, 746, L22

Koss, M., Mushotzky, R., Veilleux, S., et al. 2011, ApJ, 739, 57

Kourkchi, E., Tully, R. B., Anand, G. S., et al. 2020, ApJ, 896, 3

Kravtsov, A. V. 2013, The Astrophysical Journal, 764, L31

Kurk, J. D., Walter, F., Fan, X., et al. 2009, The Astrophysical Journal, 702, 833

—. 2007, The Astrophysical Journal, 669, 32

Kurucz, R. L. 1993, VizieR Online Data Catalog, VI/39

Lagos, C. D. P., Cora, S. A., & Padilla, N. D. 2008, MNRAS, 388, 587

Lapi, A., Salucci, P., & Danese, L. 2018, ApJ, 859, 2

Leavitt, H. S., & Pickering, E. C. 1912, Harvard College Observatory Circular, 173, 1

Lee, M. G., Freedman, W. L., & Madore, B. F. 1993, ApJ, 417, 553

Lelli, F., McGaugh, S. S., & Schombert, J. M. 2015, The Astrophysical Journal, 816, L14

Lelli, F., McGaugh, S. S., Schombert, J. M., Desmond, H., & Katz, H. 2019, Monthly Notices of the Royal Astronomical Society, 484, 3267

Leroy, A. K., Walter, F., Brinks, E., et al. 2008, AJ, 136, 2782

Lewis, B. M. 1983, AJ, 88, 1695

—. 1987, The Astrophysical Journal Supplement Series, 63, 515

Li, Y.-R., Wang, J.-M., Ho, L. C., Du, P., & Bai, J.-M. 2013, ApJ, 779, 110

Liszt, H. S., & Dickey, J. M. 1995, AJ, 110, 998

Lovell, M. R., Pillepich, A., Genel, S., et al. 2018, Monthly Notices of the Royal Astronomical Society, 481, 1950–1975

Lynden-Bell, D. 1969, , 223, 690

Lynden-Bell, D., & Rees, M. J. 1971, Monthly Notices of the Royal Astronomical Society, 152, 461

MacKenty, J. W. 1990, ApJS, 72, 231

Maddox, N., Frank, B. S., Ponomareva, A. A., et al. 2020, arXiv e-prints, arXiv:2011.09470. 2011.09470

Maddox, N., Frank, B. S., Ponomareva, A. A., et al. 2021, A&A, 646, A35

Madore, B. F., Mager, V., & Freedman, W. L. 2008, The Astrophysical Journal, 690, 389

Magorrian, J., Tremaine, S., Richstone, D., et al. 1998, AJ, 115, 2285

Makarov, D., Makarova, L., Rizzi, L., et al. 2006, The Astronomical Journal, 132, 2729

Mancera Piña, P. E., Fraternali, F., Adams, E. A. K., et al. 2019, ApJ, 883, L33

Mandelbaum, R., Seljak, U., Kauffmann, G., Hirata, C. M., & Brinkmann, J. 2006, MNRAS, 368, 715

Marconi, A., & Hunt, L. K. 2003, ApJ, 589, L21

Marganian, P., Garwood, R. W., Braatz, J. A., Radziwill, N. M., & Maddalena, R. J. 2006, in Astronomical Society of the Pacific Conference Series, Vol. 351, Astronomical Data Analysis Software and Systems XV, ed. C. Gabriel, C. Arviset, D. Ponz, & S. Enrique, 512

Marin, F. 2014, MNRAS, 441, 551

Martel, H., Premadi, P., & Matzner, R. 1998, ApJ, 497, 512

Martin, C. L., & Kennicutt, Jr., R. C. 2001, ApJ, 555, 301

Martin, M. C. 1998, Astronomy and Astrophysics Supplement Series, 131, 73

Martini, P. 2004, in IAU Symposium, Vol. 222, The Interplay Among Black Holes, Stars and ISM in Galactic Nuclei, ed. T. Storchi-Bergmann, L. C. Ho, & H. R. Schmitt, 235–241

Mauch, T., & Sadler, E. M. 2007, MNRAS, 375, 931

Maza, J., & Ruiz, M. T. 1989, The Astrophysical Journal Supplement Series, 69, 353

McGaugh, S. S. 2005, ApJ, 632, 859

—. 2012, AJ, 143, 40

McGaugh, S. S., & de Blok, W. J. G. 1997, ApJ, 481, 689

McGaugh, S. S., Schombert, J. M., Bothun, G. D., & de Blok, W. J. G. 2000, ApJ, 533, L99

McMahon, R. G., Banerji, M., Gonzalez, E., et al. 2013, The Messenger, 154, 35

Mendoza-Castrejón, S., Dultzin, D., Krongold, Y., González, J. J., & Elitzur, M. 2015, MNRAS, 447, 2437

Meyer, M. J., Zwaan, M. A., Webster, R. L., et al. 2004, MNRAS, 350, 1195

Mirabel, I. F., & Sanders, D. B. 1988, ApJ, 335, 104

Mirabel, I. F., & Wilson, A. S. 1984, ApJ, 277, 92

Misgeld, I., & Hilker, M. 2011, Monthly Notices of the Royal Astronomical Society, 414, 3699

Michell, J. 1784, Philosophical Transactions of the Royal Society of London Series I, 74, 35

Monroe, T. R., Prochaska, J. X., Tejos, N., et al. 2016, AJ, 152, 25

Mould, J. 2020, Frontiers in Astronomy and Space Sciences, 7, 21

Mundell, C., Pedlar, A., G., et al. 1995, Monthly Notices of the Royal Astronomical Society, 277, 641

Mundell, C. G., Pedlar, A., Shone, D. L., & Robinson, A. 1999, MNRAS, 304, 481

Mutlu-Pakdil, B., Seigar, M. S., Hewitt, I. B., et al. 2018, MNRAS, 474, 2594

Nandra, K., George, I. M., Mushotzky, R. F., Turner, T. J., & Yaqoob, T. 1997, ApJ, 477, 602

Netzer, H. 2015, ARA&A, 53, 365

Newton, I. 1704, Opticks (Dover Press)

Obreschkow, D., & Rawlings, S. 2009, MNRAS, 394, 1857

Oh, K., Yi, S. K., Schawinski, K., et al. 2015, The Astrophysical Journal Supplement Series, 219, 1

Onken, C. A., Ferrarese, L., Merritt, D., et al. 2004, ApJ, 615, 645

Osterbrock, D. E., & Pogge, R. W. 1987, ApJ, 323, 108

Ott, J., Stilp, A. M., Warren, S. R., et al. 2012, AJ, 144, 123

Padovani, P., Alexander, D. M., Assef, R. J., et al. 2017, , 25, 2

Pancoast, A., Brewer, B. J., & Treu, T. 2011, ApJ, 730, 139

—. 2014a, MNRAS, 445, 3055

Pancoast, A., Brewer, B. J., Treu, T., et al. 2014b, MNRAS, 445, 3073

—. 2012, ApJ, 754, 49

Panessa, F., de Rosa, A., Bassani, L., et al. 2011, MNRAS, 417, 2426

Papastergis, E., Cattaneo, A., Huang, S., Giovanelli, R., & Haynes, M. P. 2012, The Astrophysical Journal, 759, 138

Paturel, G., Theureau, G., Bottinelli, L., et al. 2003, A&A, 412, 57

Payne, C. H. 1925, PhD thesis, RADCLIFFE COLLEGE.

Peck, A. B., & Taylor, G. B. 1998, ApJ, 502, L23

Pedlar, A., Howley, P., Axon, D. J., & Unger, S. W. 1992, MNRAS, 259, 369

Pei, L., Fausnaugh, M. M., Barth, A. J., et al. 2017, ApJ, 837, 131

Peng, C. Y., Ho, L. C., Impey, C. D., & Rix, H.-W. 2002, AJ, 124, 266

—. 2010, AJ, 139, 2097

Persic, M., & Salucci, P. 1995, ApJS, 99, 501

Persic, M., Salucci, P., & Stel, F. 1996, Monthly Notices of the Royal Astronomical Society, 281, 27

Peterson, B. M. 1993, PASP, 105, 247

—. 1997, An Introduction to Active Galactic Nuclei

Peterson, B. M., Wanders, I., Horne, K., et al. 1998, PASP, 110, 660

Peterson, B. M., Ferrarese, L., Gilbert, K. M., et al. 2004, ApJ, 613, 682

Peterson, B. M., Denney, K. D., De Rosa, G., et al. 2013, ApJ, 779, 109

Peterson, S. D. 1979, ApJS, 40, 527

Pillepich, A., Vogelsberger, M., Deason, A., et al. 2014, MNRAS, 444, 237

Planck Collaboration, Aghanim, N., Akrami, Y., et al. 2020, A&A, 641, A6

Portinari, L., Sommer-Larsen, J., & Tantalo, R. 2004, MNRAS, 347, 691

Postman, M., Franx, M., Cross, N. J. G., et al. 2005, ApJ, 623, 721

Proust, D., Mazure, A., Vanderriest, C., Sodre, L., J., & Capelato, H. V. 1995, Astronomy and Astrophysics Supplement Series, 114, 565

Prugniel, P., & Heraudeau, P. 1998, A&AS, 128, 299

Puccetti, S., Fiore, F., Risaliti, G., et al. 2007, MNRAS, 377, 607

Ramella, M., Geller, M. J., Huchra, J. P., & Thorstensen, J. R. 1995, AJ, 109, 1458

Revalski, M. 2019, PhD thesis, Georgia State University, United States

Reyes, R., Mandelbaum, R., Gunn, J. E., Pizagno, J., & Lackner, C. N. 2011, MNRAS, 417, 2347

Richards, G. T., Myers, A. D., Gray, A. G., et al. 2009, The Astrophysical Journal Supplement Series, 180, 67

Richter, O.-G., & Huchtmeier, W. K. 1982, A&A, 109, 155

Rieke, G. H. 1978, ApJ, 226, 550

Riess, A. G., Casertano, S., Yuan, W., Macri, L. M., & Scolnic, D. 2019, ApJ, 876, 85

Riess, A. G., Macri, L. M., Hoffmann, S. L., et al. 2016, ApJ, 826, 56

Riffel, R., Rodríguez-Ardila, A., Aleman, I., et al. 2013, MNRAS, 430, 2002

Rines, K., Geller, M. J., Diaferio, A., Mohr, J. J., & Wegner, G. A. 2000, AJ, 120, 2338

Rines, K. J., Geller, M. J., Diaferio, A., & Hwang, H. S. 2016, ApJ, 819, 63

Roberts, C. A., Bentz, M. C., Vasiliev, E., Valluri, M., & Onken, C. A. 2021, ApJ, 916, 25

Roberts, M. S. 1962, AJ, 67, 437

—. 1969, AJ, 74, 859

Robinson, J. H., Bentz, M. C., Johnson, M. C., Courtois, H. M., & Ou-Yang, B. 2019, ApJ, 880, 68

Robinson, J. H., Bentz, M. C., Courtois, H. M., et al. 2021, ApJ, 912, 160

Sadler, E. M., Jackson, C. A., Cannon, R. D., et al. 2002, MNRAS, 329, 227

Sakai, S., Mould, J. R., Hughes, S. M. G., et al. 2000, The Astrophysical Journal, 529, 698

Salaris, M., & Cassisi, S. 1997, MNRAS, 289, 406

Salpeter, E. E. 1964, ApJ, 140, 796

Savage, B. D., & Mathis, J. S. 1979, ARA&A, 17, 73

Schaye, J. 2004, The Astrophysical Journal, 609, 667

Schlafly, E. F., & Finkbeiner, D. P. 2011, ApJ, 737, 103

Schlegel, D. J., Finkbeiner, D. P., & Davis, M. 1998, ApJ, 500, 525

Sersic, J. L. 1968, Atlas de Galaxias Australes

Seyfert, C. K. 1943, ApJ, 97, 28

Schmidt, M. 1963, , 197, 1040

Schwarzschild, K. 1916, Abh. Konigl. Preuss. Akad. Wissenschaften Jahre 1906,92, Berlin,1907, 1916, 189

Shappee, B. J., & Stanek, K. Z. 2011, ApJ, 733, 124

Shappee, B. J., Prieto, J. L., Grupe, D., et al. 2014, The Astrophysical Journal, 788, 48

Shaya, E. J., Tully, R. B., Hoffman, Y., & Pomarède, D. 2017, ApJ, 850, 207

Sheth, K., Regan, M., Hinz, J. L., et al. 2010, PASP, 122, 1397

Shi, Y., Rieke, G. H., Ogle, P. M., Su, K. Y. L., & Balog, Z. 2014, The Astrophysical Journal Supplement Series, 214, 23

Shostak, G. S. 1978, A&A, 68, 321

Silk, J., & Rees, M. J. 1998, A&A, 331, L1

Skielboe, A., Pancoast, A., Treu, T., et al. 2015, MNRAS, 454, 144

Slipher, V. M. 1917a, Proceedings of the American Philosophical Society, 56, 403

—. 1917b, Lowell Observatory Bulletin, 3, 59

Smith, B. J., Kleinmann, S. G., Huchra, J. P., & Low, F. J. 1987, ApJ, 318, 161

Smith, K. L., Boyd, P. T., Mushotzky, R. F., et al. 2015, AJ, 150, 126

Smith, G. P., Treu, T., Ellis, R. S., Moran, S. M., & Dressler, A. 2005, ApJ, 620, 78

Sorce, J. G., Tully, R. B., Courtois, H. M., et al. 2014, MNRAS, 444, 527

Spitler, L. R., & Forbes, D. A. 2009, MNRAS, 392, L1

Spitzer, L. 1998, Physical Processes in the Interstellar Medium (Wiley)

Springob, C. M., Haynes, M. P., Giovanelli, R., & Kent, B. R. 2005, ApJS, 160, 149

Staveley-Smith, L., & Davies, R. D. 1987, MNRAS, 224, 953

Steinborn, L. K., Dolag, K., Hirschmann, M., Prieto, M. A., & Remus, R.-S. 2015, MNRAS, 448, 1504

Stewart, K. R., Bullock, J. S., Wechsler, R. H., & Maller, A. H. 2009, ApJ, 702, 307

Stierwalt, S., Haynes, M. P., Giovanelli, R., et al. 2005, in Bulletin of the American Astronomical Society, Vol. 37, American Astronomical Society Meeting Abstracts, 1480

Stocke, J. T., Morris, S. L., Gioia, I. M., et al. 1991, The Astrophysical Journal Supplement Series, 76, 813

Strauss, M. A., & Huchra, J. 1988, AJ, 95, 1602

Strauss, M. A., Huchra, J. P., Davis, M., et al. 1992, The Astrophysical Journal Supplement Series, 83, 29

Tamburro, D., Rix, H.-W., Leroy, A. K., et al. 2009, The Astronomical Journal, 137, 4424

Teng, S. H., Veilleux, S., & Baker, A. J. 2013, ApJ, 765, 95

Theureau, G., Bottinelli, L., Coudreau-Durand, N., et al. 1998, A&AS, 130, 333

Theureau, G., Hanski, M., Coudreau, N., Hallet, N., & Martin, J.-M. 2006, VizieR Online Data Catalog, 346

Theureau, G., Hanski, M. O., Coudreau, N., Hallet, N., & Martin, J. M. 2007, A&A, 465, 71

Theureau, G., Coudreau, N., Hallet, N., et al. 2005, A&A, 430, 373

Thim, F., Hoessel, J. G., Saha, A., et al. 2004, AJ, 127, 2322

Tifft, W. G., & Cocke, W. J. 1988, The Astrophysical Journal Supplement Series, 67, 1

Tilton, E. M., Danforth, C. W., Shull, J. M., & Ross, T. L. 2012, ApJ, 759, 112

Tinker, J., Kravtsov, A. V., Klypin, A., et al. 2008, The Astrophysical Journal, 688, 709

Toomre, A., & Toomre, J. 1972, ApJ, 178, 623

Tonry, J. L., Dressler, A., Blakeslee, J. P., et al. 2001, ApJ, 546, 681

Tremaine, S., Gebhardt, K., Bender, R., et al. 2002, ApJ, 574, 740

Trujillo, I., Chamba, N., & Knapen, J. H. 2020, MNRAS, 493, 87

Tsvetkov, D. Y., Baklanov, P. V., Potashov, M. S., et al. 2019, Monthly Notices of the Royal Astronomical Society, 487, 3001

Tully, R. B., & Courtois, H. M. 2012, ApJ, 749, 78

Tully, R. B., Courtois, H. M., & Sorce, J. G. 2016, The Astronomical Journal, 152, 50

Tully, R. B., & Fisher, J. R. 1977, A&A, 54, 661

—. 1988, Catalog of Nearby Galaxies

Tully, R. B., & Fouque, P. 1985, ApJS, 58, 67

Tully, R. B., & Pierce, M. J. 2000, ApJ, 533, 744

Tully, R. B., Pierce, M. J., Huang, J.-S., et al. 1998, AJ, 115, 2264

Tully, R. B., Rizzi, L., Shaya, E. J., et al. 2009a, AJ, 138, 323

—. 2009b, AJ, 138, 323

Tully, R. B., Shaya, E. J., Karachentsev, I. D., et al. 2008, ApJ, 676, 184

Tully, R. B., Verheijen, M. A. W., Pierce, M. J., Huang, J.-S., & Wainscoat, R. J. 1996, AJ, 112, 2471

Tully, R. B., Courtois, H. M., Dolphin, A. E., et al. 2013, AJ, 146, 86

Tyson, J. A., Fischer, P., Guhathakurta, P., et al. 1998, AJ, 116, 102

Urry, C. M., & Padovani, P. 1995, PASP, 107, 803

van Driel, W., Marcum, P., Gallagher, III, J. S., et al. 2001, A&A, 378, 370

van Gorkom, J. H., Knapp, G. R., Ekers, R. D., et al. 1989, AJ, 97, 708

Vazdekis, A., Sánchez-Blázquez, P., Falcón-Barroso, J., et al. 2010, MNRAS, 404, 1639

Veilleux, S., Kim, D.-C., Rupke, D. S. N., et al. 2009, The Astrophysical Journal, 701, 587

Verheijen, M. A. W., & Sancisi, R. 2001, A&A, 370, 765

Vermot, P., Clénet, Y., Gratadour, D., et al. 2021, A&A, 652, A65

Vestergaard, M., & Peterson, B. M. 2006, The Astrophysical Journal, 641, 689

Volonteri, M., Dubois, Y., Pichon, C., & Devriendt, J. 2016, MNRAS, 460, 2979

Walter, F., Brinks, E., de Blok, W. J. G., et al. 2008, AJ, 136, 2563

Wang, J., Koribalski, B. S., Serra, P., et al. 2016, MNRAS, 460, 2143

Wang, J.-M., Du, P., Hu, C., et al. 2014, ApJ, 793, 108

Westmeier, T., Jurek, R., Obreschkow, D., Koribalski, B. S., & Staveley-Smith, L. 2014, MNRAS, 438, 1176

White, R. J., & Peterson, B. M. 1994, PASP, 106, 879

Whittle, M. 1992, ApJS, 79, 49

Williams, P. R., Pancoast, A., Treu, T., et al. 2018, ApJ, 866, 75

—. 2020, ApJ, 902, 74

Willott, C. J., Albert, L., Arzoumanian, D., et al. 2010, AJ, 140, 546

Wolfinger, K., Kilborn, V. A., Koribalski, B. S., et al. 2013, MNRAS, 428, 1790

Wong, D. S., Chornock, R., & Filippenko, A. V. 2008, Publications of the Astronomical Society of the Pacific, 120, 266

Wong, T., & Blitz, L. 2002, ApJ, 569, 157

Woo, J.-H., Schulze, A., Park, D., et al. 2013, ApJ, 772, 49

Woo, J.-H., Yoon, Y., Park, S., Park, D., & Kim, S. C. 2015, 801, 38

Woo, J.-H., Treu, T., Barth, A. J., et al. 2010, ApJ, 716, 269

Wu, X.-B., & Jia, Z. 2010, MNRAS, 406, 1583

Xue, Y. Q., Brandt, W. N., Luo, B., et al. 2010, The Astrophysical Journal, 720, 368

Yegorova, I., Babic, A., Salucci, P., Spekkens, K., & Pizzella, A. 2011, Astronomische Nachrichten, 332, 846

Young, J. S., & Knezek, P. M. 1989, ApJ, 347, L55

Yuan, W., Fausnaugh, M. M., Hoffmann, S. L., et al. 2020a, ApJ, 902, 26

Yuan, W., Macri, L. M., Peterson, B. M., et al. 2020b, arXiv e-prints, arXiv:2012.05931. 2012.05931

Zackrisson, E. 2005, PhD thesis, Department of Astronomy and Space Physics, Uppsala University, Sweden

Zaritsky, D., Courtois, H., Muñoz-Mateos, J.-C., et al. 2014, The Astronomical Journal, 147, 134

Zeldovich, Y., & Novikov, I. 1964, SSSR, 158, 811

Zhang, H.-X., Hunter, D. A., Elmegreen, B. G., Gao, Y., & Schruba, A. 2012, The Astronomical Journal, 143, 47

Zhao, X., Marchesi, S., Ajello, M., Baloković, M., & Fischer, T. 2020, ApJ, 894, 71

Zu, Y., Kochanek, C. S., & Peterson, B. M. 2011, ApJ, 735, 80

Appendix A

In Sec. 3.5.2, we presented the derivations of the inclination and redshift corrections for the $V-$band TF calibration. Here, we describe those derivations in detail.

To constrain the inclination-dependent correction for the V-band TF calibration, we have followed the same procedures described by Tully et al. (1998). Their analysis includes B, R, I, and K' photometric data from 2 nearby galaxy clusters. The first is the Ursa Major cluster, whose data are available from Tully et al. (1996). The second is the Pisces Cluster, whose data were used in the analysis of Tully et al. (1998), but were not made publicly available until the work of Tully & Pierce (2000). Two tests of extinction as a function of galaxy inclination were conducted by Tully et al., the first and most sensitive of which describes constructing color-magnitude diagrams of B, R, and I passbands relative to the K' passband. Reddening effects in K' are small, therefore the extinction effects on the galaxies are dominant in the color terms. We identified all galaxies in both clusters used in the analysis of Tully et al. (1998), and collected available $V-$band magnitudes from RC3, as the adopted $B-$band magnitudes of Tully et al. show an almost exact match to those listed in RC3.

We adopt the same K' apparent magnitudes and distance moduli reported by Tully et al. (1998) for each cluster (31.33 for Ursa Major, 33.88 for Pisces) to derive absolute K' magnitudes. The apparent magnitudes in their analysis include $k-$corrections and Galactic extinction corrections. They detail that the $k-$corrections were extremely small given the proximity of each cluster; specifically, they report $k-$corrections of $\sim$0 mag for the Ursa Major galaxies and $\sim 0.03 \pm 0.03$ mag for the Pisces galaxies at B, and even less significant ($\lesssim 0.01$ mag) in the redder bands. Therefore, we have not considered $k-$corrections for the $V-$band for this portion of our analysis. The Galactic

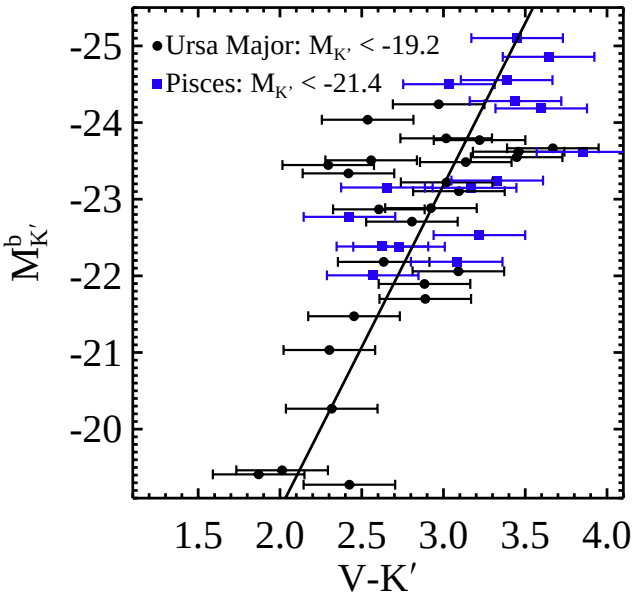

Figure A.1: Color-magnitude diagram for the Ursa Major and Pisces clusters used for the analysis of the inclination-dependent extinction correction for our TF V-band calibration. Ursa major galaxies are displayed as black circles, Pisces galaxies as blue squares.The Ursa Major cluster data is available in Tully et al. (1996), and the Pisces cluster in Tully & Pierce (2000). The $V-$band magnitudes were retrieved from RC3. The $M_{K'}$ values were derived using the same distance modulii in the original analysis of Tully et al. (1998), 31.33 for Ursa Major and 33.88 for Pisces. The cuts to $M_{K'}$ for each cluster are also consistent with their analysis. V and $K'-$band magnitude uncertainties are assumed to be 0.2 mag (see Appendix A). The line is a linear regression with uncertainties in the color.

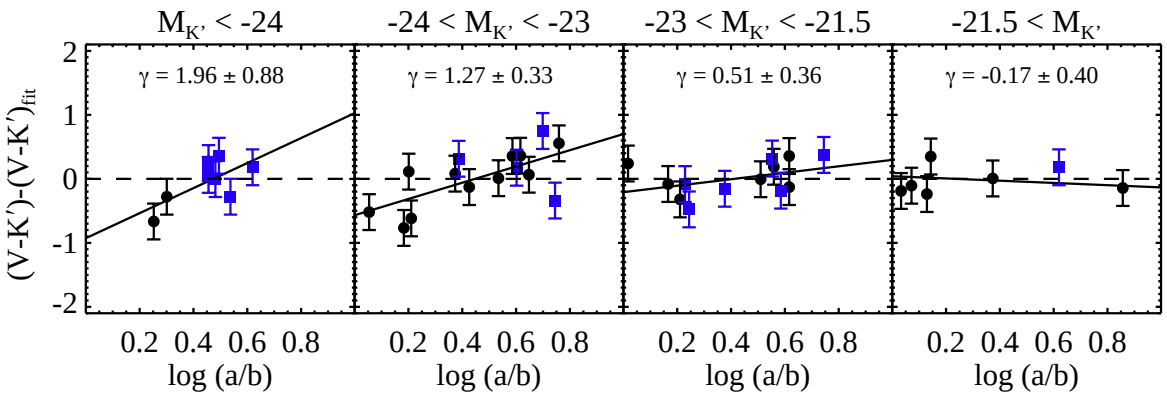

Figure A.2: Deviations of $V-K'$ from the mean (best-fit line) of the color-magnitude relation of Fig. A.1 as a function of the log of the axis ratio of each galaxy. The centers of the 4 luminosity bins are adjusted from those used by Tully et al. (1998) to better evenly separate the data. Black circles are members of the Ursa Major cluster, and blue squares are members of the Pisces cluster. The solid black lines are linear regression solutions to $A_i^\lambda = \gamma_\lambda \log(a/b)$. The lack of data in the lowest luminosity bin resulted in a non-physical negative slope, and we adopt 0.00 ± 0.40 for this bin for the remainder of our analysis.

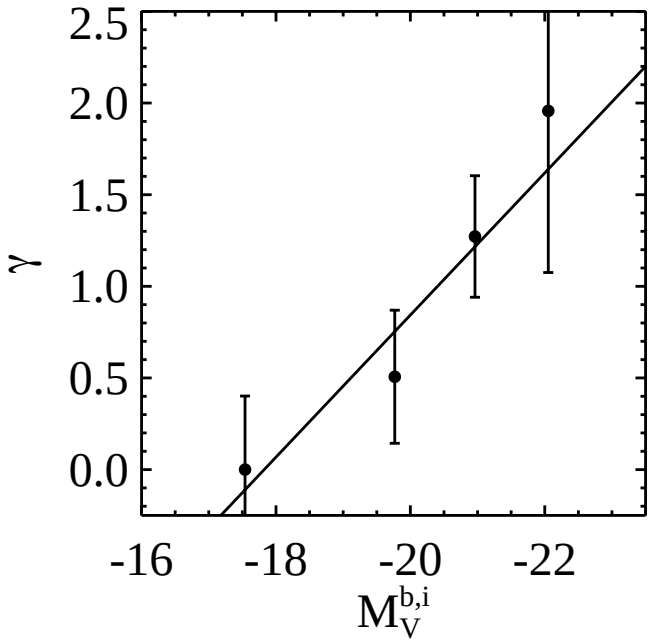

Figure A.3: Dependency of the γ values from the fits displayed in Fig. A.2 of each K' luminosity bin. The 4 points are the median $M_V^{b,i}$ values of each bin, and were derived from the distance moduli to each cluster used in the original analysis of Tully et al. (1998). The magnitudes were first corrected for galactic extinction and second for inclination-dependent extinction from each corresponding K' luminosity bin. The solid line is a linear regression with uncertainties in γ from the fits in each bin.

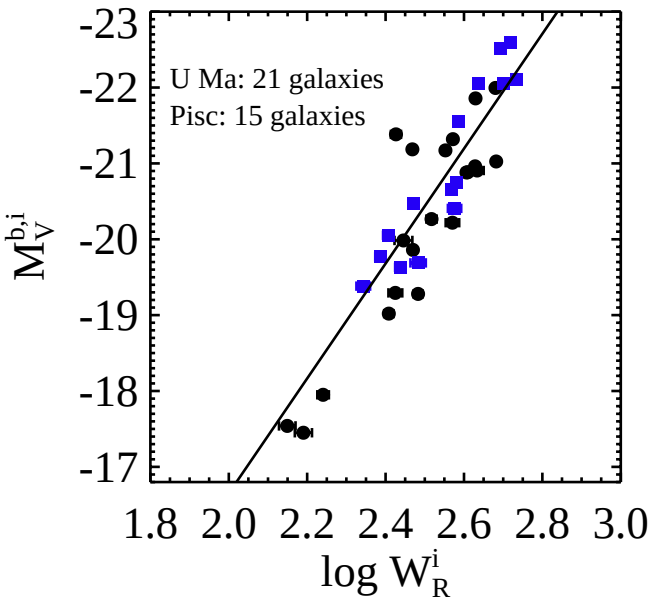

Figure A.4: The TF relation of the calibrating sample of Tully et al. (1998) for the $V-$band inclination-dependent extinction correction. Ursa major galaxies are displayed as black circles, Pisces galaxies as blue squares. The absolute $V-$band magnitudes are corrected for galactic extinction and inclination-dependent extinction using the best-fit solution for $A_i^\lambda = \gamma_\lambda \log(a/b)$ in Fig. A.3. The former width parameter W_R is used here. The solid line is the best fit to the data, with uncertainties in the HI line widths from Tully et al. (1998).

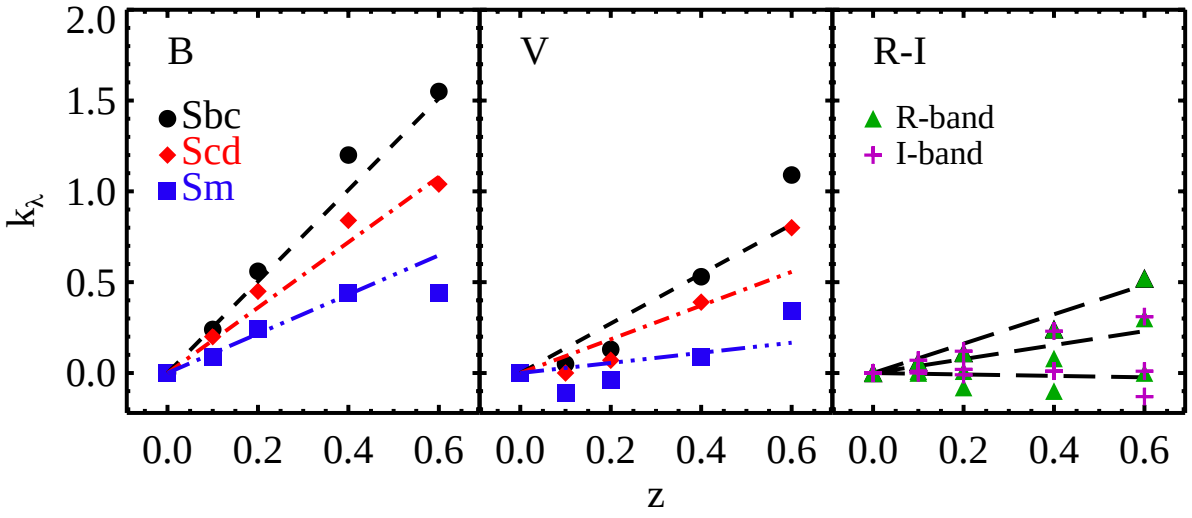

Figure A.5: k–corrections for B, V, R, and I bands. Data were retrieved from Frei & Gunn (1994). The black (dashed), red (dot-dashed), and blue (dot-dot-dot-dashed) lines in the left panel, and the black double-dashed lines in the right panel, are the B and $R-I$ k–correction prescriptions from Tully & Pierce (2000), respectively. Excellent agreement is found when Hubble type Sbc corresponds to T=3, Scd to T=5, and Sm to T=7. The fits in the right panel assume $R-I$ values of 0.45, 0.35, and 0.25 for the top, middle, and bottom lines. The middle panel displays our best-fits to the V–band k–corrections (where Sbc, Scd, and Sm correspond to T values of 4, 6, and 9, respectively), constrained such that $k_V = 0$ at $z = 0$.

extinction corrections for the B−band were drawn from Burstein & Heiles (1984), and Tully et al. report extinction ratios between the separate bands, yet do not detail how they arrived at the given ratios. In order to estimate the extinction ratio for the V band, we assumed an average extinction curve of $R = A_V/E(B-V) = 3.1$ (Savage & Mathis 1979; which also approximates the R/B and I/B extinction ratios listed by Tully et al. 1998 to within $\sim$0.05), and arrived at an extinction ratio of $V/B = 0.76$.

In Fig. A.1, we display the absolute K' magnitudes vs $V-K'$ color. Ursa Major galaxies are plotted in black circles, Pisces galaxies in blue squares. We make consistent magnitude cuts ($M_{K'} <$ -19.2 for Ursa Major, $M_{K'} <$ -21.4 for Pisces), which Tully et al. detail as the cutoffs for their K'−band completeness limits. Several of the lower-luminosity galaxies that were originally included in the Tully et al. (1998) analysis do not have V−band magnitudes available in RC3, so the low-luminosity end of the color-magnitude diagram is only sparsely populated. Tully et al. describe their linear regression to the color-magnitude diagram with uncertainties in the color, yet no uncertainties are provided for the magnitudes. We find that we can reasonably reproduce the results of Tully et al. for the B band when a typical uncertainty of 0.2 mag is assumed for the photometry. Thus, we adopt 0.2 mag uncertainty for the V and K' magnitudes, and find a best fit of $M^b_{K'} = (-4.23 \pm 0.56)(V-K') - (10.50 \pm 1.67)$.

The next portion of the analysis assumes that deviations from the mean of the color-magnitude relation (given by the best-fit line in Fig. A.1) are dominated by inclination-dependent obscuration. Tully et al. found that the extinction dependence on inclination is also a function of luminosity, where brighter galaxies have a much higher dependence than fainter galaxies. To quantify the luminosity dependencies for the $B-K'$, $R-K'$, and $I-K'$ colors, they separated the galaxies into 4 luminosity bins and plotted the deviations as a function of disk axis ratio. In Fig. A.2, we show the deviations from the $V-K'$ fit as a function of axis ratio. Following Tully et al., we have split the sample into four bins, but with slightly different bin centers that account for the small number of galaxies at the lowest luminosities.

The extinction parameter is often described as $A_i^\lambda = \gamma_\lambda \log(a/b)$, where λ is the passband and a/b is the ratio of major to minor axes. The solid black lines in Fig. A.2 are the best fits, where the slope is γ and where A_i^V is assumed to be $(V-K')-(V-K')_{fit}$. We find smaller deviations from the mean color at lower galaxy luminosities, in agreement with the findings of Tully et al. In the lowest luminosity bin, we find a best fit with a negative slope, which is nonphysical, but is also formally consistent with zero. For that bin, we therefore adopt a slope of 0.00 ± 0.40. In Fig. A.3 we display the best-fit slope for each bin versus the absolute $V-$band magnitude associated with the median luminosity of each bin, corrected for inclination and Galactic extinction. We assume a linear function for the magnitude dependence of the inclination-dependent extinction correction, and find $\gamma_V = (-0.39 \pm 0.14) M_V^{b,i} - (6.91 \pm 2.79)$. We find a negligible change if we instead employ the median $M_{K'}$ of each bin and adopt the $(V-K')$ value of the fit in Fig. A.1 to predict $M_V^{b,i}$. With this method, we find $\gamma_V (-0.36 \pm 0.13) M_V^{b,i} - (6.31 \pm 2.60)$, where the slopes are nearly identical and the intercept has shifted slightly, but is well within the uncertainties.

The last step in the analysis of Tully et al. (1998) involves applying the inclination corrections to the absolute magnitudes in order to re-derive the luminosity-HI line width relation. The definition of the line width parameter used here and in Tully et al. (1998) predates the newer definition of Courtois et al. (2009a), so we denote this previous version as $W_{\rm R}^i$ for consistency. We adopt the same line widths and uncertainties from Tully et al. (1998). We apply our derived inclination corrections to the $V-$band absolute magnitudes of the galaxies in the Pisces and Ursa Major clusters, and plot them against the corresponding $W_{\rm R}^i$ values in Fig. A.4. The solid line is the best fit, $M_V^{b,i} = (-20.44 \pm 0.01) - (7.57 \pm 0.01)(\log W_{\rm R}^i - 2.5)$. Lastly, our equations for γ_V and $M_V^{b,i}$ can now be used to derive γ_V solely in terms of the distance-independent variable $W_{\rm R}^i$, which we find to be $\gamma_V = (1.01 \pm 4.06) + (2.94 \pm 1.09)(\log W_{\rm R}^i - 2.5)$.

With the inclination-dependent extinction correction defined, we next turn to the $k-$correction. With no reference for their calibrating data set, we have assumed the data used to constrain the prescriptions of Tully & Pierce (2000) may come from the well-cited work of Frei & Gunn (1994). Their study reports $k-$corrections in the $B-$band (k_B) for various colors for galaxies with

Hubble types E, Sbc, Scd, and Sm that are located between $0 < z < 0.6$. When used with their prescription $k_B(z) = B(z) - B(z=0) - 2.5\log(1+z)$, the k–correction in any filter can be derived by taking the difference between B and another magnitude, using the corresponding color information they provide. We tested our assumption by comparing the data from Frei & Gunn (1994) to the prescriptions of Tully & Pierce (2000). The results are shown in Fig. A.5. The left panel contains the k–corrections for the B band, and the right for the R and I bands. The lines in each are best-fits to the data, where the B and $R-I$ fits are from Tully & Pierce (2000), given as $A_k^B = (3.6 - 0.36T)z$ and $A_k^R = [4.24(R-I) - 1.10]z$, respectively. We found excellent agreement for the B–band data, however only if we shift each Hubble type T to a lower integer. For example, Hubble type Sbc corresponds to $T = 4$, yet we only find a satisfactory fit to the Sbc k–corrections if $T = 3$ is used. The same is true for Scd, where we find a matching fit if $T = 5$ is used, as opposed to $T = 6$. For the Sm data, which normally corresponds to $T = 9$, we find a good fit if $T = 7$ is used. For the R and I k–corrections, Tully & Pierce (2000) prescribe one fit to characterize both sets of data. We find good agreement with the data from Frei & Gunn (1994) when $R-I$ values of 0.45, 0.35, and 0.25 are adopted for Sbc, Scd, and Sm types.

Given that our assumption of Tully et al. (1998) basing their work on the data of Frei & Gunn (1994) seems to hold, we therefore determined the k–correction in a similar way for the V band, and display it in the center panel of Fig. A.5. The corrections in the B band are highly dependent on the morphological classification, while the R and I bands have much less of a spread as a function of morphology. This is reflected in the formalisms of each correction, as T is a factor in the B–band calibration yet is absent in the $R-I$ calibration. While the V band has less of a dependence on morphology than the B band, we nevertheless sought to arrive at a morphologically-dependent calibration given the obvious spread as a function of T. We assume, as we did with the B band, that the Sbc, Scd, and Sm classifications correspond to $T = 4$, 6, and 9 respectively, and that $k_V = 0$ at $z = 0$. We fit the data for the 3 Hubble types, and solved for a universal fit such that T was a scale factor which yielded the 3 solutions, and arrived at $A_k^V = (2.23 - 0.22T)z$.

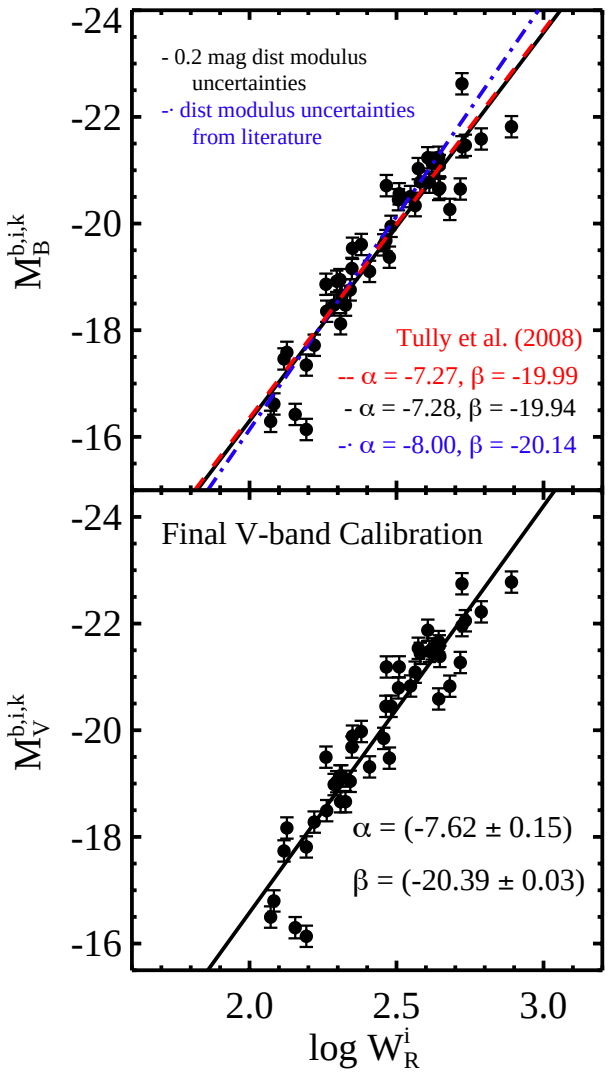

Figure A.6: TF *B*−band calibration (top) and our final TF *V*−band calibration (bottom). *B*−band magnitudes, widths, and distance moduli were retrieved from Tully et al. (2008) for galaxies which had primary distance measurements from either Cepheids, TRGB, and/or SBF. *V*−band magnitudes were retrieved from RC3. The red dashed line in the top panel is the fit reported by Tully et al. (2008). The blue dot-dashed line is our fit using published distance modulus uncertainties, which resulted in a steeper slope than that reported (the slopes and intercepts of which are displayed; the top is the fit given by Tully et al. (2008), the bottom corresponds to the blue dot-dashed fit). Adopting 0.2 mag uncertainty in the moduli achieves a near perfect match to the fit by Tully et al. (2008), shown as the solid black line and displayed as the middle slope and intercept. The solid black line in the bottom panel is our best-fit to the *V*−band TF calibration using distance moduli with 0.2 mag uncertainties, Galactic extinction corrections from Schlegel et al. (1998), and our calibrations for the *V*−band inclination correction (see equation 3.17, Fig. A.4) and *k*−correction (see equation 3.18, Fig. A.5.)

While the $k-$corrections are derived using galaxies out to $z = 0.6$, the TF method is only applicable to galaxies at $z \lesssim 0.1$ (Reyes et al., 2011), and Tully & Pierce (2000) describe the corrections as always < 0.08 mag in the B band. The maximum expected $k-$correction in the V band is 0.2, which would correspond to $T = 1$ at $z = 0.1$. This correction is larger than the upper limit reported by Tully & Pierce (2000) for the B band, however $z \lesssim 0.03$ for their sample.

Finally, with the inclination and $k-$corrections in hand, we were able to derive the $V-$band TF relation. We first identified all galaxies in the calibrating sample of Tully et al. (2008) that had distances derived from Cepheids, TRGB, and SBF. From their VizieR table, we retrieved the $B-$band magnitudes, distance moduli, and $W^i_{\rm R}$ values. In addition, we retrieved all available B and $V-$band magnitudes from RC3, as well as all original distance moduli and uncertainties from the literature for the calibrating sample. The distances reported by Tully et al. (2008) match the original published values and do not appear to have been updated in any way.

We first aimed to recreate the fit to the $B-$band relationship by Tully et al. (2008). Since the difference was negligible, we began by using the originally published values of the distance moduli and uncertainties, with $B-$band magnitudes from RC3. Galactic extinction values were retrieved from Schlegel et al. (1998), and inclination and $k-$corrections were applied with equations 3.11 and 3.14. The difference in fits using $B-$band apparent magnitudes from RC3 versus magnitudes from Tully et al. (2008) was negligible. When the published uncertainties on the distance measurements were used to convert apparent magnitudes to absolute magnitudes, the fit resulted in a slightly steeper slope than that reported, as shown in the top panel of Fig. A.6, where the reported fit from Tully et al. (2008) is the red dashed line, and our best fit is the blue dot-dashed line. Tully et al. (2008) assert that galaxies with distances from Cepheids, TRGB, or SBF are assumed to have a 0.2 mag uncertainty in their moduli. If we adopt this, we reproduce the $B-$band fit almost exactly, shown as the solid black line in Fig. A.6.

Thus, the $V-$band apparent magnitudes from RC3 for the calibrating sample of Tully et al. (2008) were corrected for Galactic extinction using values from Schlegel et al. (1998), and for inclination-dependent extinction and $k-$corrections using equations 3.17 and 3.18. The distance

moduli were then used to convert the corrected apparent magnitudes to absolute magnitudes, with 0.2 mag typical uncertainty adopted for the distance moduli. Our best fit to the relationship between $M_V^{b,i,k}$ and $W_{\rm R}^i$ for the calibrating sample is shown in the bottom panel of Fig. A.6, and is given by equation 3.19 as $M_V^{b,i,k} = (-20.39 \pm 0.03) - (7.62 \pm 0.15)(\log W_{mx}^i - 2.5)$.